UNIVERSITY OF SOUTHAMPTON

FACULTY OF ENGINEERING, SCIENCE & MATHEMATICS

OPTOELECTRONICS RESEARCH CENTRE

Study of the Physics of the Power-Scaling of End-Pumped Solid-State Laser Sources Based on Nd:YVO_4

by

Ian Oliver Musgrave

Thesis submitted for the degree of Doctor of Philosophy

September 2003

University of Southampton

ABSTRACT

FACULTY OF ENGINEERING, SCIENCE AND MATHEMATICS
OPTELECTRONICS RESEARCH CENTER

Doctor of Philosophy

Study of the physics of the power-scaling of end-pumped solid-state laser sources based on Nd:YVO_4.

by Ian Oliver Musgrave

This thesis presents a study of the physics of power-scaling end-pumped solid-state laser sources based on Nd:YVO_4. To achieve this Nd:YVO_4 is characterised and different power-scaling methodologies are considered before using a master oscillator power amplifier scheme to generate these powers.

The energy transfer upconversion (ETU) parameter is measured and its effect on lasing is examined in Nd:YVO_4. By measuring the fluorescence decay from the upper laser level it is found that the ETU parameter has a value of $3.5 \times 10^{-22} m^3 s^{-1}$ for a 1% dopant concentration. The effect of ETU on lasing is examined by using the rate equations for the upper laser level and the number of photons in the cavity to derive an equation for the pump power required to reach threshold with losses due to ETU included. The impact of the measured value of the ETU parameter on threshold pump power was investigated by building a laser in which the cavity loss could be varied. It was found that this value for the ETU parameter did not have significant impact on the threshold pump power for losses typical in the CW regime.

Using a modified Mach-Zehnder interferometer the thermal lensing in Nd:YVO_4 was measured for several different operating conditions. The thermal lens focal length can be determined from the measured transverse phase profile. It was found that the thermal lensing was weakest for π-polarised light and that the bulk expansion plays a part in modifying the power of the thermal lenses. By comparing the thermal lensing with cooling direction it was found that the providing cooling along the a-axis generated the weakest thermal lensing. Comparing the thermal lensing under lasing and non-lasing conditions demonstrated that the heating in the laser crystal under non-lasing conditions is significantly greater than under lasing conditions. The thermal lenses are almost 5 times stronger under non-lasing conditions than lasing condition for the 1% doped crystal. By comparing the effect of dopant concentration on thermal lensing the effect of ETU could be seen, with the thermal lensing for the 0.3% doped crystal being much lower than that of the 1% doped crystal under non-lasing conditions.

An amplitude modulated mode-locked laser was built based on Nd:YVO_4 generating 600mW of diffraction limited output and 100ps pulses. Multipass amplification was then investigated as a means to increase the average power of the source. This was achieved with 5W of output achieved, with the beam remaining diffraction limited.

The prospects for further power scaling are investigated and it was shown that the limit to power scaling via amplifiers is the eventual beam quality degradation that will be suffered as the signal beam passes through the thermal lenses in the laser crystal. An equation was finally presented that analysed the limitations of scaling via amplifiers, finding that when stress-fracture and beam quality degradation are considered, Nd:YVO_4 represents an excellent choice for further power scaling.

Contents

Chapter 4: Thermal Effects in Nd:YVO_4

Chapter 5: Mode-locked Nd:YVO_4 Oscillator

Chapter 6:Nd:YVO_4 Amplifier Scheme

Chapter 7: Conclusions and Further Work

DECLARATION OF AUTHORSHIP

I, IAN OLIVER MUSGRAVE, [please print name]

declare that the thesis entitled [enter title]

STUDY OF THE PHYSICS OF THE POWER-SCALING OF END-PUMPED SOLID-STATE LASER SOURCES BASED ON Nd:YVO4

and the work presented in it are my own. I confirm that:

- this work was done wholly or mainly while in candidature for a research degree at this University;
- where any part of this thesis has previously been submitted for a degree or any other qualification at this University or any other institution, this has been clearly stated;
- where I have consulted the published work of others, this is always clearly attributed;
- where I have quoted from the work of others, the source is always given. With the exception of such quotations, this thesis is entirely my own work;
- I have acknowledged all main sources of help;
- where the thesis is based on work done by myself jointly with others, I have made clear exactly what was done by others and what I have contributed myself;
- ~~none of this work has been published before submission; or~~ [delete as appropriate] parts of this work have been published as: [please list references]

  AS DETAILED IN APENDIX C.

Signed: Ian Musgrave

Date: 30/09/03

Acknowledgements

I would like to than Dr. W.A. Clarkson, for guidance, advice and supervision, without whom this project would not have been possible.

I would like to thank EPSRC for providing the funding for the work presented here.

All the members of the advanced solid-state sources group, past and present, including Rob, Nigel, Tim, Amin and Mike.

All the backroom guys that make the 'gubbins' that hold the 'pretty bits of glass'.

My friends and family for keeping me sane and providing encouragement. Especially Mark for the 'dirty' weekends that provided much needed stress relief.

I would like to especially thank Vir, who has provided immeasurable support and love when the lights flashed and when they did not.

Thank You

Chapter 1: Introduction

1.1 Introduction

Lasers have many diverse applications, where their unique properties are advantageous. The heat generated at the focus of a high power laser beam can be used in materials processing achieving more precise and cleaner machining then other more traditional methods. Lasers have been used in the restoration of monuments, allowing the minimisation of the amount of material removed, achieved by monitoring the reflected light which varies as the damage caused by pollutants is removed. The study and generation of nonlinear optical processes requires high power sources and the entertainment industry requires very bright sources of red, green and blue for use in digital projection schemes. Diode pumped solid state lasers have been successfully used in many of these applications, but the scaling of these devices has been hindered by the onset of thermal problems and the beam quality of the available pump sources.

End pumping of solid state lasers at low pump powers is an efficient method for generating laser output with the attraction that fundamental transverse mode and linearly-polarised operation are relatively straightforward to achieve. The relatively good beam quality of low power diode pump sources allows tight focusing, enabling the efficient operation of solid-state lasers on a range of different laser transitions. End pumping also allows a great deal of flexibility in resonator design and mode of operation. Retaining these attractive operating characteristics whilst scaling end pumped lasers to much higher power levels becomes increasingly difficult as the pump power is increased. This is partly due to the poor beam quality of high power diode arrays, but mainly due to heat generation within the solid-state laser medium and deleterious effects on beam quality and efficiency. Over the last decade there has been growing interest in developing methods for mitigating the effects of poor pump beam quality and heat generation. These methods include design of novel resonators and pump focusing schemes and the development of new materials. A key factor in the laser design is the choice of laser host. For many years Nd:YAG has been the crystal of choice due to its robust thermo-mechanical properties, low loss and relatively good spectral properties. However, in end pumped configurations, Nd:YAG has a number of

shortcomings including strong thermal lensing, stress-induced birefringence and high loss due to energy transfer upconversion (ETU). Recently Nd:YVO_4 has emerged as an attractive alternative to Nd:YAG in end-pumping applications. Being birefringent the laser emission is naturally polarised, and with its large $\sigma\tau$ product large gain amplifiers and low threshold lasers are relatively easy to construct. For typical dopant concentrations Nd:YVO_4 has a large absorption coefficient providing a degree of tolerance of poor diode beam quality. The wide absorption bandwidth at 809nm makes it attractive for diode pumping because it is less sensitive to variations in the emission wavelength caused by temperature fluctuations.

In spite of its successful implementation in a number of laser and amplifier systems, and several commercial products with output powers up to 33W[1], a detailed study of the power scaling potential of Nd:YVO_4 has yet to be conducted. In fact, Nd:YVO_4 has a number of interesting properties including complex thermal lensing behaviour and strong upconversion losses, which must be understood and taken into account when designing high power laser systems. Indeed, an intriguing question is: Does Nd:YVO_4 offer the potential for scaling TEM00 operation to even higher power levels and, if so, what is the upper limit and how is this affected by the resonator/ amplifier design. The goal of the project described herein was to answer this question by conducting a detailed study into thermal lensing and ETU in Nd:YVO_4 and to develop a strategy for power scaling based on the results using a master-oscillator power amplifier configuration. This configuration is based on a master oscillator, working at low powers to produce a beam with good beam quality, which is then amplified by different amplifier stages. These amplifier stages increase the power of the beam, without degrading its beam quality. In this way a high power laser source can be built, with good beam quality. This power scaling methodology can be applied to the power scaling of end-pumped lasers, to minimise the effect of thermal phenomena. The severity of these thermal phenomena is increased at high pump powers because the large population inversion densities that can be achieved that provide high levels of gain can also lead to increased rates of energy transfer upconversion. Energy transfer upconversion increases the amount of heat being generated in the laser crystal, therefore it is important to know the energy transfer upconversion parameter so that the increased heating caused by this mechanism can be determined. By measuring the

energy transfer upconversion parameter, its effect on lasing can be assessed and methods identified to reduce its impact. Determination of the focal length of the thermal lens that the heat generation causes allows a stable low power resonator to be designed with good beam quality and the optimum cooling geometry decided upon. Amplifiers can then be designed and built based on these results that can scale end-pumped lasers and retain their attractive properties to successfully generate high power pulses at 1μm.

This opening chapter briefly describes in a little more detail the historical background of diode end-pumped solid-state lasers, reviews some of the techniques used to scale their output power and in addition briefly reviews some of the key results obtained with Nd:YVO_4 as the gain medium. This chapter concludes with an outline of the thesis contents and a brief overview of the contents of each chapter.

1.2 Development of Diode End-Pumped Solid-State Lasers

A typical example of a diode end-pumped solid-state laser configuration is shown in figure (1-1). The laser has a very simple design comprising a diode array pump laser, pump beam collection and focusing optics and a two mirror stable resonator containing the gain medium. Pump light is transmitted through a dichoric mirror which forms part of the cavity and focused to a small beam waist inside the solid-state medium. The development of these lasers revolves around the development of the laser diode source and the gain medium. Different materials encouraged the development of laser diodes at certain wavelengths and the availability of new pump wavelengths allowed the use of new materials.

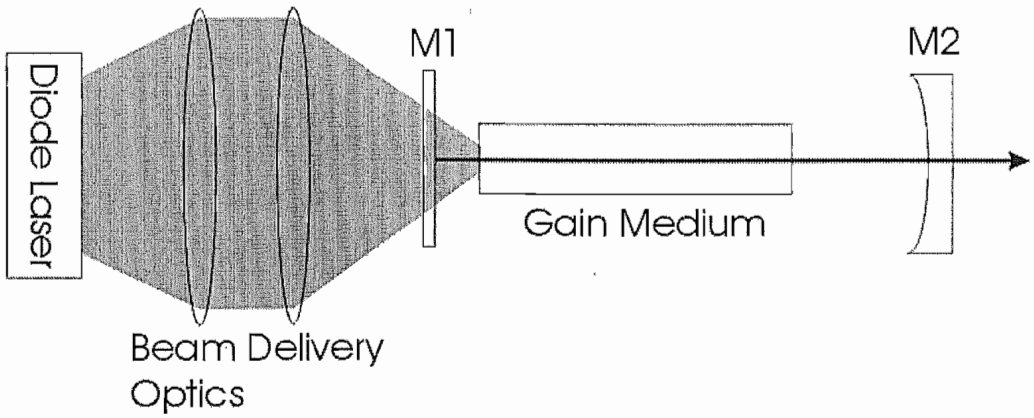

Figure (1-1). Example of a diode end-pumped solid-state laser.

Laser diodes have many advantages over traditional flash lamps. Flash lamps have higher electrical-to-optical efficiency then diodes, but their output has a much broader spectral width. A large fraction of the emitted radiation is not absorbed because it does not coincide with absorption bands of the gain material. Moreover, a significant fraction of the light that is absorbed raises the active ion to much higher energy levels and than the emitting band with the result that non-radiative decay to the emitting level results in unwanted heat generation. By carefully selecting the semi-conductor material, the laser diode emission wavelength can be chosen to match the desired pump transition, reducing thermal loading and hence improving the pumping efficiency. Controlling the operating temperature of the diode allows the emission wavelength to be fine-tuned, so that it coincides with the absorption peak or, when operating at the absorption peak leads to greater thermal loading density, can slightly be tuned away from it. The amount of tuning that can be achieved is typically ~0.3nm/K for laser diode arrays. Diodes have a much longer lifetime than lamps so need replacing less often and their quasi-spatial coherence allows coupling into multimode fibres for beam delivery.

The use of diode lasers as pump sources was initially quite unattractive because of the high cost, short lifetime and low output power of early devices. By using confinement structures and improvement in fabrication techniques, the threshold current was reduced, producing devices with longer lifetimes and higher output powers. Further scaling of the output power has been achieved by constructing devices with arrays of lasers on the same chip serving to further reduce the cost per Watt. Stacking of these arrays has lead to the development of high power diode-stack pump modules with output powers up to several kW. Scaling the power of these devices in this way however reduces their brightness, rendering their use in end-pumping applications more challenging.

Diode-pumped solid-state lasers have many advantages over the direct use of diode lasers. The output of solid-state lasers has a narrower frequency width, and improved beam quality when compared with diodes of similar powers. With their longer fluorescence lifetimes ~100s of μs for solid state-materials as opposed to ns for diode

lasers, the energy storage in solid-state materials allows high pulse energies to be achieved through Q-switching techniques.

The first report of a diode to pump a sold-state material employed a GaAs diode at 880nm to excite fluorescence in Nd:$CaWO_4$ near 1.06μm [2]. Shortly after the development of the first laser diodes, the first diode-pumped solid-state laser was demonstrated using $CaF_2:U^{3+}$ at 2.613μm. The early diode sources required cooling to achieve efficient operation and their laser assemblies were placed in liquid helium. Much of this early work concentrated on side-pumping where the number of pump diodes is more easily increased than in end-pumped configurations. However, it was recognized that end-pumping, with collinear propagation of laser and pump modes, has the advantage of more efficient pump absorption.

Due to its good thermo-mechanical properties, ease of crystal growth and popularity as a lamp pumped material, interest switched to Nd:YAG, and the first diode-pumped Nd:YAG laser was reported in 1968. Another reason for this material's popularity was the overlap between the emission of GaAs and GaAlAs diodes and the absorption band $^4F_{5/2}$ in Nd:YAG. In 1987, however, it was noted by Fields et al. that "Nd:YVO_4 is the crystal of choice for obtaining the highest cw power and lowest threshold from a diode-laser end-pumped laser device" [3].

1.3 Power Scaling End Pumped Lasers

Power scaling of end-pumped solid-state lasers is hindered by two problems, increasing the available pump power and the problems caused by higher pump power. Increasing the pump power is difficult in end-pumping because there are only two rod faces. Thermal effects at increased pump powers are a limiting factor because most of the heat is generated near the faces of the gain medium, the concentration of heat in these regions increases the risk of stress fracture and depending on the spot-size, produces thermal lenses with short focal lengths.

To increase the pump power diodes can be polarization multiplexed. This is acceptable providing the absorption coefficient of the gain medium is not strongly polarization

dependent e.g Nd:YAG. The use of fibre-delivered light from diodes carries with it the same pre-condition since the fibre is unpolarised. Multiple fibres in the form of a circular bundle can be used to increase the pump power, but at the expense of a degradation of the pump beam quality and hence a larger beam size. Diodes can also be spatially or angularly multiplexed with respect to the lasing axis in a so-called quasi-end-pumped layout [4] to increase pump power. An alternative approach employs a face-cooled thin disc laser, with multiple passes of the pump light through the gain medium using a complex arrangement of mirrors [5]. This requires the use of materials with short absorption lengths to ensure efficient pump absorption. Materials with short absorption lengths will be more susceptible to the onset of thermal problems in end-pumped configurations because the heat will be generated near the end-faces and this will increase the probability of stress fracture occurring.

The threshold for end-pumped solid-state lasers is dependent on the spot-sizes of the pump and laser mode in the laser medium, which are determined by the pump source and beam delivery optics, and the resonator design respectively. In practice, the minimum pump spot-size, and therefore the lowest threshold pump power for end-pumped configurations, is determined by the beam quality of the diode source. At low pump powers, the better overlap between pump beam and laser mode in the laser crystal means that end-pumped solid-state lasers are generally more efficient than side-pumped configurations.

1.4 Power Scaling using Nd:YVO_4

As a laser material Nd:YVO_4 benefits from several properties that make is attractive for diode-pumping. It has a stimulated emission cross-section approximately five times larger than Nd:YAG so it is capable of generating large gains and producing lasers with low threshold pump intensities.

With its wide absorption bandwidth, Nd:YVO_4 represents a good material for diode-pumping because it is less sensitive to changes in the diode emission wavelength caused by drifts in temperature and its short absorption length enables it to tolerate

pumps with poor beam quality. The stress fracture limit of Nd:YVO_4 lies between Nd:YLF and Nd:YAG restricting its use to low to medium power levels.

Reports of CW scaling of Nd:YVO_4 have been <50W, with 11.6W TEM00 for a laser pumped from a single end [6]. With pump light incident at both ends 25W has been reported [7]. Under side pumped conditions powers up to 33W have been demonstrated [1].

1.5 Master Oscillator Power Amplifier

Due to strong thermal lensing and the need to use multiple laser rods, scaling the output power in an oscillator configuration is quite challenging. For a high power source to be successful, the cavity needs to be stable over a broad range of thermal lens focal lengths. It is unlikely that the cavity will be stable in both the low and high power regimes. An alternative and potentially more practical approach is to use a master oscillator power amplifier (MOPA). MOPAs have the attraction that the desired mode of operation (e.g. mode-locked, Q-switched, single frequency) and the power scaling are de-coupled. In a MOPA system the mode of operation is primarily determined by the oscillator and the output power and final beam quality by the power amplifier stages. At high pump powers deleterious thermal effects can be reduced by increasing the beam radius of the pump beam in the crystal, or by using a crystal with low dopant concentration. However, increasing the pump beam radius will increase the required threshold pump power, reducing the overall efficiency of the system. Using low dopant concentrations places greater demands on the beam quality of the pump beam because of the longer crystals required to ensure efficient pump absorption. The use of a MOPA allows these reductions in performance to be negated to a certain degree because it enables a compromise to be found between the reduction in thermal effects generated and the loss of gain caused by an increase in the pump beam radius.

With this modular design strategy different parts perform certain roles in the final system. In this way the final system can be enhanced or added to by improving or replacing an existing module as higher pump powers or more laser diodes become available. This design approach allows greater flexibility in modifying the system.

1.6 Overview of Thesis

This thesis investigates the potential for using Nd:YVO_4 in the power scaling of end-pumped lasers to high powers. A detailed study is made of the effects of energy transfer upconversoin and thermal lensing in Nd:YVO_4. The results of these investigations are combined with a MOPA approach to scale the output of a mode-locked master oscillator to high average powers yet retaining good beam quality. This source can then be used for non-linear frequency conversion to generate a tuneable visible source with potential applications in material investigations. Prospects for further scaling using Nd:YVO_4 and this methodology are also considered.

Chapter 2 presents an overview of the theory of end-pumped four-level solid-state lasers and amplifiers. Diode pump sources and pumping schemes are briefly reviewed. The threshold and slope efficiency of end-pumped lasers are given. The problem of heat generation and thermal effects is discussed and different design strategies for power scaling end-pumped lasers and their limitations are reviewed.

Chapter 3 examines the influence of energy transfer upconversion (ETU) and in particular its effect on the performance of end-pumped Nd:YVO_4 lasers and amplifiers. The theory of upconversion is presented and the results of experiments aimed at determining the ETU parameter in Nd:YVO_4 via a measurement of the fluorescence decay are described. These results confirm that ETU is migration assisted in Nd:YVO_4. The equation for threshold for a four-level laser including the effect of ETU is derived for the first time and confirmed by measuring the threshold pump power in Nd:YVO_4 for different cavity losses and Nd^{3+} concentrations. The effect of ETU is then compared theoretically in Nd:YLF, Nd:YAG and Nd:YVO_4.

Chapter 4 presents a detailed investigation of the thermal lensing in Nd:YVO_4. The influence of ETU on thermal loading and its effects is discussed. Different techniques that have been used to determine the thermal lensing in solid-state lasers are discussed and compared. A method for measuring the thermal lensing in end-pumped lasers under lasing and non-lasing conditions based on a Mach-Zehnder interferometer is described. The results of measurements of thermal lensing in Nd:YVO_4 are given and it is found

that ETU can have a significant effect on thermal lensing. A theoretical comparison is then made of thermal lensing in Nd:YLF, Nd:YAG and Nd:YVO_4.

Chapter 5 describes an amplitude modulated (AM) mode-locked Nd:YVO_4 oscillator. The choice of Nd:YVO_4 as the gain medium is discussed and justified. The strategy used in the design of the oscillator is described and results for its performance are presented. The scope for further improvement in power and brightness is discussed.

Chapter 6 reports on a Nd:YVO_4 amplifier scheme comprising of a pre-amplifier and a power amplifier. The advantages and disadvantages of power scaling via amplifiers are discussed. The design strategy for amplifiers is presented. Equations are derived for the first time to model the effect of ETU and thermal lensing on amplifier performance. The influence of ETU on performance and the power and brightness scaling limit due to thermal lensing is considered. The design and results for the performance of the pre-amplifier are presented and discussed. The scalability of this approach is then discussed and a theoretical comparison of Nd:YLF, Nd:YAG and Nd:YVO_4 is made.

Chapter 7 presents the conclusions and future prospects for the work given in this thesis.

References

1. Thompson, B.A., A. Minassian, and M.J. Damzen, *Operation of a 33-W, continuous-wave, self-adaptive, solid-state laser oscillator.* J. Opt. Soc. Am. B, 2003. **20**(5): p. 857-862.
2. Fan, T.Y. and R.L. Byer, *Diode Laser-Pumped Solid-State Lasers.* IEEE Journal of Quantum Electronics, 1988. **24**(6): p. 895-912.
3. Fields, R.A., M. Birnbaum, and C.L. Fincher, *Highly efficient Nd:YVO_4 diode-laser end-pumped laser.* Applied Physics Letters, 1987. **51**(23): p. 1885-1886.
4. Tidwell, S.C., J.F. Seamans, and M.S. Bowers, *Highly efficient 60-W TEM_{oo} cw diode-end-pumped Nd:YAG laser.* Optics Letters, 1993. **18**(2): p. 116-118.

5. Stewen, C., et al., *A 1-kW CW Thin Disc Laser.* IEEE Journal of Selected Topics in Quantum Electronics, 2000. **6**(4): p. 650-657.

6. Zhang, J., et al., *Efficient TEM_{00} operation of Nd:YVO_4 laser end pumped by fibre-coupled diode laser.* Electon. Lett., 1997. **33**: p. 775-777.

7. Chen, Y.F., Y.P. Lan, and S.C. Wang, *High-power diode-end-pumped Nd:YVO_4 laser:thermally induced fracture versus pump-wavelength sensitivity.* Applied Physics B, 2000. **71**: p. 827-830.

Chapter 2: Theory of end-pumped four-level solid-state lasers and amplifiers

2.1 Introduction

This chapter introduces some concepts that are used throughout this thesis. The first to be considered is brightness; this is one measure of how useful a laser source is. Diode pump sources are used extensively in the experimental work presented in this thesis, they are discussed and techniques for re-shaping their output beams are reviewed and compared. The coupling of these sources into multimode fibres to improve the flexibility of these devices is also described. Equations for the laser threshold, slope efficiency and output for end-pumped four-level lasers are presented. Heat generation and its deleterious effects are considered and various resonator design strategies to alleviate the effects of thermal loading are reviewed. Finally, a brief overview of the properties of Nd:YAG, Nd:YLF and Nd:YVO_4 is made and their suitability for use in different applications is considered.

2.2 Brightness

Power scaling of lasers is very often a quest to increase brightness to fulfil the needs of various applications. Brightness, B, is defined to be the power of light, P, passing through an area, A, and contained with a solid angle, Ω, by [1]

$$B = \frac{P}{A\Omega}. \tag{2-1}$$

Many sources have different beam divergence angles in orthogonal planes, so a more useful expression of brightness is

$$B = \frac{P}{\lambda^2 M_x^2 M_y^2} \tag{2-2}$$

where M_x^2 and M_y^2 are the beam quality factors in the orthogonal directions, x and y and λ is the wavelength of the beam. The quantity M^2 is the beam propagation factor, often referred to as the beam quality factor. As a rough guide M^2 is the factor by which the far-field Gaussian beam divergence angle for a given beam waist diameter is multiplied to give the actual far-field angle [2]. The far-field divergence angle, θ, for a multimode beam from a beam waist of w_o becomes

$$\theta = \frac{M^2 \lambda}{\pi w_0}. \tag{2-3}$$

This then enables us to compare the usefulness of various laser sources where small beam waists are required, which needs laser beams with good beam quality. An example of this is second harmonic generation, if the beam waist is doubled in size and the effects of diffraction that been neglected in the nonlinear medium, the generated second harmonic will be a quarter of that achievable with the smaller spot size. Therefore if a Nd:YAG laser operating at 1064nm with $M_{x,y}^2$~1 and output power of 1W is pumped by a laser diode lasing at 808nm and with M_y^2~1 and M_x^2~50 with a power of 2W, we might have less power but it is nearly 20 times brighter.

2.3 Diode Pump Sources

In certain circumstances, especially end-pumping, the output from a diode source is not in a very convenient form, so the beam may need to be re-shaped into a more useable form. This is because the cross-section of the emitter is wider in one direction then in the other and the beam has different divergence angles in the two planes. These differences combine to produce an asymmetrical beam. For a single emitter the disparity between the different divergence angles and spot sizes can be overcome using a pair of anamorphic prisms or crossed cylindrical lenses.

Fabricating an array of emitters is the next step in increasing the output power from diode sources. The width in the plane of the array can be many times that of the plane perpendicular to the array, generating an elliptical beam with widely differing beam

divergences. This causes complications for the resulting pump delivery optics, because whilst in the plane perpendicular to the array the output is essentially diffraction limited in the other plane the output is many times diffraction limited.

Arrays can be mounted on top of each other to produce high power diode-stacks. The output power of these devices tend to be limited by heat removal from the diode lasers [3]. This is because unless the diode stack is cooled sufficiently facet fracture can occur, consequently they are often operated in a quasi-CW fashion. Producing pulses typically of ~100s of microseconds with duty ratios of ~10s%. Although the far-field divergence angle of each array remains the same in the stacking plane the effective aperture is increased. Since they cannot be stacked directly on top of each other, there will be dead space between them, thereby degrading the beam quality of the pump unit in this direction.

To transform the pump beam into a shape and size more suitable for end-pumping several schemes have been developed; lens ducts [4-6], fibre bundles [7, 8] imaging optics [9, 10] and various beam re-shaping techniques (e.g. a two mirror beam shaping technique [11]). Whilst the development of techniques for shaping diodes is not part of this thesis, extensive use is made of them, therefore a brief explanation of the above mentioned systems will be given and their usefulness for end-pumping will be reviewed.

The lens duct is a non-imaging concentrator and works by containing and channelling the diode radiation. This is achieved by the combination of lens at its curved input face and total internal reflection on its canted planar sides [6]. The lens duct is placed close to the collimated output of the diode-stack as shown in figure (2-1(A)), and light enters through the curved input face and the output facet has a square cross-section. Since the exit aperture is smaller than the input aperture, the irradiance is increased. However, if the beam quality has been reduced by passing through the device the same cannot necessarily be said of the brightness. From equation (2-3), it can be seen that the beam quality of a beam is proportional to the product of its angle of diffraction and spot-size. So if the spot size decreases but the diffraction angle increases by the same factor, the brightness remains the same. This has been confirmed when a lens duct was used to modify the output of a diode array to pump a Nd:YVO_4 laser [5]. In the array plane, the

aperture size was decreased from 10mm to 1.5mm, but the FWHM far field diffraction angle increased from 13^0 to 100^0. This means that the output face of the lens duct needs to be placed close to the laser rod being pumped. It was also noted that for rays from the diode-stack with an angle in the array plane above a critical angle (9.4^o in this case) were totally internally reflected by the output face, thereby lowering the transmission.

The output from the emitters in a diode array can be coupled into a single fibre [8] or into a series of fibres [7] figure (2-1(B)). The fibres can then be bundled together to produce a nearly circular output beam. The beam quality of the beam exiting the fibre is approximately given by

$$M^2 \approx \frac{\pi w_B NA}{\lambda} \tag{2-4}$$

Where w_B is the radius of the output bundle and NA is the numerical aperture of the fibres used to form the bundle. In the case of figure (2-1(B)) fibres with NA=0.37 are bundled to form a circular output with a 360μm diameter then the beam quality in the array plane is improved from ~1700 to ~260. The M^2 in plane perpendicular to the array however increases from ~1 to ~260 so there has been a 40 times reduction in brightness [8].

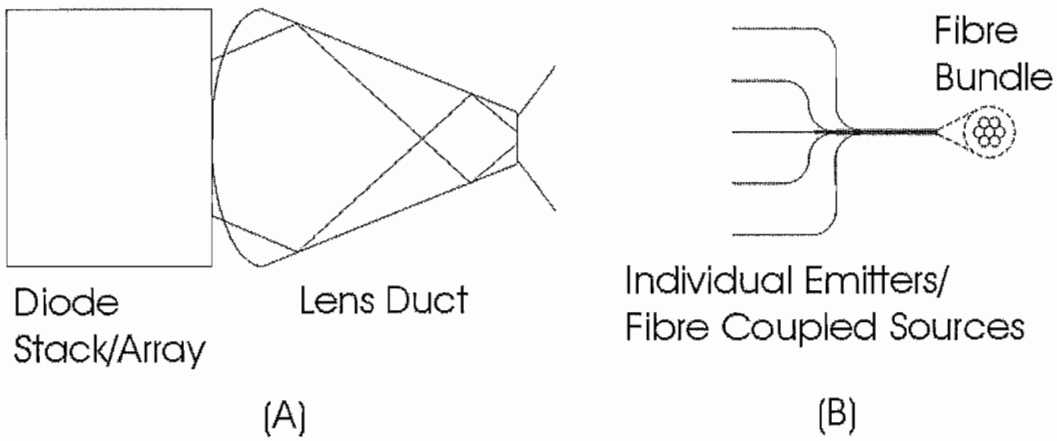

Figure (2-1). Different beam shaping techniques (A) lens duct and (B) fibre bundle.

Imaging optics produce beams that are elliptical in nature, with elliptical laser modes required to extract the maximum efficiency from the system [10]. Since nothing is done to improve the beam quality, if small beam waists are required in the laser crystal, the crystal will need to have a large absorption coefficient to compensate for the short

Rayleigh range of the pump beam, so that the pump volume is minimised. This requirement leads to crystals with relatively high dopant concentrations that can be susceptible to increased thermal loading and damage.

The two-mirror beam shaper technique when applied to an array effectively removes the 'dead space' between adjacent emitters and increases the brightness in this plane [11] figure (2-2). It achieves this by chopping the incident laser beam in the array plane and then stacking these chopped beams in the other direction. The collimated incident beam can be considered as an array of beams, 1-5 in the example shown. Beam 1 goes past both mirrors, and, assuming there are no diffraction effects at the edge of M2, continues unaffected. Beam 2 passes above mirror M1, is then reflected from mirror M2, and strikes mirror M1 below beam 1. Subsequent beams experience multiple reflections between mirrors M1 and M2 leaving the beam shaper below beam 1. In this way, the beam width is reduced in the horizontal direction yet its far-field diffraction angle is maintained, hence decreasing the value of M^2 in this plane. However, in the vertical plane the beam width is enlarged due to stacking of the beams with the result that the M^2 is increased in this plane. The output from the beam shaper has approximately the same brightness as the input beam and can be focused to a nearly circular spot with almost equal M^2 in orthogonal planes. This makes it suitable for preparing the output from a diode to directly end-pump a solid-state laser and for coupling into fibres for more flexible beam delivery.

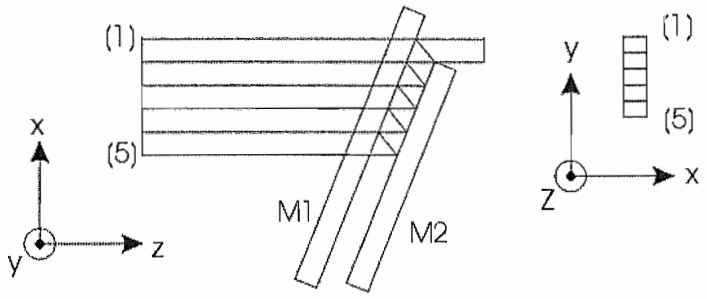

Figure (2-2). Schematic of two-mirror beam shaper.

2.4 Coupling Diodes into Fibres

The flexibility of the pump can be increased by launching it into a fibre. The flexibility of the system is increased because it allows the pumps to be changed to ones of greater power and it allows pump source and gain medium to be cooled independently. If the pump fibres have the same properties as those replaced, the rest of the system can remain unchanged. Fibres can also be used to homogenise the beam to avoid any 'hot-spots' in the focused beam, which can lead to increased beam distortion and damage. However, unless special fibres are used then the resulting output will be unpolarized and the pump brightness can be degraded, because the properties of the output beam are governed by the properties of the fibre. The coupling of a diode into a fibre is shown in figure (2-3). The diode passes through a lens of focal length, f, which brings the diode to a beam waist, w_1, at the facet of the fibre with a core radius of a_2. We can consider the losses involved in coupling the output from a laser diode into a multimode fibre by assuming it is a splice of two fibres. One fibre has the characteristics of the diode and the other has the properties of the beam delivery fibre. For a step index fibre, where there is no change in refractive index across the core we can assume there are no losses due to mismatching refractive index profiles.

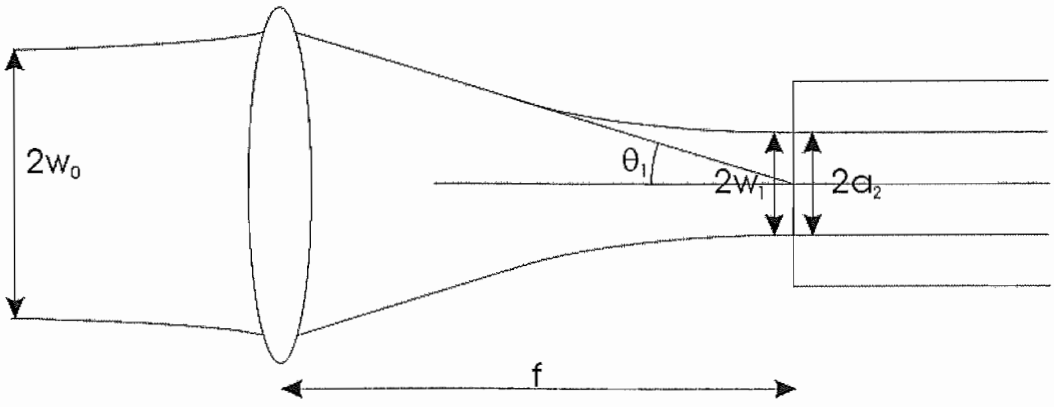

Figure (2-3). Coupling of a diode into a fibre for delivery.

If it is assumed that NA=sin(θ)≈θ, the losses due to unequal mode size and diffraction angle are given by [12]

$$Loss\begin{cases} = -10\log_{10}\frac{a_2^{\,2}}{w_1^{\,2}} - 10\log_{10}\frac{NA_2^{\,2}}{\theta_1^{\,2}}\,(\mathrm{dB}) & w_1 > a_2, \theta_1 > NA_2 \\ = 0 \qquad\qquad\qquad\qquad\qquad\quad (\mathrm{dB}) & w_1 \le a_2, \theta_1 \le NA_2 \end{cases} \tag{2-5}$$

where θ_1 is the far-field diffraction angle of the pump beam and NA_2 is the numerical aperture of the fibre. The beam waist and diffraction angle of the pump beam incident on the fibre are determined by the focal length of the focusing lens, the size of the beam incident on the lens and the beam quality of the pump equation (2-5) can then be written as

$$Loss\begin{cases} = -10\log_{10}\left(\frac{\pi w_0 a_2}{M^2 f\lambda}\right)^2 - 10\log_{10}\left(\frac{fNA_2}{w_0}\right)^2 \text{(dB)} & w_1 > a_2, \theta_1 > NA_2 \\ = 0 \text{(dB)} & w_1 \le a_2, \theta_1 \le NA_2 \end{cases} \quad (2\text{-}6)$$

Equation (2-6) shows that the losses due to a mismatch in mode sizes can be decreased by shortening the focal length of the lens, but this will increase the losses due to the mismatch in the diffraction angles, the correct lens to use is therefore the one that minimises the losses. The minimum losses that can be achieved, neglecting Fresnel losses, is given by combining the losses due to mode size mismatch and those due to diffraction losses

$$Loss_{\min} = -10\log_{10}\left(\frac{\pi NA_2 a_2}{M^2\lambda}\right)^2 \quad (2\text{-}7)$$

Equation 2-7 allows the properties of the pump to be matched with a suitable fibre when

$$M^2 = \frac{\pi NA_2 a_2}{\lambda} = \frac{V}{2} \quad (2\text{-}8)$$

where the number of modes propagating through the fibre is proportional to V^2. Equation (2-8) shows the expected result that all of the pump light would be coupled into the fibre if we match the properties of the fibre. It also shows that if the beam quality of the diode is better then that of the fibre, then again all of the light should be coupled into the fibre, but the beam quality will be degraded. However, if we try to couple light from a diode that has an M^2 greater then half the V parameter of the fibre, then not all of the light will be coupled into the fibre. The output beam from a multimode fibre has a near-field intensity profile that is typically somewhere between a Gaussian and a top-hat intensity profile. This has important consequences for threshold and slope efficiency as will be examined in the next section.

2.5 Laser Performance Equations

In neodymium, the 1μm transition is 4-level with a negligible thermally excited population in the lower lasing level, hence re-absorption losses at the laser wavelength can be ignored. By solving the rate equations for the excited-state population inversion density and the cavity photon density, the pump power required to reach threshold for an end-pumped four-level laser pumped by a Gaussian pump profile is given by [13]

$$P_{thG} = \frac{\pi h \nu_P (L+T)(w_P^2 + w_L^2)}{4\sigma \eta_q \eta_{abs} \tau} \tag{2-9}$$

where ν_P is the pump frequency, L are the cavity losses, T is the transmission of the output coupler, η_{abs} is the absorption efficiency, η_q is the fraction of absorbed pump photons that lead to an excited ion in the upper laser level, σ is the stimulated emission cross-section at the laser wavelength, τ is the fluorescence lifetime of the excited level and w_p and w_L are the pump and laser beam radii in the gain medium. It has been assumed in equation (2-9) that $(L+T)<1$, the laser cavity mode has a Gaussian profile and diffraction effects in the gain medium have been ignored.

For a top-hat beam the threshold pump power is

$$P_{thT} = \frac{\pi h \nu_P (T+L)}{2\sigma \eta_q \eta_{abs} \tau} \frac{w_P^2}{\left(1 - \exp\left(\frac{-2w_P^2}{w_L^2}\right)\right)} \tag{2-10}$$

Taking the ratio of the two threshold powers we obtain

$$\frac{P_{thG}}{P_{thT}} = \frac{1}{2}\left(1 - \exp\left(\frac{-2w_P^2}{w_L^2}\right)\right)\left(1 + \frac{w_L^2}{w_P^2}\right) \tag{2-11}$$

When the pump beam radius is larger than the laser mode size, equation (2-11) tends to ½ and only tends to 1 when the ratio of the pump radius to the laser mode radius tends to 0. Therefore, a Gaussian pump beam will have a lower threshold irrespective of the ratio of laser and pump beams.

Having determined the pump power required to reach threshold the next step is to determine the slope efficiency, η_s. This is given by [14]

$$\eta_s = \left(\frac{T}{T+L}\right)\left(\frac{\upsilon_L}{\upsilon_P}\right)\eta_q\eta_{abs}\eta_{PL}\,. \tag{2-12}$$

The last term, η_{PL}, can be considered as the effective overlap of the pump and lasing mode and at low powers, such that the intra-cavity power is less than the saturation intensity, and is given by [14]

$$\eta_{PL} \approx \frac{\left[\int\limits_{cavity} r_0(r,\theta,z)s_0(r,\theta,z)dV\right]^2}{\int\limits_{cavity} r_0(r,\theta,z)s_0^2(r,\theta,z)dV} \tag{2-13}$$

where r_0 and s_0 are normalized distributions of the pump rate and the cavity photon number and are such that

$$\int\limits_{cavity} r_0(r,\theta,z)dV = \int\limits_{cavity} s_0(r,\theta,z)dV = 1 \tag{2-14}$$

For a Gaussian pump beam η_{PL} is approximately given by [14]

$$\eta_{PL} \approx \frac{w_L^2\left(w_L^2+2w_P^2\right)}{\left(w_L^2+w_P^2\right)^2} \tag{2-15}$$

and for a top-hat pump profile it is approximately

$$\eta_{PL} \approx \frac{w_L^2\left[1-\exp\left(\frac{-2w_P^2}{w_L^2}\right)\right]^2}{w_P^2\left[1-\exp\left(\frac{-4w_P^2}{w_L^2}\right)\right]}\,. \tag{2-16}$$

If w_P=w_L then η_{PL} has a value of 0.75 for the Gaussian pump and a value of 1 for the top-hat pump. In general, η_{PL} is dependent on the laser power as well as the mode distribution and at high powers, when the laser mode intensity is greater than the saturation intensity, $\eta_{PL}\rightarrow 1$. This is because as the intensity of the circulating beam increases, the intensity in the wings of the laser mode becomes sufficient to saturate the gain generated in the wings of the pump distribution increasing the extraction efficiency of the energy stored in the wings. The output power from an end pumped laser can then be calculated by

$$P_{out} = \eta_s\left(P_p - P_{th}\right) \tag{2-17}$$

For an optimally designed laser at low power it can be assumed that, $\eta_{PL} \approx 1$ then the optimum value for the output coupler transmission can be chosen according to the following equation [13]

$$T_{opt} = -L + 2\sqrt{\frac{P_{av}\sigma\tau\eta_{abs}\eta_q L}{\pi\left(w_L^2 + w_P^2\right)h\nu_P}} \tag{2-18}$$

where P_{av} is the pump power available and has a Gaussian profile. Inserting equation (2-18) into equation (2-9) the equation for threshold pump powers become

$$P_{thopt} = \frac{1}{2}\sqrt{\frac{\pi h\nu_P\left(w_P^2 + w_L^2\right)P_{av}L}{\sigma\tau\eta_{abs}\eta_q}} \tag{2-19}$$

By inserting equation (2-18) into equation (2-12) the slope efficiency at the optimum output coupling then becomes

$$\eta_{sopt} = \left(1 - \frac{P_{thopt}}{P_{av}}\right)\left(\frac{\upsilon_L}{\upsilon_P}\right)\eta_{abs}\eta_q\eta_{PL} \tag{2-20}$$

The maximum output power achievable, with optimum output coupling

$$P_{outopt} = \left(\frac{\upsilon_L}{\upsilon_P}\right)\eta_{abs}\eta_q\eta_{PL}\left(P_{av} - \sqrt{\frac{\pi h\nu_P\left(w_P^2 + w_L^2\right)L}{\sigma\tau\eta_{abs}\eta_q}}\left(\sqrt{P_{av}} - \frac{1}{4}\sqrt{\frac{\pi h\nu_P\left(w_P^2 + w_L^2\right)L}{\sigma\tau\eta_{abs}\eta_q}}\right)\right) \tag{2-21}$$

Assuming that all of the pump power is absorbed within the laser crystal, that each absorbed pump photon creates a laser photon and the laser beams are well spatially overlapped and that the laser and pump beam radii are the same, equation (2-21) simplifies to

$$P_{outopt} = \left(\frac{\upsilon_L}{\upsilon_P}\right)\left(P_{av} - \sqrt{\frac{2\pi h\nu_P w_P^2 L}{\tau\sigma}}\left(\sqrt{P_{av}} - \frac{1}{4}\sqrt{\frac{2\pi h\nu_P w_P^2 L}{\sigma\tau}}\right)\right) \tag{2-22}$$

Equation (2-22) shows that the proportion of available power that can be extracted as output power increases with the available power.

2.6 Heat Generation and Temperature Profile

The energy level scheme and corresponding laser transitions for neodymium in Nd:YAG and Nd:YVO_4 are shown in figure (2-4). The solid lines represent radiative transitions and the dashed show non-radiative transitions. The radiative transitions are either absorption or emission. As can be seen the ions are excited from the $^4I_{9/2}$ level to

the $^4F_{5/2}$ level. They decay non-radiatively to the $^4F_{3/2}$ emitting level. This non-radiative decay is achieved by phonon emission, with the result that heat is generated in the gain medium. Heat may be generated by a number of different mechanisms. Heat generated due to non-radiative decay from the pump band to the emitting level and from the lower laser level to the ground state is known as quantum defect heating and occurs in all three and four level solid-state lasers. In this way, it can be seen that the amount of heat generated in the material is dependent on the particular laser transition. The fraction of absorbed pump energy that is converted to heat, δ_q, by quantum defect heating is given by

$$\delta_q = \frac{\nu_P - \nu_L}{\nu_P} \tag{2-23}$$

where $\nu_{P,L}$ are the pump and laser frequencies.

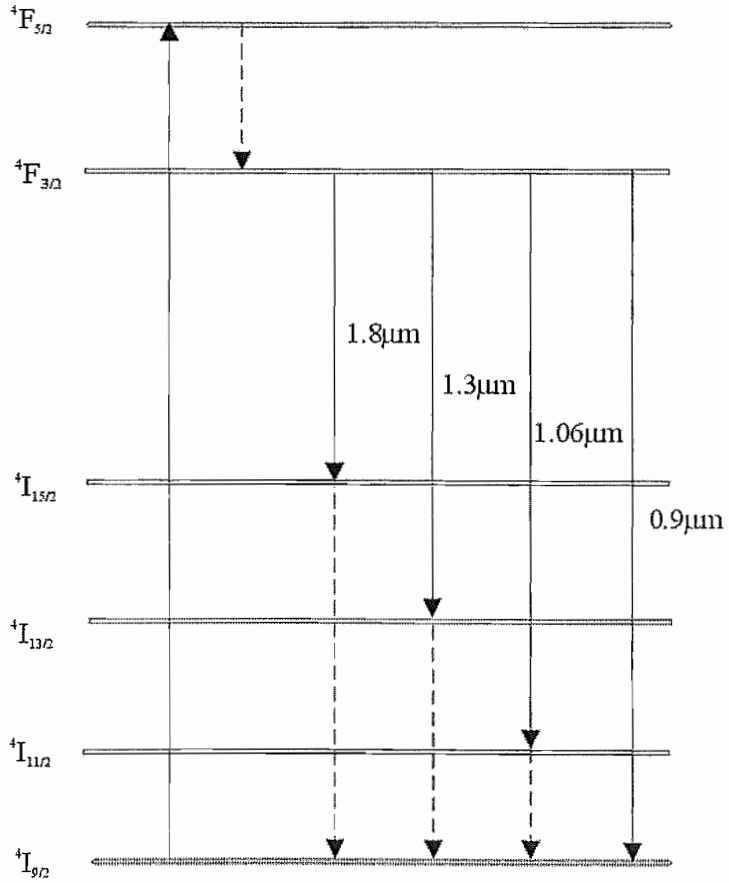

Figure (2-4). Energy level diagram for Nd:YVO_4 and Nd:YAG showing radiative (solid lines) and for non-radiative (dashed lines) transitions.

For neodymium pumped at 810nm and lasing at 1.06μm then $\delta_q \approx 25\%$ and represents the minimum amount of heat that is generated in the medium. In reality, the fraction of absorbed pump power converted to heat will be greater than this due to competing

spectroscopic processes, such as energy transfer upconversion, and any non-radiative transitions directly from the $^4F_{5/2}$ level to the $^4I_{9/2}$ level.

Having considered the amount of absorbed pump power converted to heat it would be appropriate to examine the consequences of it. This heat is deposited in the crystal, and must be conducted to the edge where it can be removed. The net result is a non-uniform temperature profile distribution in the laser crystal. The power converted to heat per unit volume can be written as

$$Q(x,y,z) = \frac{dP(x,y,z)}{dV} = \alpha_p \delta(x,y,z) I_p(x,y,z). \tag{2-24}$$

where α_p is the absorption coefficient of the material at the pump wavelength, $\delta(x,y,z)$ is the fraction of pump radiation converted to heat and $I_p(x,y,z)$ is the intensity of the pump beam. At low pump deposition densities, $\delta \approx \delta_q$ and hence the fractional heating is independent of position.

Under steady state conditions the heat flux, $h(x,y,z)$, (i.e. the heat per unit area flowing out of a volume perpendicular to its surface), must satisfy the general equation [15]

$$\underline{\nabla} \bullet \underline{h}(x,y,z) = Q(x,y,z) \tag{2-25}$$

The heat flux is related to the temperature distribution within the crystal by

$$\underline{h}(x,y,z) = -K_c \underline{\nabla} T(x,y,z) \tag{2-26}$$

where K_c is the thermal conductivity of the material.

If it is assumed that the gain medium is a longitudinally pumped rod, cooled at the edge by a copper heat sink, as shown in figure (2-5), then an approximate analytical solution for the temperature profile in the rod can be determined. In figure (2-5) the copper heat sink is given by the hashed area, the white area is the rod, the pump beam radius is w_p, the rod has a radius r_a and l is the length of the rod. If it is assumed that the heat flow is purely radial and axial heat low is neglected then equation (2-25) can be integrated to give the heat flowing from a thin slice of material at position z with thickness Δz and radius r, yielding [15]

$$2\pi r \Delta z h(r,z) = \int_z^{z+\Delta z} \int_0^r \alpha \delta I_p(r',z') 2\pi r' dr' dz'. \tag{2-27}$$

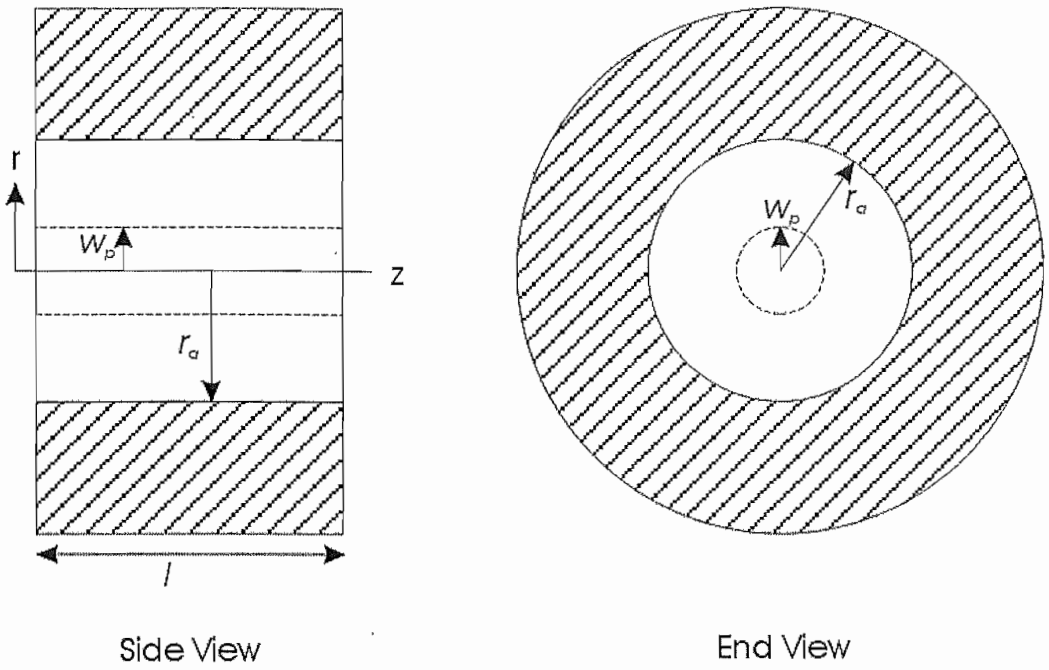

Figure 2-5. Side and end view of an edge-cooled laser rod or radius r_a and length l. The hashed area is the copper heat sink and the white area is the laser rod.

For a pump beam with a Gaussian transverse intensity profile and power, P_p, the intensity is given by

$$I_p(r,z) = \frac{2P_p}{\pi w_p^2}\exp\left(\frac{-2r^2}{w_p^2} - \alpha_p z\right). \tag{2-28}$$

Substituting equation (2-28) in to equation (2-27) yields

$$h(r,z) = \left(\frac{\alpha_p \delta_q P_p}{2\pi}\right)\exp\left(-\alpha_p z\right)\left(\frac{1-\exp\left(-2r^2/w_p^2\right)}{r}\right). \tag{2-29}$$

The temperature increase ΔT from the edge of the rod to position r, can be calculated from

$$\Delta T(r,z) = T(r,z) - T(r_a,z) = \frac{1}{K_c}\int_r^{r_a} h(r,z)dr \tag{2-30}$$

where $T(r,z)$ is the temperature at a point in the rod and $T(r_a,z)$ is the temperature of the rod at the surface. Figure (2-6) shows the predicted change in temperature for a 1% doped Nd:YAG rod calculated by inserting equation (2-29) into (2-30) and solving numerically. The values used (r_a=1.5mm, α_P=3000m^{-1}, l_c=3/α_P, absorbed power P_p=1W, w_P=230μm and K_c=5Wm^{-1}K^{-1}) are typical for and end-pumped laser configuration. It can be seen that the temperature is a maximum at the centre of the pumped face and decreases with r and z as expected.

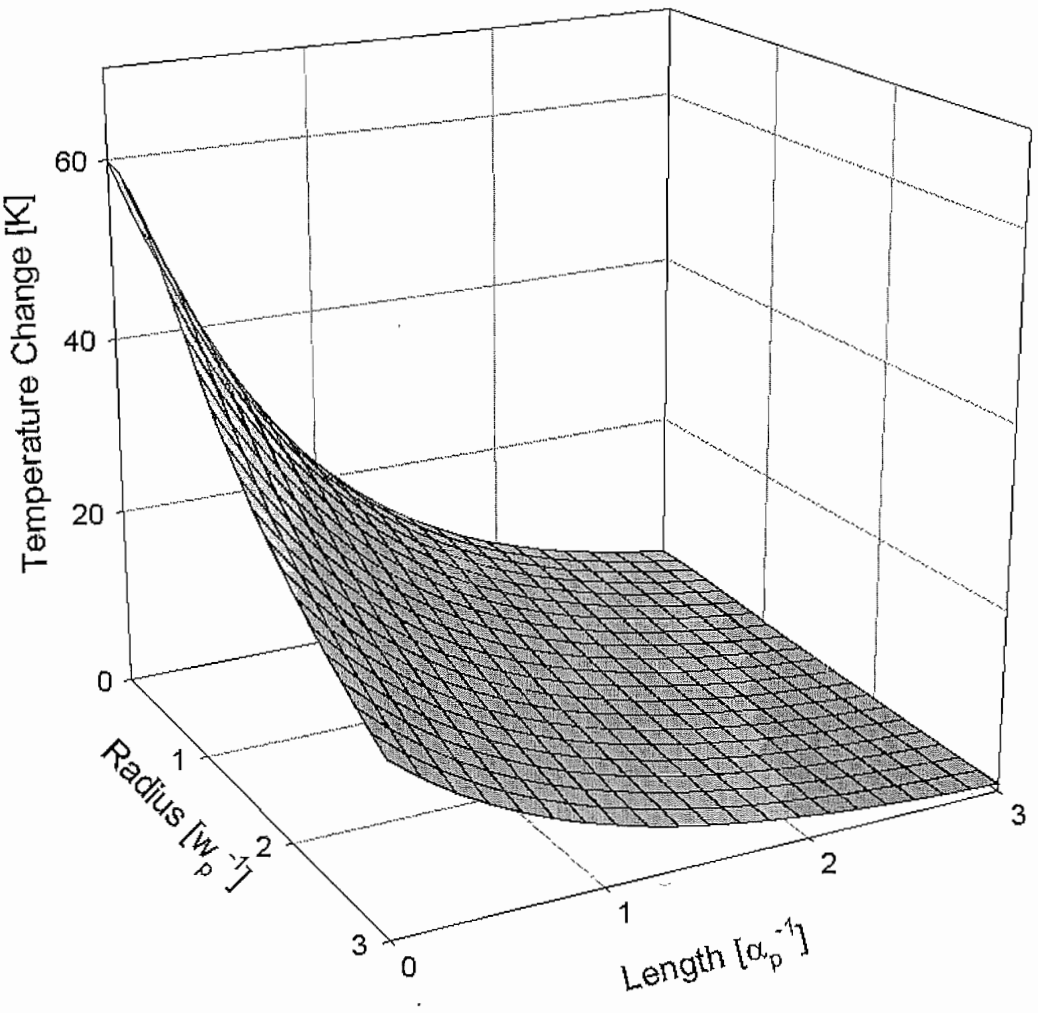

Figure (2-6). Predicted temperature distribution for a Nd:YVO_4 crystal end-pumped with 1W of absorbed power and with a pump spot radius of 230μm.

The non-uniform temperature distribution within the crystal resulting from the radial heat flow produces a temperature induced change in the refractive index, thermal expansion and thermally induced stresses.

2.7 Thermal Stresses

Since the temperature distribution is non-uniform, thermally induced stresses occur, caused by the cooler outside region preventing the hotter pumped region from expanding. For a uniformly heated isotropic rod, the radial, tangential and axial components of stress have a parabolic dependence with *r*. The radial component will go to zero and the tangential and axial components will be under tension at the surface due to the greater bulk expansion at the centre of the rod compared to the circumference [1]. These stresses lead to a change in the refractive index of the crystal via the photoelastic effect [1].

Under normal conditions, the indicatrix for a cubic crystal such as Nd:YAG is a sphere, as shown in figure (2-7). When stress is applied along one direction this indicatrix becomes an ellipsoid due to the changes in refractive index in the radial and tangential directions, causing stress-induced birefringence. This stress-induced birefringence will cause any linearly polarised light passing through the gain medium to experience depolarisation. Polarized light at point P in figure (2-7), with the electric field aligned along the vector E (in the y-direction) can be resolved into components along radial and tangential directions. After passing through the point P, the light will now be elliptically polarised due to the stress-induced birefringence. If there is an element in the cavity to enforce linearly polarized operation, stress-induced birefringence will significantly increase the cavity loss. The loss will be caused by the polarising element coupling light out of the cavity. The loss due to depolarisation can be calculated by integrating over the cross-sectional area of the rod. For a Gaussian pump and laser transverse profiles the loss factor in Nd:YAG is given by [16]

$$L_{depol} = \frac{1}{4}\left(1 + A^2\right)^{-1} \tag{2-31}$$

where

$$A = \frac{K_c \lambda}{2 P_p \eta_{abs} \delta n_0^3 \alpha C_B} \left(\frac{w_p^2}{w_L^2} \right) \tag{2-32}$$

where P_p is the incident pump power, α is the thermal expansion coefficient, $w_{p,L}$ are the beam waist radii of the pump and laser beams in the gain medium and C_B=-0.0099

is a material parameter for Nd:YAG [1]. Using values of n_0=1.82, ρ=7.5x10^{-6} K^{-1}, K_c=0.14Wcm^{-1}. For 4W of incident pump power and assuming w_L=w_P the depolarisation loss is ~0.6%. As can be seen from equation (2-32) the losses due to depolarisation are dependent on the ratio of pump and laser beam waist radii. The losses for a TEM_{00} beam are lower than for a multimode beam, which has a larger beam waist in the gain medium and thus experiences greater depolarisation.

For a birefringent material the indicatrix is an ellipsoid and, hence the change of refractive index produced by stress is a negligible change in the shape, size and orientation of the indicatrix [17]. This means that birefringent materials such as Nd:YVO_4 and Nd:YLF will not suffer such depolarisation loss. For crystals that do suffer from stress-induced birefringence the losses due to depolarisation can be reduced by inserting a quarter wave plate in the cavity [18]. This rotates the polarisation by 90^0 for a double pass through the wave plate ensuring that the retardation experienced by both polarisations is approximately the same.

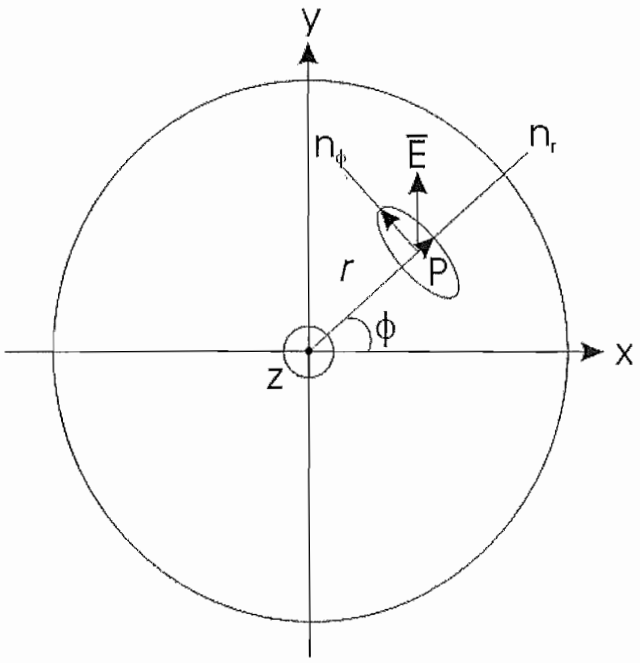

Figure (2-7). Spherical indicatrix for Nd:YAG, showing the elliptical local indicatrix caused by stress.

2.8 Stress Fracture

If the thermal loading is too high, stress fracture will occur. Stress fracture results if the generated stress is greater than the tensile strength of the material [1]. This restricts the amount of heat generated per unit length in the gain medium, and hence the absorbed pump power thus limiting the maximum power that can be produced.

Under end-pumped conditions, materials with short absorption lengths will generate large amounts of heat close to the pumped face, so if the material has poor thermo-mechanical properties it will be susceptible to stress fracture. For an end-pumped laser, with a pump top-hat pump profile, the limit of the absorbed pump power per unit length is given by [19]

$$P_{\lim} = \frac{1}{\alpha_p}\frac{4\pi R}{\delta}. \tag{2-33}$$

where R is a thermal shock parameter and depends on the mechanical and thermal properties of the material in the following way

$$R = \frac{K_c \sigma_{\max}}{\alpha_T Y} \tag{2-34}$$

where σ_{max} is the maximum surface stress at which fracture occurs, Y is the Young's modulus and α_T is the thermal coefficient expansion.

Equation (2-33) shows that the maximum power that can be absorbed before stress fracture occurs can be increased by reducing the heat generation per unit length. This can be achieved by lowering the neodymium concentration hence increasing the absorption length [20].

For a pump spot radius of 360 μm it has been shown that for a 1% doped Nd:YVO_4 rod that fracture occurs at an incident pump power of 13.5W [19, 20], resulting in a thermal shock parameter of 4.8 Wcm^{-1}. This compares to the thermal shock parameters of 2Wcm^{-1} for Nd:YLF and 11Wcm^{-1} for Nd:YAG. The value for Nd:YAG being the larger because it has the largest thermal conductivity and maximum tensile strength. By making the simplifying assumption that the pump light is absorbed linearly with

distance and is completely absorbed over two absorption lengths, then the minimum effective pump beam radius w_{pmin}, defined as r.m.s. beam radius which results in the minimum pumped volume is given by [13]

$$w_{p\min}^2 = \frac{2\lambda_p M^2}{\alpha_p \pi n \sqrt{3}} \tag{2-35}$$

Inserting equations (2-35) and (2-33) into equation (2-22) leads to the following for the optimum output coupled threshold in terms of the maximum absorbed pump power before stress fracture occurs

$$P_{thoptstress} = \frac{1}{2}\sqrt{\frac{16\pi hcLRM^2}{\sigma\tau\alpha_P^2\delta\sqrt{3}}} \tag{2-36}$$

The maximum output power is then given by inserting equations (2-33) and (2-36) into equation (2-22)

$$P_{outopt} = \left(\frac{\upsilon_L}{\upsilon_P}\right)\left(\frac{4\pi R}{\alpha_P\delta} - \sqrt{\frac{16\pi hcLRM^2}{\sigma\tau\alpha_P^2\delta\sqrt{3}}}\left(\sqrt{\frac{4\pi R}{\alpha_P\delta}} - \frac{1}{4}\sqrt{\frac{16\pi hcLRM^2}{\sigma\tau\alpha_P^2\delta\sqrt{3}}}\right)\right) \tag{2-37}$$

Using the values in table (2-1) to calculate the maximum output power before stress fracture occurs it is found that with its large thermal shock parameter can produce the greatest output power with 14W predicted with optimised output coupling. It is surprising that although it has the lowest thermal shock parameter, Nd:YLF should generate a greater output than Nd:YVO_4 before stress fracture occurs with values of 7.6W and 6.1W predicted respectively before stress fracture occurs. However, this is due to the longer absorption length, so there is less heat dissipated per unit length.

	Nd:YVO_4	Nd:YAG	Nd:YLF
σ[x10^{-19}cm^2]	15.6	4.6	1.9
λ_P/λ_L [nm/nm]	808/1064	810/1064	797/1053
τ[μs]	100	230	520
α_P[cm^{-1}]	40	3	11
R[Ẅcm^{-1}]	4.8	11	2
P_{outopt}	6.1	14	7.6

Table (2-1). Maximum optimised output power possible before stress fracture occurs for a dopant concentration of 1%.

2.9 Thermal Lensing

Thermal lensing results from the non-uniform transverse temperature distribution. There are three contributing factors, the temperature dependence of the refractive index, stress induced change in the refractive index and end-face bulging due to differential thermal expansion [1]. The contribution to the thermal lens focal length from the variation in the refractive index due to the temperature changes will be examined in this section. The contribution from thermal end face bulging has a profile that depends on the temperature distribution in the gain medium. The temperature distribution generates an optical path length difference given by

$$OPD = \Delta T l_c \chi \tag{2-38}$$

where ΔT is the temperature change from the centre to the edge of the crystal, l_c is the length of the crystal and χ is the thermooptic coefficient. The thermooptic coefficient is given by [21]

$$\chi = \frac{dn}{dT} + (n-1)(1+\nu)\alpha_T + n^3 \alpha_T C_{r,\phi} = \frac{dn}{dT} + \chi_E + \chi_{Sr,S\phi} \tag{2-39}$$

where dn/dT is the rate at which the refractive index varies with temperature (sometimes referred to as the thermo-optical coefficient), n is the index of refraction, ν is Poisson's ratio, α_T is the coefficient of thermal expansion, $C_{r,\phi}$ is the photoelastic coefficient in the two orthogonal directions, $\chi_{E,Sr,S\phi}$ are the contributions from axial expansion and stress. The values of the different thermooptical coefficients for Nd:YAG, Nd:YLF and Nd:YVO_4 are shown in table (2-2). As can be seen for the different materials the thermooptical coefficients for the change in the refractive index and axial expansion are predicted to be about the same. For Nd:YAG it can be seen that the thermooptical coefficients due to stress are much weaker than the other contributions. As can be seen from the different values, there will be different thermal lens focal lengths for different polarisations. For Nd:YLF and Nd:YVO_4 this will not be a problem because the natural birefringence will cause lasing to occur preferentially on the high gain polarisation. For Nd:YAG the bifocusing caused by the induced stress could be a problem, and might lead to different cavity modes for the different polarisations.

	Nd:YAG	Nd:YLF		Nd:YVO_4	
		c	a	c	a
α_T [x$10^{-6}K^{-1}$]	7.5	13		3.1	
ν	0.25	0.33		0.3	
dn/dt [x$10^{-6}K^{-1}$]	7.3	-4.3	-2.0	3.9	8.5
n	1.82	1.47	1.45	2.17	1.96
C_r	0.017	-		-	
C_ϕ	-0.0025	-		-	
χ_E [x10^{-6}]	7.7	7.9	7.8	4.7	3.9
χ_{Sr} [x10^{-6}]	0.77	-		-	
$\chi_{S\phi}$ [x10^{-6}]	-0.11	-		-	

Table (2-2). Different thermooptic coefficients for Nd:YAG, Nd:YLF and Nd:YVO_4 and the values used to calculate them [1, 22].

The net effect of the radial refractive index changes is to generate an optical path length difference across the crystal. Therefore there will be a transverse phase difference, $\Delta\phi(r)$ for beams traversing different parts of the laser crystal [23]

$$\Delta\phi(r) = \frac{2\pi(dn/dt)}{\lambda}\int_0^l \Delta T(r,z)dz \qquad (2\text{-}40)$$

For an end-pumped laser rod which is edge cooled where it is assumed that the heat flow is purely radial it can be shown that the phase profile is given by [23]

$$\Delta\phi(r) = \frac{P_p \delta\eta_{abs}(dn/dt)}{K_c\lambda}\int_0^r \frac{s(r')}{r'}dr' \qquad (2\text{-}41)$$

where η_{abs} is the fraction of incident pump power that is absorbed and $s(r)$ is the normalised pump distribution given by.

$$s(r) = \frac{2\pi}{P_p}\int_0^r r' I_p(r')dr' \qquad (2\text{-}42)$$

For a thin thermal lens, simple geometric considerations can be used to derive an approximate expression for the thermal lens focal length $f_t(r)$ as a function of radial position [13]

$$f_t(r) = \frac{2\pi r}{\lambda \dfrac{d\Delta\phi(r)}{dr}} \tag{2-43}$$

From equation (2-43), it can be seen that if $\Delta\phi(r) \propto r^2$ then the focal length is independent of r, consequently the lens has no phase aberration and will not degrade the beam quality. Substituting (2-41) into (2-43) yields the following for the radially varying thermal lens focal length

$$f_{th}(r) = \frac{2\pi K_c r^2}{P_p \delta \eta_{abs} (dn/dt) s(r)} \tag{2-44}$$

Equation (2-44) shows that the thermal lens focal length is dependent on the pump distribution. For a top-hat pump profile where the power is uniform across the beam of radius w_p the pump intensity is given by

$$\begin{aligned} I_p &= \frac{P_p}{\pi w_p^2} && \text{for } r \le w_p \\ &= 0 && \text{for } r > w_p \end{aligned} \tag{2-45}$$

Inserting (2-45) into (2-44) gives the thermal lens focal length for an end-pumped gain medium with a top-hat beam of

$$\begin{aligned} f_{th}(r) &= \frac{2\pi K_c w_p^2}{P_p \delta \eta_{abs} (dn/dt)} && \text{for } r \le w_p \\ &= \frac{2\pi K_c r^2}{P_p \delta \eta_{abs} (dn/dt)} && \text{for } r > w_p \end{aligned} \tag{2-46}$$

Equation (2-46) shows that the thermal lens generated in the pumped region is unaberrated, however, outside of this region the thermal lens is aberrated. This is because inside the pump region the heat deposition is uniform, generating a parabolic temperature profile. Outside this region, the temperature profile has a logarithmic dependence on the radius resulting in a radially varying focal length.

For a pump beam with a Gaussian transverse intensity profile, given by

$$I_p(r) = \frac{2P_p}{\pi w_p^2} \exp\left(\frac{-2r^2}{w_p^2}\right) \tag{2-47}$$

The focal length is given by [13]

$$f_t(r) = \frac{2r^2 f_t(0)}{w_p^2\left(1-\exp\left(-2r^2/w_p^2\right)\right)}. \tag{2-48}$$

Where $f_t(0)$ is the thermal lens focal length on axis at $r = 0$, given by

$$f_t(0) = \frac{\pi K_c w_p^2}{P_p \delta \eta_{abs} \frac{dn}{dt}} \tag{2-49}$$

Equations (2-47) and (2-49) show that the on axis focal length is inversely proportional to the absorbed pump power this is only strictly true under lasing conditions many times above threshold, where the amount of heat generated is linear with the absorbed pump power. Under other circumstances, spectroscopic mechanisms such as energy transfer upconversion can increase the rate of heat deposition. Under non-lasing conditions as the pump power increases the rate of ETU can increase as well. Under lasing conditions however, the rate of stimulated emission is far greater than these other effects and the rate of increase of heat deposition is proportional the absorbed pump power.

As can be seen by a comparison of equations (2-46) and (2-49) the on axis the top-hat pump focal length is twice that of the Gaussian profile. Moving away from the axis the focal length due to the Gaussian profile increases until at the pump beam radius, it is less then that of the top-hat profile. Beyond the pump beam radius, the top-hat focal length increases with r^2 and the Gaussian profile tends to this behaviour. This means that the laser mode inside the gain medium will see some average thermal lens focal length. This suggests that whilst equation (2-49) can be used to estimate the thermal lens focal length on axis, the beam will actually experience a lens with a longer focal length than this. This change in thermal lens focal length across the beam will cause beam quality degradation and is discussed in a later section.

Strictly speaking the thermal lensing in the laser crystal should be considered as a complex duct. The thermal changes and the gain profile generate a radial variation in the refractive index. This radial variation guides the laser mode therefore acting as a guide or a duct. The thermal changes alter the real part of the refractive index, whilst the gain is represented by the complex part of the refractive index. The consequence of

the laser crystal acting as a duct is that the thermal lens will not bring the laser mode to a focus within the crystal [24].

2.10 Beam Quality Degradation

The variations of equations 2-35 and 2-37 with radial position show that the phase difference created by the refractive index change is not parabolic with r, this means that the thermal lens cannot simply be considered as a perfect lens. The higher order terms in r will result in beam distortion. Siegman [25] analysed the beam quality degradation caused by quartic aberration to a Gaussian beam with an initial beam quality factor M_i^2 propagating through a lens that has a focal length f and a phase distortion $\Delta\phi(r)$ of the form

$$\Delta\phi(r) = \frac{2\pi}{\lambda}\left(\frac{r^2}{2f} - C_4 r^4\right) \tag{2-50}$$

The additional contribution to the beam quality factor due to the quartic phase aberration coefficient, C_4, is given by

$$M_q^2 = \frac{8\pi C_4 w_L^4}{\lambda\sqrt{2}}. \tag{2-51}$$

The resultant degradation in the beam quality, M_f^2 will be given by [25]

$$M_f^2 = \sqrt{\left(M_i^2\right)^2 + \left(M_q^2\right)^2} \tag{2-52}$$

For a top-hat pump beam and $r<w_p$, there is no beam quality degradation. For a Gaussian beam even when keeping $r<w_p$, there is beam quality degradation and M_q^2 is approximately given by [23]

$$M_q^2 = \frac{2P_p\delta_q\eta_{abs}(dn/dT)}{K_c\lambda\sqrt{2}}\left(\frac{w_L}{w_p}\right)^4 \tag{2-53}$$

where w_L is the laser mode size in the gain medium. As shown by equation (2-53) the beam quality is strongly influenced by the ratio of the laser mode and pump spot size. This suggests that low power high brightness diodes, were equally able to cause beam quality degradation through thermal lensing, but because of the small laser mode sizes the magnitude of the degradation was not as evident as with high power devices. This also means that the beam quality degradation cannot be reduced by simply increasing the pump beam radius because, to extract the gain efficiently the laser mode size needs

to increase proportionally. By increasing the laser mode size, its Rayleigh is increased as well, increasing the beams susceptibility to phase aberration degradation.

To maintain diffraction-limited output of a beam making a single pass of an aberrated thermal lens as discussed above, then it is desirable that $M_f^2 \leq 1.1$. For a diffraction limited incident beam this means that the beam quality degradation due to the quartic phase aberration is $M_q^2 \leq 0.46$. This enables a maximum pump power before beam quality degradation becomes such that the laser is no longer diffraction limited is given by

$$P_{\max,d} = \frac{0.32 K_c \lambda}{\rho^4 \delta_q \eta_{abs} (dn/dT)} \tag{2-54}$$

where ρ is the ratio of laser and pump beam radii. The maximum pump power for different materials and ratios of laser and pump radii is shown in figure (2-8). In figure (2-8) the solid line is the maximum pump power before beam quality degration becomes too great for Nd:YAG, the dashed line is for Nd:YVO_4, the dotted line is for the 1.047μm line in Nd:YLF and the dashed and dotted line is for the 1.053μm line. The values for the thermal conductivity and thermo-optical coefficients are shown in table (2-2). In figure (2-8) it has been assumed that δ_q=0.25, that all of the incident pump power is absorbed and the modulus of the change in refractive index has been used for the Nd:YLF traces. This is only a rough guide since the effects of end face bulging have been neglected, which will increase the maximum pump power for Nd:YLF. It can be seen that the 1.053μm line in Nd:YLF is the least susceptible to beam quality degradation, and that the 1.047μm line is the most susceptible. If the maximum pump power before beam quality degradation becomes pronounced and the maximum pump power before stress fracture occurs, shows that the ratio of the beam radii to maintain beam quality until stress fracture occurs. This reduction in beam radii will leave undepleted gain in the pump beam though, which might lead to lasing on higher order modes.

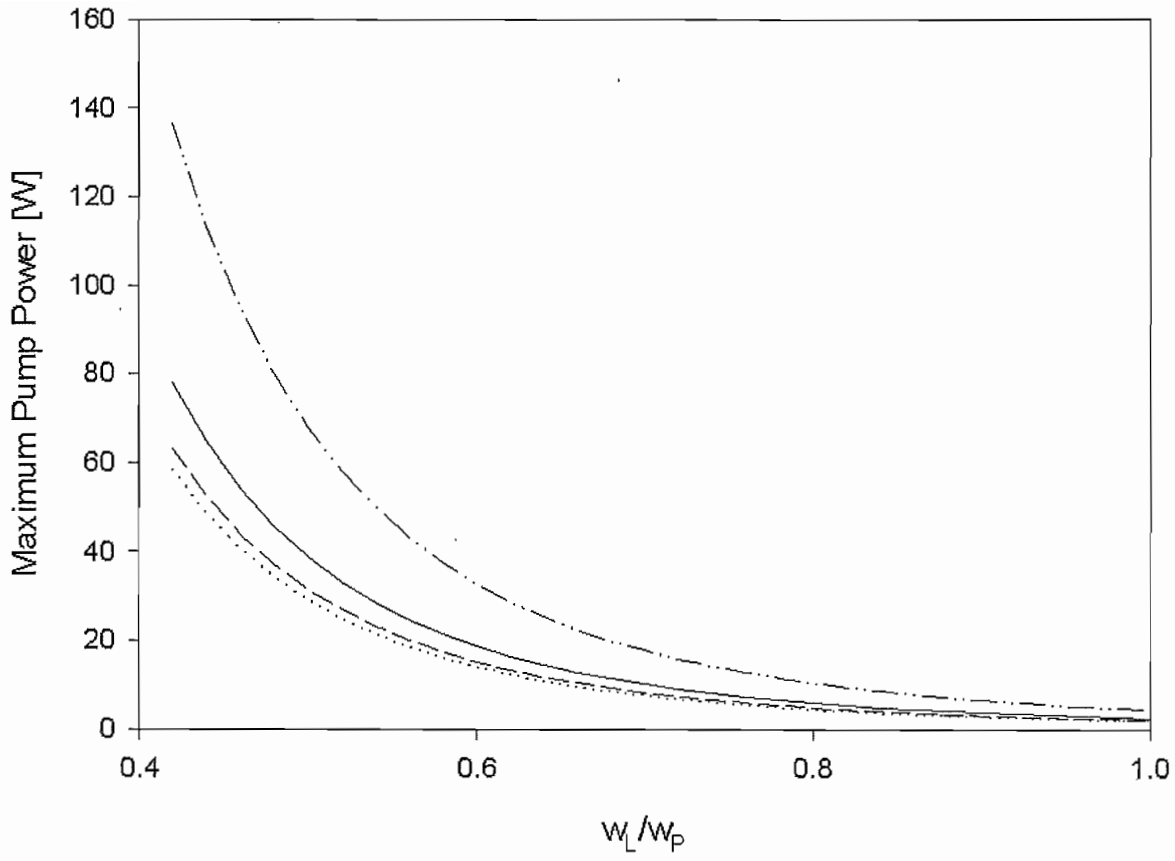

Figure (2-8). Maximum absorbed pump power before beam quality degradation becomes significant. The solid line is for Nd:YAG, the dashed line is for Nd:YVO_4, the dotted line is for the 1.047μm line in Nd:YLF and the dashed and dotted line is for the 1.053μm line.

	Nd:YAG	Nd:YVO_4	Nd:YLF	
K_c [$Wm^{-1}K^{-1}$]	13	5.2	6.3	
dn/dt [$x10^{-6}K^{-1}$]	7.3	3.9	-4.3	-2.00
λ[μm]	1.064		1.047	1.053

Table (2-2). Values used to determine the maximum pump power shown in figure (2-8)

2.11 Cavity Design Considerations

In this section the impact of thermal lensing and thermally-induced birefringence on the performance of a simple end-pumped solid-state laser will be considered. For this purpose, we restrict our consideration to the simple Nd:YAG cavity shown in figure (2-9(A)), it is a semi-confocal cavity such that the length of the cavity is equal to half the radius of curvature of mirror M_2 and a Brewster plate is inserted into the cavity to select a linearly-polarised output. As the pump power is increased, the heat generated within the gain medium induces a thermal lens and stress induced-birefringence.

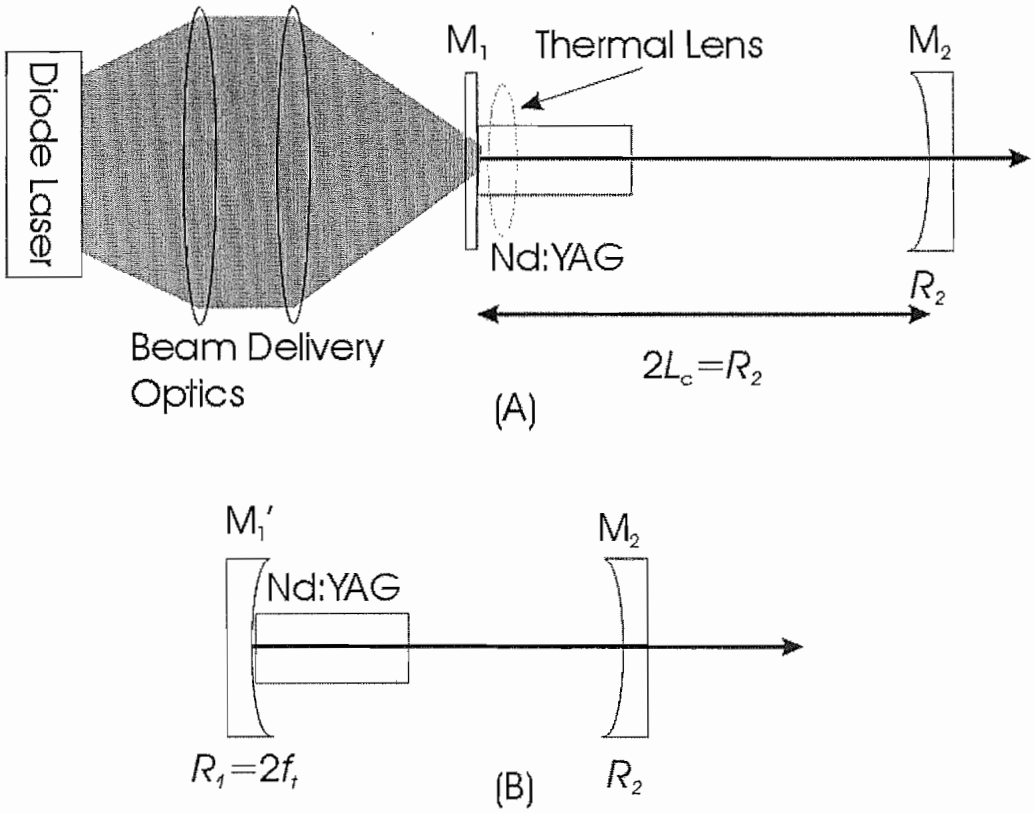

Figure (2-9). (A) Semi-confocal resonator showing the induced thermal lens and (B) the equivalent two mirror cavity.

Figure (2-9B) shows the equivalent two mirror cavity where the effect of the thermal lens has been modelled by assuming it is close to the end of the gain medium and is equivalent to making mirror M_1 a curved mirror. Mirror M1' then has a radius of curvature which is dependent on the pump power and beam radius. Since the laser mode makes two passes of the thermal lens the radius of curvature of M_1' is given by $R_1=f_t$ where the thermal lens focal length is f_t.

The condition for a stable cavity for a cavity length of L and with curved mirrors R_1 and R_2 is given by [26]

$$0 < \left(1 - \frac{L}{R_1}\right)\left(1 - \frac{L}{R_2}\right) < 1 = 0 < \frac{1}{2}\left(1 - \frac{R_2}{2f_t}\right) < 1 \qquad (2\text{-}55)$$

where it has been assumed that $L=L_c$. As can be seen from equation (2-48) if the thermal lens focal length becomes shorter then $R_2/2$ the laser becomes unstable, this means that the laser might lase on higher order modes that are stable, or simply may not lase at all. The cavity can be stable for shorter thermal lens focal lengths by decreasing the radius of curvature of mirror M2. However, this will decrease the cavity length and restrict the opportunity for inserting intra-cavity elements.

The beam radius at mirror M1 for the curved mirror and the plane mirror in the example semi-confocal cavity, i.e. when there is no thermal lensing, is given by [1]

$$w_1^2 = \left(\frac{\lambda}{\pi}\right)\left[L(R_2 - L)\right]^{1/2} = \frac{\lambda R_2}{2\pi}. \qquad (2\text{-}56)$$

where again it has been assumed that $L=L_c$. For efficient low power operation equation (2-49) can be used to determine the pump beam radius so that $w_p=w_L$ in the laser crystal. The pump beam radius given by equation (2-49) can then be inserted into equation (2-38) to determine the on-axis thermal lens focal length for a Gaussian pump beam profile. It can be shown that the maximum absorbed pump power before the cavity becomes unstable for the TEM_{00} mode is

$$P_p = \frac{K_c \lambda}{\delta(dn/dt)}. \qquad (2\text{-}57)$$

For Nd:YAG this limits the power to ~8W before this type of cavity becomes unstable. This power is well below that permitted before stress-fracture occurs, therefore different resonator designs will be required to scale to powers above this.

This section has shown that the thermal lensing and stress-induced birefringence can have a serious impact on laser performance and beam quality. Thermal lens focal length can limit the output power from a laser by making the cavity unstable; stress - fracture can limit the potential of a laser through failure of the gain medium; and stress –induced birefringence can reduce the possible output power for polarised operation through the increase of the cavity loss.

2.12 Resonator Design for Power-Scaling

At low pump powers the generated thermal lens focal lengths can largely be ignored in comparison with the curvatures of mirrors typically used in the laser resonators. Diffraction limited output can be ensured by designing the cavity so that the radius of the TEM_{00} mode should be equal to or even larger than the pump beam radius. This ensures that undepleted gain in the wings of the pumped region, which might lead to lasing on unwanted higher-order transverse modes is depleted. The minimum laser mode radius and consequently the threshold pump power are fixed by the pump beam quality, as given by equation (2-27). As the powers are increased, the beam quality degradation due to the thermal lens becomes more pronounced. For uni-axial crystals, that do not suffer from stress-induced birefringence, the beam quality degradation will set the upper limit for power-scaling diffraction limited output from end-pumped lasers. It can be seen from equation (2-47) by decreasing the ratio of the laser radius to the pump beam radius the effect of beam quality can be reduced. However, the smaller the ratio becomes the greater is the amount of undepleted gain in the wings of the pump beam. This undepleted gain can result in higher order laser modes beginning to lase, producing a non-diffraction limited output. These higher order modes could be discriminated against by the use of an aperture inserted in the cavity, however, this might lead to increased losses for the TEM_{00} mode. As shown in the previous section, the thermal lens will change the laser mode radius in the laser crystal, and as shown by equation (2-37) the focal length varies with radial distance. By choosing a resonator design where the laser mode decreases with increasing focal length it is possible to provide the required discrimination between the fundamental and higher order modes [13]. This discrimination is achieved because the higher order-mode has a larger mode size than the fundamental mode, so experiences a longer thermal lens focal length than the fundamental mode. This decreases the ratio of the beam sizes between the higher-order mode and the fundamental. The fundamental mode, with its better spatial overlap with the pump beam experiences the stronger gain suppressing the lasing on the higher modes.

As discussed above, efforts to power-scale end-pumped solid-state lasers revolve around the delivery of the pump power and removal of the heat generated by the operation of the laser. In section 2.3, diode pump sources and their beam shaping were discussed, to improve their brightness and consequently the minimum beam waist that they can achieve. In section 2.8, it was shown that stress-fracture represents the limit to which a gain medium can be pumped before catastrophic failure occurs. By pumping the gain medium from both ends, the absorbed pump power can be increased and consequently the output power. For short rods, the temperature rise from pumping one end produces a temperature rise at the opposing end so the absorbed pump power before stress-fracture is not doubled [21]. Therefore, to fully realise the potential of double end-pumping the gain medium needs to be sufficiently long enough that the two ends are thermally independent. The available pump power available can be increased by angularly multiplexing the diode pumps around the end faces as shown in figure (2-10). The diode bars are collimated in the fast axis and the outputs of the diodes are imaged into the laser crystal using a lens. In this way 8 15W laser diodes can be multiplexed around a single Nd:YAG rod with about 100W absorbed [27]. Using a single rod, pumped in this fashion approximately 50W of output power were achieved in a multimode output beam.

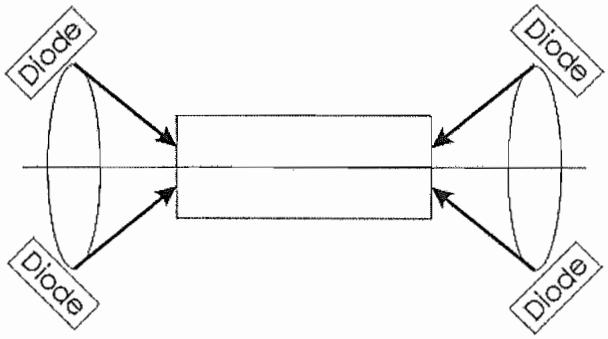

Figure (2-10). Multiple pump geometry angular multiplexing [27].

Cooling the gain medium axially leads to weaker thermal lensing because the thermal gradient is collinear to the laser beam. An example of this geometry is the thin disc laser shown in figure (2-11) [28]. In figure (2-11), the hashed area is the heat sink and the gain medium is mounted directly onto this. For low aspect ratios where the thickness of the gain medium is much smaller than the radius of the gain medium the stress fracture limit is increased. For efficient absorption of the pump beam, the gain medium needs to have a short absorption length and to make multiple passes of the gain medium. This is achieved by using gain materials that allow large dopant

concentrations without suffering concentration quenching, Yb:YAG is a popular choice for the gain material. As shown in figure (2-11) any unabsorbed pump power is re-imaged into the gain medium using mirrors, if the angle of the mirror is suitably chosen then the pump beam can make multiple passes. If the heat generated in the gain medium is too great, the gain medium can become deformed and lose contact with the heat sink. The laser cavity is formed by the cooled face of the gain medium being coated to be highly reflecting and another mirror.

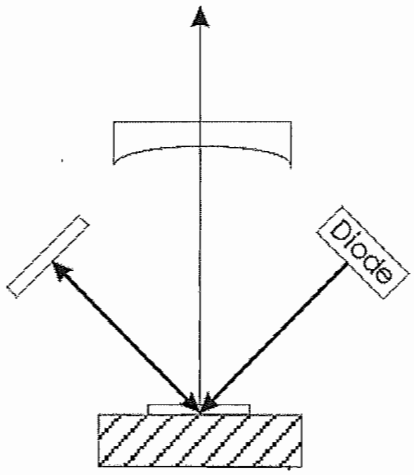

Figure (2-11). Thin disc geometry for power scaling.

As has been discussed, the output power for a laser using a single laser rod, is limited by stress induced fracture. To increase the output power of end-pumped solid-state lasers further multiple rods can be placed in the same resonator. With more than one gain medium in the cavity, it would be expected that the total amount of pump power that can be absorbed before stress fracture occurs would be increased. With more than one gain medium in the cavity, there will of course be more than one thermal lens generated in the cavity and this can make the full potential of this approach difficult to achieve. Dreidger et al extensively analysed multirod resonators for high-power solid-state lasers [29]. It was found that for a symmetric resonator, there is a single stable region of operation between two critical powers of the thermal lens focal lengths, for all other resonators there are two regions of stability between these critical focal lengths. Two-rod resonators producing twice the output power can be achieved by matching two single-rod resonators together. Their analysis showed that in the case of asymmetric resonators, the radiation field in the two rods was neither the same nor

independent of the refractive power of the thermal lens. They concluded that a two-rod high-power laser resonator should be a plane-plane one, with the two rods located symmetrically.

A simple example of this power-scaling approach with two Nd:YAG rods in the same cavity [27] is shown in figure (2-12). The pumping scheme used in figure (2-12) is the same as that shown in figure (2-10) above, mirrors M1 and M2 are flat with M2 being the output coupler. The quartz rotator is inserted in the cavity to compensate for stress-induced birefringence by rotating the polarization of the laser between laser rods. The aspheric lens in figure (2-12) is to compensate for first-order thermal focusing, the aspheric surface is designed to compensate for thermally induced spherical aberration. The proper asphere shape is that which reverses the phase at the symmetry plane, effectively acting as a phase conjugator. Using the cavity shown in figure (2-12) a stable output power of 60W was achieved with near-diffraction-limited beam quality with a total incident pump power of 235W.

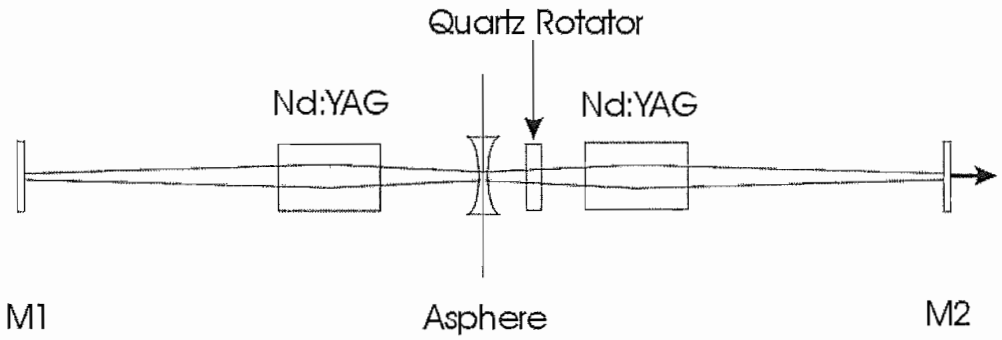

Figure (2-12). Multi-rod cavity with a degree of thermal lens compensation adapted from [27].

With multi-rod geometries the laser mode will experience two passes through each thermal lens, and with more then one thermal lens in the cavity beam degradation can be suffered easily. As shown in the example above using a negative lens the focal length of the thermal lens can be compensated for to first order, however, this will only compensate for the thermal lens at one particular pump power. If this compensation scheme is used, then the laser will have to be operated at this pump power, and attenuated after the laser, potentially resulting in degradation or movement of the output laser beam as it is attenuated. The effect of the aspheric surface at the point of symmetry in figure (2-12) is to act as a phase conjugator. Phase conjugation can also be

achieved by generating a gain grating in an amplifying medium [30, 31]. The gain grating is produced by gain saturation in an amplifying medium at the intersection of a pair of coherent beams. Deformable mirrors have been used to compensate for thermal lensing [32, 33]. This method however, only compensates for the effect of the thermal lens focal length on the laser mode in the cavity and does not correct for the phase aberrations caused by the thermal lens. This compensation will only work for a single pump power unless complex electronics are used to monitor the wavefronts leaving the resonator and the deformable mirror adjusted accordingly.

2.13 Material Selection for Diode-Pumped Solid-State Lasers

Several hosts have become popular for Neodymium, and new hosts are being developed on a regular basis. Popular choices are glass [34, 35], yttrium aluminium garnet (YAG) [36-38], lithium yttrium fluoride (YLF) [39, 40], yttrium aluminium perovskite (YAP or YALO) [41] and yttrium orthovanadate (YVO_4) [20, 42, 43].

This section examines which materials are suitable for particular applications. When scaling the power of CW-lasers equations (2-8) and (2-34) can be used to guide the choice of material. Summarising both of these equations, the threshold power is inversely proportional to the stimulated emission cross-section and the fluorescence lifetime and the on axis thermal lens focal length is proportional to the thermal conductivity and inversely proportional to the thermo-optical coefficient. Therefore, the greater the product of the stimulated emission cross-section and the fluorescence lifetime the smaller the pump power at threshold. This reduces the impact of thermal effects, because under lasing operation many times above threshold the heating mechanism is essentially due to quantum defect heating. However, below threshold under non-lasing conditions other spectroscopic conditions such as energy transfer upconversion can increase the amount of absorbed pump power converted to heat, leading to stronger thermal effects. A material with a large thermal conductivity combined with a small thermo-optical coefficient will have weaker thermal lensing.

Three of the more popular materials for use in diode-pumped solid-state lasers are Nd:YAG, Nd:YLF and Nd:YVO_4, so these materials will be compared. Comparing the

$\sigma\tau$ products of the three materials YAG has the smallest at $6.2x10^{-23}cm^2s$, YVO_4 has the largest with $1.56\ x10^{-23}cm^2s$ and YLF lies between with $8.6\ x10^{-23}cm^2s$. This suggests that for similar cavities, YVO_4 should have the lower threshold and with its higher gain, allow the use of higher transmission output couplers leading to a greater slope efficiency.

Apart from the lasers for the initiation of nuclear fusion where glass is used at a low repetition rate, Nd:YAG is used extensively. This is because YAG has good thermal and structural properties. Therefore, it can be pumped harder and is the choice for very high power oscillators. YAG has a cubic crystalline structure, so when the pump power is increased it suffers from the problem to stress-induced birefringence. A quarter-wave plate can be used to reduce the losses caused by stress-induce birefringence when a polarized output is required [44].

Nd:YLF has a negative thermo-optical coefficient so the thermal lens caused by the change in refractive index is negative. This compensates to a certain degree for the positive lens caused by end-face bulging. The thermo-optical coefficient is different for the two possible polarizations with the σ-polarisation having the smaller thermo-optical coefficient and stimulated emission cross-section, the stimulated emission cross-section being about 2/3 of the π-polarization and the thermo-optical coefficient being half that of the π-polarization. The stress fracture limit of Nd:YLF is substantially lower then that of Nd:YAG making it more challenging to use in many situations.

With its large $\sigma\tau$ product threshold should be achieved in Nd:YVO_4 before thermal effects become pronounced, by the extra heating that occurs due to non-lasing conditions present before threshold. The stress fracture limit of Nd:YVO_4 being between that of Nd:YAG and Nd:YLF means that it has to be considered for use at low to medium powers before the risk of stress-fracture becomes too great.

For pulsed operation, the two regimes require slightly different properties. For mode-locked operation, the heating is similar to CW conditions. The energy storage time for Q-switched lasers is of the order of the lifetime of the upper laser level. This suggests that Nd:YLF is more suitable as a choice for Q-switched lasers. However, under Q-

switched operation there is a greater population inversion density than achievable under lasing conditions where the relative populations are set at threshold. This not only leads to greater small-signal gains but other spectroscopic processes such as energy transfer upconversion. Energy transfer upconversion is discussed in greater detail in chapter 3, but in the context of this discussion the effect of upconversion is to increase the amount of absorbed pump power converted to heat, through the non-radiative transition of ions excited to higher states. This increased thermal lensing adds the additional requirement that the material must have good thermo-mechanical properties. For mode-locked operation, the pulse duration achievable is inversely proportional to the gain bandwidth. Both Nd:YLF and Nd:YVO_4 have larger bandwidths than Nd:YAG so will be able to support shorter pulses.

The choice of material for an amplifier is similar to that required for Q-switching, in that in the absence of lasing there will be greater thermal loading, which could lead to beam quality degradation. The small signal gain coefficient is given by the product of the stimulated emission cross-section and the population inversion density. Neglecting ETU, the population inversion density is proportional to the product of the absorption coefficient and the fluorescence lifetime. Therefore, to a first approximation the material with the largest stimulated emission cross-section, fluorescence lifetime and absorption coefficient should give the greatest small signal gain. Comparing the three materials, Nd:YAG has the lowest product with Nd:YVO_4 having the greatest and Nd:YLF lies between the two.

From the analysis above it can be seen that whilst Nd:YAG is the material for use in very high power oscillator situations, where its power handling capabilities exceed those of Nd:YLF and Nd:YVO_4. If the thermal lensing in Nd:YVO_4 is known, then for operation at low to medium powers then Nd:YVO_4 suggests itself as the gain medium, however as the power is extended to high powers the use of Nd:YAG might be preferred.

2.14 References

1. Koechner, W., *Solid-State Laser Engineering*. 5 ed. Springer Series in Optical Sciences, ed. T. Tamir. Vol. 1. 1999, Berlin: Springer.
2. Sasnett, M.W., *The Physics and Technology of Laser Resonators*, ed. P.E. Jackson. 1989, Bristol and New York: Adam Hilger.
3. Beach, R., et al., *Modular Microchannel Cooled Heatsinks for High Average Power Laser Diode Arrays.* IEEE Journal of Quantum Electronics, 1992. **28**(4): p. 966-976.
4. Beach, R., et al., *Scalable diode-end-pumping technology applied to a 100-mJ Q-switched Nd^{3+}:YLF laser oscillator.* Optics Letters, 1993. **18**(16): p. 1326-1328.
5. Feugnet, G., et al., *High-efficiency TEM_{00} Nd:YVO_4 laser longitudinally pumped by a high-power array.* Optics Letters, 1995. **20**(2): p. 157-159.
6. Beach, R., *Theory and optimization of lens ducts.* Applied Optics, 1996. **35**(12): p. 2005-2015.
7. Zbinden, H. and J.E. Balmer, *Q-switched Nd:YLF laser end pumped by a diode-laser bar.* Optics Letters, 1990. **15**(18): p. 1014-1016.
8. Berger, J., et al., *Fiber-bundle coupled, diode end-pumped Nd:YAG laser.* Optics Letters, 1988. **13**(4): p. 306-308.
9. Verdun, H.R. and T. Chuang, *Efficient TEM_{00}-mode operation of a Nd:YAG laser end pumped by a three-bar high-power diode-laser array.* Optics Letters, 1992. **17**(14): p. 1000-1002.

10. Shannon, D.C. and R.W. Wallace, *High-power Nd:YAG laser end pumped by a cw, 10mm x 1μm aperture, 10-W laser-diode bar.* Optics Letters, 1991. **16**(5): p. 318-320.

11. Clarkson, W.A. and D.C. Hanna, *Two-mirror beam-shaping technique for high-power diode bars.* Optics Letters, 1996. **21**(6): p. 375-377.

12. Senior, J.M., *Optical Fiber Communications.* 2 ed. Prentice Hall International Series in Optoelectronics, ed. B. Weiss. 1992, New York: Prentice Hall.

13. Clarkson, W.A. and D.C. Hanna, *Optical Resonators-Science and Engineering*, ed. R. Kossowsky. 1998: Kluwer Academic Publishers.

14. Clarkson, W.A. and D.C. Hanna, *Effects of transverse-mode profile on slope efficiency and relaxation oscillations in a longitudinally-pumped laser.* Journal of Modern Optics, 1989. **36**(4): p. 483-498.

15. Innocenzi, M.E., et al., *Thermal modeling of continuous-wave end-pumped solid-state lasers.* Appl. Phys. Lett., 1990. **56**(1831-3).

16. Fluck, R., M.R. Hermann, and L.A. Hackel, *Birefringence compensation in single solid-state rods.* Appl. Phys. Lett., 2000. **76**(12): p. 1513-1515.

17. Nye, J.F., *Physical Properties of Crystals Their representation by tensors and matrices*. 1957, Oxford: Clarenden Press.

18. Clarkson, W.A., N.S. Felgate, and D.C. Hanna, *Simple method for reducing the depolarization loss resulting from the thermally induced birefringence in solid-state lasers.* Optics letters, 1999. **24**(12): p. 820-822.

19. Chen, Y.F., *Design criteria for concentration optimization in scaling diode end-pumped lasers to sigh powers: Influence of thermal fracture.* IEEE Journal of Quantum Electronics, 1999. **35**(2): p. 234-239.

20. Zhan, J., et al., *Efficient TEM_{00} operation of Nd:YVO_4 laser end pumped by fibre-coupled diode laser.* Electon. Lett., 1997. **33**: p. 775-777.

21. Tidwell, S.C., et al., *Scaling CW Diode-End-Pumped Nd:YAG Lasers to High Average Powers.* IEEE Journal of Quantum Electronics, 1992. **28**(4): p. 997-1009.

22. VLOC, *VLOC Data Sheets and product catalouge.*

23. Clarkson, W.A., *Thermal effects and their mitigation in end-pumped solid-state lasers.* Journal of Physics D-Applied Physics, 2001. **34**(16): p. 2381-2395.

24. Driedger, K.P., R.M. Ifflander, and H.P. Weber, *Multirod Resonators for High-Power Solid-State Lasers with Improved Beam Quality.* IEEE Journal of Quantum Electronics, 1988. **24**(4): p. 665-674.

25. Siegman, A.E., *Analysis of Laser-Beam Quality Degradation Caused by Quartic Phase Aberrations.* Applied Optics, 1993. **32**(30): p. 5893-5901.

26. Kogelnik, H.W. and T. Li, *Laser Beams and Resonators.* Applied Optics, 1966. **5**(10): p. 1550-1567.

27. Tidwell, S.C., J.F. Seamans, and M.S. Bowers, *Highly efficient 60-W TEM_{00} cw diode-end-pumped Nd:YAG laser.* Optics Letters, 1993. **18**(2): p. 116-118.

28. Stewen, C., et al., *A 1-kW CW Thin Disc Laser.* IEEE Journal of Selected Topics in Quantum Electronics, 2000. **6**(4): p. 650-657.

29. Driedger, K.P., R.M. Ifflander, and H. Weber, *Multirod Resonators for High-Power Solid-State Lasers with Improved Beam Quality.* IEEE Journal of Quantum Electronics, 1988. **24**(4): p. 665-674.

30. Trew, M., et al., *Multiwatt continuous-wave adaptive laser resonator.* Optics Letters, 2000. **25**(18): p. 1346-1348.

31. Mailis, S., et al., *High-phase-conjugate reflectivity (>800%) obtained by degenerate four-wave mixing in a continuous-wave diode-side-pumped Nd:YVO_4 amplifier.* Optics Letters, 1999. **24**(14): p. 972-974.

32. Pavel, N., T. Dascalu, and V. Lupei, *Variable reflectivity mirror unstable resonator with deformable mirror thermal compensation.* Optics Communications, 1996. **123**: p. 115-120.

33. Greiner, U.J. and H.H. Klingenberg, *Thermal lens correction of a diode-pumped Nd:YAG laser of high TEM_{00} power by an adjustable-curvature mirror.* Optics Letters, 1994. **19**(16): p. 1207-1209.

34. Kozlovsky, W.J., T.Y. Fan, and R.L. Byer, *Diode-pumped continuous-wave Nd:glass laser.* Optics Letters, 1986. **11**(12): p. 788-790.

35. Yanovsky, V.P., M.C. Richardson, and E.J. Miesak, *Compact, Single-Frequency, High-Power ND:Glass Laser.* IEEE Journal of Quantum Electronics, 1994. **30**(4): p. 884-886.

36. Fan, T.Y. and R.L. Byer, *Modeling and CW Operation of a Quasi-Three-Level 946nm Nd:YAG Laser.* IEEE Journal of Quantum Electronics, 1987. **23**(5): p. 605-612.

37. Agnesi, A., et al., *High-repetition-rate Q-switched diode-pumped Nd:YAG laser at 1.444μm.* Applied Optics, 1998. **37**(18): p. 3984-3986.

38. Marling, J., *1.05-1.44μm Tunability and performance of the CW Nd^{3+}:YAG Laser.* IEEE Journal of Quantum Electronics, 1978. **14**(1): p. 56-62.

39. Murray, J.E., *Pulsed Gain and Thermal Lensing of Nd:$LiYF_4$.* IEEE Journal of Quantum Electronics, 1983. **19**(4): p. 488-491.

40. Louyer, Y., et al., *Efficient cw operation of diode-pumped Nd:YLF lasers at 1312.0 and 1322.6nm for a silver atom optical clock.* Optics Communications, 2003. **217**: p. 357-362.

41. Boucher, M., et al., *Multiwatt CW diode end-pumped Nd:YAP laser at 1.08 and 1.34 μm: influence of Nd doping level.* Optics Communications, 2002. **212**: p. 139-148.

42. Damzen, M.J., et al., *Continuous-wave Nd:YVO_4 grazing-incidence laser with 22.5W output power and 64% conversion efficiency.* Optics Communications, 2001. **196**: p. 237-241.

43. Graf, T., et al., *Multi-Watt Nd:YVO_4 laser, mode locked by a semiconductor saturable absorber mirror and side-pumped by a diode-laser.* Optics Communications, 1999. **159**(1-3): p. 84-87.

44. Clarkson, W.A., N.S. Felgate, and D.C. Hanna, *Simple method for reducing the depolarization loss resulting from thermally induced birefringence in solid-state lasers.* Optics Letters, 1999. **24**(12): p. 820-822.

Chapter 3: $Nd:YVO_4$ and the influence of upconversion on performance

3.1 Introduction

In this chapter spectroscopic processes which can affect the performance of end-pumped solid-state lasers are discussed. The effect of energy transfer upconversion (ETU) at high population inversion densities, which are easily achievable under end-pumped operation, is greater than these other processes and consequently the rest of the chapter examines the impact of ETU in further detail. The theory of ETU is presented with both static and migration assisted forms discussed and their effect on the fluorescence decay time from the excited level is considered. The fluorescence decay from the excited level is then used to determine the ETU parameter in $Nd:YVO_4$ for different dopant concentrations. With knowledge of the ETU parameter and the particular form of ETU, its impact on laser performance is examined. This expression is then confirmed by measuring the threshold pump power for different cavity losses. By comparing the effect of pump distribution on ETU, a saturation intensity is then derived. This can be inserted into the expression for threshold pump power and a figure of merit is developed from the ratio of the gain saturation intensity and the ETU saturation intensity. Finally a comparison of the influence of ETU in Nd:YAG, Nd:YLF and $Nd:YVO_4$ is made.

3.2 Theory of ETU

At low pump deposition densities, the behaviour of solid-state lasers is well understood. By maintaining a good spatial overlap between pump and laser modes, end-pumping provides an efficient route to TEM_{00} operation with flexibility in operating wavelength and mode of operation. As the pump deposition is increased, the large population inversion densities that can be achieved through end-pumping lead to deviations from this well defined behaviour with spectroscopic loss processes that are negligible at low powers becoming appreciable at high powers.

Spectroscopic processes that can degrade the performance of solid-state lasers include cross-relaxation, excited state absorption of pump or laser radiation and energy transfer upconversion. Cross relaxation is the process by which an excited ion transfers part of its excitation energy to an unexcited ion. Excited state absorption of pump radiation (ESAPR) occurs when an excited ion in the upper lasing level absorbs a pump photon, and is excited to a higher energy level. Excited state absorption of laser radiation (ESALR) is similar to ESAPR however, the excited ion absorbs a laser photon. The effect of ESALR is to reduce the effective stimulated emission cross-section through the competition between emission and absorption. When ESALR occurs at the laser wavelength the net gain cross-section, σ_n is given by [1].

$$\sigma_n = \sigma_e - \sigma_{ESA}^L \tag{3-1}$$

where σ_e is the stimulated emission cross-section and σ^L_{ESA} is the cross section for ESALR. If the net gain cross section is decreased then the threshold pump power will be increased. Excited state absorption for Nd^{3+} has been studied in several different materials including YLF [1-3], YAG [1, 2], YVO_4 [4], BNN [5] and LMA [1, 2]. These studies have shown that for these materials the effect of ESALR is generally negligible. The effect of ESAPR has also been studied [2], where it was found that ESAPR would perturb the performance of the laser system only if the ESAPR cross section was of the same order of magnitude as that of the stimulated emission. In the same study, it was found that ESAPR alone could not explain the measured excitation spectra and required the addition of ETU terms.

Since it has been shown that the effect of excited state absorption is negligible on the 1064nm transition [4], the effect of ETU will be examined in greater detail. ETU is detrimental to the power scaling of neodymium doped laser materials because it reduces potential gain [6] and increases the amount of heat deposited in the crystal, leading to stronger thermally induced effects [7-10]. Therefore, knowledge of ETU occurring in the material being used is essential for the proper design of high brightness laser and amplifier systems. ETU arises because paramagnetic ions in solids can only be treated as isolated ions when they are well separated. As the concentration is increased or if non-random distribution occurs, the ion spacing may become small enough that the ions interact. The coupling of adjacent paramagnetic ions can arise via

exchange interactions if their wavefunctions overlap, via super-exchange interactions involving intervening ions, or via various electric and magnetic multipolar interactions [11]. These can occur through the electric multipolar coupling arising from the Coulomb interaction between the electron charge clouds of two ions.

Early work on ETU and cross relaxation was carried out by Förster [12] and Dexter [13] to explain sensitised luminescence. 'Sensitised luminescence refers to the process whereby an impurity atom (activator) having no appreciable absorption band in a given region of the (visible or UV) spectrum is made to emit radiation upon excitation in this region as a result of absorption by and transfer from another impurity atom (sensitiser) or from the host lattice' [13]. The theory of sensitised luminescence can be applied to ETU and cross-relaxation because they are all concerned with the transfer of energy from an excited ion to another ion. ETU, is observed experimentally through the shortening of the effective decay lifetime of luminescence, by changing the time-dependent shape of the decay and the observation of 'yellow' fluorescence in Nd^{3+} systems resulting from emission from the transition from the excited levels directly to the ground state. However, this 'yellow' fluorescence is negligible when compared with the non-radiative decays from the excited levels. ETU occurs when two neighbouring excited ions exchange energy such that one of the ions is excited to a higher energy level whilst the other ends up in a lower lying level as shown in figure (3-1). In figure (3-1), the solid lines represent an exchange of energy between the two ions, promoting one and demoting the other and the dashed lines represent non-radiative decays from one level to another. The acceptor decays non-radiatively from the higher excited level to return to the upper laser level whilst the donor non-radiatively decays from the lower level to the ground level. The two sets of non-radiative transitions cause extra heat to be generated in the gain medium, exacerbating thermal problems caused by the conversion of absorbed pump power into heat.

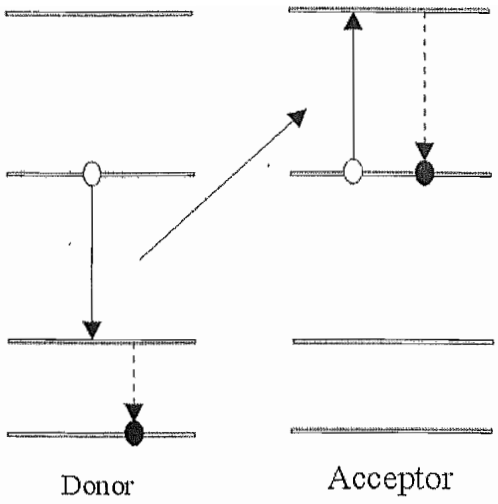

Figure (3-1) Example of ETU with the energy from a donor, exciting an acceptor to a higher energy level. The solid lines show the direction of the exchange of energy in the ETU process and the dashed lines show non-radiative decays

As shown for Nd-doped glass in figure (3-2) there are different upconversion transitions in the Nd^{3+} system [14]. Although the ETU processes are not caused by the emission and absorption of photons, the potential upconversion processes that can take place are governed by the overlap of energy levels involved in laser transitions and higher energy levels. Each ETU process will have a different parameter and therefore relative rate of transition associated with each process.

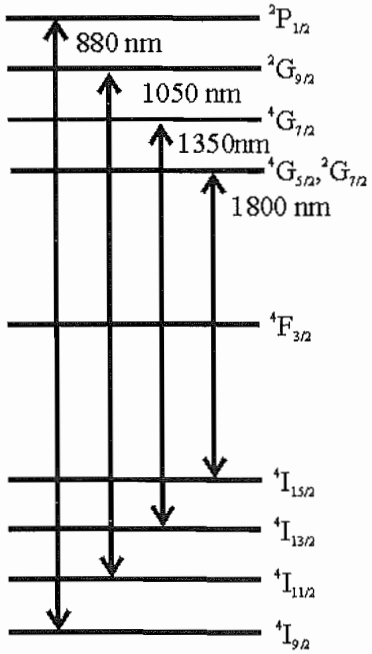

Figure (3-2) Energy levels of Nd^{3+} in glass and depiction of the resonant interactions that lead to ETU involving two Nd^{3+} ions [14].

The particular transitions that will occur depend upon the Stark energy levels, which are in turn governed by the Nd^{3+} host. Table 3-1 lists the lowest energy levels for different bands, the width of these bands and the difference in energy between the lowest energy of each band and that of the upper lasing level for Nd:YVO_4 and Nd:YAG [15]. For Nd:YVO_4 it can be seen that there are good overlaps between the $^4F_{3/2}\rightarrow{}^4G_{5/2}$, $^4F_{3/2}\rightarrow{}^4G_{7/2}$, $^4F_{3/2}\rightarrow{}^4G_{9/2}+{}^4G_{11/2}+{}^2K_{15/2}$ with the $^4F_{3/2}\rightarrow{}^4I_{15/2}$, $^4F_{3/2}\rightarrow{}^4I_{13/2}$, $^4F_{3/2}\rightarrow{}^4I_{11/2}$ transitions respectively, and possible phonon assisted overlap between the $^4F_{3/2}\rightarrow{}^2D_{3/2}$ and $^4F_{3/2}\rightarrow{}^4I_{9/2}$ transitions. For Nd:YAG the equivalent pairings are the upconversion processes of $^4F_{3/2}\rightarrow{}^4G_{5/2}$, $^4F_{3/2}\rightarrow{}^4G_{7/2}$, $^4F_{3/2}\rightarrow{}^4G_{5/2}$ or $^4G_{11/2}$, $^4F_{3/2}\rightarrow{}^2D_{3/2}$ correlating with the downward transitions of $^4F_{3/2}\rightarrow{}^4I_{15/2}$, $^4F_{3/2}\rightarrow{}^4I_{13/2}$, $^4F_{3/2}\rightarrow{}^4I_{11/2}$ and $^4F_{3/2}\rightarrow{}^4I_{9/2}$.

Transition	Nd:YVO_4			Nd:YAG		
Down-conversion	Stark Energy cm^{-1}	ΔE cm^{-1}		Stark Energy cm^{-1}	ΔE cm^{-1}	
$^4I_{9/2}$	0	433	11366	0	857	11427
$^4I_{11/2}$	1966	216	9400	2002	519	9425
$^4I_{13/2}$	3910	260	7456	3922	576	7505
$^4I_{15/2}$	5834	484	5532	5758	976	5669
$^4F_{3/2}$	11366	18	-	11427	85	-
Possible Upconversion						
$^4G_{5/2}$	16824	146	5458	16849	193	5422
$^2G_{7/2}$	17215	53	5849	17241	334	5814
$^4G_{7/2}$	18772	153	7406	18723	263	7296
$^2G_{9/2}+{}^2K_{13/2}$	19055	374	7689	19154	894	7727
$^4G_{9/2}+{}^4G_{11/2}+{}^2K_{15/2}$	20794	767	9428	-		
$^4G_{9/2}$	-			20730	73	9303
$^4G_{11/2}$	-			20962	200	9535
$^2K_{15/2}$	-			21522	384	10095
$^2D_{3/2}$	21935	-	10569	22036	-	10609
$^2P_{1/2}$	23041	-	11675	23155	-	11728
$^2D_{5/2}$	23596	45	12230	23674	175	12247

Table (3-1). Stark energy levels for Nd:YVO_4 and Nd:YAG [15].

Whilst ETU can enhance the performance of certain laser transitions in other rare earth doped crystals, but is generally detrimental to the performance of Nd-doped crystals and so methods for reducing the effect of ETU is essential. By considering the lifetime of the upper laser level the negative effect that these processes can be highlighted. By combining the radiative and non-radiative transition rates from an excited level the lifetime τ_a of an excited state a is given by [11]

$$\frac{1}{\tau_a} = \sum_b W_{ab}^R + \sum_b W_{ab}^{NR} \tag{3-2}$$

In equation (3-2) the summations are over all final terminating states b and W^R and W^{NR} are the radiative and non-radiative transition probabilities. The non-radiative transition probabilities include energy transfer rates arising from ion-ion interactions and leads to a definition of the radiative quantum efficiency η_a defined by

$$\eta_a = \frac{\sum_b W_{ab}^R}{\sum_b W_{ab}^R + \sum_b W_{ab}^{NR}} = \tau_a \sum_b W_{ab}^R \tag{3-3}$$

Therefore, any reduction in the lifetime of the upper lasing level, through an increase of W^{NR} for example, will reduce the quantum efficiency of the level.

The electric multi-pole interaction rate between two ions separated by $R_{ij}=|\mathbf{r}_i-\mathbf{r}_j|$ can be expressed as [16]

$$W_{ij} = \frac{C^{d-d}}{R_{ij}^6} + \frac{C^{d-q}}{R_{ij}^8} + \frac{C^{q-q}}{R_{ij}^{10}} + \ldots\ldots \tag{3-4}$$

where C^{d-d} is the interaction micro-parameter for dipole-dipole coupling, C^{d-q} is for dipole-quadrupole coupling and C^{q-q} is for quadrupole-quadrupole coupling, the quadrupole moment arising due to asymmetric charge distribution [17].

However, each micro-parameter can be further divided and associated with different interactions, migration (C_{dd}), self-quenching (C_{da}) and ETU (C_{da}^{*}). The subscripts indicate donor-donor or donor-acceptor interactions in which donors transfer their energy to acceptors [16, 18]. Migration leads to a spatial redistribution of energy, self–quenching annihilates a single excitation, and ETU converts two excitations into a single higher energy excitation.

Depending on the relative rates of upconversion and migration ETU can be static or migration assisted. Static upconversion occurs when excited ions do not leave the site of their origin before upconverting. In migration-assisted upconversion, an excitation migrates over donors before it reaches an acceptor. Relaxation by migration-assisted upconversion is a multi-step process involving resonant energy transfer from one ion to another in a random walk manner and finally to an acceptor which acts as a quenching centre. Migration-assisted transfer can have a diffusion or hopping character. In the diffusion regime the average distance between two neighbouring donor centres is much less than the characteristic spatial scale of donor-acceptor interaction, this defines a quenching sphere around acceptors [19, 20]. In this situation, the neighbouring donors are excited practically uniformly and the density of donor excitation gradually changes spatially. In the hopping regime, the average distance is much larger than the radius of the quenching sphere and an excitation takes only one hop into or out of the sphere [21]. The ETU processes for rare-earth-doped laser crystals are typically best represented by the hopping model [16, 21]. The ratio of the micro-parameters of donor-donor and donor-acceptor interactions controls the nature of the migration. If $C_{da}/C_{dd}<N^{(s-m)/3}$ then the hopping regime is realized and if $C_{da}/C_{dd}>N^{(s-m)/3}$ then diffusion occurs, where N is the net concentration of donors and s and m are the multi-polarities of donor-donor and donor-acceptor interaction [21]. For dipole-dipole interactions $s=m$ and the nature of the migration is then determined by whichever micro-parameter is the greatest.

The energy levels involved in an ETU process are shown in figure (3-3). In figure (3-3) energy level 0 is the ground level, level 1 is the lower level to which the donor is de-excited to, level 2 is the upper lasing level and level 3 is the higher level that the acceptor is excited to. In the following analysis the rates of multiphonon decay are assumed to be fast, so that there is negligible population in levels 1 and 3. It is also assumed that there is no ground state bleaching so that only the population dynamics of level 2 need to be considered. The dynamics of the decay of the population inversion density, $n(t)$, in the absence of stimulated emission is determined by the nature of the ETU; It has one form in the static regime and another in the migration assisted regime. The decay of the excited population is given by [21]

$$\frac{dn(t)}{dt} = -\frac{n(t)}{\tau} - F(t)n^2(t) \tag{3-5}$$

where $F(t)$ is the non-linear quenching rate and τ is the fluorescence lifetime. The first term of equation (3-5) represents the depopulation due to fluorescence and the second that due to non-linear quenching. The non-linear quenching rate is the product of the probability that a donor did not transfer its energy and the probability of a donor-acceptor interaction occurring. This is then averaged over the ensemble of donors. In a simple model where upconversion is approximated in terms of Wn^2, $F(t)$ is assumed to be time-independent and $F(t)=W$.

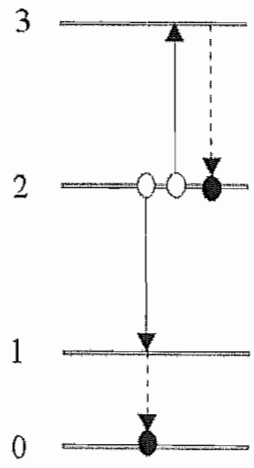

Figure (3-3). Energy levels used for the ETU analysis.

If the hopping migration-assisted regime dominates than the temporal population density of the excited level after excitation is given by [21]

$$n(t) = \frac{n(0)\exp(-t/\tau)}{1 + Wn(0)\tau[1-\exp(-t/\tau)]} \tag{3-6}$$

where W is the time-independent upconversion macroparameter. This equation holds at the initial stage of decay and when the de-excitation rate is smaller then the donor-donor hopping rate. If the de-excitation rate is larger than the donor-donor hopping rate then the excitation does not have time to migrate and luminescence quenching occurs in the static regime. The non-linear luminescence decay kinetics in the static regime of upconversion can be presented in the form [21]

$$n(t) = \frac{n(0)\exp(-t/\tau)}{1 + (2/3)n(0)\sqrt{\tau C_{da}}\pi^2 \operatorname{erf}(\sqrt{t/\tau})} \tag{3-7}$$

Where C_{da} is a microparameter that depends on the donor-acceptor interaction and erf(x) is the error function given by

$$\operatorname{erf}(x) = \frac{2}{\sqrt{\pi}}\int_0^t e^{-t^2}\,dt \tag{3-8}$$

At large t equations (3-6) and (3-7) both tend to an exponential decay with a lifetime equal to the de-excitation lifetime. As the population inversion density decreases, the reduced rate of ETU will cause the de-excitation rate to become larger than the hopping rate and the decay will become static.

The temporal nature of the population inversion can be determined by recording the fluorescence decay from the upper lasing level. The nature of ETU can then be determined by plotting $\left[\frac{n(0)\exp(-t/\tau)}{n(t)} - 1\right]$ versus $[1-\exp(-t/\tau)]$ or $\left[\operatorname{erf}(\sqrt{t/\tau})\right]$ a linear relationship resulting for whichever regime provides the most suitable description of the behaviour [18].

If the ETU process is migration assisted, then the excited population density for non-lasing conditions can be modelled subject to the conditions above by the following equation

$$\frac{dn(r,z,t)}{dt} = R(r,z,t) - \frac{n(r,z,t)}{\tau} - Wn^2(r,z,t) \tag{3-9}$$

It has been assumed in equation (3-9) that due to the high rate of multi-phonon decay the populations in the upconverted states are negligible and R is the pumping rate per unit volume and is dependent on the pump beam deposition density. Under steady-state non-lasing conditions, $dn/dt=0$ and can be solved for n.

$$n(r,z) = \frac{-1+\sqrt{1+4R(r,z)W\tau^2}}{2W\tau} \tag{3-10}$$

As $R\rightarrow\infty$ the maximum steady-state population inversion density becomes $(R/W)^{1/2}$ as compared to the value of $R\tau$ achieved when ETU is neglected.

3.3 Experimental Determination of the ETU parameter

The method used to determine the ETU parameter in materials usually falls within two methodologies, spectroscopic and non-spectroscopic. Using spectroscopic techniques ETU has been studied in Nd:YAG [2, 6, 22] and in Nd:YLF [2, 7, 23] with values for W of 0.5 $x10^{-16}cm^3s^{-1}$ [6] and 1.7 $x10^{-16}cm^3s^{-1}$ [2] being reported respectively. The ETU parameter has been measured in Nd:YVO_4 by measuring the ratio of thermal loading under lasing and non-lasing conditions resulting in a value for W of $(1.5\pm0.5)x10^{-15}cm^3s^{-1}$ [22]. Measurement of the transient output intensity as the gain medium in a single-mode standing-wave laser is suddenly translated has been used to determine a value of $(1.5\pm0.5)x10^{-15}cm^3s^{-1}$ for Nd:YVO_4 [24].

As can be seen from equation (3-10) an accurate measurement of the ETU parameter requires an accurate knowledge of the pump rate. To characterise the pump rate, requires knowledge not only of the incident pump power, but the absorption coefficient and the beam radius in the laser crystal. The population dynamics of the upper laser level can be determined recording the intensity of the fluorescence decay from the upper level and the ETU parameter calculated from fits to the decays. The initial

section of the decay can be used to determine an effective lifetime which is a product of the fluorescence lifetime, upconversion parameter and the steady state population inversion density [18]. The intensity of the fluorescence was compared under different pump powers, and a computer model used to determine the relative rates of upconversion based on these measurements [25]. In fluorescence decay studies based on Nd-doped $LaSc_3(BO_3)_4$ and $GdVO_4$ similar values for the upconversion coefficients were found under Ti:Sapphire and laser diode pumping despite the differences in the spectral width of the pump source [18]. In the same study, the population inversion was achieved through pulsed excitation, for pulse durations from 30-400μs where there was no significant variation in the measured ETU parameter. The decay of the 'yellow' fluorescence generated during Q-switching has also been used, where during periods of high loss and therefore non-lasing conditions, the population inversion density is high so there is greater ETU occurring and thus more yellow fluorescence generated then under lasing conditions, where the circulating pulse depletes the population inversion density [3]. By measuring the fluorescence decay of the upper laser level, the particular nature of the ETU processes occurring can be determined, this is important because as shown above depending on the nature of any migration, the decay shape and population inversion characteristics change.

The value obtained by the analysis of the population dynamics of a standing wave cavity was achieved by investigating the nature of spatial hole burning [24]. Using this method the upconversion parameter in Nd:YVO_4 has been measured to be ($3x10^{-15}cm^3s^{-1}$). The phenomena of spatial hole burning arises when single longitudinal mode operation of a laser causes there to be nodes in the electric field of the lasing mode thus causing regions where the population inversion is not depleted by stimulated emission. This can lead to multi-mode operation of a laser with the peaks of the inversions contributing to the oscillation of another mode. In this case, single mode operation was ensured by using a Fabry-Perot etalon; this enables the population inversion in the holes to build up so when the laser crystal is displaced the laser mode experiences higher gain causing the output of the laser to increase from its previous CW output. In the analysis of the population dynamics used in this experiment, the diffusion arises from transfer of energy from excited ions to ions in the ground state, however, as discussed above ETU can be migration assisted, and will lead to a 'diffusion' of

excitations. Although the process of ETU is assumed to be static, leading to no contribution to the diffusion of excitation migration assisted dynamics are used to model it. The oscillations seen in the output intensity can be attributed to relaxation oscillations. The pump and laser modes may not be well matched, so that there might be ETU occurring in the wings, the displacement of the laser crystal will affect this overlap.

By comparing the amount of heat deposited in a laser crystal during lasing and non-lasing conditions the ETU parameter has been measured in Nd:YVO_4, finding a value of ($1.5x10^{-15}cm^3s^{-1}$) [22]. In this study, a migration-assisted form of ETU is assumed to determine the population dynamics. The ETU parameter was determined by by observing the temperature change of the copper housing cooling the crystal under lasing and non-lasing conditions. The difference in thermal loading could then be calculated from these temperature measurements. Under non-lasing conditions the heat deposited in the crystal is greater than under lasing conditions. This is caused by the increase in non-radiative decay produced by ETU compared to the quantum defect heating generated under lasing conditions. There are a number of assumptions that are inherent to this technique, which may not be valid. It is assumed that the temperature flows are unaffected by the amount of heat generated in the crystal. It is assumed that the temperature of the copper-cooling block remains constant. It is also assumed that the principal cause of heating under lasing conditions is due to quantum defect heating however, this is only strictly true for operation many times above threshold. The temperature rise is determined at a point away from the optical axis, where the temperature was kept low so as to avoid thermal changes in the thermal conductivity of the material. This has the consequence that any temperature rise will be small exacerbating any relative errors in the measurements. Again the pump and laser modes may not be well matched, so that there might be ETU occurring in the wings, the displacement of the laser crystal will affect this overlap.

As shown above, spectroscopic measurement of the ETU parameter in Nd-doped materials, provide a reliable way to determine the population dynamics directly of the upper lasing level, and the observation of their decays enable the determination of the ETU parameter. As a consequence, to determine the nature of the upconversion processes taking place in Nd:YVO_4 the fluorescence decays of crystals with different

neodymium concentrations were measured. The samples were excited using a fibre-coupled laser diode and the subsequent fluorescence decay observed using a photo-diode. As discussed in section 3.2 above, there are several different ETU pathways, by which neighbouring ions can interact. By recording the fluorescence decay from the upper laser level, the effect of the individual pathways can be lumped together and an effect rate of ETU determined. By observing the fluorescence from the upper lasing level, the average emission wavelength does not need to be found to calculate some average for quantum-defect heating. By observing the fluorescence decay, an average is not being taken of all the decays occurring in the laser rod, this is important because the likelihood of ETU occurring is population inversion dependent and consequently will vary through the laser rod.

A schematic of the experimental layout is shown in figure (3-4). The output of the fibre-coupled diode is collimated and then brought to a tight focus where it is modulated by an optical chopper. The combination of focus and chopper speed used in this experiment produced rise and fall times of 6μs. The pump was then imaged to a waist incident on the crystal and this was measured to have a radius of 120μm and a maximum incident power of 5.3W. The duration of the pump was sufficient for steady state conditions to be achieved; confirmed by the observation of the measured fluorescence levelling off.

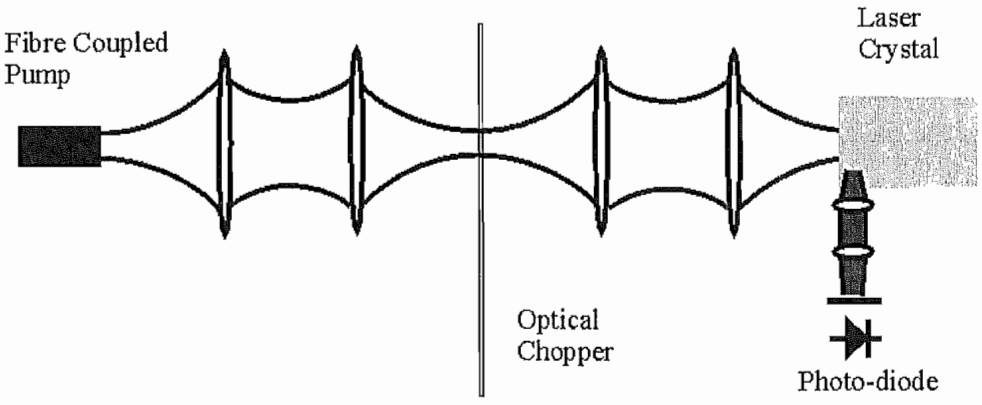

Figure (3-4). Showing the experimental set-up used to determine the upconversion parameter.

Crystals with three different Nd^{3+} concentrations of 1%, 0.5% and 0.3% were compared. All crystals were 10mm long with both ends AR coated at 808 and 1064nm. The fluorescence emanating from the side of the crystal was imaged through a pinhole onto a fast photo-diode. The fluorescence emanating from the side of the crystal was used to prevent any absorption of fluorescence, minimise stimulated emission that might occur. The pinhole served to limit the effect of diffraction of the pump allowing accurate determination of the pumping rate. The pinhole was aligned by maximising the signal from the detector at low pump powers thus ensuring that the initial section of the fluorescence was being detected. The signal was maximised at low pump powers so that ground state bleaching and ETU could be considered negligible, which might serve to reduce the fluorescence intensity at the beam waist, in comparison to the fluorescence intensity either side of it. This ensured that the beam waist was located at the centre of the pinhole, allowing the pumping rate to be confidently known, thus allowing an accurate determination of the ETU parameter. In figure (3-5) an example of the observed fluorescence decay, $I(t)$, for the 1% doped crystal under high excitation is shown. In figure (3-5) the solid lines is the recorded fluorescence the dashed line is for an exponential decay with a 62μs lifetime and the dotted line is for an exponential decay with a 105μs lifetime. As can be seen from figure (3-5) there is an initially rapid non-linear decay before the fluorescence begins to decay with the expected fluorescence lifetime. The lifetime of 62μs for the dashed line was determined from the gradient of the initial decay. The lifetime of 105μs for the dotted line was determined from the gradient of the decay at large t.

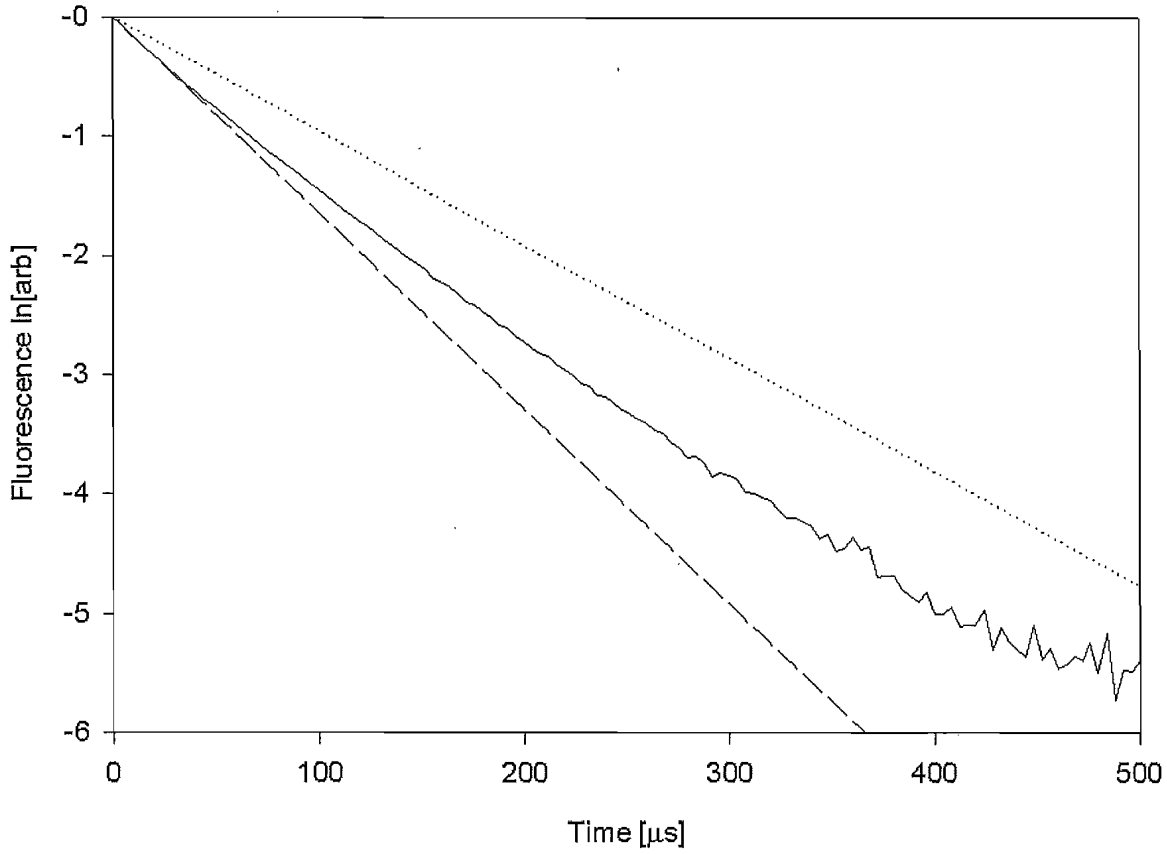

Figure (3-5). An example of the observed fluorescence from the 1% doped crystal. The solid line is the measured decay, the dashed line is for an exponential decay of 62μs and the dotted line is for an exponential decay with a lifetime of 105μs.

In figure (3-6) it has been assumed that the recorded fluorescence is directly proportional to $n(t)$ where the fluorescence decay is plotted against an exponential and nonlinear decay. As can be seen from this plot the decay is best described by migration assisted ETU and hence equation (3-6) can be used to describe the population dynamics. This is the first time that the nature of the ETU occurring in Nd:YVO_4 has be determined. This justifies the approach that is employed later to determine the population inversion density and hence the pump power required to achieve threshold. The departure from the migration-assisted regime is attributed to the reduced rate of hopping occurring at lower population inversion densities caused by the decay in the population from the upper laser level.

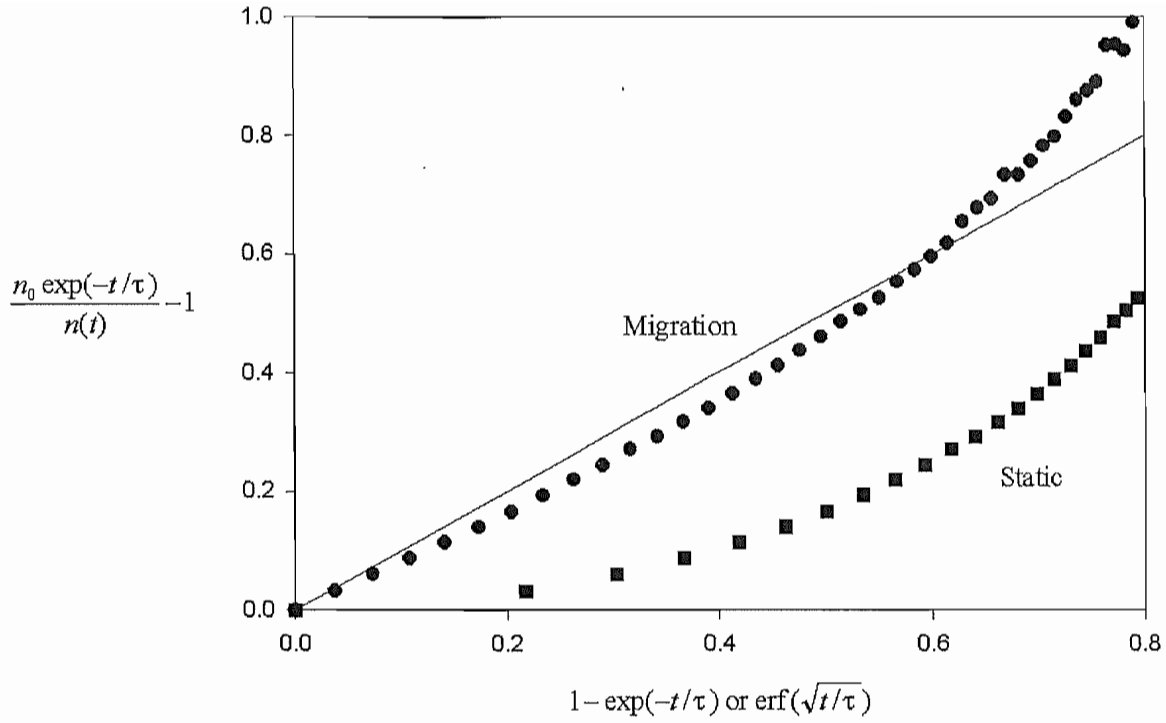

Figure (3-6). A plot of the relative observed fluorescence against exponential (circles) and error function (squares) decays to determine the nature of the upconversion processes. The solid line is for y=x, the black circles are the exponential decay and the squares are for the non-linear decay.

An average lifetime $<\tau>$ for the fluorescence decay can be defined [6]

$$\langle\tau\rangle = \frac{\int I(t)dt}{I(0)} = \frac{\int n(r,z,t)rdrdzdt}{\int n(r,z,0)rdrdz} \qquad (3\text{-}11)$$

The variation of the average lifetime with pump power for the three different crystals is shown in figure (3-7), it can be seen that the lifetime decreases dramatically with increased pump power due to increase in loss caused by upconversion increase. This is expressed in table (3-2) where it is shown that there is on average a 20% decrease in the average lifetime at high pump powers. At low powers due to the small population inversion densities, the effect of ETU is reduced and the average lifetimes at these powers are assumed to be the fluorescence lifetime in the absence of ETU. The measured lifetimes under low excitation compare favourably with other published values for Nd:YVO_4 which are in the region of 100μs [26-30].

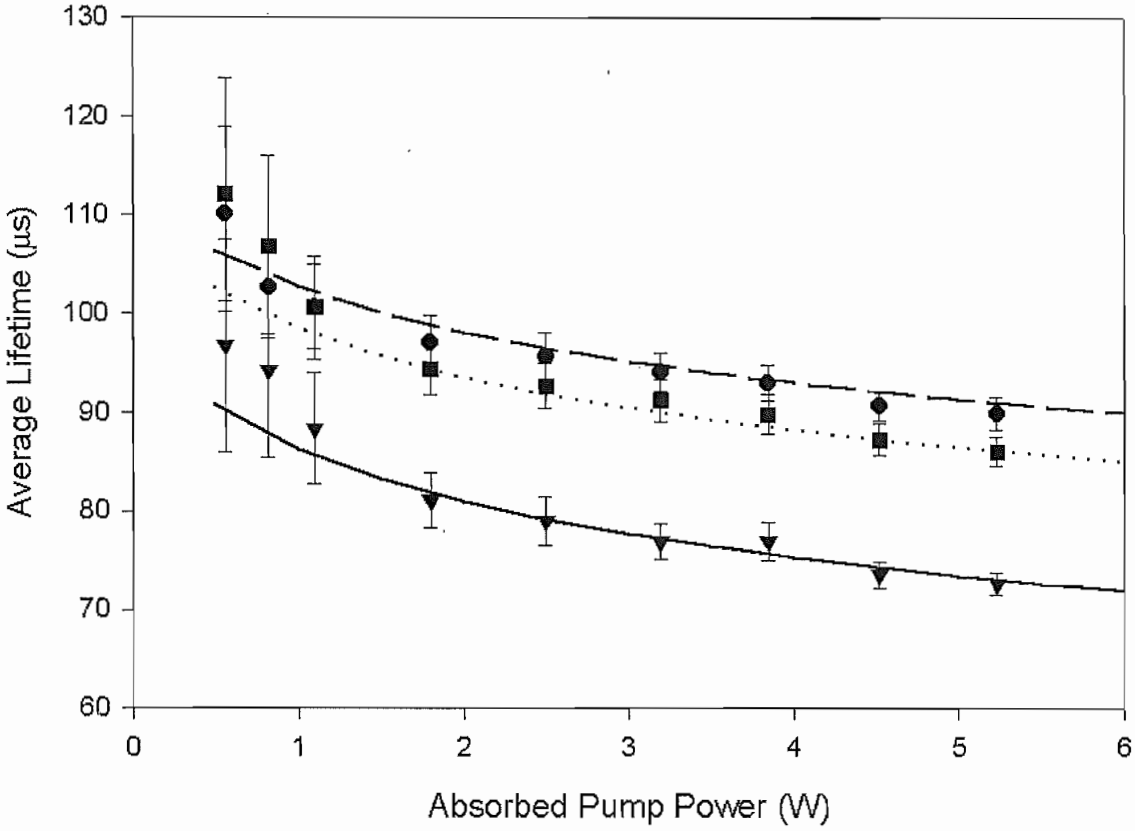

Figure (3-7). The measured variation of average lifetime with absorbed pump power in Nd:YVO_4 the circles are for the 0.3% crystal, the squares are for the 0.5% crystal and the triangles are for the 1% crystal. The lines are calculated variation of the average lifetime, using the values in table 3-2 and the already stated experimental parameters, the dashed line is for the 0.3% crystal, the dotted line is for the 0.5% crystal and the solid line is for the 1% crystal.

$[Nd^{3+}]$	$\langle\tau\rangle$ [μs]		% Decrease	$\alpha_p(m^{-1})$	$\alpha(x10^{-22}m^3s^{-1})$
	Low Power	High Power			
0.3%	110	90	18	900	3
0.5%	112	86	23	1500	2
1%	97	73	25	3000	3.5

Table 3-2. Average lifetimes for low and high pump powers for the different dopant concentrations.

The upconversion parameter can be determined by computing the following calculations. First, the spatially dependent initial population inversion density, $n(r,z,0)$, is evaluated. The pump beam is assumed to have a Gaussian transverse intensity distribution and diffraction is neglected, so that $R_p(r,z)$ can be approximated by

$$R_p(r,z) = \frac{\alpha_p}{h\upsilon_p}\frac{2P_p}{\pi w_p^2}\exp\left[\frac{-2r^2}{w_p^2} - \alpha_p z\right]. \qquad (3\text{-}12)$$

where α_p is the absorption coefficient, P_p is the incident pump power and w_p is the pump spot size. The beam quality of the pump beam is M^2=100 and with the pump beam waist radius used, has a Rayleigh range of 1.1mm in the crystal, the diameter of the pinhole is the same as this. Therefore, if the beam waist is located at the centre of the pinhole, it can be assumed that the radius of the beam remains constant. With these simplifying assumptions, n(r,z,0) can be determined by inserting equation (3-12) into equation (3-10). The spatially resolved time-dependent population inversion, $n(r,z,t)$ can be determined by inserting $n(r,z,0)$ into equation (3-6). The average lifetime can then be determined by putting $n(r,z,t)$ and $n(r,z,0)$ into equation (3-11). The upconversion parameter is found by varying its value to give the best fit to the data in figure (3-7). The upconversion parameters measured in this way and the data used to obtain them are shown in table (3-2).

For the 1% doped crystal the upconversion parameter giving the best fit to the observed data is $3.5\text{x}10^{-16}\text{cm}^3\text{s}^{-1}$, for the 0.5% case it is $2\text{x}10^{-16}\text{cm}^3\text{s}^{-1}$ and the value is $3\text{x}10^{-16}\text{cm}^3\text{s}^{-1}$ for the 0.3% crystal. Previous studies in Nd:YAG have shown that the upconversion parameter varies with the square of the Nd concentration [6], this is only strictly true if the upconversion process is static rather then migration assisted. This suggests that ETU in Nd:YAG is best modelled by the static regime in this material.

Whilst these ETU parameters are much larger then those measured in Nd:YAG, and Nd:YLF, they are approximately ten times smaller than the value determined by the laser output dynamics [24] and three times lower than the value determined by comparison of the thermal generation under lasing and non-lasing conditions [22]. As can be seen from equations (3-10) and (3-12) the population inversion density is controlled by the product of the material spectroscopic parameters of $\alpha_P W\tau^2$. The values used to calculate the ETU parameter here and in Ref [22] is shown in table (3-3).

As can be seen from the data in the table, similar values for the absorption coefficients and fluorescence lifetimes have been used in the two experiments, so they cannot be used to explain the difference between the two experimental results. However, there is quite a variation in the different measured parameters for different materials as shown in table (3-4). Table (3-4) shows that the measurement of the ETU parameter in Nd:YLF shows reasonable consistency. However, both Nd:YAG and Nd:YVO_4 show a considerable degree of variation in the measured value of the ETU parameter. The two extreme values for Nd:YAG were determined by spectroscopic techniques, so even through a direct measurement of the upper laser level. In an effort to ascertain which value of ETU parameter is the correct value in Nd:YVO_4 the threshold pump power under different cavity losses will be determined in the next section.

Ref	[22]	Measured
$[Nd^{3+}]$	0.5%	0.5%
α $[m^{-1}]$	1000	1500
τ [μs]	100	112
W $[x10^{-21}\ m^3s^{-1}]$	1.5	0.2
$\alpha_p W\tau^2$ $[x10^{-26}\ m^2s]$	1.5	0.4

Table (3-3). Comparison of the different parameters used to determine the ETU parameter here and in Ref [22].

Ref	W $[x10^{-16}\ cm^3s^{-1}]$		
	Nd:YAG	Nd:YLF	Nd:YVO_4
[2]	2.8	1.7	-
[25]	-	1.7	-
[6]	0.5	-	-
[22]	1.8	-	15
[24]	-	-	30
[16]	-	1	-
Measured	-	-	3

Table 3-4. Different measured values for the upconversion parameter.

3.4 Impact of ETU at Threshold

To examine the influence of ETU on lasing its effect on the threshold pump power are examined in this section. As shown in chapter 2, the slope efficiency is only dependent on the overlap efficiency, absorption efficiency, losses and the pump and lasing frequencies. Therefore, the slope efficiency will not be affected by ETU. However, as shown earlier, the population inversion density is modified by ETU, this reduces the potential gain. Another simplistic way to view this is that ETU reduces the time that an ion spends in the upper laser level, reducing the effective lifetime of the level. The effect of ETU therefore is to increase the pump power required to reach threshold. The rate equation analysis of Kubodera and Otsuka [31] is extended here to include ETU terms. The rate equations for the excited population density is

$$\frac{dn(r,z,t)}{dt} = r_p(r,z,t) - c_n\sigma s(r,z,t)n(r,z,t) - \frac{n(r,z,t)}{\tau} - \alpha n^2(r,z,t) \qquad (3\text{-}13)$$

where $r_p(r,z,t)$ is the pumping rate density, c_n is the speed of light in the gain medium, σ is the stimulated emission cross-section, $s(r,z,t)$ is the photon density, τ is the fluorescence lifetime and α the upconversion parameter. The first term on the right hand side is the increase in population inversion density due to pumping, the second is the de-population due to stimulated emission, the third is the depopulation due to spontaneous emission and the final term is de-population caused by upconversion. Each upconversion process only reduces the population inversion by one because the rate of multiphonon decay is assumed to be fast enough for there to be a negligible population in the higher excited levels and the transitions from the higher excited levels to the ground states have been neglected. The rate equation for the total number of photons in the cavity is given by

$$\frac{dS(t)}{dt} = \int_{cavity} c_n\sigma s(r,z,t)n(r,z,t)dV - \gamma S(t) \qquad (3\text{-}14)$$

where $\gamma=1/\tau_c$, with τ_c being the cavity lifetime and the total number of photons in the cavity is given by

$$S(t) = \int_{cavity} \gamma s(r,z,t)dV \qquad (3\text{-}15)$$

In equation (3-14), the first term on the right hand side is the increase in the number of photons in the cavity by stimulated emission and the second term is the decrease in the number of photons caused by cavity losses.

Under steady-state conditions equations (3-13) and (3-14) can be solved. This is done for the first time in appendix A, and leads to the following expression for the threshold pump power

$$P_{th} = P_{th\alpha 0}\left(1+\frac{(L+T)\tau W\alpha_P}{4\sigma\left[1-\exp\left(\frac{-2w_P^2}{w_L^2}\right)\right]}\right) \tag{3-16}$$

where, $P_{th\alpha 0}$ is the threshold pump power without upconversion, α_P is the absorption coefficient of the pump in the laser medium, σ is the stimulated emission cross-section, L is the cavity loss, T is the transmission of the output coupler and $L+T<1$. In the derivation of equation (3-16) a top-hat beam profile with a spot size of w_P has been assumed for the pump beam and a Gaussian profile with a beam waist of w_L for the laser mode. It has also been assumed the neither beam radii changes with distance (i.e. neglecting diffraction) in the gain medium. It has been assumed that all of the pump power is absorbed and ground state bleaching is negligible. Equation (3-14) demonstrates that ETU increases the pump power required to reach threshold. It shows that the larger the lifetime or absorption coefficient the greater the effect of ETU at threshold. This is to be expected since at long lifetimes the chance of ETU processes occurring increases and larger absorption coefficients generate greater population inversion densities. From equation 3-16 it can be seen that generally for a low-power end-pumped solid-state laser $w_p \sim w_L$ and for low losses the increase in the threshold pump power is given by a figure of merit defined as

$$FOM = \frac{\sigma}{\tau W\alpha_p} \tag{3-17}$$

This figure of merit is simply a comparison of the relative rates of upconversion and stimulated emission. For materials with a large figure of merit, the effect of ETU at threshold will be small.

3.5 Laser Threshold Experiment

The effect of ETU on threshold for Nd:YVO_4 was determined by varying the losses inside a laser cavity. The cavity losses were altered by changing the angle of a flat glass plate in the cavity. The pumping level was then adjusted until relaxation oscillations were observed thus confirming that threshold had been achieved. Both the 1% and 0.3% crystals were used in the experiment.

Figure (3-8) shows a schematic of the layout used in the threshold experiment. The unpolarized output of the fibre-coupled diode is collimated using lens L1 and then passes through a polarizing beam splitter. The incident pump power on the crystal is governed by the relative orientation of the half-wave plate and the second beam splitter with a maximum of 600mW available. The lens L2 focuses the pump beam to a beam waist of 150μm in the crystal. Lens L2 and mirror M2 was mounted on an X stage so that the displacement of the laser mode in the laser crystal as the glass plate is rotated could be compensated for. With an M^2 of 22 from the fibre, the pump has a Rayleigh range of 8mm in the crystal so it can be assumed that the pump size is approximately constant in the gain medium. The crystal was orientated so that the c-axis was parallel to the transmitted polarization of the second beam splitter.

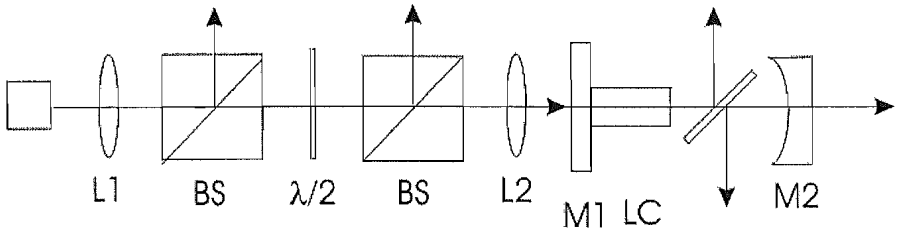

Figure (3-8). Schematic showing the threshold pump power experiment.

The laser cavity is formed by mirrors M1 and M2. Mirror M1 is anti-refection coated at the pump wavelength and highly reflecting at 1μm with mirror M2 having a reflection of 99.5% at 1μm, to keep the minimum threshold power low. Mirror M2 has a 70mm radius of curvature and the cavity is 35mm long producing a laser mode size of 100μm in the crystal. The losses in the cavity are varied using the etalon in the cavity and the power coupled out of the cavity by the etalon is measured to determine the total output

power of the laser. The losses due to the reflections from the glass plate can then be determined from the relative values of the reflected power to the transmitted power. A photo-diode was used to monitor the output level of the laser checking for the presence of relaxation oscillations. The laser is aligned by setting the angle of the etalon to Brewster's angle, this ensures that the losses in the cavity are minimised. The glass-plate is then tilted away from Brewster's angle increasing the losses and the pump power required to reach threshold.

Figure (3-9) shows the pump power required to reach threshold for different cavity losses. In figure (3-9) the black circles are the measured values, the solid line is calculated by inserting the measured value for the ETU parameter into equation (3-16) and using logarithmic losses. The stimulated emission cross-section was taken to be 15.6×10^{-21} and the intrinsic cavity losses were taken to be 2.5%. The dotted line in figure (3-9) is the threshold pump power calculated from chapter 2 for the threshold pump power and the dashed line is calculated by inserting a value of $1 \times 10^{-21} m^3 s^{-1}$ into equation (3-16). As can be seen from figure (3-9) there is reasonable agreement between the measured values of the threshold pump power and the calculated values using the measured value for the ETU parameter. It can also be seen from the difference between the dotted and dashed lines that the effect of ETU at these cavity losses and ETU parameter is small. It can also be seen that the threshold pump powers calculated for the higher ETU parameter significantly deviate from the values at low losses and do not provide a good fit to the data, thus lending further support for the lower measured value above.

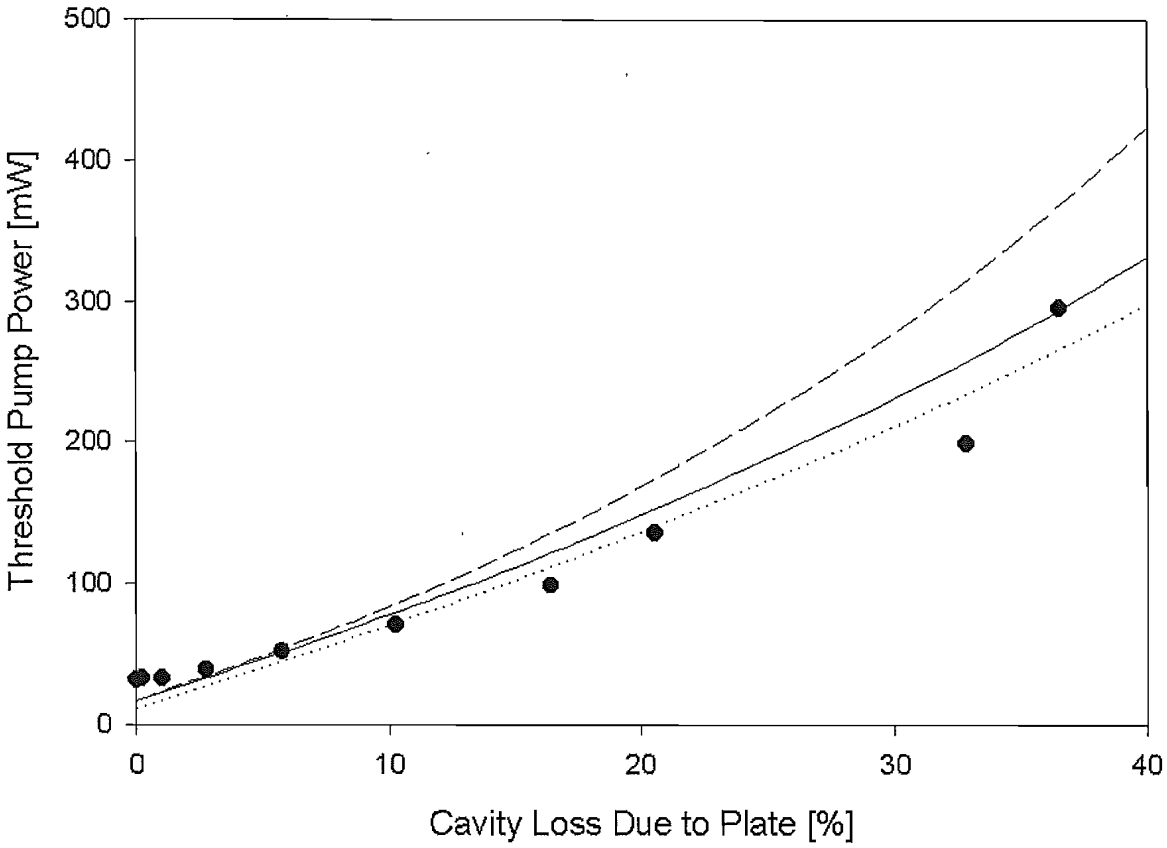

Figure (3-9). Threshold pump power as a function of the cavity loss due to the glass plate. The black circles are for the measured threshold pump powers, the solid line is for the measured ETU parameter, the dotted line is for the calculated threshold pump power without ETU, and the dashed line is the threshold pump power calculated using the value of the ETU parameter from [22]

Figure (3-10) shows the measured threshold pump powers for different cavity losses for the 0.3% doped crystal. In figure (3-10) The black circles are the measured values, the solid line is calculated by inserting the measured value in equation (3-16), the dotted line is calculated with ETU neglected and the dashed line is for the value from [22]. The intrinsic cavity loss was 1.5%.

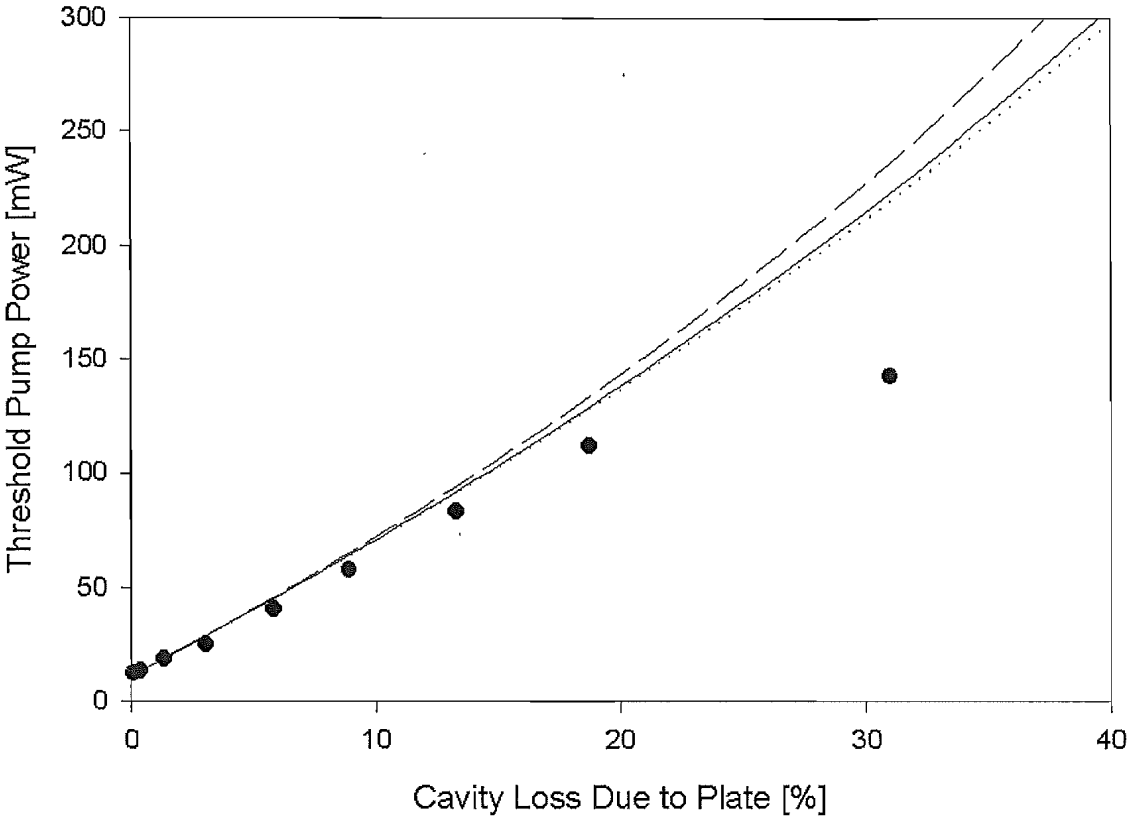

Figure (3.10). Threshold pump power as a function of glass plate angle for the 0.3% doped crystal. The black circles are the measured values, the solid line is calculated by inserting the measured value in equation (3-16), the dotted line is calculated with ETU neglected and the dashed line is for the value from [22].

3.6 Discussion and Conclusions

Both top-hat and Gaussian pump beam profiles have been assumed at different stages in this chapter. When ETU is neglected the difference in laser performance is due to the overlap of the pump and laser modes. The effect of ETU is dependent on the pump intensity, but can it be assumed that the net effect is the same for a Gaussian and top-hat profile?

Figure (3-11) shows the relative population inversion in a thin disc as a function of the radial distance for different pump beam transverse profiles with and without ETU. In figure (3-11) the solid lines are calculated neglecting ETU and the dashed lines are calculated including ETU. All the populating inversion densities are relative to the on axis vale of the Gaussian profile without ETU. For a Gaussian transverse intensity profile the pumping rate for a Gaussian beam is given by

$$R_{P,G} = \frac{2P_P\alpha_P}{h\nu_P\pi w_p^2}\exp\left(\frac{-2r^2}{w_p^2}\right) \tag{3-18}$$

The top-hat pumping rate is given by

$$R_{P,TH} = \frac{P_P}{\pi w_P^2} \text{ for } r \leq w_p \text{ and } 0 \text{ for } r > w_p \tag{3-19}$$

The profiles without ETU are generated by multiplying the pumping rate by the fluorescence lifetime. The values including ETU are calculated by inserting the pumping rate into equation (3-10). If ETU is neglected then on axis the Gaussain pump profile generates an excited population that is twice that of the top-hat profile, as shown by the solid lines in figure (3-12). The dashed lines in figure (3-12), are the radial populations generated where the effect of ETU has been included. For all calculations the incident pump power of the plot is given by

$$P_{P,ETU} = \frac{h\nu_P\pi w_P^2}{\alpha_P W\tau^2} \tag{3-20}$$

At this power level it can be seen that the relative population on axis for the Gaussian profile is half that generated without ETU. For the top hat profile the generated population inversion is 60% of the non-ETU profile. The importance of this will be highlighted later, when the effect of ETU on small signal gain will be discussed with the context of an end-pumped amplifier. The value of $P_{P,ETU}$ under typical end-pumping conditions such that the pump beam has a beam radius of 100μm gives a value of 0.7W for a 1% doped Nd:YVO_4 crystal with $\alpha_P=3000m^{-1}$, $W=3.5x10^{-22}m^3s^{-1}$ and $\tau=100\mu s$. The equivalent value for 0.1% doped crystal is 7W where it has been assumed that $\alpha_P=300m^{-1}$ and the other values remain the same. This highlights the dramatic reduction in the losses to ETU that can be achieved by reducing the dopant concentration of a crystal.

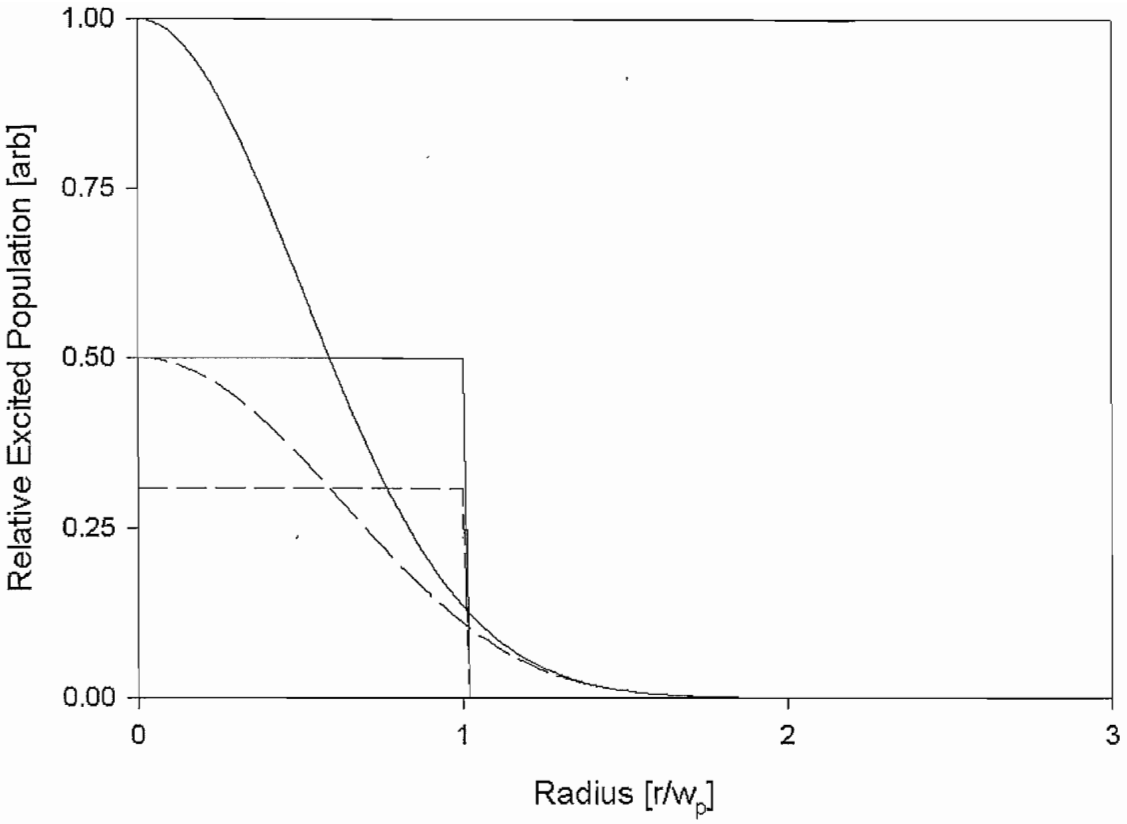

Figure (3-12). Excited population relative to that value generated by the Gaussian profile on axis at a pump power of $P_{P,ETU}$.

Table (3-5) shows the figure of merit defined in equation (3-17) for Nd:YAG, Nd:YLF and Nd:YVO_4 for the same dopant concentration. As can be seen in table (3-5), Nd:YAG has the highest figure of merit and can tolerate significant losses before ETU becomes appreciable at threshold. Nd:YLF on the other hand is very susceptible to ETU at threshold, and the losses have to be minimised to reduce its effect at threshold. Nd:YVO_4 lies somewhere between these two materials.

	Nd:YLF	Nd:YAG	Nd:YVO_4
Nd Conc. (%)	1	1	1
τ (μs)	520	230	98
α_p (cm^{-1})	10.8 (π)	3.3	40.7 (π)
σ_e (10^{-19} cm^2)	1.9 (π)	4.6	15.6 (π)
W (10^{-16} cm^3 s^{-1})	1.7	0.5	3.5
FOM	0.20	12	1.1

Table 3-5. The susceptibility of Nd:YLF, Nd:YAG and Nd:YVO_4 to ETU at threshold and the values used to determine them.

As discussed above, the figure of merit for a material can be improved by reducing the dopant concentration, and hence lowering the absorption coefficient. The result is that the pumping rate is reduced, and consequently the population inversion density reducing the occurrence of ETU.

In conclusion the ETU parameter in Nd:YVO_4 has been determined finding it to be migration assisted. For a 1% doped crystal we measured a value of $3.5x10^{-16}cm^3s^{-1}$ which is significantly stronger then for the equivalently doped Nd:YAG and Nd:YLF. Further evidence for this value was obtained from the measurements of the threshold pump power for a laser with varying losses. These measurements also show that this value of ETU does not have a significant impact on threshold. The theoretical model developed here for the pump power required to reach threshold produces predictions which are in good agreement with the measured values. When the larger reported value for the ETU parameter is used to determine the required threshold pump power it predicts powers significantly higher then those measured. These results provide strong support for the lower value presented here rather than the higher value reported elsewhere. A theoretical comparison of Nd:YAG, Nd:YLF and Nd:YVO_4 at the same dopant concentration shows that Nd:YAG is the least susceptible to the impact of ETU on threshold pump power. This is due to its relatively weak absorption and lower ETU parameter.

3.7 References

1. Guyot, Y. and R. Moncorge, *Excited-State Absorption in the Infrared-Emission Domain of Nd3+-Doped Y3al5o12, Ylif4, and Lamgal11o19.* Journal of Applied Physics, 1993. **73**(12): p. 8526-8530.
2. Guyot, Y., et al., *Excited-State-Absorption and Up-Conversion Studies of Nd3+- Doped-Single Crystals Y3al5o12, Ylif4, and Lamgal11o19.* Physical Review B, 1995. **51**(2): p. 784-799.
3. Chuang, T. and H.R. Verdun, *Energy transfer up-conversion and excited state absorption of laser radiation in Nd:YLF laser crystals.* IEEE Journal of Quantum Electronics, 1996. **32**(1): p. 79-91.

4. Fornasiero, L., et al., *Excited state absorption and stimulated emission of Nd^{3+} in crystals. Part2:YVO_4,$GdVO_4$, and $Sr_5(PO_4)_3F$.* Applied Physics B, 1998. **67**: p. 549-553.
5. Romero, J.J., et al., *Excited state absorption around 1060 nm of Nd3+ ions in Ba2NaNb5O15 crystal.* Optics Communications, 2001. **191**(3-6): p. 371-375.
6. Guy, S., et al., *High-inversion densities in Nd : YAG: Upconversion and bleaching.* IEEE Journal of Quantum Electronics, 1998. **34**(5): p. 900-909.
7. Hardman, P.J., et al., *Energy-transfer upconversion and thermal lensing in high-power end-pumped Nd : YLF laser crystals.* IEEE Journal of Quantum Electronics, 1999. **35**(4): p. 647-655.
8. Blows, J.L., et al., *Heat generation in Nd : YVO4 with and without laser action.* IEEE Photonics Technology Letters, 1998. **10**(12): p. 1727-1729.
9. Clarkson, W.A., *Thermal effects and their mitigation in end-pumped solid-state lasers.* Journal of Physics D-Applied Physics, 2001. **34**(16): p. 2381-2395.
10. Pollnau, M., et al., *Upconversion-induced heat generation and thermal lensing in Nd : YLF and Nd : YAG.* Physical Review B, 1998. **58**(24): p. 16076-16092.
11. Riseberg, L.A. and M.J. Weber, *Relaxation Phenomena in Rare-Earth Luminescence*, in *Progress in Optics*, E. Wolf, Editor. 1976, North-Holland: New York. p. 91-159.
12. Förster, T., Ann. Physik, 1948. **2**: p. 55.
13. Dexter, D.L., *A Theory of Sensitized Luminescence in Solids.* Journal of Chemical Physics, 1953. **21**(5): p. 836-850.
14. Payne, S.A., et al., *Auger up-Conversion Losses in Nd-Doped Laser Glasses.* Optics Communications, 1994. **111**(3-4): p. 263-268.
15. Kaminskii, A.A., *Laser Crystals*. 2 ed. 1990, Berlin: Springer. 130-138&323.
16. Zuegel, J.D. and W. Seka, *Upconversion and reduced $^4F_{3/2}$ upper-state lifetime in intensely pumped Nd : YLF.* Applied Optics, 1999. **38**(12): p. 2714-2723.
17. Haken, H. and H.C. Wolf, *The Physics of Atoms and Quanta*. 4 ed. 1993: Springer-Verlag.
18. Ostroumov, V., et al., *Study of luminescence concentration quenching and energy transfer upconversion in Nd-doped $LaSc_3(BO_3)_4$ and $GdVO_4$ laser crystals.* Journal of the Optical Society of America B-Optical Physics, 1998. **15**(3): p. 1052-1060.

19. Zusman, L.D., *Quenching of luminescence when migration on solid solutions is present.* Opt. Spectrosc., 1974. **36**(3): p. 287-289.
20. Zusman, L.D., *Kinetics of luminescence damping in the hopping mechanism of quenching.* Sov. Phys. JETP, 1977. **46**(2): p. 347-351.
21. Zubenko, D.A., et al., *Different mechanisms of nonlinear quenching of luminescence.* Physical Review B, 1997. **55**(14): p. 8881-8886.
22. Chen, Y.F., et al., *Determination of the Auger upconversion rate in fiber-coupled diode end-pumped Nd : YAG and Nd : YVO4 crystals.* Applied Physics B-Lasers and Optics, 2000. **70**(4): p. 487-490.
23. Russell, D.L. and K. Holliday, *Upconversion and energy transfer dynamics in Nd3+: LiYF5.* Optics Communications, 2001. **191**(3-6): p. 277-294.
24. Meilhac, L., G. Pauliat, and G. Roosen, *Determination of the energy diffusion and of the Auger upconversion constants in a Nd:YVO4 standing-wave laser.* Optics Communications, 2002. **203**(3-6): p. 341-347.
25. Pollnau, M., et al., *Upconversion, lifetime quenching, and ground-state bleaching in Nd^{3+}:$LiYF_4$.* Optics Communications, 1998. **147**: p. 203-211.
26. Koechner, W., *Solid-State Laser Engineering.* 5 ed. Springer Series in Optical Sciences, ed. T. Tamir. Vol. 1. 1999, Berlin: Springer.
27. Xia, H.R., et al., *Spectral parameters of Nd-doped yttrium orthovanadate crystals.* Journal of Applied Physics, 2000. **88**(9): p. 5134-5137.
28. Tucker, A.W., M. Birnbaum, and C.L. Fincher, *Stimulated emission cross sections of Nd:YVO_4 and Nd:$La_2Be_2O_5$ (BeL).* Journal of Applied Physics, 1981. **52**(4): p. 3067-3068.
29. Tucker, A.W., et al., *Stimulated-emission cross section at 1064 and 1342 nm in Nd:YVO_4.* Journal of Applied Physics, 1977. **48**(12): p. 4907-4911.
30. Fields, R.A., M. Birnbaum, and C.L. Fincher, *Highly efficient Nd:YVO_4 diode-laser end-pumped laser.* Applied Physics Letters, 1987. **51**(23): p. 1885-1886.
31. Kubodera, K. and K. Otsuka, Journal of Applied Physics, 1979. **50**: p. 653.

Chapter 4: Thermal Effects in Nd:YVO_4

4.1 Introduction

It was shown in chapter 2 that thermal lensing in the gain medium plays an important role in limiting the output power of end-pumped lasers. The thermal lens focal length changes with pump power, causing the laser mode in the cavity to change with the focal lens of the thermal lens. It was shown that if the product of the power of the thermal lens and the laser crystal is smaller than one the thermal lens can be considered as a lens. However, if the product approaches one then the effect of the thermal lens on the laser cavity must be modelled as a complex waveguide. This means that thermal lens does not become short enough to generate a focus in the laser crystal. It was shown that if the strength of the thermal lens becomes too great then the cavity could become unstable, preventing lasing. It was also shown that the aberrated nature of the lens could lead to beam quality degradation. However, was also shown that by the insertion of lenses then the effect of the thermal lens can be corrected for a specific pump power, and if the lens has aspheric surfaces, then it can act as a phase conjugator, helping to reduce the beam quality degradation. Deformable mirrors can also be used to correct for the changes in the laser mode in the laser cavity due to the thermal lens focal. Unless the output of the laser is monitored, and the deformation of the mirror can be controlled electronically, the compensation is again only for a specific pump power. Since these correction techniques only work at specific pump powers, a design strategy was presented in chapter 2 for end-pumped lasers, with the laser mode in the laser crystal decreasing with increasing focal length. In this way, the variation in the thermal lens focal length with radius can be used to suppress the higher-order modes. This is achieved because the thermal lens reduces the ratio of the sizes of the fundamental mode and the higher order modes. The better overlap of the fundamental mode with the pump beam reduces the gain for the higher-modes. In this chapter, the thermal lensing in Nd:YVO_4 caused by thermal effects due to end-pumping is investigated. The influence of ETU on thermal lensing and hence on beam quality is considered by deriving the increase in thermal loading due to ETU. Methods for determining the focal

length of thermal lenses are then reviewed and then our approach, based on a modified Mach-Zehnder interferometer is presented. This approach allows very accurate measurement of thermal lensing in end-pumped solid-state lasers. The results of a detailed study of thermal lensing in Nd:YVO_4 are presented, which include the influence of polarisation, cooling geometry, mode of operation and dopant concentration are investigated. As a result of the study it is found that ETU can have a significant impact on thermal lensing increasing the strength of the generated thermal lens and causing it to have a non-linear relationship with the absorbed pump power in Nd:YVO_4. A comparison is then made of thermal lensing in Nd:YLF, Nd:YAG and Nd:YVO_4.

4.2.1 The Effect of ETU on Thermal Lensing

In the preceding chapter, the effect of ETU on the population density in the upper lasing level was examined. Here the effect of ETU on heating in the crystal and its consequences are considered. In chapter 2, the fraction of absorbed pump power that is converted into heat in the gain medium under lasing conditions was discussed. It was shown that the fraction of absorbed pump power converted to heat under lasing conditions many times above threshold, is principally due to the difference in energy between the pump and lasing photons, i.e. quantum defect heating is given by

$$\delta_q = \frac{\nu_p - \nu_L}{\nu_p} \tag{4-1}$$

where $\nu_{p,L}$ are the pump and laser frequencies. Under non-lasing conditions, spontaneous emission can occur along a number of fluorescence pathways. The laser frequency in equation (4-1) must therefore be replaced by that of the average transition frequency and the fraction of the absorbed energy converted to heat by fluorescence is then δ_{nl}. If the fraction of ions that decay radiatively is given by γ, and it is assumed that ETU is the only other pathway for decay, those ions that decay by fluorescence contribute a fraction of $\delta_{nl}\gamma$ to the amount of absorbed pump power converted to heat. When ETU occurs, the acceptor non-radiatively decays back to the upper laser level, and the donor decays to the ground level. The fraction of ions that are in the ground state due to ETU is given by 1-γ and contribute the equivalent of a whole of a pump

photon to the amount of absorbed pump power converted to heat. The depopulation of the higher excited levels, is assumed to occur principally via non-radiative decay, rather then by fluorescence to the ground level, and that the non-radiative decay is assumed to be very fast so that there are negligible populations in these higher levels so that the rate equation for the upper laser level is the only equation that needs to be solved.

For any Nd-doped material this can be generalised to determine the fraction of absorbed pump power converted to heat in the gain medium under non-lasing conditions and is given by

$$P_{heat} = (1-(1-\delta_{nl})\gamma)P_{abs}\,. \tag{4-2}$$

where P_{abs} is the fraction of absorbed pump power converted to heat and P_{abs} is the absorbed pump power. When all of the decays are via fluorescence pathways γ=1 and equation (4-2) simplifies to $P_{heat}=\delta_{nl}P_{abs}$. By comparing the rate equations of the population inversion density with and without ETU, the fraction of ions that decay by fluorescence can be calculated this is given by

$$\gamma(r,z) = \frac{-1+\sqrt{1+4W\tau^2 r_p(r,z)}}{2W\tau^2 r_p(r,z)} \tag{4-3}$$

where τ is the fluorescence lifetime, W is the ETU parameter and $r_p(r,z)$ is the pumping rate. From equation (4-3) it can be seen that under non-lasing conditions the fraction of ions that decay by fluorescence has a spatial dependence, consequently the fraction of absorbed pump power converted to heat will as well. By inserting equation (4-3) into equation (4-2) and integrating over the pumped volume the increase in thermal loading due to ETU can be determined. For a Gaussian pump beam where the entire pump beam is absorbed this solution of equation (4-2) is solved in appendix B and the result is given here

$$P_{heat} = P + \frac{(1-\delta_{nl})8}{\beta}\left\{1-\sqrt{\beta+1}+\ln\left(\frac{1+\sqrt{\beta+1}}{2}\right)\left(1+\frac{1}{4}\ln\left(2+2\sqrt{\beta+1}\right)\right)\right.$$
$$\left.+\frac{\ln(2)}{2}\left(\ln\left(\sqrt{\beta+1}-1\right)-\ln\left(\frac{\beta}{2}\right)\right)+\frac{1}{2}\int_{\frac{1}{2}+\frac{1}{2}\sqrt{\beta+1}}^{1}\frac{\ln(t)}{1-t}dt\right\} \tag{4-4}$$

where β is a measure of the magnitude of the effect of upconversion on the overall decay rate from the upper laser level and is given by

$$\beta = \frac{8WP\alpha_p\tau^2}{\pi w_p^2 h\upsilon_p} \tag{4-5}$$

where P is the absorbed pump power, α_P is the absorption coefficient and ν_P is the pump frequency. In figure (4-1) the fraction of absorbed pump power converted to heat with ETU is compared to absorbed pump power. At low powers, the fraction of absorbed pump power converted to heat with ETU is the same as that without ETU, i.e the quantum defect. Under lasing conditions, it would be expected that the pump power converted to heat to be the same as that under non-lasing conditions until threshold is achieved. Above threshold the amount of heat generated, is then given by the quantum defect.

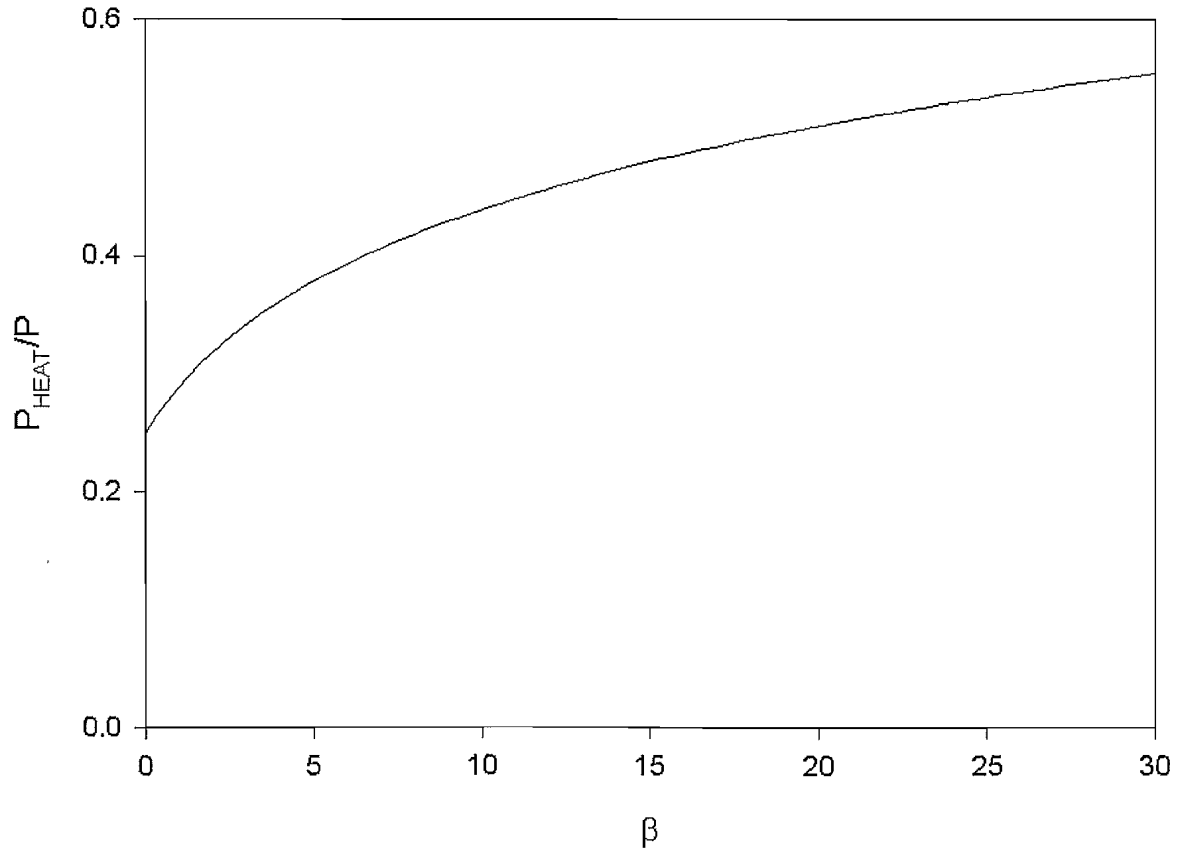

Figure (4-1). Fraction of absorbed pump power converted to heat.

This rapid increase in the amount of heat generated, leads to greater thermal effects. By inserting equations (4-3) and (4-2) into the analysis for the thermal lens focal length

given in chapter 2, it has been shown that ETU modifies the on axis thermal lens dioptric power under non-lasing conditions, D_{nl}, in the following way [1]

$$D = D_{\max}\left\{1-\frac{2(1-\delta)}{\beta}\left[2\left(\sqrt{1+\beta}-1\right)+\ln\left(\frac{4\sqrt{1+\beta}-1}{\beta\sqrt{1+\beta}+1}\right)\right]\right\}. \tag{4-6}$$

The maximum dioptric power, D_{max}, is the dioptic power of the thermal lens if all of the absorbed pump power was converted to heat

$$D_{\max} = \frac{P(dn/dT)}{\pi w_p^2 K_c} \tag{4-7}$$

where K_c is the thermal conductivity and dn/dT is the change in refractive index with temperature. In the absence of ETU, β=0, equations (4-5) and (4-7) reduce to $D=\delta D_{max}$ which is the result from the analysis in chapter 2. Under CW lasing conditions the inversion density is clamped at the threshold value, consequently there is no increase in the rate of ETU due to the stimulated emission. The dioptric power under lasing conditions, D_{las}, is given by

$$D_{las} = D_{th} + \frac{(P-P_{th})\delta_{nl}(dn/dT)}{\pi w_p^2 K_c}. \tag{4-8}$$

where D_{th} is the dioptric power of the thermal lens at threshold determined by inserting the pump power at threshold into equation (4-5). The ratio of the on axis thermal lens focal lengths with and without ETU yields a dimensionless coefficient Γ is given by

$$\Gamma = \frac{1}{\delta_{nl}}\left\{1-\frac{2(1-\delta_{nl})}{\beta}\left[2\left(\sqrt{1+\beta}-1\right)+\ln\left(\frac{4}{\beta}\left(\frac{\sqrt{1+\beta}-1}{\sqrt{1+\beta}+1}\right)\right)\right]\right\}. \tag{4-9}$$

The value of Γ indicates how strongly ETU impacts on thermal lensing in any given situation. Figure (4-2) shows the variation of Γ with β parameter. From figure (4-2) it can be seen that $\Gamma\approx2$ when β=0. However, the total amount of heat generated in the crystal has not doubled as shown in figure (4-1). The reason for the difference is because figure (4-2) is for the thermal lensing on axis, and figure (4-1) is the fraction of absorbed pump power converted to heat for all of the crystal. As can be seen from this the effect of ETU rapidly increases at small values of β. Therefore, in order to keep the effect of ETU negligible β must be kept small. The value of β can be reduced if the

absorption coefficient can be lowered. This can be achieved by decreasing the dopant concentration and for some materials leads to a decreased ETU parameter.

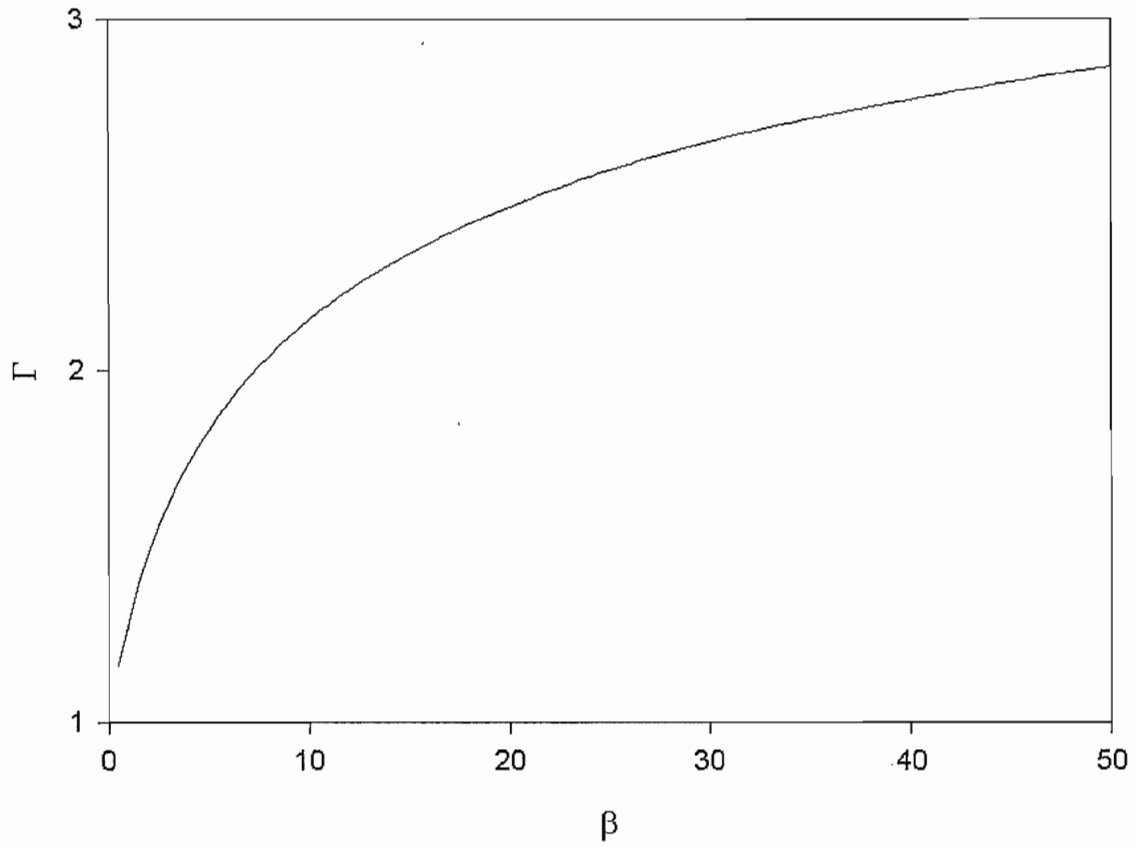

Figure (4-2). Variation of Γ with β parameter and with absorbed pump power.

Typical values for β for end-pumped Nd:YVO_4 ~11 for 1% dopant concentration, using P=1W, α_P=3000m^{-1}, τ=100μs, W=3.5x$10^{-22}m^3s^{-1}$ and w_p=100μm. It can be seen that at this value of β, the ratio of thermal lensing with and without ETU is nearly 2. To decrease the value of β, the dopant concentration can be reduced, decreasing the absorption coefficient. If a 0.1% doped Nd:YVO_4 crystal is used instead the value of β becomes 1, and there is now very little difference between the thermal lensing with and without ETU.

4.2.2 Effect of ETU on Beam Quality

It was shown in chapter 2, that the aberrated nature of the thermal lensing in end-pumped solid-state lasers, could lead to beam quality degradation for laser beams passing through them. It was found that the relationship between the incident and output beam quality are related by [2]

$$M_{OUT}^2 = \sqrt{\left(M_{IN}^2\right)^2 + \left(M_Q^2\right)^2} \tag{4-10}$$

where M_{OUT}^2 is the beam quality after passing through the lens, M_{IN}^2 is the incident beam quality and M_Q^2 is the beam quality degradation due to quartic phase aberrations. It has been shown that for a Gaussian pump beam the beam quality degradation due to the quartic phase aberration terms is given by [3]

$$M_Q^2 = \frac{2P_p\delta_q\eta_{abs}(dn/dT)}{K_c\lambda\sqrt{2}}\left(\frac{w_L}{w_P}\right)^4 \tag{4-11}$$

As was shown above, the net effect of ETU is to increase the fraction of absorbed pump power converted into heat. This means that the beam quality degradation with ETU will not increase linearly with absorbed pump power.

4.3 Techniques for Measuring Thermal Lensing in Solid-State Lasers

In the previous section, it was shown that when ETU becomes appreciable, it would be expected that the dioptric power of the thermal lens would increase nonlinearly with absorbed pump power. Knowledge of how the thermal lens varies with absorbed pump power is crucial for the design of end-pumped solid-state lasers and amplifiers, because it can still be strong even without ETU. In this section, we review some of the different techniques for measuring thermal lensing in solid-state lasers. The methods that have been used generally fall into two categories, interferometric and non-interferometric. In the first case, the optical path length difference across the thermal lens is used to determine the focal length by generating an interferogram of the lens, which is generally captured using a CCD. In non-interferometric techniques, the changes that occur to a probe beam as it passes through the thermal lens or the output beam from a

laser is measured to determine the focal length of the thermal lens. This section first examines interferometric techniques and then non-interferometric techniques.

4.3.1 Interferometric Techniques

Lateral Shear [4-6], Mach-Zehnder [7, 8] and Twyman-Green [9] interferometry have all been used to determine the focal length of thermal lenses. A probe beam passes through the gain medium either once or twice picking up a spatially dependent phase difference due to the changes in the optical path length, and is then compared with a reference beam to determine the distortion to the wavefronts and from this calculate the thermal lens focal length.

Figure (4-3) shows an example of lateral shear interferometry, the probe beam is aligned along the pump axis and passes through a partially reflecting mirror. It then makes a pass through the laser crystal where it is reflected off the rear face its wavefront curvature becomes distorted due to the optical path length difference generated by the thermal lens. The reflected probe beam is then imaged onto a holographic shearing plate, HSP. The HSP is a single gelatine plate with two holographic gratings written into it, each grating has a slightly different spatial frequency with the result that the probe beam is diffracted into two first order beams, with identical wavefronts to the original but with slightly different directions. These two first order beams interfere generating an interferogram, which is then captured using a CCD. Any wave front curvature on the probe beam caused by passing through the thermal lens will result in distortion of the fringes recorded by the CCD. The image recorded by the CCD is then processed on a computer using a Fourier transform technique to analyse the distortion in the fringes and retrieve the thermal lens focal length. The sensitivity of this technique, increases at the expense of the resolution as the lateral shear distance is increased. The lateral shear distance being, the distance by which the two wavefronts have been diffracted. The accuracy of the technique is strongly dependent on the correct positioning of the imaging optics, so that the wavefront distortions occurring in the crystal is imaged onto the HSP.

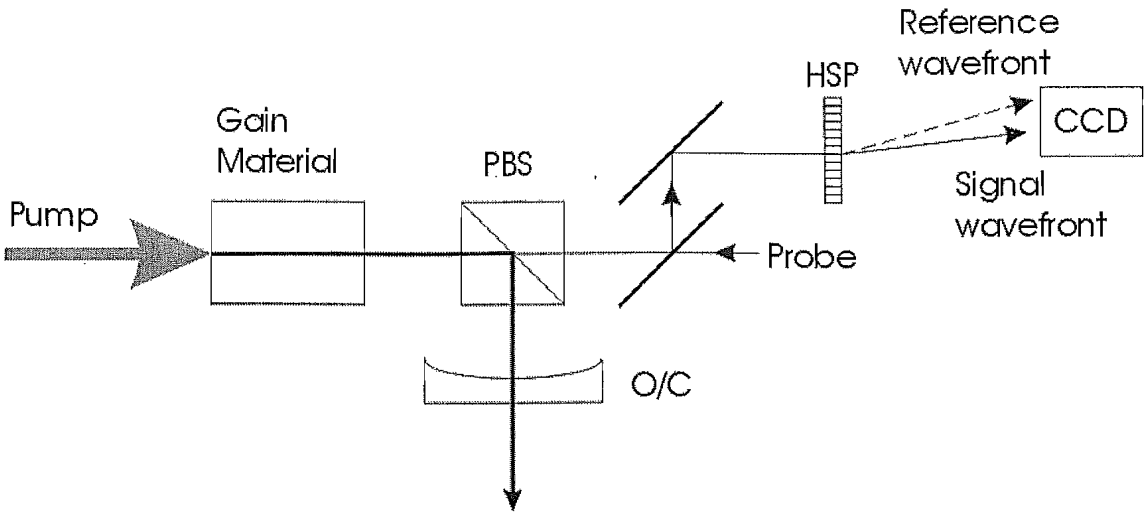

Figure (4-3). Example of lateral shear interferometry.

By inserting a polarising beam splitter, PBS, and an output coupler this technique can be used to determine the thermal lensing under both lasing and non-lasing conditions. However, this will limit the interferometer to determining the focal length of the thermal lens in the non-lasing polarisation. For birifringent materials where the refractive index change with temperature is different for the two polarisations, this technique will not allow a full characterisation of thermal lensing behaviour in the material. This technique has been used to determine thermal lensing in Nd:YAB [6], Nd:YAG [4] and Nd:YVO_4 [5]. In the Nd:YVO_4 measurements the thermal lens focal length was determined for both lasing and non-lasing conditions finding that the change in focal length with absorbed pump power under non-lasing conditions was highly non-linear.

In Twyman-Green interferometry, the interference occurs between the wavefronts reflected from the front and the back surface of the crystal as shown in figure (4-4). This is achieved by aligning a probe beam along the axis of the pump using a beam splitter, with reflections occurring at the first face generating a reference wave front. The transmitted probe beam then passes through the laser crystal where it is reflected off the rear face generating the signal wavefront, that then passes through the laser crystal again. An interference pattern is then generated at the front surface where the reference and signal beams interfere. This interference pattern is then imaged onto a CCD camera. The measured interferograms are then used to determine the space resolved OPD's in the laser crsytal. This is achieved by counting the number of fringes

in the interferogram to determine the phase profile across the beam. The measured phase profile is then compared with the interferogram generated by the unpumped laser crystal. In this way any wedges or misalignement in the interferometer can be corrected for. The polarization of the probe beam, in this case a HeNe, can be arbitrarily selected in relation to the gain medium. The thermal lensing under lasing conditions can be determined by inserting a mirror between the beam splitter and the laser crystal to form a cavity.

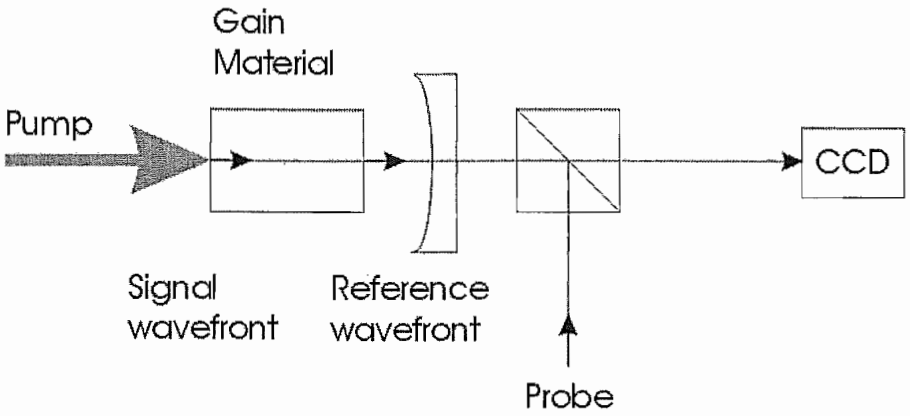

Figure (4-4). Example of Twyman-Green interferometry.

This method has been used to determine the thermal lensing in Nd:YAG, Nd:GSGG and Nd:YLF [9], where it was found that under the same pumping conditions that Nd:YLF the thermal lensing for the σ-polarization had a positive lens but was an order of magnitude weaker then those measured for the other materials and polarisations.

Mach-Zehnder interferometry has been used to determine the thermal lensing in side pumped lasers. A Nd:YAG rod was placed in one arm of a Mach-Zehnder interferometer where a HeNe laser provided the probe beam [7]. The output of the intererometer was imaged onto a CCD and the optical path difference was determined from the fringes of the interferogram. Measurements of slab geometry Nd:YAG rods, also using a HeNe have been reported [8]. Here the probe beam diameter was adjusted to that of the diameter of the laser rod and followed the zig-zag path of the totally internally reflected laser mode. The interferogram again recorded by imaging the output pattern onto a CCD.

As can be seen these techniques use CCD cameras to capture the interferogram generated by the wavefront distortions occurring in the laser crystal. The determination

of the phase profile of the optical path difference is then based on counting the number of interference rings, or some computer analysis of the captured image. There are a number of disadvantages that might arise through these measuring techniques. If the pump beam is much smaller than the probe beam the size of the interference rings will be small. This will make it difficult to identify and resolve them in the probe beam. If the phase distortions of the thermal lens only generate a small number of rings it will be difficult to determine the phase profile accurately across the beam, by counting the number of rings. If a computer program is used to retrieve the information about the phase distortions, then the intensity profile of the probe beam must be known accurately, and care needs to be taken when recording the interferogram so that saturation effects do not limit the information that can be extracted from the CCD image, the intensity of the beams in the two wavefronts being interfered need to be kept the same to ensure the maximum visibility of the fringes.

4.3.2 Non-interferometric Techniques

Techniques that do not require the alignment of highly sensitive interferometers and allow simple measurements of the thermal lens focal length have also been reported. These are generally non-interferometric in nature and measure the changes that occur to a probe beam after it passes through the thermal lens. Some the measurements include the transmission of a probe beam through an aperture or slit, the deviation of a beam or the expansion of the rod.

Low coherence reflectometry has been used to resolve the optical expansion of a pumped gain medium to determine the thermal lens focal length [10, 11]. A 1.3μm source with a short coherence length was used to probe the thermally induced properties of the gain medium. This is achieved by aligning the probe beam so that it makes a double pass of the laser crystal being examined. To minimise interference effects the coherence length of the source needs to be kept short. The source beam is pulsed and the time duration between detected reflections of the probe beam are measured. From these time measurements the change in optical path length can be determined having a reported measurement resolution of 0.5μm changes in path length.

The transverse index gradient can be obtained by scanning the probe beam across the gain medium, and detection the relative optical length expansion. The spatial resolution of this measurement will be limited by the size of the probe beam. If the probe beam radius is large, then the probe beam will experience an average of the changes in optical path difference over a large area. However, as the radius of the probe beam is reduced the Rayleigh range of the probe beam is reduced, with the probe beam potentially changing in radius as it passes through the laser crystal, leading to an error in the generated phase profile. For 15W of pump power a focal length as short as 4cm was reported for 1% doped Nd:YVO_4 under end-pumped conditions.

The focal length of the thermal lens can be determined by measuring the transmitted power of a probe beam through a slit after having passed through a gain medium as shown in figure (4-5). The intensity of the probe beam transmitted through the slit without the laser crystal being pumped is determined as shown by the dashed line in figure (4-5). This is then compared with the intensity of the transmitted probe beam after passing through the thermal lens. If the focal length of the thermal lens is shorter then the distance between the laser crystal and the slit, the radius of the probe beam will be greater then the slit width and the beam will be attenuated on passing through the slit as shown by the solid line in figure (4-5). If the focal length is greater then the distance between the laser crystal and the slit, the radius of the probe beam will be smaller then that of the original probe beam and there will be less attenuation for the probe passing through the slit as shown by the dotted line in figure (4-5). This technique has also been used to determine thermal lensing in a mode-locked Nd:YLF laser [12]. The HeNe probe beam is expanded so that it illuminates the full aperture of the rod. Using a slit rather then a circular aperture allows the thermal lens to be resolved in two orthogonal planes unlike a simple aperture. Varying the polarisation of the probe beam allows the thermal lensing for different polarisation to be measured. This is a poor technique, because it is not practical for determining long or short thermal lens focal lengths. As can be seen from figure (4-5) if the generated thermal lens has a short focal length the beam will be attenuated by the slit and it will be attenuated if the beam has a long focal length. If the probe beam is much larger than the pump beam radius, then only a small part of the probe beam will experience the ´real´ thermal lens, this means that it will be difficult to accurately determine the thermal lens focal length. The variation of the thermal lens with radius will also effect the different portions of the

probe beam leading to some confusion as to the position of the focus of the beam and the transmission of the probe beam through the slit. Diffraction effects on the probe beam are not taken into account with this technique.

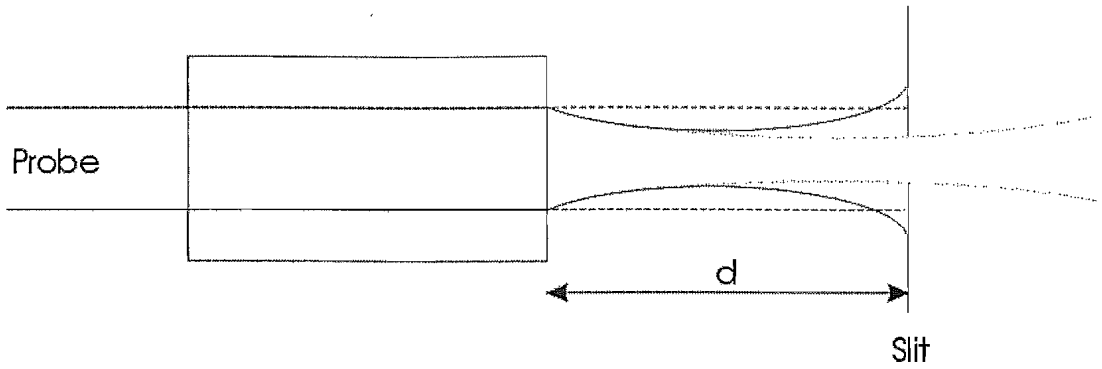

Figure (4-5). Schematic of thermal lens focal length determination by measuring the transmission through a slit.

Off axis rays are either diverted towards or away from the optical axis depending on whether the lens is converging or diverging. The beam will be deviated towards the axis for a converging lens or away from the axis for a diverging lens. A position-sensitive detector, PSD, can be used to monitor the deviation of a probe beam passing through a thermal lens and determine thermal lens focal lengths as shown in figure (4-6) [13]. In figure (4-6) the dotted line is the probe ray passing through the laser crystal without a thermal lens and the solid line is the path of the ray being deviated by the thermal lens towards the optical axis shown by the dashed line. In both cases, the probe beam is incident on a PSD. The PSD is a semi-conductor device that can monitor the movement of an incident laser beam in either direction. This is because the PSD generates a photocurrent in two directions the strength of the current in the two directions determined by the position of the beam. The two currents can then be used to find the centre position of the probe beam spot. The thermal lens focal length can be calculated from the angle of deviation of the probe beam, the focal length being the point at which the different rays cross the optical axis. As discussed in chapter 2 the focal length of the thermal lens varies with position, however, this technique assumes that the thermal lens of the focal length is constant with radial distance to enable the focal length to be determined.

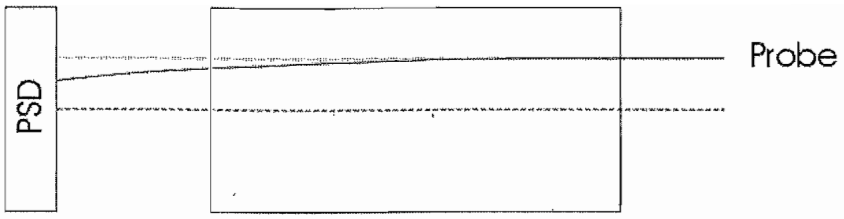

Figure (4-6). Schematic of the determination of the thermal lens focal length by measuring the probe beam deviation.

Deviations from the predicted performance or a sudden change in performance of laser have been used to estimate the thermal lens in the gain medium. It was shown in chapter 2 that the thermal lens focal length can cause a cavity to become unstable. By monitoring the output power of a plane-plane laser cavity with an internal lens, the stability range of the laser can be inferred. ABCD matrix analysis can be used to calculate the range of thermal lens focal lengths for which the cavity is stable, and a comparison of the two lads to an estimate of the thermal lens focal length [14]. ABCD matrices can be used to predict the spot size at the output coupler of a laser cavity. By comparing the measured beam radius with the predicted value gives an estimate of the thermal lens focal length. This technique has been reported by measuring the output beam width with a knife-edge method, slit scanning method and using CCD cameras [15-17]. An alternative technique uses ABCD matrices to determine the thermal lens focal length after passing through a thermal lens and measuring the probe beam as it consequently propagates [18].

As can be seen from the discussion above non-interferometric techniques generally have poor spatial resolution. So that if the probe beam is much larger than the pump beam radius, it experiences an average of the thermal lens. This is critical if the pumped region of the laser crystal is much smaller than the probe beam when the effect of the thermal lens might only be on a small portion of the probe beam. This means that any changes to the probe beam caused by the thermal lens be ´lost´ in the background of the measurement. Since the thermal lens varies with radial position, there may not be a clear focal distance or beam waist created, leading to vagaries in the estimate of the thermal lens focal length. The same is true for measuring thermal lenses with long focal lengths where the focal point might be poorly defined. For some of the techniques there

needs to be certain assumptions that need to be made, i.e. that the thermal lens focal length is constant with radial position, which are not strictly true. If the beam quality of the probe beam is degraded as it passes through the thermal lens, then the accuracy of some of these measurement techniques will be decreased. Astigmatic thermal lenses can be generated in laser crystals and these can be difficult to resolve using some of these techniques. It is difficult to measure strong focal length lenses by using the stability of cavities because it requires the construction of short cavities, of the order of the focal length and the output is dominated by the lensing in the stronger direction. The effects of higher-order modes are often neglected, and as a consequence the accuracy of these techniques can be reduced. Interferometric techniques have ample spatial resolution, but require many optical elements and are sensitive to vibrations. Where the interferogram is captured using CCDs unless the thermal lens generates images that can easily be identified complex Fourier analysis is required to determine the generated optical path difference. These techniques require, equal intensities in the two arms of the interferometer to maximise the visibilities of the fringes. The intensity profile of the probe beam is also required if the intensity of the fringes are to be counted using a computer. The method employed to determine the thermal lensing in laser crystals also needs to be able to characterise the thermal lensing in orthogonal directions, for arbitrary polarisations and for both lasing and non-lasing conditions for the thermal lensing to be fully studied. In the next section, a Mach-Zehnder interferometer is presented with sufficient spatial resolution to determine thermal lensing, in end-pumped solid-state lasers the use of a time varying phase shift on one of the arms, a reduced sensitivity to vibrations is achieved allowing the optical path difference, to be determined in a simple manner.

4.3.3 Modified Mach-Zehnder Interferometer to Accurately Measure Phase Distortions

As discussed previously only interferometric techniques have the spatial resolution to fully measure the optical path difference generated by a thermal lens. The interferometers so far discussed have not been used to measure the thermal lens focal length under lasing and non-lasing conditions for arbitrary polarisation. For Nd:YVO_4 this is important because the two orthogonal polarizations, experience different changes in refractive index with temperature and under non-lasing conditions it would be expected that the greater heat load will cause stronger thermal lensing. Therefore, a method that can measure the thermally-induced phase profile and consequently the thermal lens, also needs to be able to determine the different profiles for arbitrary polarizations and for different operating conditions. To that end, a Mach-Zehnder interferometer is presented to determine the phase profiles generated in Nd:YVO_4 with different dopant concentration, under lasing and non-lasing conditions, for both polarisations and for different cooling arrangements.

The schematic for the Mach-Zehnder interferometer used in the thermal lens measurements is shown in figure (4-7). A single frequency Nd:YLF laser [19] operating on the 1.053μm transition provides the probe beam for the interferometer. This source is chosen to be the probe beam because, it will experience negligible gain on passing through the Nd:YVO_4 The first lens collimates the output of the laser producing a beam with a radius of 600μm. The probe beam wavelength is sufficiently close to 1.064μm, which is the designed wavelength of the anti-reflecting, AR, and highly reflecting, HR, coatings on the mirrors and beam splitters resulting in satisfactory throughput of the interferometer. By rotating the half wave plate, that the beam passes through next, arbitrary polarization direction can be selected allowing the thermal lens to be investigated for the two orthogonal polarisations. The probe beam is then split into two as it passes through the first 50-50 beam splitter, BS1. The reflectivity of the beam splitter is approximately independent of polarisation. The transmitted beam forms the signal arm and contains the phase distortion under study. The reflected beam forms the reference beam and has a linear phase variation impinged

upon it. The linear phase variation is introduced to the reference arm of the interferometer by mounting mirror M1, which is a 45° turning mirror, on a piezoelectric stage. The position of the stage is then varied by applying a triangular wave voltage source to a piezoelectric driver connected to the stage moving the reference arm horizontally with respect to the signal arm. This displacement has the effect of linearly increasing and decreasing the path length difference between the two arms at the second beam splitter. The horizontal displacement is much smaller than the width of the probe beam so that the alignment of the interferometer is unaffected.

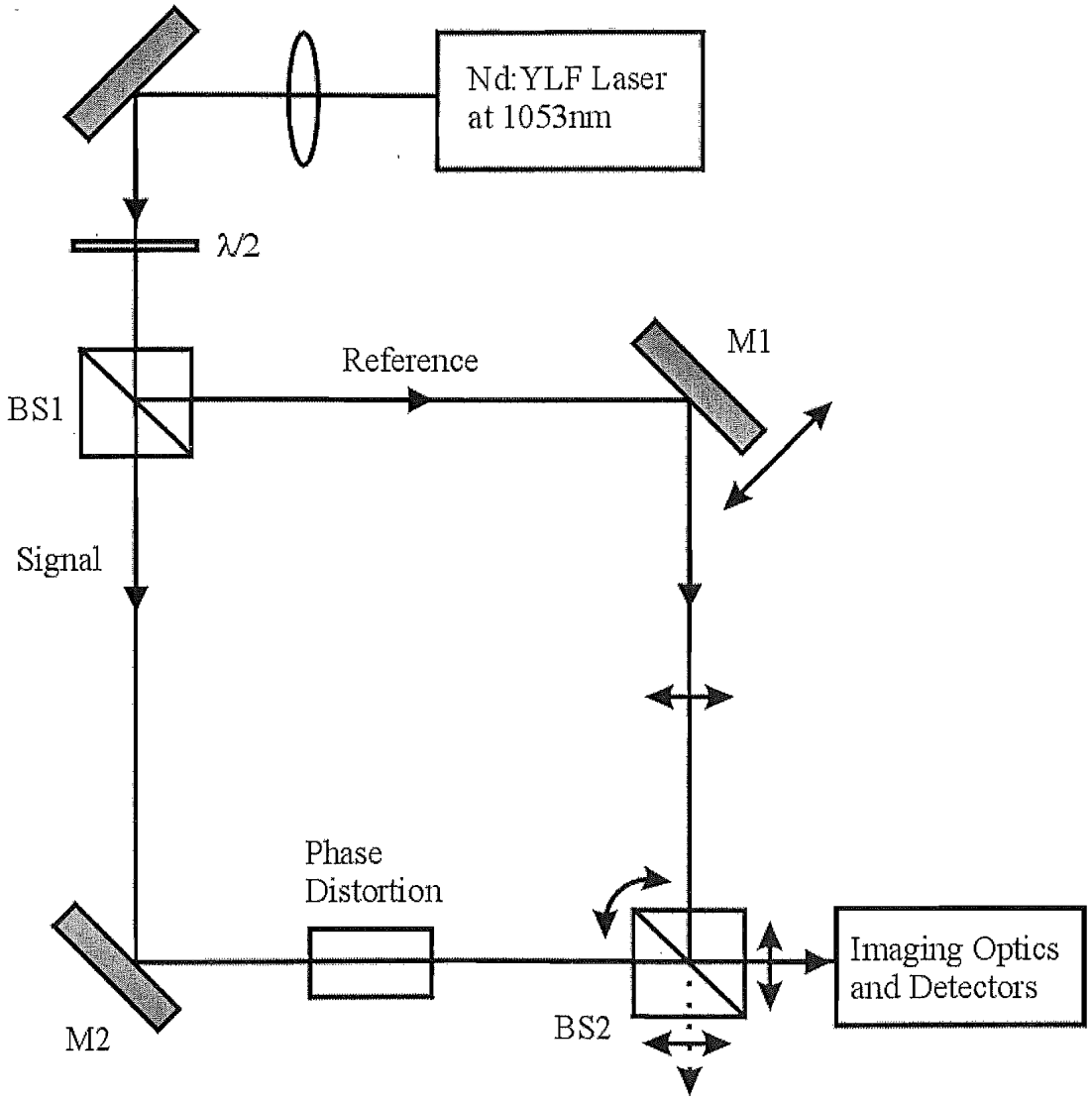

Figure (4-7). Mach Zehnder Interferometer used to determine the phase profile.

The signal arm reflects off the 45° turning mirror M2, before passing through the middle of the laser crystal. The signal beam picks up a phase distortion dependent on the position of the beam. The two arms of the interferometer are then overlapped when they pass through the second 50-50 beam splitter, BS2. BS2 was mounted on a rotation and an x-y stage. To align the two beams their separation was measured using a CCD

close to and far away from BS2 for both exits. If the beams were separated close to BS2, then the x- or y-position of BS2 was adjusted, if the beams were separated at a distance the rotation of BS2 was altered. The alignment of the interferometer is such that the two beams leave the interferometer aligned collinearly. The combined beams then pass through relay imaging optics.

The relay imaging optics are used to image the phase front generated by the phase distortion, which is in the front focal plane of the first lens, into the plane of the back focal length of the second lens, where the two detectors are positioned as shown in figure (4-8). The separation of the two lenses is equal to the sum of the focal lengths of the two lenses. This means that the probe beam radius and phase profile is imaged in the plane of the detector plane. This occurs irrespective of the effect of the thermal lens, so that any beam degradation that occurs in the laser crystal is negated by the relay-imaging optics. The relay imaging optics also interferes that part of the signal beam, which lies at the same distance from the source as the reference beam this means that those changes that occur to the wavefront curvature as a consequence of propagation after the thermal lens are also negated. This has the consequence that the phase profile measured in the detector plane is a direct measurement of that occurring in the laser crystal, and the propagation of the probe beam does not need to be compensated for. The overlapped beam is split into two by a 50%R mirror, it then passes through two pinholes adjacent to photo-diodes in the focal plane of lens 2. The spatial resolution of the interferometer is limited by the size of the pin-hole, and is governed by the sensitivity of the photo-diodes, and the power in the probe beam. To improve the spatial resolution of the measurements and to limit the area being averaged by the measurement, 5μm pinholes were used in front of the detectors. Allowing sufficient signal to be measured at the wings of the probe beam. The imaging optics have a magnification of 1 and preserve the phase differences that occur on transition through the phase distortion, so the detectors make a direct measurement of the phase front in the plane of the sample. The relay imaging optics also ensure that the image generated in the detector plane is the same size as that of the probe beam in the crystal, irrespective of the phase distortion.

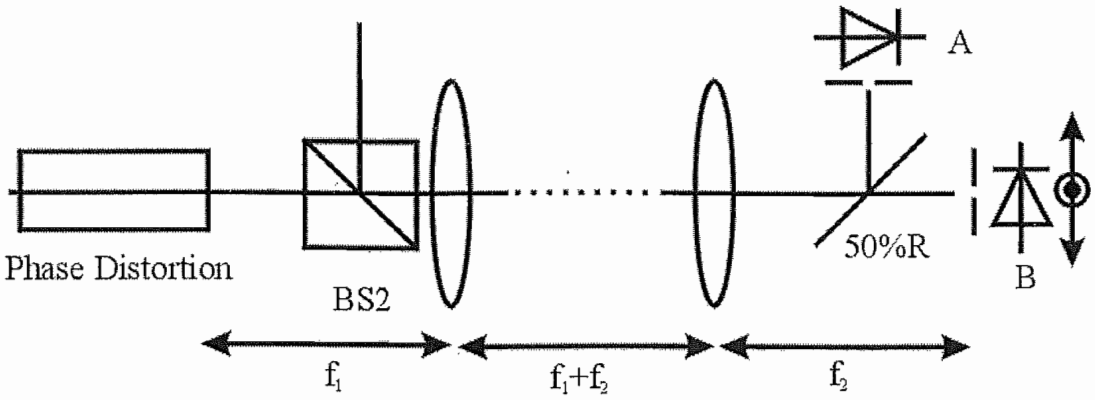

Figure (4-8). Relay imaging and detecting optics.

If the signal and reference beams are of equal intensity in both arms, the intensity of the light leaving the interferometer varies sinusoidaly as the path difference is scanned as shown in figure (4-9). The solid trace in the upper part of figure (4-9) shows the displacement of the piezoelectric mounted mirror. The lower trace shows an example of what the corresponding measured intensity might be. The solid trace could be that produced by photo-diode A and the dotted trace that produced by photo-diode B. The phase difference between the two traces is determined when mirror M1 is away from a turning point so its motion is linear as shown by the dashed line. The phase difference is calculated by determining the period of one of the signals and then the time between two matching points of the traces. The phase is then given by the ratio of the time between signal and the period multiplied by 2π. The phase difference between the two sinusoidal signals was measured using a digital oscilloscope. The oscilliscope could determine the phase difference of the two signals to within a fifth of a degree. This is equivalent to $\lambda_{signal}/1800$, however it was found that due to vibrations and air currents the measured phase difference varied by $\pm 0.5^0$ giving an optical path length of $\lambda_{signal}/720$. Limitations on the accuracy of the technique are given by the detected signal. If the detected signal is too low for measurement of the phase to be possible, then this can be increased through amplification increasing the noise on the signal, increasing the size of the pin-hole decreasing the spatial resolution unless the probe beam power can be increased. Further limitations are given by the single-frequency nature of the probe beam. If the probe beam is not single-frequency then the interference experienced by the other wavelengths will act as noise on the phase signal being measured. The phase profile generated in the laser crystal could be determined by keeping one photo-diode stationary whilst scanning the other photo-diode with respect

to the first one. The second photo-diode was mounted on an x-y stage so that the phase profile could be measured in orthogonal directions.

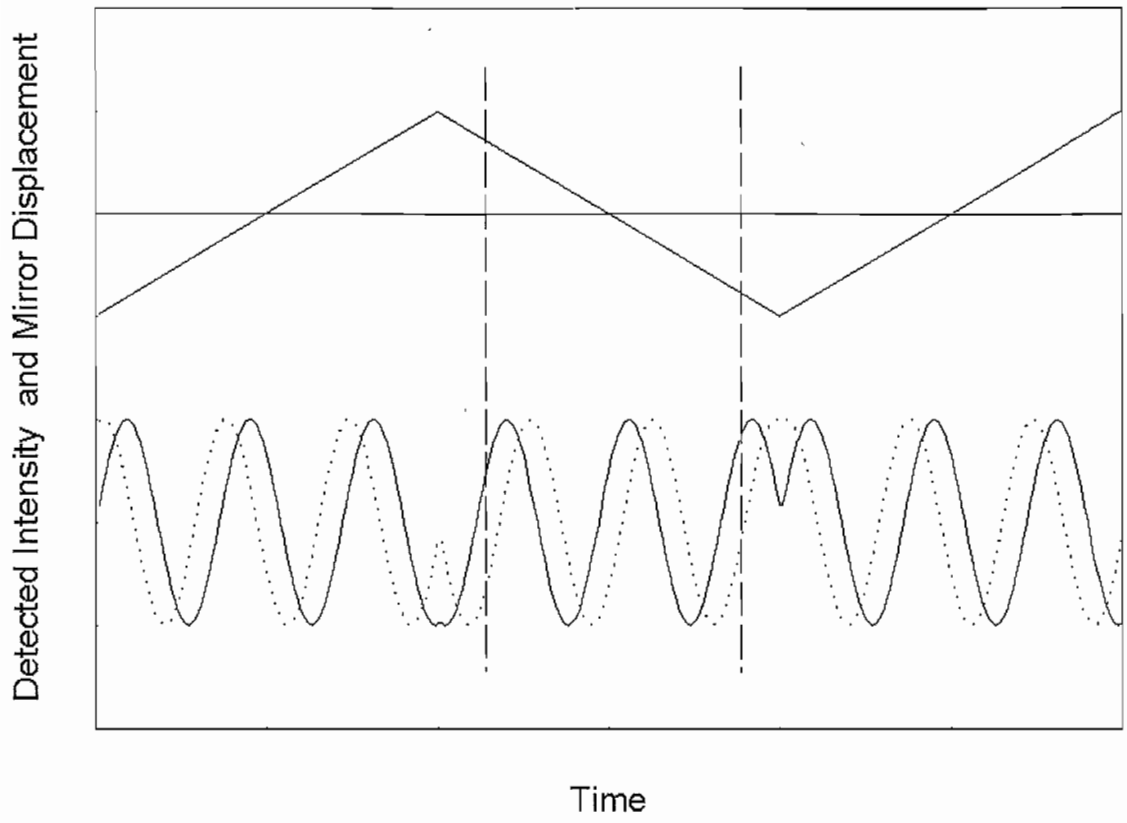

Figure (4-9) .The displacement of the movable mirror and the detected intensity.

The above described Mach-Zehnder interferometer allows a phase profile to be determined in an accurate way. Without suffering some of the failings of many of the other techniques previously described. The linearly varying phase variation on the signal beam, means that there is no need to try and count the number of fringes to determine the phase profile across the beam. This is important when trying to determine the thermal lens focal lengths of end-pumped lasers, where the pump beam radius is typically of the order of 100s of μm. If the thermal lens is only strong enough to generate a small number of fringes, then they may not be full resolved. Because this technique compares the phase difference between the interference occurring at two points in the same plane, the intensity profile of the probe beam is not important. The effect of the thermal lens on the probe beam is also of no consequence because the relay imaging optics, recreate the phase and beam profile of the beam in the laser crystal, irrespective of the thermal lens. Since the phase of the probe beam is being measured in the laser crystal, the strength of the thermal lens is not important, because

it is independent of the beam waist and position of the probe beam after passing through the thermal lens.

To ensure that the interferometer is able to determine the focal length of a lens accurately, the phase profile of a test lens with a nominal focal length of 150mm was measured. The phase profile, $\phi(r)$, measured for the lens is shown in figure (4-10). The focal length of the lens is the determined from the phase profile using

$$f = \frac{\pi r^2}{\lambda \phi(r)} \tag{4-19}$$

where r is the distance from the centre of the lens and λ is the wavelength of the single frequency laser. The focal length of the lens was determined by the interferometer to be 145mm.

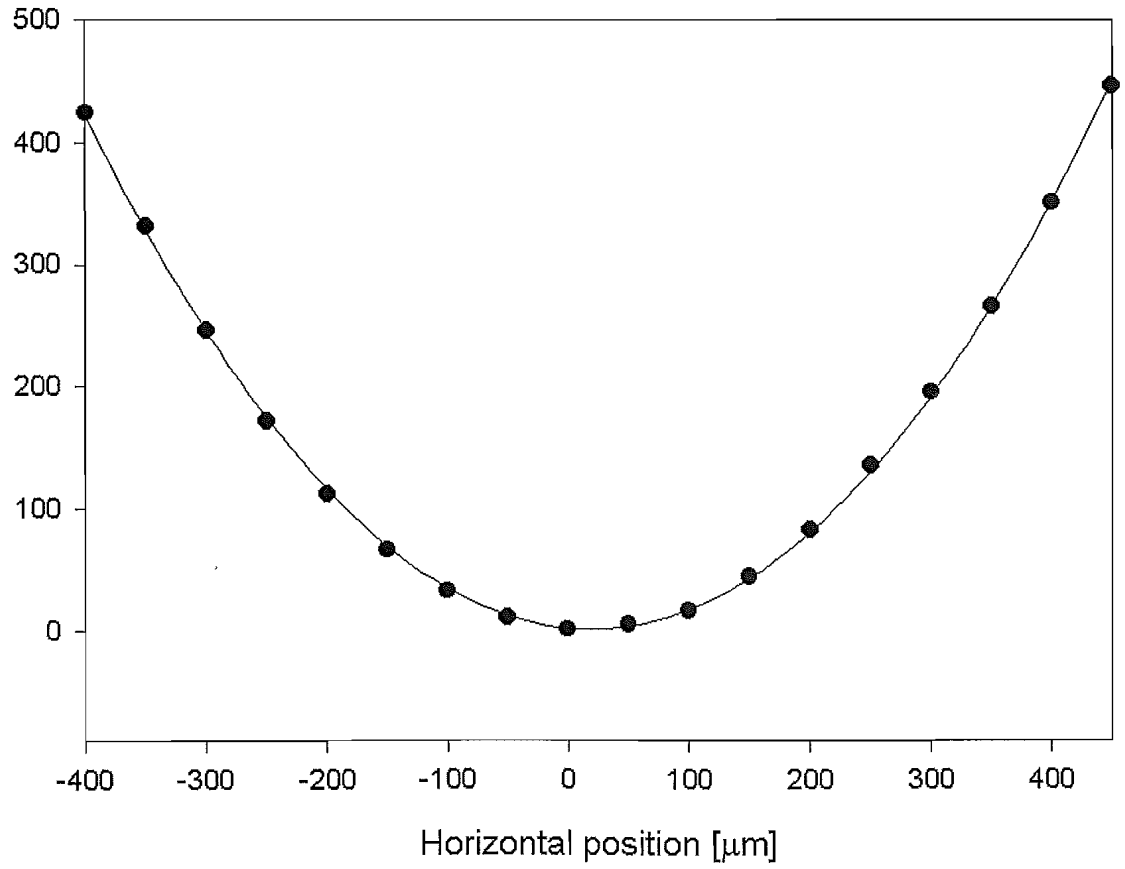

Figure 4-10. Phase profile of 150mm spherical lens.

4.4 Measurement of Thermal Lensing in Nd:YVO_4

The thermal lensing in Nd:YVO_4 was determined using the Mach-Zehnder interferometer described in the previous section. The focal length of the thermal lens was determined for crystal with different dopant concentrations, probe beam polarisation directions and cooling directions, lasing conditions and polarisations under lasing and non-lasing conditions. In this was way the influence of ETU on thermal lensing could be ascertained and the optimum cooling conditions, polarisation direction and dopant concentration found.

4.4.1 Modified Mach-Zehnder

Nd:YVO_4 crystals with two different dopant concentrations were used, with 1% and 0.3% doping levels were investigated. Both of the crystals were 10mm long and had a $3x3mm^2$ square cross-section. Each end of the crystal was AR coated at 810nm and 1.064μm. The crystal was cooled by mounting it between two cooling blocks with a layer of indium foil between the crystal and the blocks to ensure good thermal contact between them as shown in figure (4-11). The cooling blocks were attached to a water-cooled copper heat sink. The probe beams propagated along the Z-axis, with cooling along the Y-direction. No cooling was applied along the X-direction with these sides exposed to the air so they were convectively cooled. The unequal cooling in the X and Y directions generates an astigmatic thermal lens.

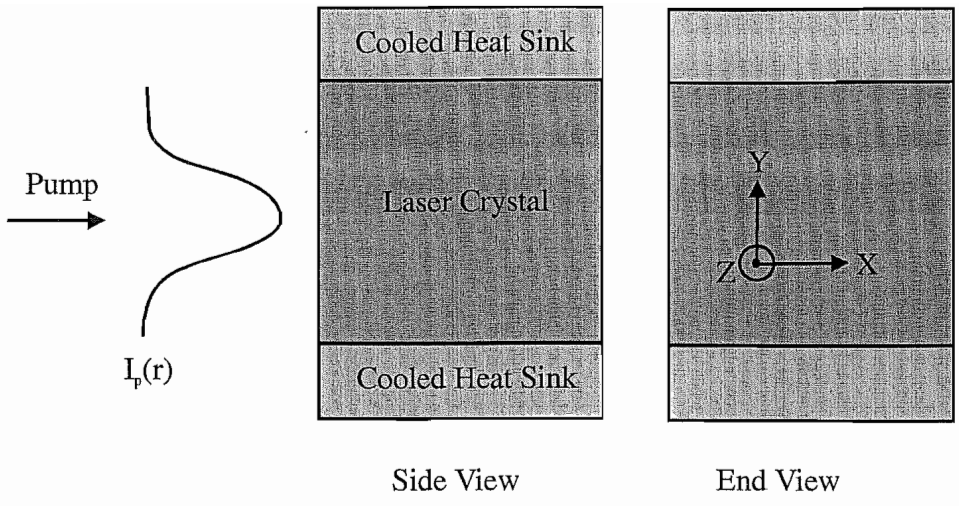

Figure (4-11). The geometry of the crystals and the directions of cooling.

As shown in figure (4-12) the crystals were pumped through mirror M2 by a fibre coupled diode bar. Mirror M2 was coated to be highly reflecting at 1.064μm and anti-reflecting at 810nm. The signal beam was aligned collinearly with the pump beam, which was transmitted through M2. The output of the fibre was 1:1 imaged into the crystal producing a spot-size of 130μm and had a maximum incident power of 5.3W. The pump beam had an M^2 of 110 and a Rayleigh range of 1mm inside the crystal. The probe beam experiences negligible gain on passing through the Nd:YVO_4 crystal. A non-collinear cavity is added to the interferometer by using mirror M2 as a folding mirror and is completed by the addition of a curved mirror and a plane output coupler as shown by the dashed line in figure (4-12). The curved mirror that has a radius of curvature of 7cm and the cavity has an optical length of 3.5cm forming a semi-confocal cavity. This cavity enables the thermal lensing under lasing conditions to be measured as well as under non-lasing conditions. The use of a short cavity helps to avoid the cavity becoming unstable due to the strong nature of thermal lensing in Nd:YVO_4 at high pump deposition rates. The threshold pump power is kept to a minimum by using an output coupler with a low transmission of 2%, to minimise the impact of ETU under where the principal impact is to increase the pump power to reach threshold, increasing the amount of pump power converted to heat. The angle between the signal beam and the non-collinear laser beam was kept to a minimum without either the output coupler or the curved mirror interfering with the signal beam. The probe beam radius was

several times greater than the pump beam waist on the laser crystal, so that the optical path difference could be determined across the entire thermal lens.

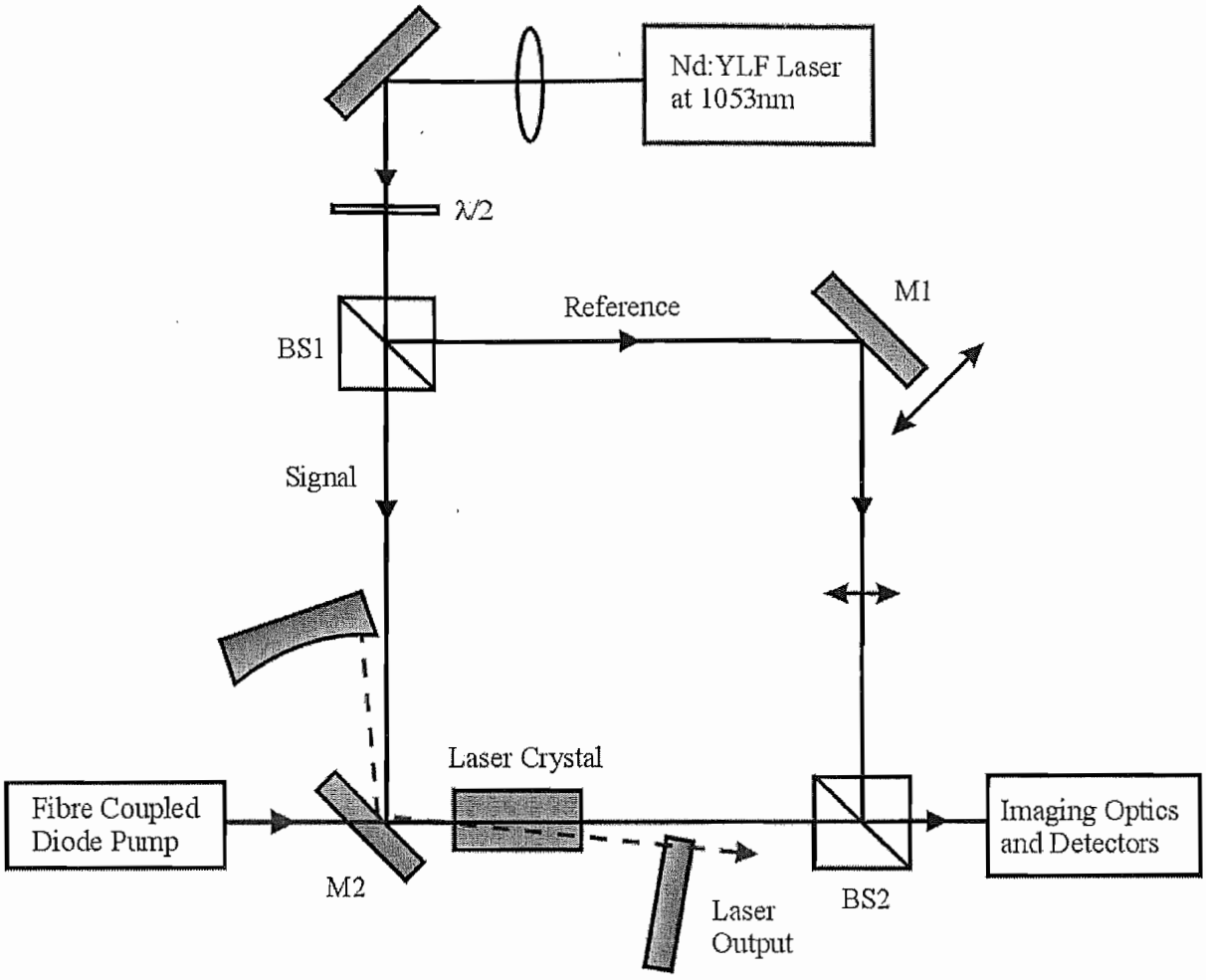

Figure (4-12). Modified Mach-Zehnder showing pump beam and non-collinear cavity.

The outputs of the two lasers are shown in figure 4-13 where the black circles are the measured output for the 1% crystal and the white circles are those for the 0.3% crystal. The thresholds and slope efficiencies for the two crystals being approximately the same at 400mW and 38%, respectively.

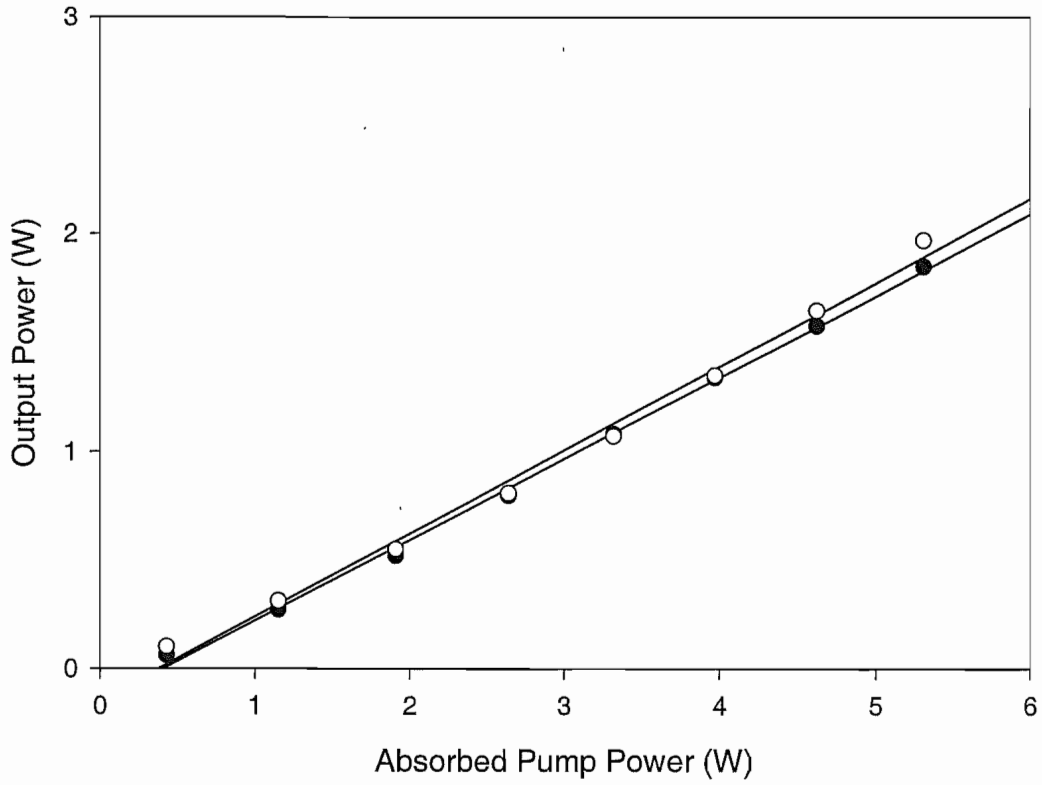

Figure (4-13). Output from the non-collinear lasers, 0.3% doped crystal white circles and 1% doped crystal black circles.

Figure (4-14) shows a typical phase profile measured by the interferometer for the 1% doped crystal under non-lasing conditions. The black circles are the experimental data and the solid line is the equivalent parabolic lens. The thermal lens that is created is highly aberrated, and the phase profile it generates is not a simple parabolic as shown in figure (4-14). This means that higher order terms in the radial distance need to be considered, to ensure a good fit to the measured phase profile. As discussed in section 4.2.2 above, these terms add phase aberrations passing to beams passing through the thermal lens and degrade its beam quality. In this section it was also shown how the degradation in beam quality due to the quartic phase aberration terms can be calculated for a single pass of the thermal lens. To that end, a polynomial equation was fitted to the measured phase difference to determine the radial phase difference,

$$\Delta\phi(r) = a + b(r - r_0) + c(r - r_0)^2 + d(r - r_0)^4 + e(r - r_0)^6 + f(r - r_0)^8 \qquad (4\text{-}20)$$

The linear term is used to remove any asymmetries that might arise through misalignment of the interferometer or unequal cooling and any wedges. The quadratic

term is used to calculate the on axis focal length and the quartic term can be used to calculate the degradation in beam quality.

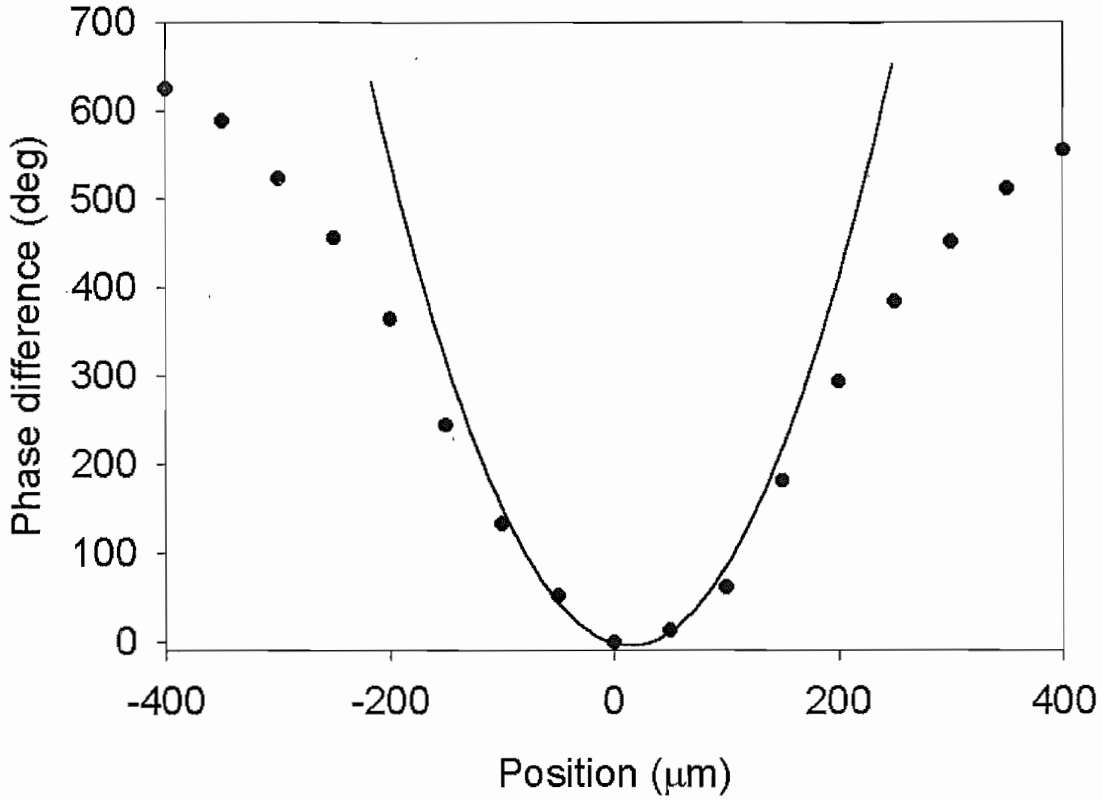

Figure (4-14). A typical measured phase profile (circles) for the 1% crystal under non-lasing conditions. The solid line represents the phase profile of the equivalent ´ideal´ parabolic lens.

In figure (4-14) it can be seen that there is good agreement between the parabolic profile and the measured profile for small probe beam radii. This is expected because for small probe beam radii, and therefore, pump beam radii, the heating is more uniform generating a parabolic temperature profile. This is especially true for end-pumping by fibre-coupled diode sources because output from the highly multi-mode fibres typically used has a transverse intensity profile somewhere between a top-hat and Gaussian distribution. The difference between the measured and the parabolic profiles is shown in figure (4-15). In figure (4-15) the black circles show the difference between the measured phase profile and the perfect parabolic lens with the solid lines showing the pump beam radius. As can be seen the agreement between the two profiles is reasonable until the pump beam radius after which the thermal lens then rapidly deviates from the parabolic profile. This suggests that by keeping the laser mode size

less than that of the pump beam will result in the laser mode experiencing a near parabolic lens.

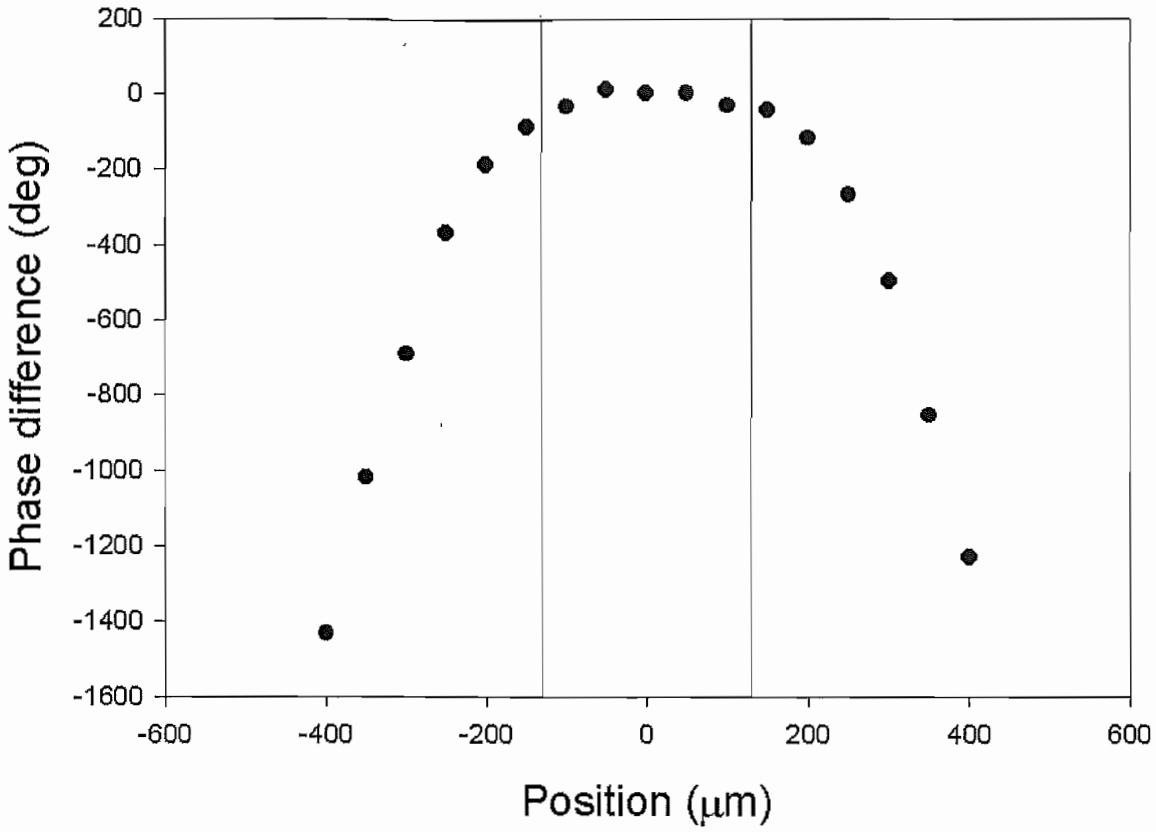

Figure 4-15. Comparison of the measured phase profile and the parabolic profile of an equivalent lens. The circles are the difference between a parabolic phase profile and the measured one and the pump waist radius is shown as the solid lines.

4.4.2 Effect of Polarisation on Thermal Lensing

Nd:YVO_4 is a uniaxial crystal with different values for the change in the refractive index with temperature for the π and σ polarisations. The coefficient for the σ-polarisation is approximately 3 times that of the coefficient in the π-direction. The result of this difference means that it would be expected from equation (4-7) that the power of the thermal lens for the E-field polarised in the σ direction would be ~3 times that for the E-field polarised in the π direction. Figure (4-16) shows the thermal lens power under non-lasing conditions for the two different polarisations for the 1% doped crystal. In figure (4-16) the black circles are the thermal lens powers for light polarised

along the σ-axis and the white circles are the thermal lens powers of light polarised along the π-axis. In each case the crystal was aligned with the cooling direction (Y) parallel to the E-field. For all cases it was found that the lensing for ordinary polarised light, was stronger than the extra-ordinary polarisation, as expected from the comparison of the thermal optical coefficients. The ratio of the powers of the thermal lenses is (~1.4) at the maximum pump power this is however not as great as would be expected from a direct comparison of the two (~3).

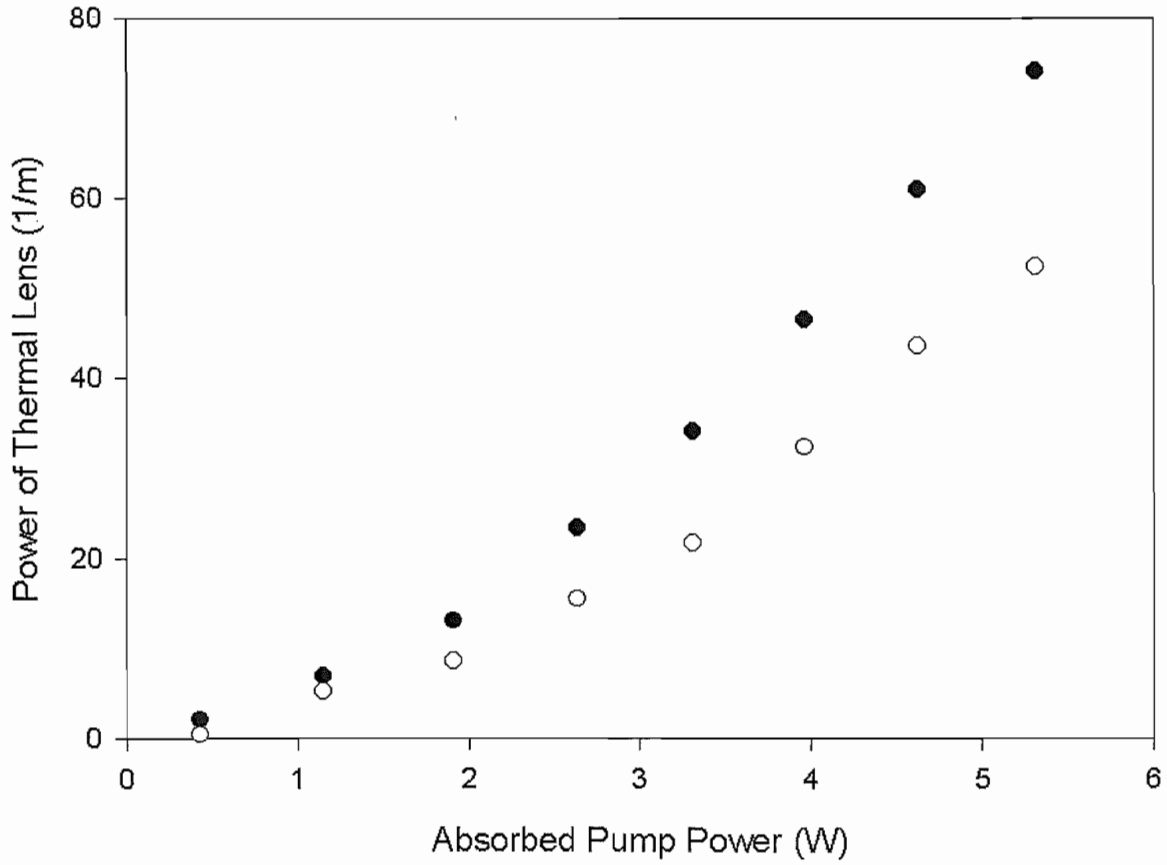

Figure (4-16). Thermal lens power for the ordinary and extra-ordinary polarisations. The black circles are the thermal lens powers for light polarised along the σ-axis and the white circles are the thermal lens powers of light polarised along the π-axis.

Taking into account the effect end face curvature, but neglecting that contribution due to stress, the equation for the dioptric power of the thermal lens on axis becomes

$$D_{\max} = \frac{P[(dn/dT) + (n_0 - 1)(1+\nu)\alpha_T]}{\pi w_p^2 K_c} \qquad (4\text{-}21)$$

where n_0 is the nominal refractive index, ν is Poisson's ratio and α_T is the thermal expansion coefficient. For an a-cut Nd:YVO_4 the π-axis is perpendicular to the optical

axis, this means that any expansion occurs along the σ-axis. Using the values for the shown in table (4-1) and a Poisson's ratio of 0.3, the ratio of the dioptric powers for the σ- and π-axis for an a-cut crystal, including expansion becomes 1.32 and is close to the measured value.

	a-axis	c-axis
dn/dt ($x10^{-6}$ K^{-1})	8.5	3.9
n_0 (@1064 nm)	1.958	2.168
α_T ($x10^{-6}$ K^{-1})	4.43	11.37
K_c ($W\ m^{-1}K^{-1}$)	5.1	5.23

Table (4-1) Values for the change in refractive index with temperature, refractive index, thermal expansion coefficient and thermal conductivity.

4.4.3 Effect of Cooling Geometry

The effect of cooling geometry was investigated by determining the thermal lensing in the cooled and un-cooled directions and comparing the cooling along the a- and c- axes. The dioptric powers of the thermal lenses for the 1% doped crystal under non-lasing conditions are shown in figure (4-17). The circles are for the cooling along the c-axis so the crystal was mounted with the c-axis in the Y-direction and the triangles are for the cooling along the a-axis. The black symbols are for the thermal lens in the cooled direction and the white symbols are for the un-cooled direction. The polarisation of the probe beam for both sets of measurements was along the c-axis. From figure (4-17) it can be seen that the weaker thermal lensing occurs when cooling along the a-axis. From table (4-1) the a-axis has the smaller thermal conductivity, so according to equation (4-11) it should also suffer the greater thermal lensing. The ratio of the strength of the lenses for the cooled directions is 1.25 with the ratio between the thermal conductivities being ~1. For the 0.3% case there is no significantly discernable difference between the lensing in the two axes. Figure (4-17) also shows that the lensing in the non-cooled direction is weaker than that it is in the cooled. This is because the sides are

convectively cooled as opposed to being maintained at a constant temperature leading to a lower thermal gradient.

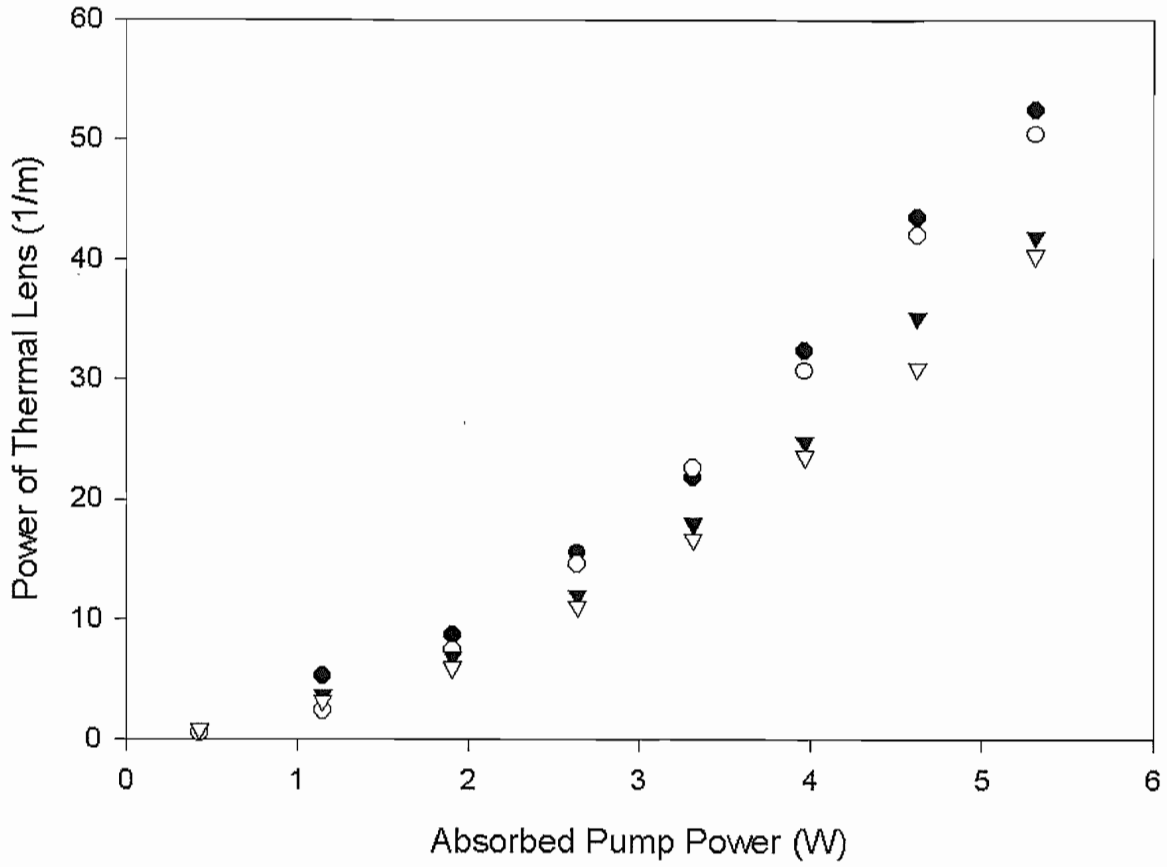

Figure 4-17. Effect of cooling geometry on thermal lens power. The circles are for cooling parallel to the σ-aixs and the triangles are for cooling parallel to the π-axis. The black circles are for the lenses in the cooled direction (Y-axis) and the white circles are for the uncooled direction (X-axis).

To investigate further the reason behind the difference in thermal lensing when cooling is along the a- and c-axes. A further experiment was carried out to determine the change in optical path length that is induced due to stress. This was achieved by modifying the interferometer so that the probe beam is split into two producing two beams travelling collinearly 5mm apart as shown in figure (4-18). The probe beam was divided by inserting a beam splitter (BS1) between the half-wave plate and the first beam splitter of the interferometer (BS2), this divides the beam into 2 each with the same polarisation, a mirror (M1) was then used to direct the second probe beam so that it is aligned parallel to the first beam. One beam passes through the crystal under test, whilst the other passes beside the crystal. This enables a comparison to be made of the

change in path length that occurs due to the change in refractive index of the crystal due to stress. The crystal was mounted such that stress could be applied along a crystal axis, without shearing forces occurring. Measurements were made for both the a- and c-axes and for both polarisations.

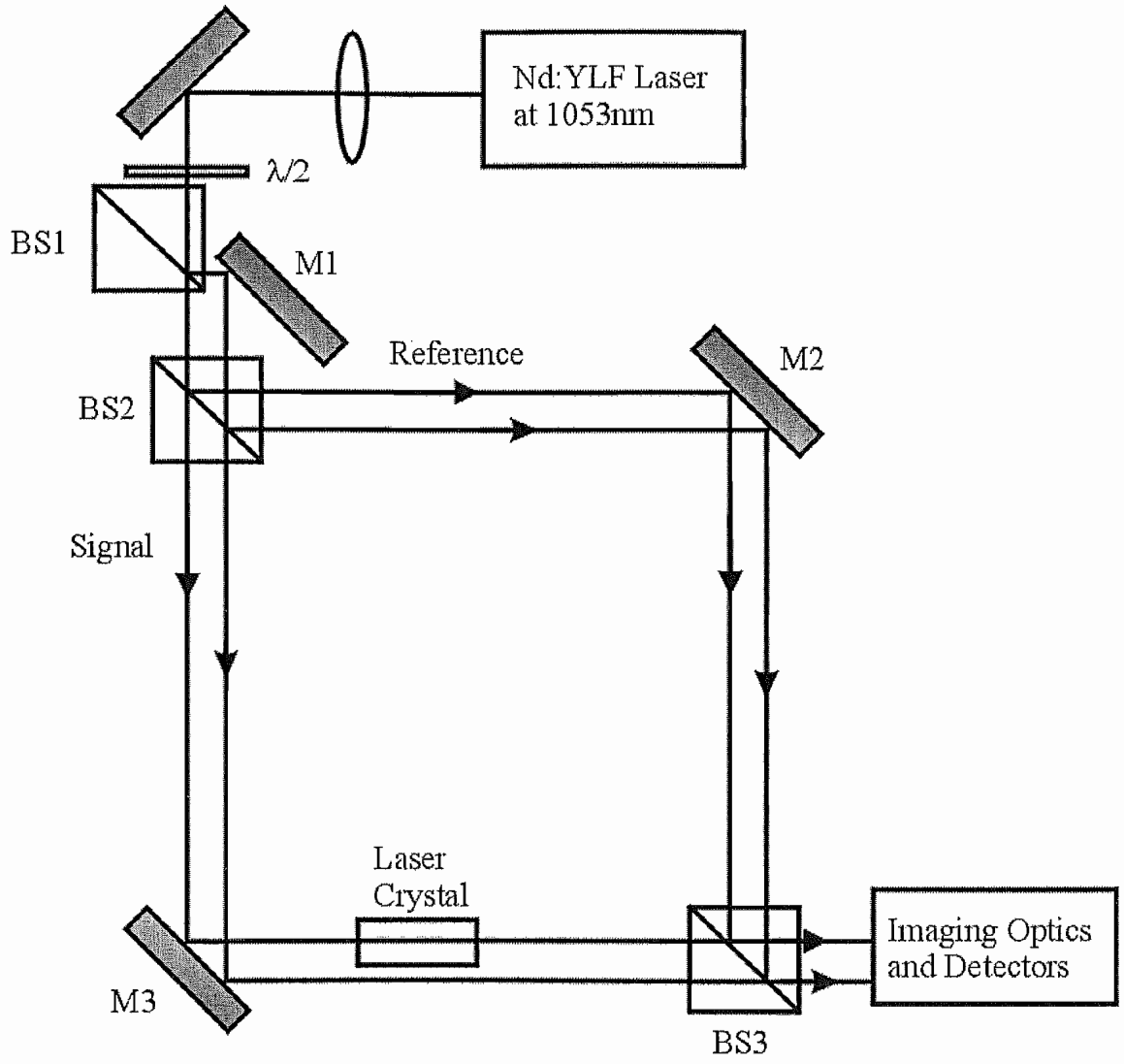

Figure (4-18). Modified Mach-Zehnder interferometer used to determine the changes in refractive index due to stress.

As the stress was applied, it was seen that there was an increase in the phase difference between the two paths implying that the refractive index increased with the applied stress as shown in figure (4-19). Figure (4-19) shows the changes in optical path length due to applied pressure, with the black circles being the change in optical path length when pressure was applied along the c-axis and the white circles those for the a-axis. The results showed that the increase in refractive index was larger when the stress was applied along the c-axis than along the a-axis. Combining this with the thermal

expansion coefficients then the difference in the strengths of the lensing can be explained. The value for the thermal expansion coefficient for the c-axis is nearly three times that for the a-axis so that for a similar thermal gradient it would be expected that there would be a three times greater expansion for the c-axis. However when the crystal is cooled along either of the axes it is unable to expand due to the cooling blocks and the cooler un-pumped region, thus stresses form within the crystal. With the consequent induced refractive index change being greater for the c-axis causing stronger lensing in this direction.

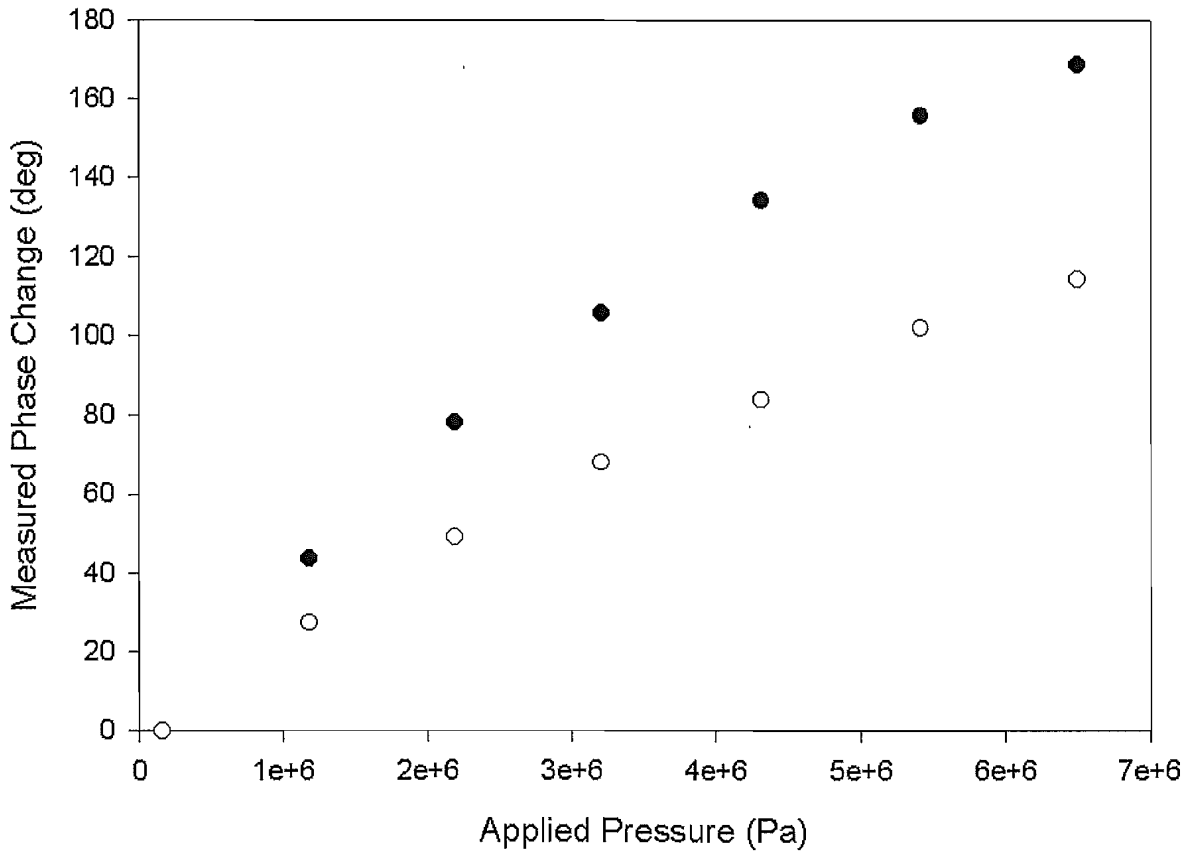

Figure (4-19) Change in optical path length with applied stress. The black circles are for stress applied parallel to the π-axis and the white symbols are for stress applied along the π-axis.

4.4.4 Effect of Lasing Conditions

The effect of lasing conditions is shown in figure (4-20) for the 1% doped crystal. The cooling and polarisation are all along the π-axis, the focal length of the lens is

measured in this direction as well. The dioptric powers of the thermal lenses under non-lasing conditions are the black circles and for the lasing conditions are the white circles. As can be seen there is a significant difference between the power of the thermal lenses under lasing and non-lasing conditions. The power of the thermal lens under lasing conditions is approximately proportional to the absorbed pump power. The power of the thermal lens under non-lasing conditions is highly non-linear. At maximum pump power the strength of the thermal lens under non-lasing conditions is nearly 5 times that under lasing conditions. However, according to equation (4-9) the ratio, Γ, of thermal lensing with and without ETU tends to 4 at high inversion densities as would be expected from the value for quantum defect heating in Nd:YVO_4 . The increased power of the thermal lens is attributed to non-linear changes to the thermal conductivity and the coefficient of change in refractive index with temperature.

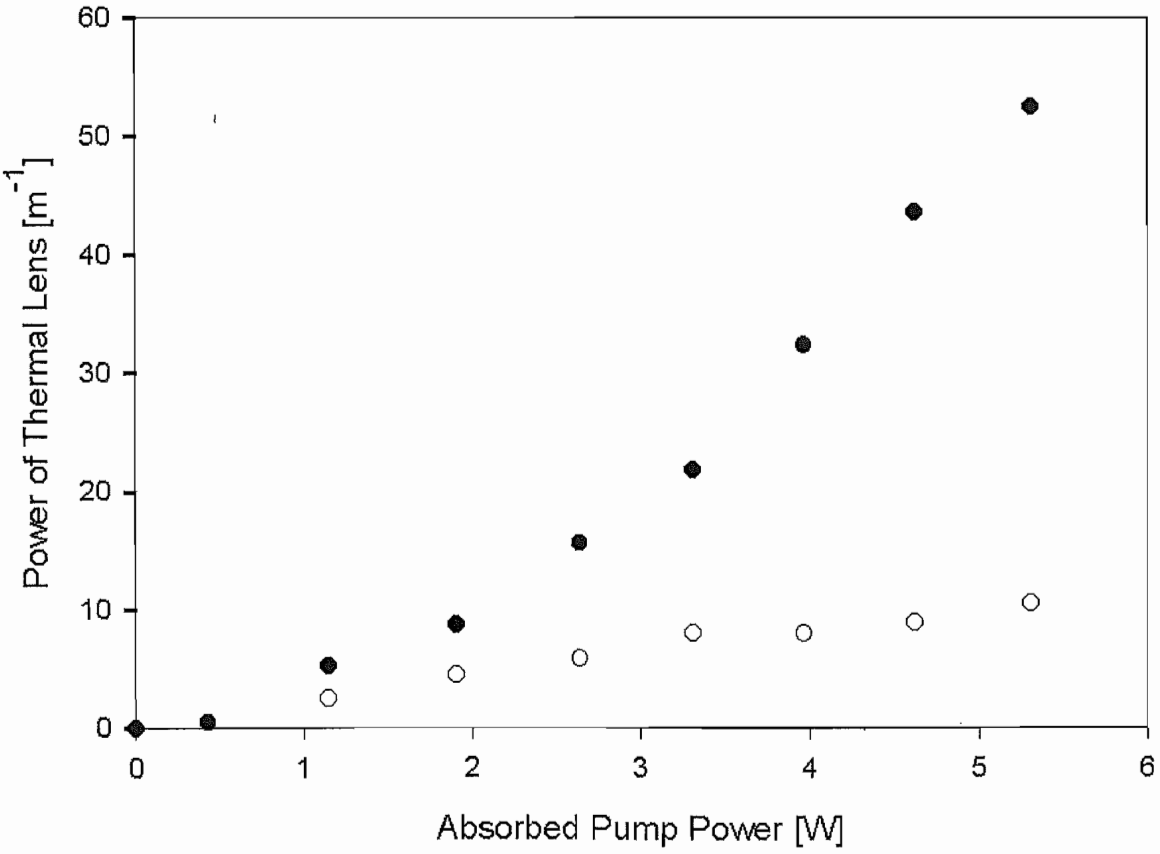

Figures (4-20). Thermal lensing for lasing and non-lasing conditions for the 1% crystal. The black circles are for non-lasing conditions and the white circles are for lasing conditions.

4.4.5 Effect of Dopant Concentration

The effect of dopant concentration is determined by comparing the thermal lensing experienced by the 1% and 0.3% doped crystal. Figure (4-21) shows the thermal lensing under lasing and non-lasing conditions for the 0.3% doped crystal. The black circles are non-lasing and the white circles are under lasing conditions. With the same cooling, polarisation and direction of lensing as for the 1% crystal. The scales for the power of the thermal lenses are the same in figures (4-20) and (4-21) showing that by lowering the dopant concentration reduces the strength of the thermal lensing reduces significantly. At the maximum pump power, the thermal lensing under non-lasing conditions is approximately 2 times stronger than that under lasing conditions for the 0.3% crystal. Comparing the power of the thermal lenses under non-lasing conditions the power of the 1% doped crystal is 4 times that of the 0.3% crystal. It would be expected that the thermal lensing for the 1% doped crystal is greater than that of the 0.3% doped crystal, because although the measured ETU parameter for the crystals is similar, the absorption coefficient for the 1% doped crystal is much shorter therefore the population inversion density is much larger. The power of the thermal lenses under lasing conditions is approximately the same, with the thermal lensing being slightly stronger for the 1% doped crystal. The difference between the thermal lensing is attributed to the larger rate of ETU occurring at threshold for the 1% doped crystal.

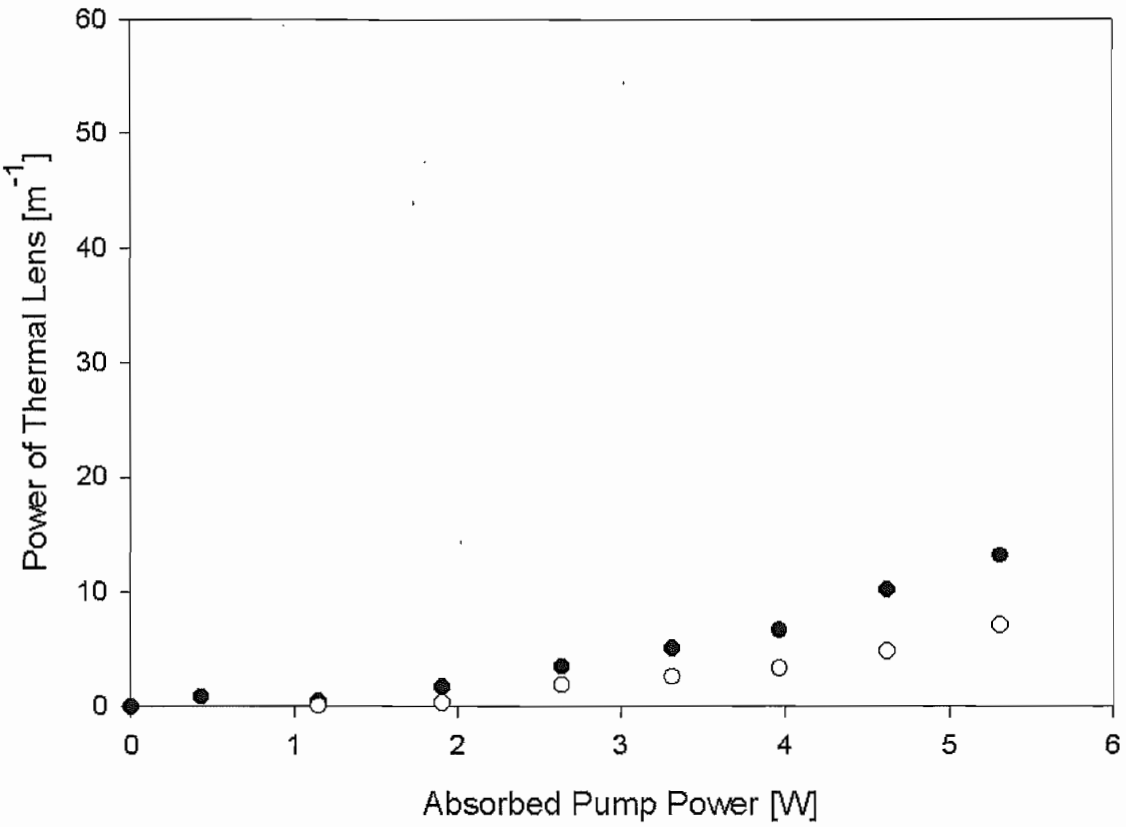

Figure (4-21). Power of the thermal lensing for the 0.3% crystal. The black circles are for non-lasing conditions and the white circles are for lasing conditions.

4.4.6 Effect of ETU on Thermal Lensing

Taking the ratio of the power of the thermal lensing under lasing and non-lasing conditions enables Γ to be determined for the crystals as a function of the absorbed pump power. The ratio of the power of thermal lensing with and without lasing for the 1% doped crystal is shown in figure (4-23). The circles are the measured values and the solid line is the calculated of Γ evaluated from equation (4-9) where the data used to calculate β are w_p=130μm, α_p=3000m^{-1}, τ=100μs and W=3.5x10^{-22}m^{3}s^{-1}, which is the ETU parameter determined in chapter 3 into equation (3-21) and the values of the pump spot size used in this experiment. As can be seen at low powers there is reasonable agreement between the theoretical line and the measured values. However, the measured value of Γ then rapidly increases and begins to deviate considerably from the theoretical curve. This is not due to an incorrect ETU parameter because as stated above, the ratio at maximum pump power is ~5. This could be due to thermal changes

to the refractive index and non-linear changes to the refractive index change with temperature.

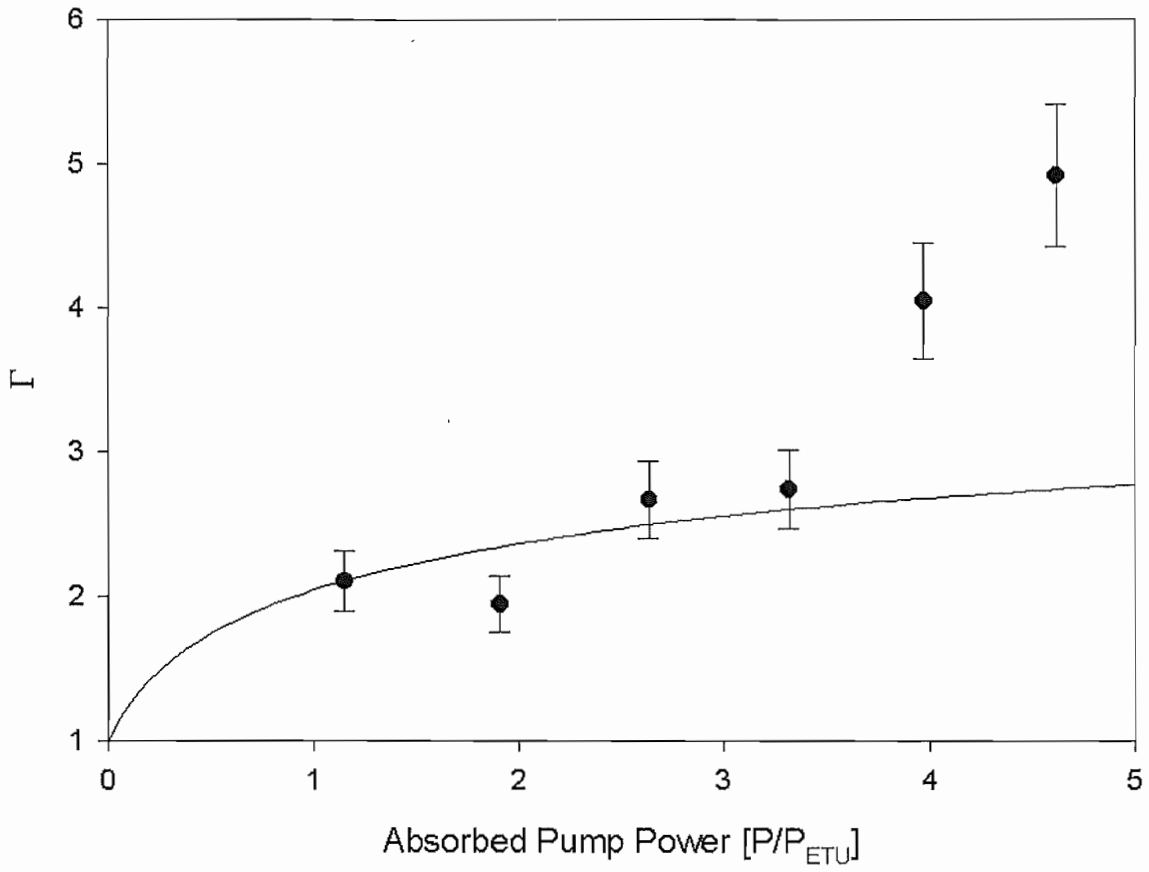

Figure (4-23). Measured and calculated values of Γ for the 1% doped crystal. The solid line is the calculated value for Γ and the circles are the measured values for Γ.

Figure (4-24) shows the measured and calculated values of Γ with α_p=800m^{-1}, τ=110μs and W=3.0x10^{-22}m^{3}s^{-1} used in the calculations. In figure (4-24), the circles are the measured values of Γ and the solid line is the calculated values using the figures above. As can be seen there is good agreement between the theoretical line and the measured values for large pump powers. However, the fit is not so good at low pump powers where the measured value of Γ is as high as 10. This is attributed to the long focal lengths at low powers so any error in measurement will be exaggerated in the plot of Γ. The good agreement between the measured and calculated values of Γ shown in figures (4-23) and (4-24) provides further confirmation for the value of the ETU parameter determined in the previous chapter.

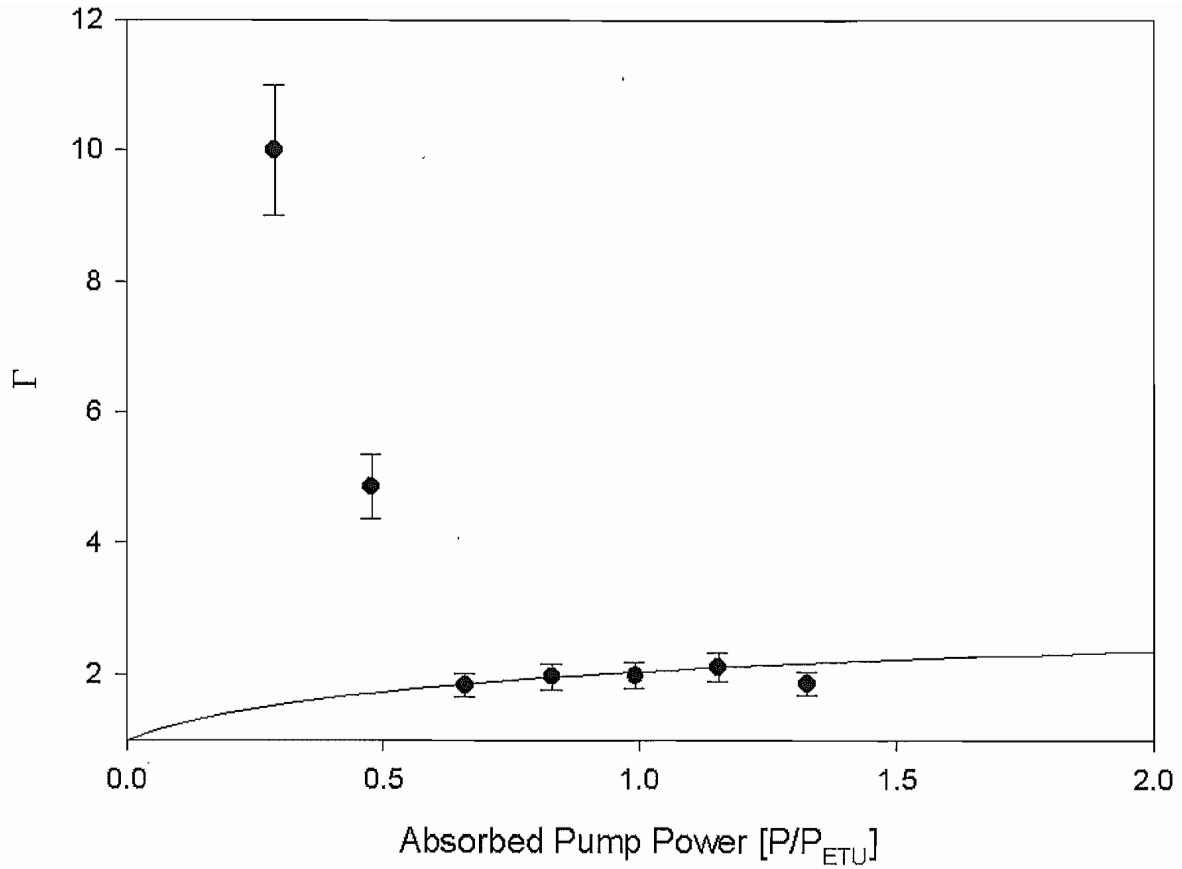

Figure (4-24). Measured and calculated value of Γ for the 0.3% doped crystal. The solid line is the calculated value of Γ and the circles are the measured values of Γ.

4.4.7 Beam Quality with ETU

By fitting a polynomial to the measured phase profile, the quartic phase aberration coefficient can be determined. Using equations (4-13) and (4-14) above to calculate the resultant beam quality after a single pass of the crystal under non-lasing conditions the predicted beam quality after a single pass of the crystal is shown in figure (4-25). Where it has been assumed that the incident beam has a M^2 of 1 and that the laser and pump mode sizes are the same. The black circles are those calculated for the 1% crystal and the white circles are those calculated for the 0.3% crystal. The solid line in figure (4-25) is determined from equation (4-11). It was found at these low powers that although, there is a difference in the amount of ETU occurring under non-lasing conditions, it was not sufficient to cause significant difference in the predicted beam quality degradation. From figure (4-25) it can be seen that the predicted beam quality

degradation under estimates the measured degradation for the 1% crystal, and over estimates the degradation for the 0.3% crystal. This suggests that the effect of ETU on beam quality is more then simply just to increase the heating but also changes, the shape of the thermal loading density, which degrades the beam quality further.

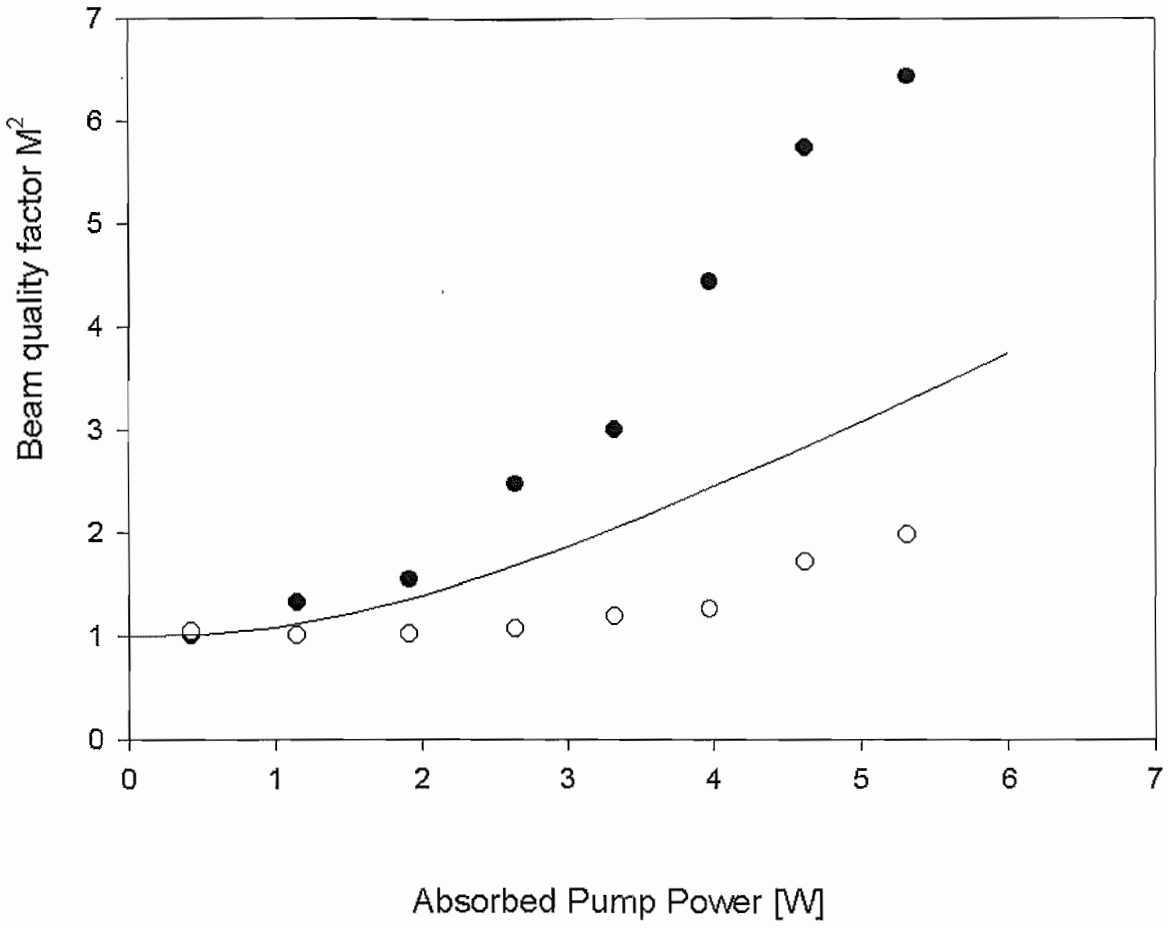

Figure (4-25). Calculated beam quality after a single pass through the thermal lens under non-lasing conditions for the 1% doped crystal (black circles) and the 0.3% doped crystal (white circles) for $w_L=w_p$ the solid line is a theoretical calculation of the expected beam quality after a single pass for $\delta=0.25$.

Figure (4-26) shows the changes in beam quality expected under lasing conditions, the black circles are for the 1% doped crystal and the white circles are for the 0.3% doped crystal. As can be seen the beam quality does not degrade much over the range of available pump power for the lasing case, this suggests that the shape of the thermal lens is not changing, even though the amount of heat generated increases. The scale for

the beam quality factors in figures in (4-25) and (4-26) is the same, showing the reduced beam quality degradation in the absence of strong ETU processes.

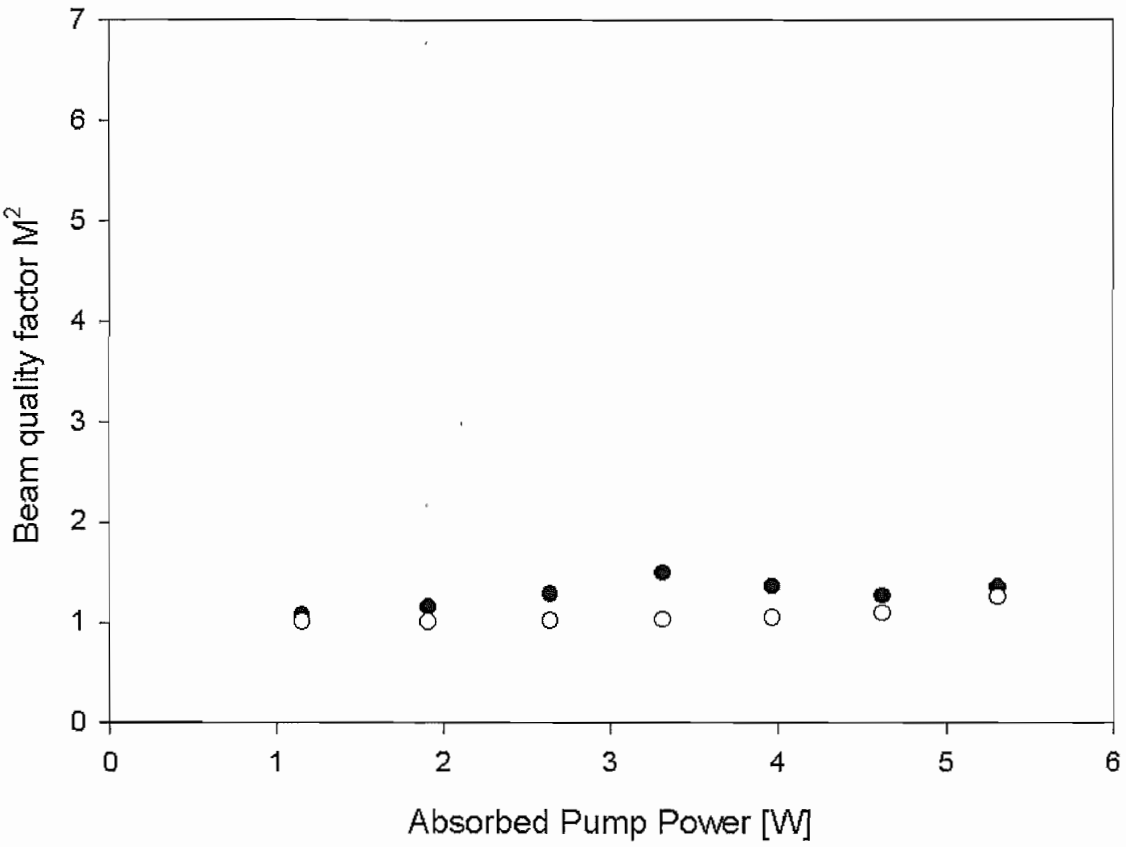

Figure (4-26). Resultant beam quality after a single pass through the thermal lens under lasing conditions for the 1% doped crystal (black circles) and the 0.3% doped crystal (white circles) for $w_L=w_p$.

4.5 Discussion

Table 4-2 summarises the results taken for the power of the thermal lenses at maximum pump power under non-lasing conditions in Nd:YVO_4 for the different polarisation and cooling orientations. As can be seen the weaker thermal lensing occurs for the c-polarisation, and is attributable to the smaller change in refractive index with temperature for this polarisation. Since this is the high-gain transition for Nd:YVO_4 this is fortunate, and allows the full benefit of the better spectroscopic properties when compared to Nd:YAG and Nd:YLF to be utilised. It appears that it is best to cool the crystals along the a-axis, so that weaker lensing occurs. If cooling is directed along

both axes, then there will be a certain degree of astigmatism in power of the thermal lensing, with the lensing in the c-axis being 1.3 times that of the a-axis.

Cooling direction	Polarisation	D_{nl} (m^{-1})
// c-axis	// c-axis	53
// c-axis	⊥ c-axis	70
⊥ c-axis	// c-axis	42
⊥ c-axis	⊥ c-axis	68

Table (4-2). A summary of the powers of the thermal lens measured for the 1% doped crystal under non-lasing conditions.

To compare the effect of ETU on thermal lensing for Nd:YAG, Nd:YLF and Nd:YVO_4 the maximum on axis dioptric power of the thermal lens can be calculated at the ETU saturation power

$$D_{MAXETU} = \frac{P_{ETU}(dn/dt)}{\pi w_p^2 K_c} = \frac{h\nu_P(dn/dT)}{\alpha_P \alpha \tau^2 K_c} \qquad (4\text{-}27)$$

The values of D_{MAXETU} for the different materials and the values used to calculate them combined with the values in table (3-3) are shown in table (4-3). As can be seen Nd:YLF has the weakest on axis power at P_{ETU} and Nd:YAG surprisingly has the highest. This can be attributed to the large vale of P_{ETU} for Nd:YAG. Comparing Nd:YLF and Nd:YVO_4 it can be seen that the on axis powers of the focal lengths are lower in Nd:YLF. This will be further exacerbated because of the bulk expansion in Nd:YLF helping to compensate for the negative lens generated by the refractive index change.

	Nd:YAG	Nd:YVO_4		Nd:YLF	
Polarisation	N/A	C	A	C	A
dn/dT [x10^{-6} K^{-1}]	7.3	4	8.5	-4.3	-2
K_c [Wm^{-1} K^{-1}]	13	5		6.3	
D_{MAXETU} [m^{-1}]	173	19	40	-14.2	-6.6

Table (4-3). Values of D_{MAXETU} and the values used to calculate them.

4.6 References

1. Hardman, P.J., et al., *Energy-transfer upconversion and thermal lensing in high-power end-pumped Nd : YLF laser crystals.* IEEE Journal of Quantum Electronics, 1999. **35**(4): p. 647-655.
2. Siegman, A.E., *Analysis of Laser-Beam Quality Degradation Caused by Quartic Phase Aberrations.* Applied Optics, 1993. **32**(30): p. 5893-5901.
3. Clarkson, W.A., *Thermal effects and their mitigation in end-pumped solid-state lasers.* Journal of Physics D-Applied Physics, 2001. **34**(16): p. 2381-2395.
4. Blows, J.L., J. Dawes, and T. Omatsu, *Thermal lensing measurements in line-focus end-pumped neodymium yttrium aluminium garnet using holographic lateral shearing interferometry.* Journal of applied physics, 1998. **83**(6): p. 2901-2906.
5. Blows, J.L., et al., *Heat generation in Nd : YVO4 with and without laser action.* IEEE Photonics Technology Letters, 1998. **10**(12): p. 1727-1729.
6. Shimosegawa, M., et al., *Transient thermal lensing measurement in a laser diode pumped $Nd_xY_{1-x}Al_3(BO_3)_4$ laser using a holographic shearing interferometer.* Optics Communications, 1997. **140**: p. 237-241.
7. Lucianetti, A., et al., *Thermooptical Properties of Transversely Pumped Composite YAG Rods with a Nd-Doped Core.* IEEE Journal of Quantum Electronics, 2000. **36**(2): p. 220-227.
8. Mudge, D., et al., *Power Scalable TEM_{00} CW Nd:YAG Laser with Thermal Lens Compensation.* IEEE Journal of selected topics in quantum electronics, 2000. **6**(4): p. 643-649.

9. Pfistner, C., et al., *Thermal beam distortions in end-pumped Nd:YAG, Nd:GsGG, and Nd:YLF rods.* IEEE Journal of Quantum Electronics, 1994. **30**: p. 1605-1615.

10. Wu, W.L. and S.L. Huang, *Low-Coherence Reflectometry of Thermal Properties in Diode-Laser-Pumped High-Power Solid-State Laser.* IEEE Photonics Technology Letters, 1998. **10**(6): p. 851-853.

11. Huang, S.L., W.L. Wu, and P.L. Huang, *Measurement of temperature gradient in diode-laser-pumped high-power solid-state laser by low-coherence reflectometry.* Appl. Phys. Lett., 1998. **73**: p. 3342-3344.

12. Vanherzeele, H., *Thermal lensing measurement and compensation in a continuous-wave mode-locked Nd:YLF laser.* Optics letters, 1988. **13**(5): p. 369-371.

13. Paugstadt, R. and M. Bass, *Method for temporally and spatially resolved thermal-lensing measurements.* Applied Optics, 1994. **33**(6): p. 954-959.

14. Sennaroglu, A., *Influence of neodymium concentration on the strength of thermal effects in continuous-wave diode pumped Nd:YVO_4 lasers at 1064nm.* Opt. and Quant. Elect., 2000. **32**: p. 1307-1317.

15. Mukhopadhyay, P.K., et al., *An alternative approach to determine the fractional heat load in sold state laser materials:application to diode-pumped Nd:YVO_4 laser.* Optics and Laser Technology, 2002. **34**: p. 253-258.

16. Zheng, J., S. Zhao, and L. Chen, *Thermal lens determination of Ld end-pumped solid-state laser with stable resonator by slit scanning method.* Optics and Laser Technology, 2002. **34**: p. 439-443.

17. Neuenschwander, B., R. Weber, and H.P. Weber, *Determination of the Thermal Lens in Sold-State Lasers with Stable Cavities.* IEEE Journal of Quantum Electronics, 1995. **31**(6): p. 1082-1087.

18. Fluck, R., M.R. Hermann, and L.A. Hackel, *Energetic and thermal performance of high-gain diode-side-pumped Nd:YAG rods.* Applied Physics B:Lasers and Optics, 2000. **70**: p. 491-498.

19. Clarkson, W.A. and D.C. Hanna, *Single frequency Q-sitched operation of a diode-pumped Nd:YLF ring laser.* Optics Communications, 1991. **84**: p. 51-54.

Chapter 5: Mode-locked Nd:YVO4 oscillator

5.1 Introduction

There are many applications, which require coherent light at wavelengths which are not directly attainable from solid-state lasers. One attractive way to generate output at these wavelengths is via nonlinear frequency conversion. The efficiency of nonlinear frequency conversion is dependent on intensity, hence the power and the beam quality of the fundamental wavelength are very important parameters. To generate the high peak powers required for efficient nonlinear frequency conversion it is often necessary to configure the laser source to operate in pulsed mode. Two standard techniques for producing high peak power pulses are Q-switching and mode-locking. The former is achieved by actively or passively controlling the cavity loss so that energy can be stored in the gain medium by applying a high loss and later released in the form of a giant Q-switched pulse when the cavity loss is restored to a low level. In the later approach different axial modes in the laser are made to lase in phase producing short pulses. The duration of pulses produced by Q-switching, is generally much longer then those produced under mode-locked operation. The usually lower repetition rate of Q-switching means that the energy contained within a pulse can be larger than in the mode-locking regime determined by the effective lifetime of the upper laser level. The cavity length determines the repetition rate of a mode-locked laser. Therefore, a laser with a 1.5m cavity length will have a pulse repetition rate of 100MHz. The frequency spacing between adjacent axial modes is equal to the repetition rate under mode-locked conditions. As a consequence of the very high repetition rates for mode-locked operation, the laser can be considered as operating under continuous-wave conditions as far as the implications of heat loading and spectroscopy on the design of the laser cavity are concerned. This is not strictly true for operation under the Q-Switching regime because the pump rate is maintained during the period of high loss, which builds up the population inversion (and hence the gain), but in the absence of lasing the thermal loading generally increases. As discussed in the previous chapter, under non-lasing conditions the thermal lensing in the crystal is stronger due to increased heat generation. A further consideration for the particular method to be employed is the ability to generate tuneable output via nonlinear frequency conversion and without the

risk of damage due to high fluence. One attractive approach is via synchronous pumping of an optical parametric oscillator (SPOPO). This requires a mode-locked source, and the cavity length of the SPOPO needs to be set so that the round trip time matches the inter-pulse time. The motivation for building a high power pulsed system is so that a chain of nonlinear frequency conversions can be achieved efficiently. In this way the output fundamental can be doubled to generate a high power pulsed green laser, this can be used to pump a SPOPO providing tuneable output in the red region of the spectrum, the output of the SPOPO can finally be frequency doubled, providing a tuneable source in the blue/UV region of the spectrum. Such a source would find application in investigating the phenomena of photo-sensitivity, where UV light can be used to permanently change the refractive index of materials, as has been used in the writing if fibre-Bragg gratings. For this proposed chain of nonlinear frequency conversions to work efficiently, high peak powers are required. To satisfy this demand a master oscillator power amplifier approach will be employed, so that the pulses produced by a low power mode-locked laser will be amplified up to high average powers, so that multiple efficient nonlinear frequency conversions are possible.

In this chapter the design and preliminary results for the performance of the mode-locked Nd:YVO_4 oscillator are described. The theory of amplitude modulated mode-locking is briefly covered, and the design procedure used for the master-oscillator is explained. The results of the master oscillator are then presented, and the use of a pulse picker as a means to enhance the final peak power from the MOPA is discussed.

5.2 Justification for the choice of Nd:YVO_4

In this section the reasons for choosing Nd:YVO_4 as the gain medium are briefly reviewed. Its properties are compared with those of other commonly used ´diode-pumped´ gain materials (Nd:YAG and Nd:YLF). A comparison is made of the predicted threshold pump powers, absorption coefficients for diode pump emission, thermal lensingand the effect of ETU in the three materials.

There has been a resurgence in the interest in the use of Nd:YVO_4 as a gain medium for solid-state lasers in recent years [1-3]. The potential of Nd:YVO_4 as a laser system was

recognised in 1966 [4]. However, early crystals were of poor optical quality due to the formation of YVO_3, within the YVO_4 structure, producing lossy micron-sized scattering centres and absorbing colour-centre defects. The combination of these defects and the requirement for larger crystals for flash lamp pumping initially made YVO_4 ineffective as a laser material. Improved growth methods reducing the metavanadate problem combined with the relaxation in the need for large crystals with the smaller beam waists, greater directionality and better spectral overlap of the emission wavelength with the absorption band, made possible with diode pumping has enabled YVO_4 to be employed successfully in diode pumped laser systems. YVO_4 is a crystal with D4h tetragonal space group of the zircon ($ZrSiO_4$) type with lattice parameters of a=b=7.123Å and c=6.292Å [5], as shown in figure (5-1). In Nd:YVO_4 the Nd^{3+} ions substitute for the Y^{3+} ions. The site symmetry leads to a large positive birefringence with the optical axis aligned along the c-axis and thus the crystal naturally produces polarized laser output.

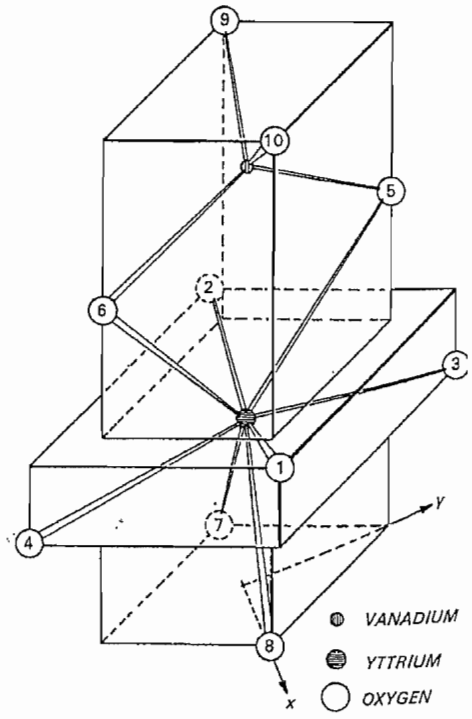

Figure 5-1. Crystal structure of YVO_4 [5].

5.2.1 Lasing Properties

With a similar pump wavelength and matching emission wavelength, Nd:YVO_4 can be retro-fitted into a number of Nd:YAG laser systems. Its larger stimulated emission cross-section and fluorescence lifetime product ($\sigma\tau$) and its improved pump absorption characteristics for standard dopant concentrations can yield improvements in performance. The larger $\sigma\tau$ than Nd:YAG [6] means that Nd:YVO_4 has a smaller saturation intensity, this has the consequence that energy can be extracted more efficiently. Its short absorption length allows tighter focusing of poor beam quality diode pump sources lowering threshold pump powers. Table (5-1) shows the spectroscopic data for Nd:YAG, Nd:YLF and Nd:YVO_4. The equation for the threshold pump power for a pump with a Gaussian transverse profile can be re-written in the form of the saturation intensity so that the threshold pump power is given by

$$P_{th} = \frac{I_s \nu_P}{2\nu_L}(L+T)\pi w_P^2 \tag{5-1}$$

where it has been assumed that all of the pump power is absorbed and that the pump and laser spot sizes in the laser crystal are the same, $\nu_{P,L}$ are the pump and laser frequencies, L is the round-trip cavity loss, T is the transmission of the output coupler and w_p is the radius of the pump beam waist in the crystal. It has been assumed that the combined losses are low, i.e. $(L+T)<1$. The saturation intensity is then given by

$$I_s = \frac{h\nu_L}{\sigma\tau} \tag{5-2}$$

where σ is the stimulated emission cross-section and τ is the fluorescence lifetime. Table (5-1) shows the calculated values of I_s for Nd:YAG, Nd:YLF and Nd:YVO_4 and the values for σ and τ used to calculate them. As can be seen from the respective values of I_s it would be expected that the threshold pump power for Nd:YVO_4 will be lower than for Nd:YAG and Nd:YLF with equivalent cavities and pumping arrangements. With the similarity in the pump and emission wavelengths, it would be expected that the slope efficiencies of the three materials would be approximately the same. It would also be predicted that the slope efficiency of Nd:YVO_4 might be better than that of Nd:YAG and Nd:YLF because the lower threshold, would enable operation many times above threshold with the consequence that the slope efficiency would be improved for a similar pump power. The threshold pump power depends on the pump and beam radii

in the laser crystal, since the laser resonator defines the laser mode size, the combination of the pump beam quality and the absorption coefficient govern the possible threshold pump power because it limits the smallest beam size achievable. If linear pump absorption is assumed, and that all of the incident pump light is absorbed within two absorption lengths, then the minimum effective pump beam radius defined as the r.m.s beam radius, is given by [7]

$$w_{p\,\min}^2 = \frac{2\lambda_p M^2}{\alpha_p \pi n \sqrt{3}} \tag{5-3}$$

where λ_P is the pump wavelength, M^2 is the beam quality factor for the pump and α_P is the pump absorption coefficient. Inserting equation (5-3) into equation (5-2) gives the minimum possible threshold pump power of

$$P_{p\,\min} = \frac{I_s c_n M^2}{\nu_L \alpha_P \sqrt{3}}(L+T) \tag{5-4}$$

In chapter 3, it was shown that the threshold pump power is increased in the presence of upconversion. Using the equation for the threshold pump power it was shown that if

$$(L+T) = \frac{\sigma}{\tau W \alpha_P} \tag{5-5}$$

then the threshold pump power will be 25% higher because of ETU. Inserting equation (5-5) into equation (5-4), the threshold pump power at which there is a 25% increase due to ETU is given by

$$P_{25\%} = \frac{hcM^2}{W\tau^2\alpha_p^2 n\sqrt{3}} \tag{5-6}$$

The larger the value of $P_{25\%}$ the less susceptible the material is to ETU at threshold. Values for $P_{25\%}$ and the data used to calculate them are given in table (5-1). As can be seen when the materials are compared for the same dopant concentration, Nd:YVO_4 has the lowest saturation intensity, this means that for similar pump and resonator conditions Nd:YVO_4 will have the lowest threshold. The lower value for the stimulated emission also means that it will be easier to extract the gain in the amplifier sections of the MOPA system. However comparing the values of $P_{25\%}$ shows that Nd:YVO_4 will suffer from ETU more strongly and at a lower power, for the same dopant concentrations. If the dopant concentration is reduced to 0.1%, the value of $P_{25\%}$ is increased, reducing the impact of ETU, whilst retaining the superior value of the saturation intensity.

	Nd:YAG	Nd:YLF		Nd:YVO_4	
		π	σ		
Nd^{3+} conc [%]	1	1		1	0.1
λ_L [μm]	1.064	1.047	1.053	1.064	
λ_P [nm]	810	792	797	808	
σ[x10^{-23} m^2]	2.8	1.8	1.2	15.6	
τ[μs]	230	480		100	110
I_s [MWm^{-2}]	29	22	33	12	11
W [x$10^{-22}m^3s^{-1}$]	0.5	1		3.5	3
α_p [m^{-1}]	333	1000	350	3000	300
n	1.82	1.47	1.45	2	
$P_{25\%}$ [W]	15	0.24	2	0.13	13

Table (5-1). Lasing properties of Nd:YAG, Nd:YLF and Nd:YVO_4.

As shown in the previous chapter the power of the thermal lenses generated in the laser crystal by the conversion of the absorbed pump power to heat can be reduced by lowering the dopant concentration because the rate of ETU is reduced. However, reducing the dopant concentration will reduce the potential gain of the amplifiers, because the population inversion densities achievable will be reduced.

5.2.2 Absorption

The output spectrum from high-power diode-stacks is generally broader than for low power diode lasers. This is because with more than one emitter in an array and multiple arrays in a stack, there will naturally be a spread in emission wavelengths. Therefore, when scaling to high powers using diode stacks it must be ensured that there will be efficient absorption. High power diode-stacks have an output which typically ≥3nm wide, the temperature variation of the wavelength is also very important factor (especially for high-power diode-stacks), with the wavelength changing by as much as 6nm or more as the current applied to the diode is changed. Therefore the chosen material needs a sufficiently broad absorption bandwidth. A greater absorption

bandwidth also reduces the sensitivity to variation in the pumping wavelength caused by ageing or temperature fluctuations of the pump source.

The absorption spectrum around 810nm in Nd:YVO_4 was measured to determine the width of the absorption bandwidth of this level. This was achieved by placing a 3mm long, 0.5% doped crystal of Nd:YVO_4 in the path of a collimated Ti:Saphire laser. The beam radius of the Ti:Saphire was kept large to ensure that ground-state bleaching and any other spectroscopic effects were kept to negligible levels. The beam from the Ti:Saphire passed through a half-wave plate so that the polarization direction of the beam could be varied. In this way, the absorption for the orthogonal polarizations parallel and perpendicular to the optic axis could be determined. The Ti:Saphire emission wavelength was then tuned and the wavelength monitored using an optical spectrum analyser. The absorption coefficient was calculated by comparing the amount of light transmitted through the sample to that incident on the crystal. The absorption coefficient as a function of pump wavelength is shown figure (5-2). The black circles in figure (5-2) are for the π polarisation (parallel to the c-axis) whilst the white circles are for light polarised in the σ direction (parallel to the a-axis). As can be seen for the two polarisations there is significant absorption at 808nm and 805nm with there also being an absorption peak at 813nm for the π polarisation. The full-width-half-maximum of this peak at 808nm is 2.44nm and is comparable to the spectral width of diode arrays. With such pronounced peaks at 805nm and 813nm, there is significant absorption across a 10nm bandwidth.

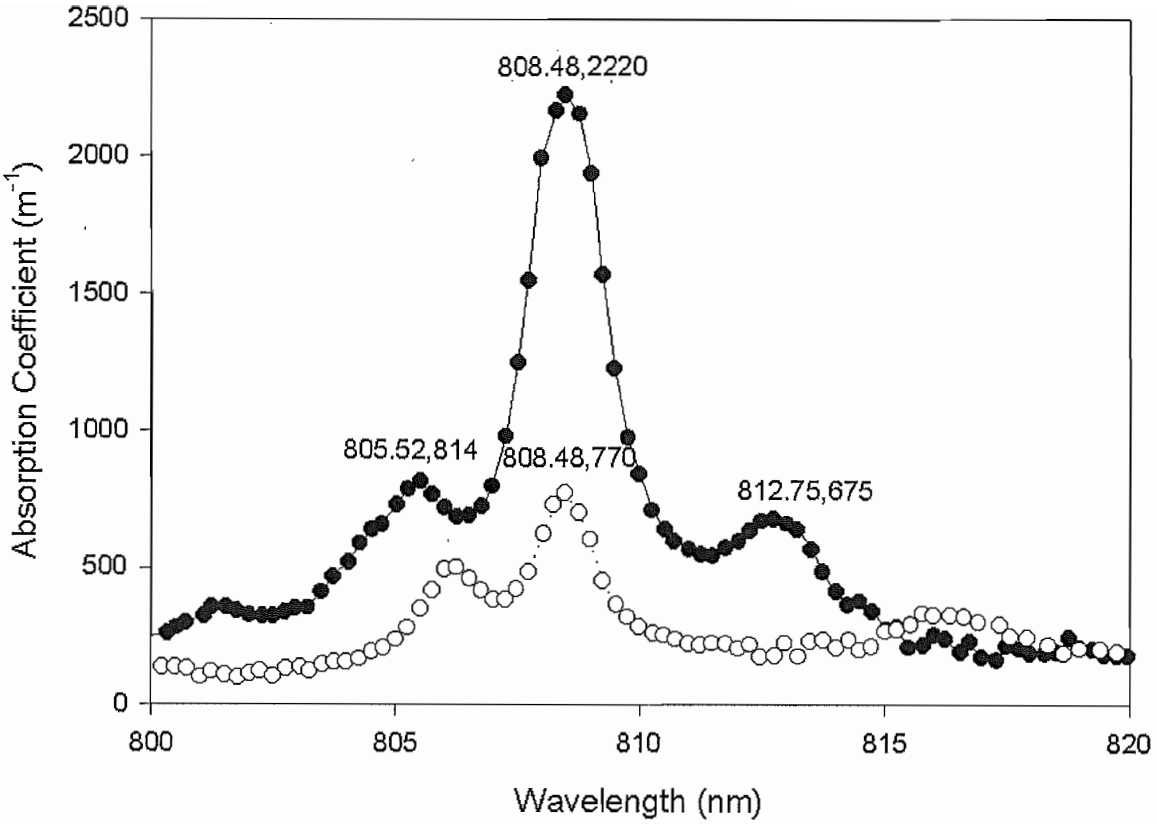

Figure (5-2). The absorption spectrum for 0.5% doped Nd:YVO_4, black circles are for the π-polarisation and the white circles are for the σ-polarisation. The peak wavelength and the corresponding absorption coefficient are also shown.

5.3.1 Mode-locking Theory

Mode-locking can be achieved by both passive and active techniques. In passive mode-locking, an optical element is inserted into the cavity that locks the different modes together by producing an intensity dependent loss. In active mode locking, the optical element provides a frequency shift, or acts as a time-varying transmission, each pass through the element. For homogenously broadened laser materials, where there are typically only one or a few axial modes that lase, the optical element acts to transfer energy from the stronger central modes to the weaker modes in the wings [8]. Pulses generated by passive mode-locking tend to be shorter than those achieved by active mode-locking because the bandwidth of the optical element used for passive mode locking is dependent on the material response to the circulating optical pulse. Passive mode-locking elements typically take the for of saturable absorbers, these have a

constant absorption at low-intensities, but saturates and decreases to lower values as the laser intensity rises, shorter pulses are encouraged because they experience a lower loss at the saturable absorber. Passive mode locking, therefore, makes full use of the gain bandwidth of the gain medium unlike active mode locking where the bandwidth of the modulator is the limiting factor.

In a passively mode-locked laser the modulation effect is produced by the mode-locked laser pulse itself, so the modulation always remains in perfect synchronisation with the circulating pulse, and ideally the modulation effect becomes stronger and faster as the pulse shortens [8]. The pulses in passively mode-locked lasers are initiated by the amplification and modulation of noise. So, depending on the circumstances, passively mode-locked lasers can also oscillate with pulses occurring at harmonics of the laser cavity. The pulses in this situation may not be equally spaced in time, because each pulse can, more or less independently, burn its way through the saturable absorber cell [8]. Frequency modulation, FM, and amplitude modulation, AM, can be used to achieve active mode-locked operation. In FM mode-locking a sinusoidaly varying temporal phase modulation is applied to the circulating laser field. This acts to give the field a Doppler shift on each successive pass through the modulator. As the number of passes increase, the pulse begins to form because the modulator locks progressively more and more modes together generating a pulse. The modulator in FM mode-locking is generally an electro-optic phase modulator. With AM mode-locking, there is a time varying loss, usually caused by a standing acoustic wave generated an acousto-optic modulator. Under steady-state conditions both AM and FM modulators produce the same pulse width, for similar modulation frequencies and depths. In AM mode-locking the pulses pass through the modulator when the transmission is a maximum, i.e. at a low loss point. The pulse passes through the modulator when the change in phase with time is zero, which occurs twice per period with FM [9]. The existence of two-phase extrema per period creates a phase uncertainty in the mode-locked pulse position, because the pulse can occur at either of two equally probable phases relative to the modulating signal. Since pulses can occur equally well at either of two phase positions that are 180^0 apart relative to the modulation signal, FM mode-locked lasers tend to jump back and forth randomly between these two 'phase-states' or even to oscillate in both states simultaneously [8]. The pulses pass through the phase modulator at the point that the change in phase with time is zero. Since the pulse duration of the pulse is

much smaller than that of the modulation signal, the sinusoidal phase variation can be assumed quadratic. This quadratic variation of the temporal phase modulation about the pulse arrival time produces a frequency 'chirp' within the short mode-locked pulses [10]. This chirp could be used to compress the pulse after the oscillator.

Mode-locking in homogenous laser media occurs as the result of a competition between the side-band-generating active modulator, which acts to push energy outward from the central 'peak gain' axial modes into axial modes further out in the spectrum, and the limited-band-pass laser gain medium, which continually acts to narrow the oscillation spectrum and broaden the mode-locked pulse [11]. Dallas made a direct comparison of Nd:YLF, Nd:YAG, Nd:YVO4 and Nd:S-VAP under FM mode-locking concluding that Nd:YLF and Nd:YVO4 were crystals of choice based upon lasing slope efficiency and pulse width [12]. Based upon this discussion, AM mode-locking will be used as a relatively simple and robust method of mode-locking without the requirement of complex electronics or optics to ensure a stable train of pulses. By using active mode-locking the mode-locked pulses can be generated 'on demand', allowing the laser to be run in a continuous-wave mode if required.

5.3.2 Amplitude Modulation Mode-locking

With AM mode-locking the circulating field inside the laser cavity is amplitude modulated and rapidly shaped into a very closely Gaussian pulse which is shortened on each successive pass through the modulator. This pulse narrowing continues until the modulator pulse shortening process becomes limited at the steady-state value by the spectral narrowing effects of the laser medium [11]. From a frequency-domain viewpoint, introducing a time-varying transmission by inserting an amplitude modulator inside the laser resonator, creating sidebands on each oscillating axial mode which overlap with adjoining axial modes. The operation can be described by assuming that the mode with frequency ν_0, nearest the peak of the laser gain profile, will begin to oscillate first. If a loss modulator operating at a frequency f_m is inserted into the resonator, the carrier frequency ν_0 will develop sidebands at $\pm f_m$. If the modulating frequency is chosen to be equal to the axial mode frequency separation $f_m=c/2l_c$, where l_c is the cavity length of the laser. The coincidence of the sidebands with the adjacent

axial mode resonances will couple the modes with a well-defined amplitude and phase. These sidebands will also develop sidebands as they pass through the modulator and the process will continue until all axial modes falling within the laser line width are coupled [10]. Some published values for pulse durations achieved by AM mode locking are given in table (5-2).

Wavelength	Material	Pulse Duration	Repetition Rate	Average Power	Reference
1055nm	Nd:Glass	5.8ps	90MHz	13mW	[13]
1053nm	Nd:Glass	9ps	240MHz		[14]
1064nm	Nd:YAG	105ps	90MHz	105ps	[13]
	Nd:YAG	55ps	228MHz		[15]

Table (5-2). Some reported pulse durations achieved using AM mode locking.

The predicted pulse duration, τ_p, achievable using AM mode-locking can be calculated by (assuming that the circulating pulse is Gaussian) using [8]

$$\tau_p \approx \gamma \left(\frac{\ln(1/R)}{2\Delta_m} \right)^{1/4} \left(\frac{1}{f_m \Delta f_a} \right)^{1/2} \tag{5-7}$$

where R is the reflectivity of the output coupler, l_c is the length of the laser crystal, Δ_m is the modulation depth, f_m is the modulation frequency, Δf_a is the gain bandwidth and γ=0.53 for Bragg deflection and γ=0.45 for Raman-Nath modulation. In equation the assumption that the saturated small signal gain is equal to the reflectivity of the output coupler and other cavity loss has been neglected (i.e. $gl_c \approx \frac{1}{2}\ln(1/R)$). The modulation depth for an acoustooptic modulator is proportional to the applied RF power so the pulse duration should vary by $1/P_m^{1/4}$, where P_m is the RF power applied to the modulator. So increasing the RF power applied to the modulator will slowly reduce the pulse duration. The ratio of the output coupler and the modulation depth reduced to the one-quarter power has values not far from unity in most situations. The pulse width is then primarily determined by $1/(f_m \Delta f_a)^{1/2}$. Equation (5-7) also shows that the greater the

modulation frequency the shorter the pulse duration. For Nd:YVO_4 with a 50MHz modulator, 5% output coupling, 6% modulation depth a gain bandwidth of 212GHz, it would be predicted that ~120ps pulses should be achievable using Bragg modulation.

5.4 Cavity Design Considerations

In chapter 2 it was shown that, certain properties are required in a diode end-pumped cavity to ensure diffraction limited output. There has to be a balance struck between several competing demands on the laser mode size in the laser crystal, caused by the generation of thermal lensing in the laser crystal. At low pump powers when the effect of thermal lensing is small, then to prevent higher-order modes from oscillating due to undepleted gain in the wings of the pump beam, the laser mode should be larger than the pump beam radius. This is only possible at low powers when the thermal lens is not too aberrated to cause beam quality degradation to the laser beam. As the pump power is increased however, the strength of the thermal lens and consequently its aberrated nature can lead to beam quality degradation of the laser beam. To prevent the laser mode from being degraded due to the aberatted nature of the thermal lens it should have a mode size that is smaller than the pump beam radius, with the laser mode decreasing with decreasing thermal lens focal length. However, the problem arises again that the undepleted gain in the wings of the pump region might cause higher-order modes to lase preventing diffraction limited operation. To surmount this dilemma, it was proposed in chapter 2, that the cavity mode in the laser crystal should decrease with increasing thermal lens focal length. In this way, higher-order modes will experience longer thermal lens focal lengths in the crystal, with the consequence that the ratio of the sizes of the higher-order mode and the TEM_{00} mode will be reduced. The reduction of the ratio effectively suppresses the lasing on the higher-order modes because the TEM_{00} mode with its superior overlap with the pump beam will saturate the gain. The pump power required to reach threshold is essentially determined by the pump beam radius therefore, because the resonator can be designed to generate a suitable mode size in the gain medium. With the beam quality of the pump source governing the achievable mode size.

As discussed above it would be ideal if the cavity could be designed to behave in a certain way with the power of the thermal lens, however, there are other restrictions placed on the cavity caused by the insertion of the AM modulator. The AM modulator needs to be inserted in a collimated section of the laser mode in the cavity. A small beam waist in the laser crystal and a collimated section can be achieved in a cavity if an internal lens is used. To prevent increases in loses and the chanced of etalon effects as discussed later a 3-mirror folded cavity can be used instead. If the correct choice of folding mirror and arm lengths is chosen, the curved folding mirror generates a focus in one arm and the other arm will be collimated. The use of the MOPA power-scaling strategy enables the master oscillator to be of a low power, so that the laser mode size can be larger than the pump mode size in the laser crystal without suffering from beam quality degradation. However, the beam waist at the output of the laser is imaged throughout the system, so that is the thermal lens causes changes to the beam radius in the collimated arm, the beam waists will change in all of the subsequent stages. This might lead to a reduction in the efficiency of nonlinear frequency conversions or degrade the beam quality as the passes through amplifier stages.

Apart from the effects of the thermal lens on the cavity there are other factors that must be considered. Any etalons in the cavity will act to increase the pulse duration, by restricting the number of oscillating modes. The use of angled components in the cavity could lead to astigmatic output if they are not compensated for. This will lead to an increase in the number and complexity of the optics used if this is achieved after the master oscillator.

5.4.1 Pulse Broadening Effects

The position of the gain medium in the cavity not only has implications for the pumping arrangements and the laser mode beam radius in the crystal it can also have an influence on the pulse duration produced by mode-locking. It has been found that the pulse durations produced when the gain medium is at the end of the cavity can be approximately a third of those generated when the gain medium is positioned in the middle of the cavity [16]. This difference was attributed to spatial hole burning which leads to a broader free running linewidth when the gain medium is at the end of the

cavity [14]. The broadening can be quite considerable with a free-running bandwidth of 41GHz reported for a Nd:YAG laser with the rod at the end of the cavity and with a free-running bandwidth of 1 GHz with the rod located away from the end of the cavity [17, 18]. These results were compared with a unidirectional ring laser, unidirectionalty was enforced by placing the Nd:YAG crystal in a permanent magnet and compensating for the Faraday rotation by making the ring non-planar. Because the laser is uni-directional, it is also single frequency. A FM modulator was inserted in the cavity and the laser run under FM operation. In this condition, the axial mode spacing (i.e. the cavity length) and the modulator repetition rate are detuned. In this situation, pulses are not produced, but the frequency of the laser is scanned. For the unidirectional laser it was found that the laser had a FM bandwidth of 116GHz [18]. With FM bandwidths of 70GHz and 21GHz achieved for the standing wave lasers with the laser crystal at the end, and away from the end respectively. To force the laser into uni-directional ring operation will increase the number of optical components and the risk of introducing etalon effects.

Etalon effects limit the effective gain bandwidth increasing the pulse duration of mode-locked pulses. Such etalon effects will effectively cause a periodic spectral variation in the round-trip gain inside the laser cavity created by a periodic spectral variation in transmission. An etalon has a free spectral range which is typically much smaller than the gain bandwidth and even though the peak-to-peak transmission modulation of the etalon may be quite small a transmission peak near carrier frequency can act to modify the gain profile so that it is much narrower than would otherwise be the case withough etalon effects. The risk of etalon effects can be minimised by using Brewster cut elements because for p-polarized light, which is polarized in the plane of the Brewster face, there is no reflection from the surface when the incident beam is at Brewster's angle.

5.4.2 Astigmatism

An astigmatic beam is one that has different spot sizes, wave front curvatures, and beam-waist positions in orthogonal directions [19]. Although astigmatism can be corrected for, it generally increases the number of optical components required, and hence the complexity of the system. Astigmatism can be introduced into an originally circular non-astigmatic beam by interacting with optical elements that lack axial symmetry. Two such examples that will be considered in detail are the reflection at an oblique angle of a beam from a curved mirror [20, 21] and the influence of Brewster-angled elements (or more generally wedged components) on a beam passing through them [19, 20].

For a beam incident on a mirror at an oblique angle, the mirror has different focal lengths in orthoganal planes [21]. The focal lengths of the mirror are changed in the following way [20];

$$f_{sag} = \frac{f}{\cos\theta} \tag{5-8}$$

$$f_{\tan} = f \cdot \cos\theta \tag{5-9}$$

where $f_{sag,tan}$ are the focal lengths in the sagittal and tangential planes, f is the on-axis focal length of the mirror and θ is the angle of incidence. The sagittal and tangential planes and the angle of incidence are defined in figure (5-4) where mirror M3 is aligned at an angle θ to the laser cavity. From equations (5-3) and (5-4) it can be seen that a circular beam incident on the mirror at an angle will then have two separate focal points. The beam area generated at the focus will not be as small as that generated if the beam was at normal incidence.

Brewster elements have essentially two different effective optical path lengths in the two orthogonal planes [19]. Therefore, because they have travelled different distances the beam radii and radius of curvatures in the two planes will be different upon exiting the Brewster element. The effective lengths in the two different planes for a Brewster window of thickness t and refractive index n are [20];

$$d_{sag} = \frac{t\sqrt{n^2+1}}{n^2} \tag{5-10}$$

$$d_{\tan} = \frac{t\sqrt{n^2+1}}{n^4} \tag{5-11}$$

where $d_{sag,tan}$ are the effective distances in the sagittal and tangential planes respectively and are defined in figure (5-4) where BE is an element of thickness t aligned at Brewster's angle. Brewster's angle is given by θ_B=arctan(n).

A laser cavity containing a combination of these elements is likely to have different waist positions and sizes in the different planes. This has the consequence that the stability regime in each plane may not overlap, and the design of the laser can be such that it is stable in one plane but not in the other. Compensation of astigmatism is necessary to produce a maximum overlap of the stability regimes and the designed laser mode characteristics, and can be achieved by the combination of a Brewster element and an inclined mirror with a common plane of incidence in the same cavity, as shown in figure (5-4).

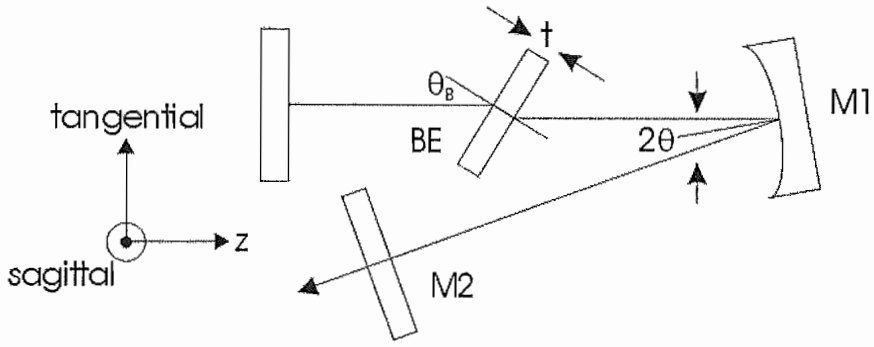

Figure (5-4). Arrangement of an astigmatically compensated cavity with a Brewster cut element and an off axis curved mirror.

Compensation of astigmatism occurs when the angle of incidence of laser mode with the folding mirror is adjusted such that the difference in effective path lengths through the Brewster element is equal to the difference between the focal lengths of the folding mirror in the two planes. This is satisfied when both sides of the following equation are equal [20]

$$\frac{t(n^2-1)}{f}\frac{\sqrt{n^2+1}}{n^4} = \sin\theta\tan\theta = x \tag{5-12}$$

However, whilst the compensation produces a maximum overlap of the stability ranges and equal beam waists in orthogonal planes, it does not mean that the modes have the

same size all the way through the cavity, or that the beam waists will be the same size in the Brewster element. Equation (5-12) can be solved by using trigonometric identities to re-write the right hand side as

$$x\cos(\theta) = \sin^2(\theta) = 1 + \cos^2(\theta) \tag{5-13}$$

Equation (5-13) can then be solved for cos(θ) using the quadratic formula

$$\cos(\theta) = \frac{-x \pm \sqrt{x^2 + 4}}{2} \tag{5-14}$$

For a 10mm long Brewster cut Nd:YVO_4 crystal with n=2 and a folding mirror of 750mm radius of curvature, the required angle of incidence to compensate for astigmatism is 6^0. Although the cavity compensates for the astigmatism in the air, when the beam enters the Brewster element, due to the refractional change of the direction of propagation a change in the tangential beam radius takes place. This means that laser will have an elliptical mode in the laser crystal, with an elliptical pump beam required to achieve optimum overlap between the pump beam and the laser mode.

5.4.3 Effect of Thermal Lensing on Cavity Design

Having decided on a general cavity configuration that satisfies the requirements of a small beam waist in the gain medium and a collimated beam for the mode-locker, the effect of thermal lensing on the cavity modes needs to be considered, to allow a robust design to be produced. A simplified schematic of the cavity (A) and its optical equivalent (B) are shown in figure (5-5). In figure (5-5 (A)) R_1 is a mirror formed by a di-electric coating on a face of the laser crystal, R_f is the folding mirror, R_2 is the output coupler and $d_{1,2}$ are the distances between the laser crystal and the folding mirror and the output coupler and the folding mirror respectively.

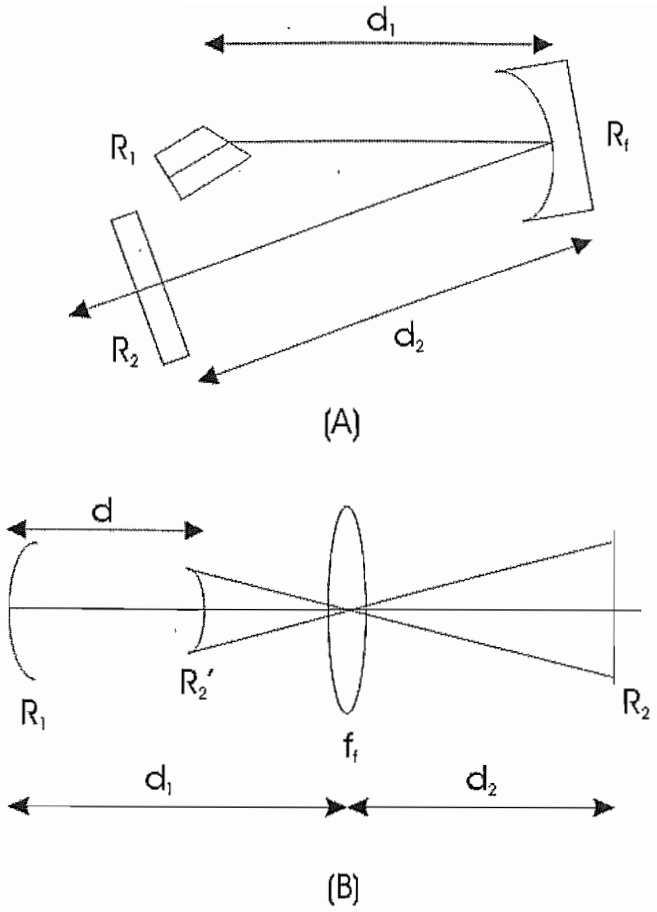

Figure (5-5). Astigmatically compensated cavity and its optical equivalent.

Cavities with internal lenses have been analysed by Kogelnik [20, 22]. As shown in figure (5-5(B)), the cavity with an internal lens can be simplified by transforming mirror R_2 through the folding mirror. The curvature of the reference surface then acts as the radius of curvature of an imaginary mirror R_2'. The curvature of the imaginary mirror, R_2' is given by [20]

$$R_2' = \frac{R_2 f_f^2}{(d_2 - f_f)(d_2 - R_2 - f_f)} \tag{5-15}$$

where f_f is the focal length of the folding mirror, R_2 is the radius of curvature of the output coupler and d_2 is the distance between the folding mirror and R_2. When the output coupler is plane, $R_2=\infty$ and equation simplifies to

$$R_2' = \frac{f_f^2}{(f_f - d_2)} \tag{5-16}$$

The distance, d, between the mirror on the laser crystal and the surface of the imaginary mirror (i.e. R_1 and R_2')is given by

$$d = d_1 - \frac{d_2 f_f}{(d_2 - f_f)} \tag{5-17}$$

where d_1 is the distance between R_1 and the folding mirror. The radius of the beam at R_1 is then given by [23]

$$w_1^4 = \left(\frac{\lambda R_1}{\pi}\right)^2 \frac{(R_2'-d)d}{(R_1-d)(R_1+R_2'-d)} \tag{5-18}$$

where R_1 is the radius of curvature of R_1. The thermal lens generated in the laser crystal can be modelled by assuming its focal length is the same as the curvature mirror R_1. Using equations (5-16) and (5-17) equation (5-18) can be re-written as

$$w_1^4 = \left(\frac{\lambda R_1}{\pi}\right)^2 \frac{(f_f - d_1)(d_1(d_2 - f_f) - d_2 f_f)}{((R_1 - d_1)(d_2 - f) + d_2 f)(R_1 + f_f - d_1)} \tag{5-19}$$

To examine the properties of the cavity, the cavity lengths can be assumed to be $d_1=f_f+\Delta d$ and $d_2=l_c-(f_f+\Delta d)$, where l_c is the optical length of the cavity and Δd is the range of adjustment. Substituting these lengths into equation (5-19) the beam radius in the laser crystal is given by

$$w_1^4 = \left(\frac{\lambda R_1}{\pi}\right)^2 \frac{\Delta d\left(f_f^2 - \Delta d\left(l_c - \Delta d - 2f_f\right)\right)}{\left((R_1 - \Delta d)\left(l_c - \Delta d - 2f_f\right) + f_f^2\right)(R_1 - \Delta d)} \tag{5-20}$$

For the unpumped cavity, with $R_1 \to \infty$, the beam radius is given by [24]

$$w_{1,UP}^4 = \left(\frac{\lambda}{\pi}\right)^2 \frac{\Delta d\left(f_f^2 - \Delta d\left(l_c - \Delta d - 2f_f\right)\right)}{\left(l_c - \Delta d - 2f_f\right)} \tag{5-21}$$

Examining equation (5-18) for the cavity (with thermal lensing neglected) there are several interesting points for different values of the cavity adjustment. When Δd=0, w_1=0, the cavity becomes hemispherical. However, the cavity becomes unstable when Δd<0, with $w_{1,UP}$ becoming complex. The folding mirror can have values for its focal length of $0<f_f<l_c/2$. With $w_{1,UP}$ becoming complex for folding mirror focal lengths outside this range. The range of adjustment, Δd is given by $0<\Delta d<l_c-2f_f$, although the cavity might become unstable for values within this range, specifically when $\Delta d=f_f$. The cavity is at a point of symmetry when $f_f=l_c/4$, with two stable branches for the length of Δd, when $\Delta d<f_f$ then $d_1<d_2$ and when $\Delta d>f_f$ then $d_1>d_2$. As the focal length of the

folding mirror decreases, this region of instability around $\Delta d=f_f$ increases and the cavity is unstable for $f_f^2/(l_c\Delta d)<1-(\Delta d+2f_f)/l_c$ this is illustrated in figure (5-6). Figure (5-6), shows the variation of the beam waist in the laser crystal under unpumped conditions for different cavity adjustments. The solid line in figure (5-6) is for $f_f=l_c/4$ and represents the point of symmetry, the dotted line is for $f_f=l_c/4.1$ and the dashed line is for $f_f=l_c/3.9$.

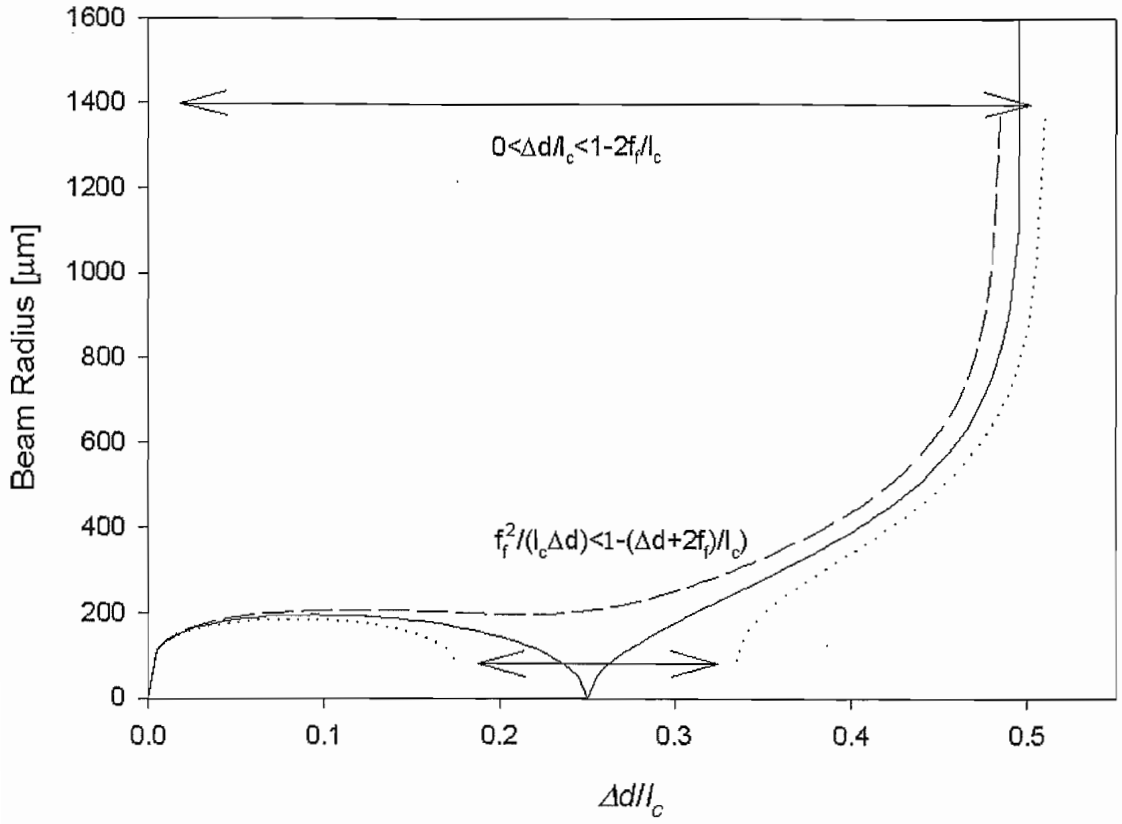

Figure (5-6). Change of spot size in crystal with adjustment length. The solid line is for a folding mirror with a focal length of $f_f=l_c/4$, the dotted line is for a focal length of $f_f=l_c/4.1$ and the dashed line is for a focal length of $f_f=l_c/3.9$.

As can be seen from figure (5-6) at either edge of stability the beam radius in the laser crystal is very sensitive to cavity length adjustments. In the region around $\Delta d/l_c$=0.1 the sensitivity of the beam radius in the laser crystal to cavity length adjustments decreases as the focal length of the folding mirror increases. For folding mirrors with focal lengths, $f_f<l_c/4$ the region for which the cavity adjustment is bounded by the two solutions of

$$\Delta d_{\min,\max} = \frac{l_c - 2f_f \pm \sqrt{l_c^2 - 4l_c f_f}}{2} \tag{5-22}$$

where $\Delta d_{min,max}$ are the minimum and maximum values for the cavity adjustment at either edge of the unstable region. The point at which the beam radius in the crystal is at its greatest for the first region of stability is given by half the value of Δd_{min}. At this point the change in the beam radius with cavity length adjustment is the least as well.

The effect of thermal lensing on the laser mode size can be determined by taking the ratio of the beam radii in the laser crystal with and without thermal lensing. This is shown in figure (5-7) where the ratio of equations (5-20) and (5-21) is plotted, for different thermal lens focal length (radius of curvature for R_1) and folding mirror focal lengths. In figure (5-7) the solid line is for a folding mirror with a focal length of $f_f=l_c/4$, the dotted line is for a folding mirror with a focal length of $f_f=l_c/3$ and the dashed line is for a folding mirror with a focal length of $f_f=l_c/5$. For folding mirrors with a focal length greater than or equal to a quarter of the cavity length (i.e. when $f_f \geq l_c/4$) the chosen value for the cavity adjustment was given by $\Delta d_{min}/2$ when calculated for $f_f=l_c/4$. For folding mirror focal lengths shorter than a quarter of the cavity length ($f_f<l_c/4$) the chosen cavity length adjustment used was given by $\Delta d_{min}/2$ for f_f.

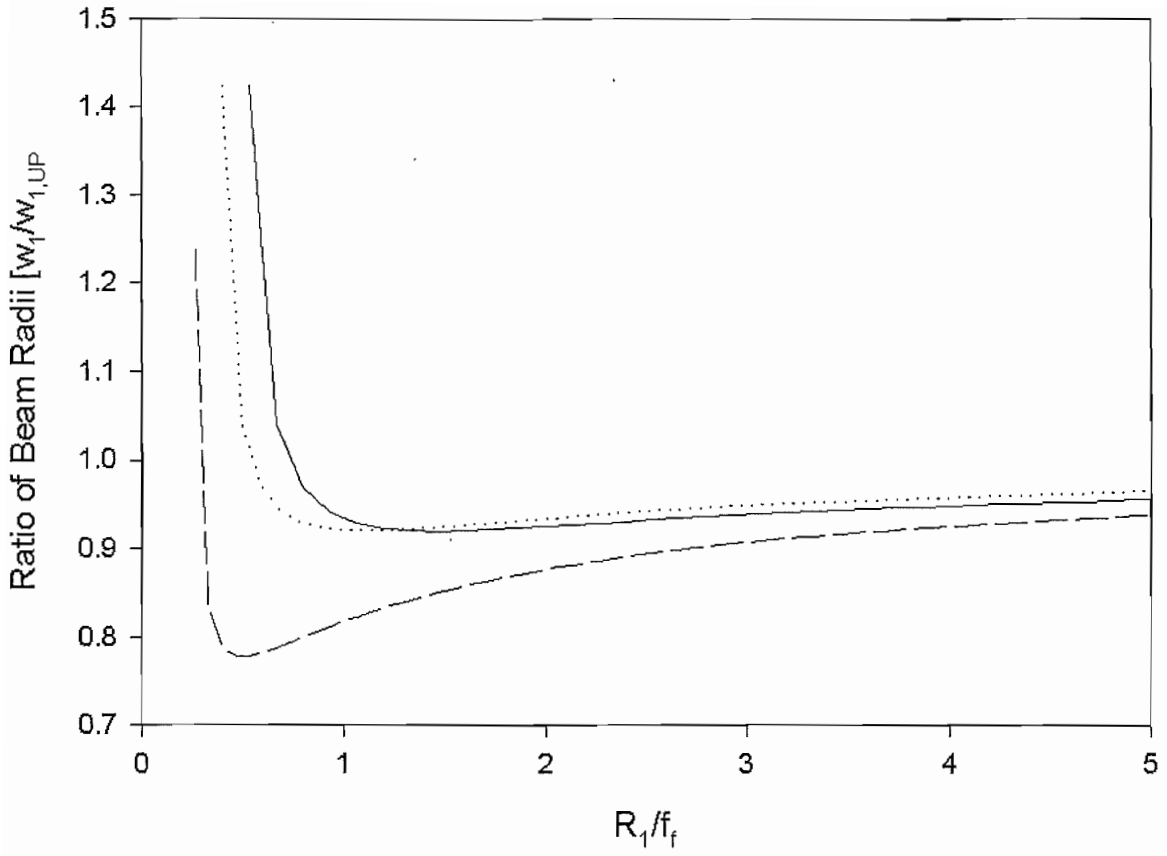

Figure (5-7) Effect of thermal lens focal length on the cavity. The solid line is for a folding mirror with a focal length of $f_f=l_c/4$, the dotted line is for a folding mirror with a focal length of $f_f=l_c/3$ and the dashed line is for a folding mirror with a focal length of $f_f=l_c/5$.

From figure (5-7) it can be seen that for all folding mirror focal lengths the beam radius in the cavity decreases with decreasing thermal lens focal length. This satisfies the requirement that the beam radius decrease in the laser cavity as the thermal lens gets stronger, minimising its impact on beam quality. At the edge of stability, the beam radius rapidly increases, satisfying the requirement that the laser mode size should increase with decreasing thermal lens focal length to suppress the lasing on the higher order modes. In figure (5-7) the solid line begins to increase first, as the thermal lens becomes stronger, so that this value of the folding mirror focal length begins to satisfy the later requirement before the other folding mirror focal lengths. It can be seen from figure (5-7), that the shorter the focal length the more able the cavity is to tolerate short thermal lens focal lengths. Although folding mirror with focal lengths longer than a quarter of the cavity length can also tolerate short thermal lens focal lengths. For larger

thermal lens focal lengths the beam radius illustrated by the solid line also varies less than the other folding mirror focal lengths. From figures (5-6) and (5-7) and the above discussion, the folding mirror that will offer the most consistant performance for different cavity length adjustments and thermal lens focal lengths is given by $f_f=l_c/4$. With the optimum length of $d_1=\frac{3}{8}l_c$ and that of $d_2=\frac{5}{8}l_c$. So for an AM mode-locked laser with a modulator operating at 50MHz, the pulse repetition rate of the laser will be 100MHz, defining a cavity length of ~1.5m. The folding mirror should therefore, have a focal length equal to 375mm, which is equivalent to a radius of curvature of 750mm. The lengths d_1 and d_2 should correspondingly be 0.56m and 0.94m respectively.

5.4.4 Transmission of Unpolarized Light through a Brewster Window

As discussed above, to minimise the risk of unwanted back reflections increasing the pulse duration Brewster cut gain media and surfaces are often used in mode-locked cavities. The laser will be end-pumped from both ends to increase the amount of available pump power in order to increase the output from the laser. Since the pump will be delivered by multimode fibre, it will emerge from the fibre essentially unpolarised. For the light entering the crystal through the plane end (coated to be AR at the pump wavelength) there will only be attenuation of the pump due to the imperfection of the dielectric coating itself. For the pump light entering the Brewster face however, there will be a certain amount of attenuation due to the polarisation dependent reflectivity of this face. Figure (5-8) shows the laser being pumped through the Brewster face. For Nd:YVO_4 with a refractive index of 2.168 at 1064nm for beams polarised along the c-axis which corresponds to a $\theta_B=\tan^{-1}(2.168)=65.2^0$ the fraction of light that is transmitted into the crystal is ~80% of the incident pump power.

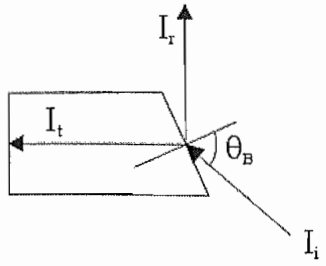

Figure (5-8). Brewster cut crystal with an un-polarized beam incident and the transmitted and reflected beams.

5.5 Master Oscillator

In this section, the layout of the master oscillator will be explained, and the results for its operation discussed.

5.5.1 Master Oscillator Layout

To reduce the effect of ETU under lasing conditions, and to enable a small spot size for the pump beam without causing severe thermal effects, therefore decreasing the value of the threshold pump power. Nd:YVO_4 with a dopant concentration of 0.1% was chosen. The crystal used was 10mm long and had a 3x3mm^2 square cross-section. One end was formed by a dielectric coating, which is HR at 1.064μm and AR coated at 810nm. Using this combination of coatings at the pump and lasing wavelengths, the crystal forms one end of the laser cavity and can be pumped through this face preventing the limiting of the gain bandwidth discussed above. The other end was cut at Brewster's angle, so that it has no reflection for p-polarized light. The consequences of the Brewster face are that there will be different beam radii within the crystal for the orthogonal directions of the laser mode. From equations (5-9) and (5-10) it can be seen that there will be an elliptical laser mode inside the laser crystal and that the beam radius in the tangential plane will be approximately twice that in the sagittal plane. To ensure a good spatial overlap within the crystal of the pump and laser beams, the pump entering the laser crystal through the coated face has to be modified so that it is elliptical in nature to. This is achieved by collimating the beam emerging from the fibre using a spherical lens and then focussing with 2 different cylindrical lenses aligned in the orthogonal directions to generate an elliptical beam. The beam entering the laser crystal through the Brewster face, does not need to be transformed in the same manner because as the pump beam enters the crystal it is transformed from an initially circular beam into an elliptical beam. The difference in pump beam radii will lead to astigmatic thermal lensing.

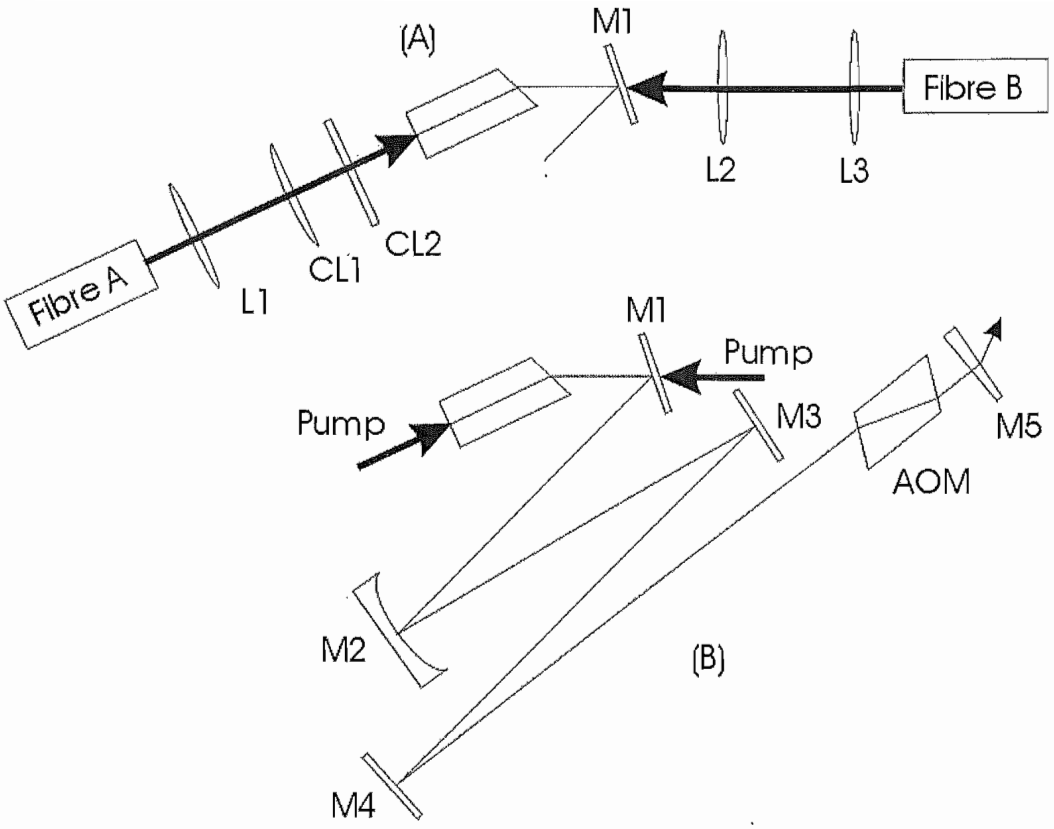

Figure (5-8). Schematic layout of the master oscillator, with an expansion of the pumping arrangement of the laser crystal.

The layout of the master oscillator is shown in figure (5-8) with laser crystal being pumped from both ends. The pump diodes used were 2 2W laser diodes that were polarisation coupled, beam shaped and then focused into a 50μm diameter fibre. The delivery fibres had a NA of 0.2 so that the beam leaving the fibre having a beam quality factor of 20. The output from fibre A is collimated by lens L1, having a focal length of 15mm, the beam is then focused in the tangential plane using les CL1 with a focal length of 150mm and is focused in the sagital plane using cylindrical lens CL2 with a focal length of 63mm. The output from fibre B is collimated using lens L3, which has a focal length of 15mm and then focussed using L2, which has a focal length of 63mm. Mirrirs M1, M3, and M4 are plane-plane mirrors and are coated to be HR at 1.064μm. Mirror M1 allows the laser crystal to be pumped from both ends and was also coated to be AR at 810nm and was thin substrate, so that it caused minimal astigmatism to the pump beam passing through it. Using this pumping arrangement fibre A produced beam waists of 105μm in the sagital plane and 250μm in the tangential plane and fibre B generated a beam radius of 105μm incident on the Brewster face. There was a maximum pump power available of 2W and 1.5W available from fibre B. Mirror M2

was curved, with a radius of curvature of 750mm. Mirror M5 is the output coupler with 95% reflectivity at 1.064μm on one face and AR at 1.064μm on the other face and was also wedged to reduce etalon effects. The distance between M3 and the mirror on the laser crystal was 440mm and the distance from M3 to M5 was 1060mm. With the radius of curvature of M3 and these lengths, the laser mode radius at the Brewster face is calculated to be 200μm and is calculated to be 500μm in the collimated arm between M3 and M5.

The acousto-optic modulator was inserted in this arm to enforce AM mode-locking is inserted. The AOM is made from fused quartz and has Brewster faces at both ends of the modulator crystal. Because of the length of this arm it is assumed that the difference in thickness for the two orthogonal directions is negligible. The AOM was specified as having a 6% modulation depth with 1W of RF power applied to it at 1.064μm. The resonance frequency of the modulator and the transducer used to generate the acoustic standing wave in the crystal is 50MHz. So that the pulse repetition rate is 100MHz, corresponding to the 1.5m cavity length. Mirror M5 was mounted on a translation stage so that the cavity length could be tuned to the exact operating frequency of the modulator. When the cavity was detuned, the temporal profile of the laser output was simply a cw signal with a slight modulation. As the cavity length was tuned to the correct cavity length, the output began to be pulsed and when the cavity length was matched the signal from the photo-diode showed saturation effects and the pulse duration was minimised. The angle of incidence on M2 for the laser mode was 6^0 obtained by solving equation (5-8) graphically using the values as discussed above for the laser crystal and the radius of curvature of M2. Mirrors M3 and M4 were used to fold the cavity, minimising its 'foot-print' on the optical table.

5.5.2 Output Power

Operation of the master oscillator under CW and mode-locked conditions is shown in figure (5-9). The black circles are the output power under CW conditions with absorbed pump power and the white circles are for the average output power under mode-locked conditions. As can be seen the slope efficiency is 30% and the laser has a threshold value of 300mW under CW conditions. Using the equation for slope efficiency given in chapter 2, implies that the cavity has a loss of 4%. Inserting this loss into the equation for threshold pump power suggests that the threshold pump power should be 180mW. The measured value is greater than this, which might be due to the fact that the pump power was varied by adjusting the current through the laser diode and at this power level the laser diode is approximately at threshold. This would serve to increase the apparent threshold pump power, because the diode might be fluorescing rather than lasing. When the laser is operating with the mode-locker running, the slope efficiency is reduced to 25% and the threshold pump power is increased to 400mW. This is attributable to the mode-locker acting as an amplitude modulator, so there is some loss as beams are diffracted out of the cavity, however the increase in loss ~2% is neither the same as the predicted modulation depth nor sufficient to account for the increase in threshold power.. Whilst running under CW conditions it was found that the output from the laser was diffraction limited with an $M^2<1.1$ in both planes. The beam radii at the output were measured and it was found that the beams had the same radius in the two planes. The beam quality of the laser was monitored over the range of available pump power finding that it remained diffraction limited and that there was no significant change in the laser beam radii. With the modulator on, there was no real measured change to the output of the cavity, other than the slight drop in output power.

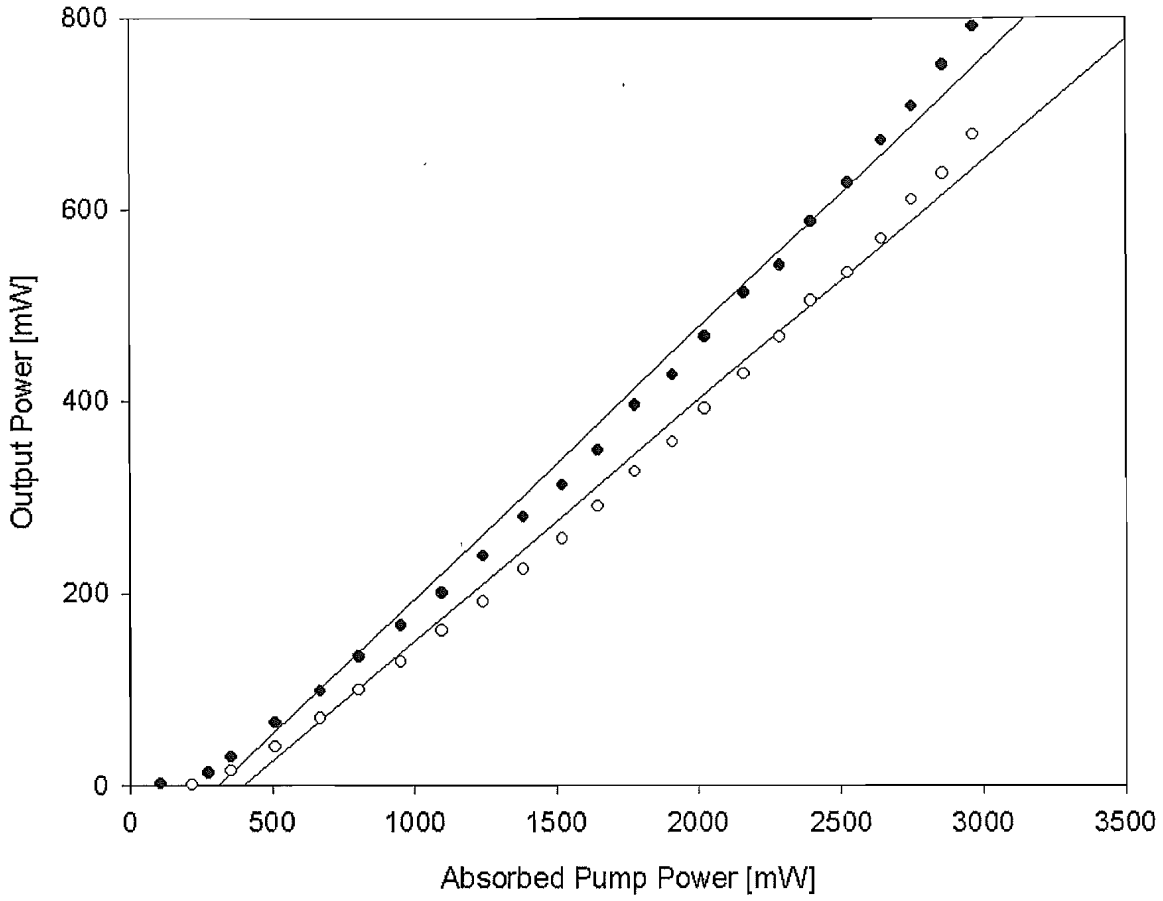

Figure (5-9). Output power of Laser under CW (black circles) and average power under mode-locked conditions (white circles).

5.5.3 Pulsed Output

The output from the laser was monitored using a fast photo-diode to monitor the formation of pulses. With the a RF signal applied to the modulator pulses were seen to form as shown in figure (5-9). From the figure (5-9) it can be seen that the laser is pulsing at a repetition rate of 100MHz which corresponds to a frequency twice that of the applied RF signal to the modulator. The response time of the photodiode is not sufficient to determine the pulse duration directly. This was achieved by coupling the output of the laser into a single mode fibre and inserting the output of the fibre into an optical to electrical converter, and using a sampling oscilloscope to determine the pulse duration. In this way, the pulse durations were found to be 100ps. Good agreement is obtained by putting the values outlined above into equation (5-2) of the pulse duration expected from theory, which for Nd:YVO_4 with a 50MHz modulator, 5% output

coupling, 6% modulation depth a gain bandwidth of 212GHz, it would be predicted that ~120ps pulses should be achievable using Bragg modulation.

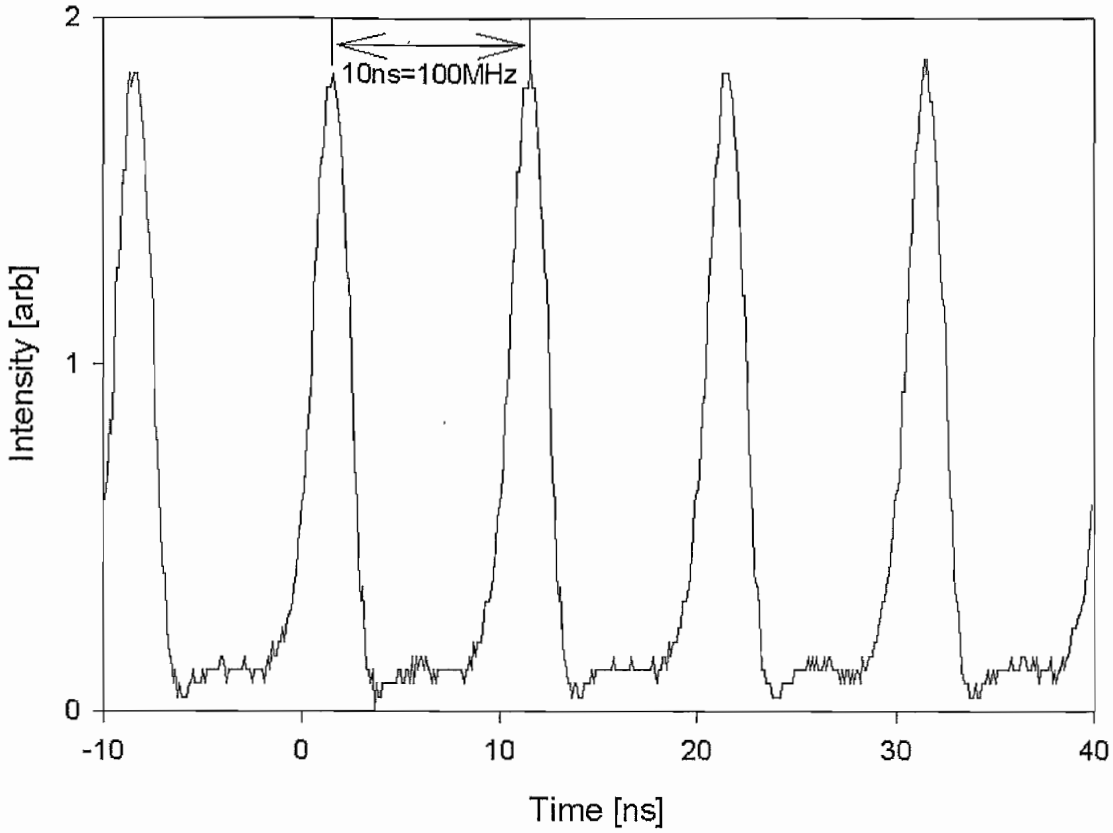

Figure (5-9). Pulses from the laser under mode-locked conditions.

5.6 Pulse Picker

The output of the laser was focused into an acousto-optic beam deflector as shown in figure (5-11) so that a smaller train of pulses could be selected. The laser passes through lens L1, which has a focal length of 125mm generating a beam waist of 90μm in the acousto-optic deflector. The beam is then co-incident on an aperture, such that when the acousto-optic deflector is on and an acoustic wave is being generated the laser is diffracted into the first order beam and passes through the aperture without attenuation. Using this system, up to 80% of the incident laser light on the deflector was made to pass through the aperture.

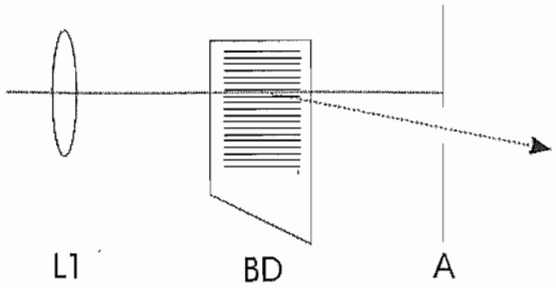

Figure (5-10). Schematic of the 'pulse picker' the undeflected path is shown by the solid line and the deflected beam is shown by the dotted line

Using the pulse picker, pulse trains as short as 50 ns could be achieved as shown in figure (5-11), where it can easily been seen that there are several pulses within the envelope of the beam deflector. It can also be see that when operating at such short pulse durations the beam deflector does not have a rectangular response to the applied signal.

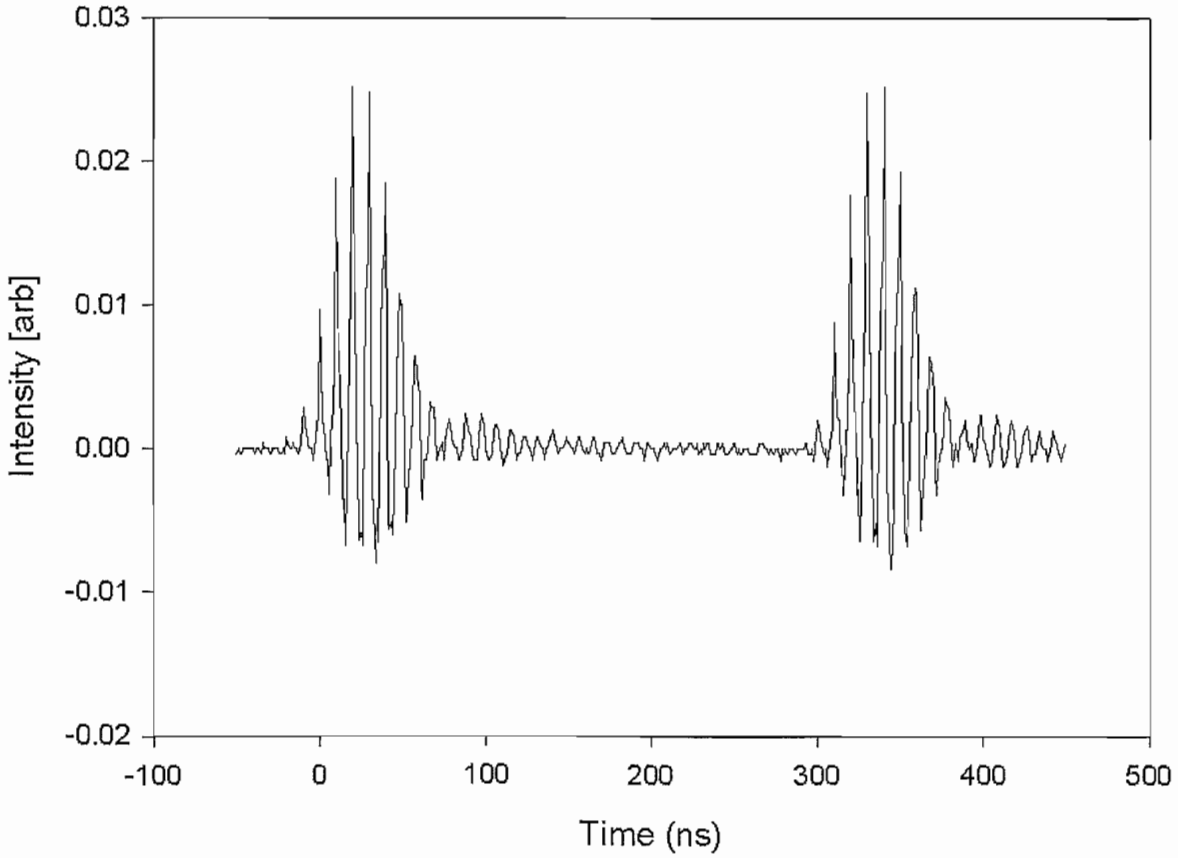

Figure (5-11). 50ns pulse trains generated using the laser under mode-locked conditions.

5.7 Further Improvements

Further improvements to the master oscillator lie in two main areas, decreasing the pulse duration and increasing the average power. Equation (5-1) shows that the pulse duration is inversely proportional to the square root of the modulation frequency and the gain bandwidth. Therefore increasing either of these will lead to a decrease in the pulse duration. An increase in the modulation frequency might be achieved by driving the current AOM at a harmonic, say 100MHz, and in this way reduce the pulse duration. However, the modulation depth is likely to decrease as the crystal and the electronics used to drive the transducer in the AOM are designed to operate at 50MHz. This may not be so much of a problem, since the modulation depth has a weaker influence on the pulse duration, and the formation of the pulse occurs after several roundtrips of the laser cavity. Another method would be to increase the gain bandwidth available to generate pulses, this might be achieved by replacing the Nd:YVO_4 gain medium for a Nd:glass. However, care would be needed to ensure that the emission wavelength of the glass, matched that of Nd:YVO_4 because even small deviations away from the centre wavelength of the gain profile will significantly reduce the gain experienced in the amplifiers. An alternative method to decrease the pulse duration might be to combine passive and active mode-locking in the same cavity. This might be achieved by inserting a Kerr-lens medium in the cavity, so that the pulses are initiated by the AOM, creating a set of pulses with a stable repetition rate and by a robust method. The Kerr-lens media combined with either hard of soft aperturing could then be used to decrease the pulse duration further, maximising the use of the full bandwidth of Nd:YVO_4. Insertion of the Kerr media, combined with the use of soft aperturing will have the interesting effect of reducing the size of the laser mode in the laser crystal with increased thermal lensing, because there will be an increase in the intra-cavity power increasing the Kerr effect. The output power of the laser could be increased by increasing the amount of pump power available. This could be achieved by using higher power diode sources. Care is required however, because the laser mode in the cavity is currently larger than the pump beam waist, this ensures that there is no lasing on higher order modes, but at larger pump powers the beam degradation due to the aberrated nature of the thermal lens might negate this. As shown by figure (5-6) the cavity is dynamically stable over a wide range of thermal lens focal lengths, however, it

must be ensured that the increased power doesn't change the laser mode sizes significantly when increasing the pump power.

5.8 References

1. Damzen, M.J., et al., *Continuous-wave Nd:YVO_4 grazing-incidence laser with 22.5W output power and 64% conversion efficiency.* Optics Communications, 2001. **196**: p. 237-241.
2. Graf, T., et al., *Multi-Watt Nd:YVO_4 laser, mode locked by a semiconductor saturable absorber mirror and side-pumped by a diode-laser.* Optics Communications, 1999. **159**(1-3): p. 84-87.
3. Zhan, J., et al., *Efficient TEM_{00} operation of Nd:YVO_4 laser end pumped by fibre-coupled diode laser.* Electon. Lett., 1997. **33**: p. 775-777.
4. O'Connor, J.R., *Unusual crystal-field energy levels and efficient laser properties of YVO_4:Nd.* Applied Physics Letters, 1966. **9**: p. 407-409.
5. Baglio, J.A. and G. Gashurov, *A refinement of the crystal structure of yttrium vanadate.* Acta Cryst, 1968. **B24**: p. 292-293.
6. Tucker, A.W., M. Birnbaum, and C.L. Fincher, *Stimulated emission cross sections of Nd:YVO_4 and Nd:$La_2Be_2O_5$ (BeL).* Journal of Applied Physics, 1981. **52**(4): p. 3067-3068.
7. Clarkson, W.A. and D.C. Hanna, *Optical Resonators-Science and Engineering*, ed. R. Kossowsky. 1998: Kluwer Academic Publishers.
8. Siegman, A.E., *Lasers*. 1986, Sausalito, California: University Science Books.
9. New, G.H.C., *The generation of ultrashort laser pulses.* Reports on progress in physics, 1983. **46**: p. 877-971.
10. Koechner, W., *Solid-State Laser Engineering*. 5 ed. Springer Series in Optical Sciences, ed. A.L. Schawlow, A.E. Siegman, and T. Tamir. Vol. 1. 1999, Berlin: Springer.
11. Siegman, A.E. and D.J. Kuizenga, *Active mode-coupling phenomena in pulsed and continuous lasers.* Opto-electronics, 1974. **6**: p. 43-66.
12. Dallas, J.L., *Frequency-modulation mode-locking performance for four Nd^{3+}-doped laser crystals.* Applied Optics, 1994. **33**(27): p. 6373-6376.

13. Basu, S. and R.L. Byer, *Continuous-wave mode-locked Nd:glass laser pumped by a laser diode.* Optics Letters, 1988. **13**(6): p. 458-460.
14. Hughes, D.W., et al., *A laser-Diode-Pumped Nd:Glass Laser:Mode-Locked, High Power, and Single Frequency Performance.* IEEE Journal of Quantum Electronics, 1992. **QE-28**(4): p. 1010-1017.
15. Maker, G.T., S.J. Keen, and A.I. Ferguson, *Mode-locked and Q-switched operation of a didoe laser pumped Nd:YAG laser operating at 1.064μm.* Applied Physics Letters, 1988. **53**(18): p. 1675-1677.
16. Braun, B., et al., *Continuous-wave mode-locked solid-state lasers with enhanced spatial hole-burning 1:Experiments.* Applied Physics B-Lasers and Optics, 1995. **61**(5): p. 429-437.
17. Maker, G.T. and A.I. Ferguson, *Frequency-modulation mode locking of a diode-pumped Nd:YAG laser.* Optics Letters, 1989. **14**(15): p. 788-790.
18. Adams, C.S., G.T. Maker, and A.I. Ferguson, *FM Operation of Nd:YAG Lasers With Standing Wave and Ring Cavity Configuration.* Optics Communications, 1990. **76**(2): p. 127-131.
19. Hanna, D.C., *Astigmatic Gaussian Beams Produced by Axially Asymmetric Laser Cavities.* IEEE Journal of Quantum Electronics, 1969. **QE-5**(10): p. 483-488.
20. Kogelnik, H.W., et al., *Astigmatically Compensated Cavities for CW Dye Lasers.* IEEE Journal of Quantum Electronics, 1972. **QE-8**(3): p. 373-379.
21. Jenkins, F.A. and H.E. White, *Fundamentals of Optics*. 1976: McGraw-Hill Book Company.
22. Kogelnik, H.W., *Imaging of Optical Modes-Resonators with Internal Lenses.* Bell System Technical Journal, 1965. **44**: p. 455-494.
23. Kogelnik, H.W. and T. Li, *Laser Beams and Resonators.* Applied Optics, 1966. **5**(10): p. 1550-1567.
24. Sasnett, M.W., *The Physics and Technology of Laser Resonators*, ed. D.R. Hall and P.E. Jackson. 1989, Bristol and New York: Adam Hilger.
25. Gerrard, A. and J.M. Burch, *Introduction to Matrix Methods in Optics*. Wiley Series in Pure and Applied Optics. 1975, London: Wiley.
26. Brosseau, C., *Fundamentals of polarized light.* 1998, New York: John Wiley & Sons.

Chapter 6: Nd:YVO_4 Amplifier Scheme

6.1 Introduction

The role of the amplifier section of a master oscillator power amplifier, MOPA, is to increase the power and brightness of the output from the master oscillator. This brings two different conflicting problems into contention that of increasing power and avoiding degradation in beam quality. To increase the brightness of a diffraction-limited beam the power of the beam needs to be increased. However, heat generation in the amplifying laser material results in thermally-induced phase aberrations that can degrade beam quality and hence brightness even though the power is increased. Because they do not need to be dynamically stable over a range of thermal lens focal lengths, the effect of thermal lensing is more easily tolerated in amplifiers than in oscillators. For efficient extraction of the available power from an amplifier, it must be operated in the saturated regime and herein lies the main challenge with power-scaling via a MOPA approach because it is difficult to saturate single-pass amplifiers based on 'bulk' laser crystals. Multi-pass amplifier schemes help to alleviate this problem by allowing the intensity of the signal beam to become sufficiently high to saturate the amplifier improving the extraction efficiency. Increasing the number of passes in an amplifier, exacerbates the problems caused by thermal lensing though with the result that the effective focal length is much reduced and phase aberrations are increased, parasitic lasing is also more difficult to avoid. Unless this is taken into consideration, not only could this lead to greater aberrations but the thermal lensing can reduce the overlap of the signal and pump beams in the amplifier reducing gain and extraction efficiency. This is because the thermal lenses act to displace the signal beam waists from the desired image planes of the amplifier altering the designed signal beam radii in the amplifier crystals.

In this chapter, a novel power-scalable multi-pass diode-end-pumped amplifier design based on Nd:YVO_4 and its performance is described. This chapter begins with a brief introduction deriving the single-pass gain for a simple end-pumped amplifier. The effect of energy transfer upconversion and pump beam quality on gain will then be examined. The analysis will then be extended to multiple crystal amplifiers. The influence of thermal lensing on the amplifier performance will also be discussed with a view to formulating a

strategy for the design of more complex multi-pass amplifiers. The results for a single pass amplifier, based on Nd:YVO_4 are presented. The analysis is finally extended to include multi-pass amplification. The results for a multi-pass Nd:YVO_4 amplifier are presented for both CW and pulsed operation. Finally, the prospects for further power and brightness power-scaling based on this approach will be discussed.

6.2 Single Pass End-pumped Amplifiers

The following discussion is restricted to end-pumped 'bulk' amplifiers based on four-level schemes as shown in figure (6-1). In figure (6-1) level 0 is the ground level, level 1 is the lower lasing level, level 2 is the upper lasing level and level 3 is the pumping level. The solid arrows represent radiative transitions, the dotted arrows are non-radiative transitions and the dashed arrows represent signal beam photons in figure (6-1). Ions initially in the ground level are excited to the pumping level after having absorbed a pump photon. The ions then non-radiatively decay from the pumping level to the upper laser level. The non-radiative decay from the pumping level to the upper laser level is assumed fast so that there is a negligible population in this level. As the signal beam passes through the amplifier medium with an excited population, the photons making up the signal beam cause stimulated emission to occur, which amplifies the signal beam. If the intensity of the signal beam is high then it might depletes the population of the upper laser level leading to saturation of the amplifier. Having emitted some of their energy, those ions that have contributed to the amplification process end up in the lower laser level, from which they decay via non-radiative emission. Again, it is assumed that the rate of non-radiative decay from the lower laser level to the ground level is fast so that there is a negligible population in the lower laser level. In this way only the population dynamics of the upper laser level need to be considered when calculating the gain of four-level amplifying media.

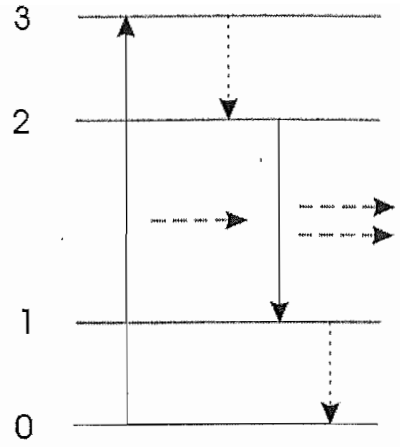

Figure (6-1). Simplified four-level energy diagram for amplification. The solid arrows represent radiative transitions, the dotted arrows are non-radiative transitions and the dashed arrows represent signal beam photons.

Figure (6-2) is a single gain medium with a signal and pump beam passing through it. The dashed line in figure (6-2) is the signal beam with a radius w_s, the dotted line is the pump beam with a radius of w_p and diffraction effects have been neglected (i.e. both radii are considered to remain constant in the amplifier medium). The incident signal intensity at $z=0$ is I_{in} and the amplified signal intensity at $z=l_c$ is I_{out}, where l_c is the length of the amplifier crystal.

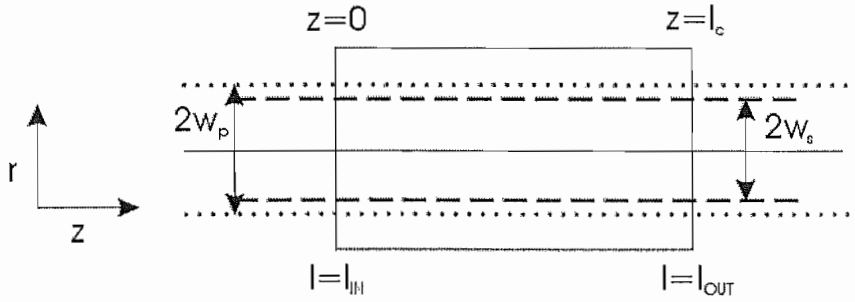

Figure (6-2). A signal beam passing through a single crystal amplifier. The dotted line is the pump beam with a radius w_p, and the dashed line is for the signal beam with a radius w_s.

The gain per unit length experienced by a beam with a frequency at the gain peak with emission cross-section σ, is given by

$$g_0(r,z) = \sigma n(r,z) \tag{6-1}$$

where $g_0(r,z)$ is the gain per unit length at a position z for a ray distance r from the axis, σ is the stimulated emission cross-section and $n(r,z)$ is the population inversion density in the amplifier crystal. Neglecting ETU, the population inversion density under steady-state conditions neglecting saturation (i.e. for small signal gain) is given by

$$n(r,z) = R_p(r,z)\tau \tag{6-2}$$

where τ is the fluorescence lifetime and $R_p(r,z)$ is the pumping rate density of ions into the upper lasing level. For an end-pump amplifier with a Gaussian transverse pump profile the pumping rate is given by

$$R_p(r,z) = \frac{2\alpha_p P_p}{h\nu_p \pi w_p^2} \exp\left(\frac{-2r^2}{w_p^2} - \alpha_p z\right) \tag{6-3}$$

where α_p is the absorption coefficient, P_p is the incident pump power, ν_p is the pump frequency and w_p is the pump beam radius. Integrating over the signal beam area, the effective gain per unit length at position z can be written [1]

$$g_{eff}(z) = \frac{\int g_0(r,z) I_s(r,z) 2\pi r dr}{\int I_s(r,z) 2\pi r dr} \tag{6-4}$$

where $I_s(r,z)$ is signal beam intensity at r,z. The integration over the signal and pump beams are required, because the gain is not constant across the signal beam. This is due to the gain coefficient having a radial variation and the signal beam having a higher intensity at the centre leading to greater saturation effects than at the wings of the signal beam. Equation (6-4) leads to some average value for the radial variation of the gain coefficient, with the consequence that signal powers need to be considered rather then signal intensities, and this will be used throughout the following analysis. A more compete discussion of the effects of the radially varying gain and signal beam is given later. As the signal beam passes through the amplifier medium the signal intensity changes according to [2]

$$\frac{dP(z)}{dz} = \frac{g_{eff}(z)P(z)}{1 + P(z)/P_{sat}} \tag{6-5}$$

where P_{sat} is the saturation intensity of the laser medium given by

$$P_{sat} = \frac{h\nu_s \pi w_s^2}{\sigma_e \tau} \tag{6-6}$$

where ν_s is the frequency of the signal being amplified. At the saturation intensity, the intensity is sufficient to cause significant depletion of the population inversion. Under end-pumped conditions the pump power is absorbed as it passes through the amplifier medium so there is a variation in the gain coefficient with distance. By re-arranging equation (6-5) and integrating over the boundary conditions specified above leads to

$$\int_{P=P_{in}}^{P=P_{out}} \left[\frac{1}{P(z)} + \frac{1}{P_{sat}}\right] dP(z) = \int_{z=0}^{z=l_c} g_{eff}(z) dz \tag{6-7}$$

where P_{in} is the incident intensity at the point z=0, P_{out} is the output intensity at the point z=l_c, and l_c is the length of the amplifier crystal. Inserting equation (6-3) into equation (6-4) and solving equation (6-7) gives

$$\ln\left[\frac{P_{out}}{P_{in}}\right] + \frac{1}{P_{sat}}(P_{out} - P_{in}) = \ln(G_0) = \frac{2\sigma\tau P_p}{h\nu_p \pi w_p^2 \left(1 + \frac{w_s^2}{w_p^2}\right)}\left[1 - \exp(-\alpha_p l_c)\right] \tag{6-8}$$

where $\ln(G_0)$ is the unsaturated small-signal gain of the amplifier crystal. When the gain is constant throughout the amplifier crystal the small signal gain increases with crystal length, however, for end-pumped amplification only the absorption efficiency of the pump increases with crystal length having a smaller impact on the small signal gain. The saturated gain is then given by rewriting equation (6-8) giving

$$G = \frac{P_{out}}{P_{in}} = G_0 \exp\left[-\frac{P_{out} - P_{in}}{P_{sat}}\right] \tag{6-9}$$

The extracted power, which is the power increase of the signal beam due to the amplifier is given by

$$P_{extr} = P_{out} - P_{in} = \ln\left(\frac{G_0}{G}\right) P_{sat} \tag{6-10}$$

This equation shows that as the amplifier begins to saturate ($G \rightarrow 1$), the extracted power approaches a limiting value, which is the maximum power available to be extracted from the amplifier. The maximum available power from the amplifier is given by [2]

$$I_{avail} = \ln(G_0) I_{sat} \tag{6-11}$$

The extraction efficiency for a single-pass amplifier is given by [2]

$$\eta_{extr} = \frac{P_{extr}}{P_{avail}} = \frac{\ln(G_0) - \ln(G)}{\ln(G_0)} = 1 - \frac{\ln(G)}{\ln(G_0)} \tag{6-12}$$

Equation (6-14) demonstrates that in order to extract a substantial amount of the power available, a sacrifice has to be made in the amount of power gain. Herein lies the principle defect of a MOPA design; to drive a single-pass amplifier hard enough to extract most of the energy stored in the amplifier medium is difficult. One way around this problem is to use multi-pass amplification.

To complete this section a more detailed discussion of the radial effects of the gain and signal beam intensity will now be made. Siegman [2], analysed the situation for pump and signal intensities with Gaussian profiles. If diffraction effects are negligible, that the signal beam is collimated and that the amplifier is either short enough or heavily saturated then it can be assumed that the signal beam remains Gausssian at every plane z through the amplifier. Equation (6-15) should strictly be written for the local intensity changes according to

$$\frac{\partial I(r,z)}{\partial z} = \frac{g_0(r) I(r,z)}{1 + I(r,z)/I_{sat}} \tag{6-13}$$

The equivalent equation to (6-8) is now given by

$$\ln\left[\frac{I_{out}(r)}{I_{in}(r)}\right] + \frac{1}{I_{sat}}\left(I_{out}(r) - I_{in}(r)\right) = \ln\left(G_0(r)\right) \tag{6-14}$$

Given an input beam profile $I_{in}(r)$ equation (6-14) must be solved to find $I_{out}(r)$, this is generally achieved numerically, and then integrated to find the input and output powers P_{in} and P_{out}. Because it has been assumed that the signal beam essentially remains Gaussian through the amplifier equation (6-14) can be integrated over the amplifier cross section to give the result

$$\frac{dP(z)}{dz} = \int_0^\infty \frac{\partial I(r,z)}{\partial r} 2\pi r dr = \int_0^\infty \left(\frac{g_0(r) I(r,z)}{1 + I(r,z)/I_{sat}} \right) 2\pi r dr \tag{6-15}$$

For a constant gain profile the solution of (6-15) suggests that in the weak-saturation limit the effective area of a Gaussian beam for power extraction is not $\pi w^2/2$ but $A_{eff} \sim \pi w^2$ [2]. In physical terms, the outer wings of the Gaussian beam are at low intensity, and thus do not saturate the laser medium. The Gaussian beam therefore acts as if its area were larger than might be expected. Because of this the pump beams will be restricted to a top-hat

profile, so that it can be assumed that the gain is uniform across the signal beam. This is possible for diode-end-pumped amplifiers, because the output from large multi-mode fibres is somewhere between a top-hat and a Gaussian profile.

6.3 Effect of ETU on end-pumped amplification

Having discussed the gain that would be expected without ETU and ignoring thermal lensing effects. The previous analysis will now be extended for the first time to include these effects. I will begin by deriving the small-signal gain with ETU present in this section and then examine the effect of thermal lensing of the beam being amplified on passing through the amplifier in the next one. As shown in chapter 3, the population inversion density is modified by energy transfer upconversion, hence reducing the potential gain available. Under non-lasing conditions the inversion density in the presence of ETU becomes

$$n(r,z)=\frac{-1+\sqrt{1+4R_p(r,z)W\tau^2}}{2W\tau} \tag{6-16}$$

where W is the upconversion parameter. For a pump beam with a top-hat transverse profile the pumping rate is given by

$$R_p(r,z)=\frac{\alpha_p P_p}{h\nu_p \pi w_p^2}\exp(-\alpha_p z) \quad \text{for } r\leq w_p \text{ and } R_p(r,z)=0 \text{ for } r>w_p \tag{6-17}$$

The gain for a top-hat pump profile including ETU can be found by inserting equations (6-16) and (6-17) into equation (6-1) leading to

$$g_{0,UP}(r,z)=\frac{\sigma}{2W\tau}\left(-1+\sqrt{1+\frac{4\alpha_p P_p W\tau^2}{h\nu_p \pi w_p^2}\exp(-\alpha_p z)}\right) \tag{6-18}$$

The effective gain coefficient is determined by inserting equation (6-18) into equation (6-4) and assuming a Gaussian profile for the signal beam results in

$$g_{eff,UP}(z)=\frac{\sigma}{2W\tau}\left(-1+\sqrt{1+\frac{4\alpha_p P_p W\tau^2}{h\nu_p \pi w_p^2}\exp(-\alpha_p z)}\right)\left(1-\exp\left(\frac{-2w_p^2}{w_s^2}\right)\right) \tag{6-19}$$

The unsaturated small-signal gains is by integrating equation (6-19) over the crystal length yielding

$$\ln\left(G_{0,UP}\right)=\frac{\sigma}{2W\tau}\left(1-\exp\left(\frac{-2w_p^2}{w_s^2}\right)\right)\left(-\int_0^{lc}dz+\int_0^{lc}\sqrt{1+\frac{4\alpha_p P_p W\tau^2}{h\nu_p\pi w_p^2}\exp\left(-\alpha_p z\right)}dz\right) \quad (6\text{-}20)$$

The second integral of (6-20) can be evaluated by making the substitution

$$V^2=\frac{4\alpha_p P_p W\tau^2}{h\nu_p\pi w_p^2}\exp\left(-\alpha_p z\right) \quad (6\text{-}21)$$

$$\ln\left(G_{0up}\right)=\frac{\sigma}{2W\tau}\left(1-\exp\left(\frac{-2w_p^2}{w_s^2}\right)\right)\left(-l_c+\frac{2}{\alpha_p}\int_{\sqrt{\frac{4\alpha_p P_p W\tau^2}{h\nu_p\pi w_p^2}\exp\left(-\alpha_p l_c\right)}}^{\sqrt{\frac{4\alpha_p P_p W\tau^2}{h\nu_p\pi w_p^2}}}\frac{\sqrt{1+V^2}}{V}dV\right) \quad (6\text{-}22)$$

Equation (6-22) can be solved using the following identity [3]

$$\int\frac{\sqrt{x^2+a^2}}{x}dx=\sqrt{x^2+a^2}-a\ln\left(\frac{a+\sqrt{x^2+a^2}}{x}\right)+C \quad (6\text{-}23)$$

The small signal gain with ETU for a single pass of an amplifier crystal is given by

$$\ln\left(G_{0up}\right)=\frac{\sigma}{W\tau\alpha_p}\left(1-\exp\left(\frac{-2w_p^2}{w_s^2}\right)\right)\left[\sqrt{1+\frac{4\alpha_p P_p W\tau^2}{h\nu_p\pi w_p^2}}-\sqrt{1+\frac{4\alpha_p P_p W\tau^2}{h\nu_p\pi w_p^2}\exp\left(-\alpha_p l_c\right)}+\ln\left(\frac{1+\sqrt{1+\frac{4\alpha_p P_p W\tau^2}{h\nu_p\pi w_p^2}\exp\left(-\alpha_p l_c\right)}}{1+\sqrt{1+\frac{4\alpha_p P_p W\tau^2}{h\nu_p\pi w_p^2}}}\right)\right] \quad (6\text{-}24)$$

If all of the pump power is absorbed then equation (6-24) can be simplified to

$$\ln\left(G_{0up}\right)=\frac{\sigma}{W\tau\alpha_p}\left(1-\exp\left(\frac{-2w_p^2}{w_s^2}\right)\right)\left[\sqrt{1+\frac{4\alpha_p P_p W\tau^2}{h\nu_p\pi w_p^2}}-1+\ln\left(\frac{2}{1+\sqrt{1+\frac{4\alpha_p P_p W\tau^2}{h\nu_p\pi w_p^2}}}\right)\right] \quad (6\text{-}25)$$

The size of the two terms in the square brackets of equation (6-25) is shown in figure (6-3). In figure (6-3), the solid line is $\sqrt{1+x}-1$ and the dotted line is for $\ln\left(\frac{2}{1+\sqrt{1+x}}\right)$. As can be seen for small values of x both terms have a similar magnitude, but as the power is

increased the square root term is much larger than the logarithm term. So for large pump powers with equal beam radii the small signal gain with ETU can be approximated by

$$\ln\left(G_{0up}\right)\approx\frac{\sigma}{W\tau\alpha_p}\left[\sqrt{1+\frac{4\alpha_p P_p W\tau^2}{h\nu_p\pi w_p^2}}-1\right]\approx 2\sigma\sqrt{\frac{P_P}{h\nu_P\pi w_P^2 W\alpha_P}} \tag{6-28}$$

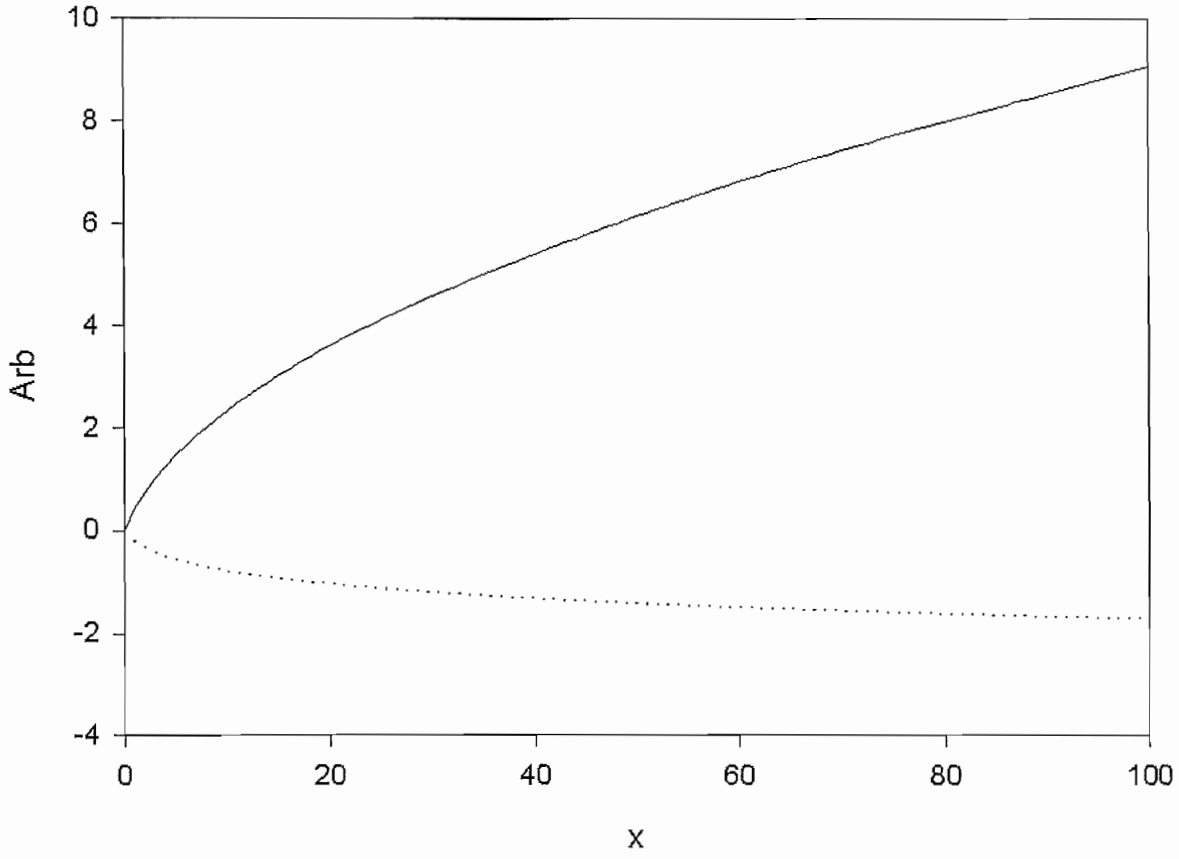

Figure (6-3). Comparison of $\sqrt{1+x}-1$ and $\ln\left(\frac{2}{1+\sqrt{1+x}}\right)$. The solid line is $\sqrt{1+x}-1$ and the dotted line is for $\ln\left(\frac{2}{1+\sqrt{1+x}}\right)$.

The effective gain without upconversion for a pump beam with a top-hat pump profile is given by inserting (6-17) into equations (6-1), (6-2) and (6-4) yielding

$$g_{eff}\left(z\right)=\frac{\sigma\tau\alpha_p P_p}{h\nu_p\pi w_p^2}\exp\left(-\alpha_p z\right)\left(1-\exp\left(\frac{-2w_p^2}{w_s^2}\right)\right) \tag{6-27}$$

Integrating equation (6-27) over the crystal length gives

$$\ln\left(G_{0,th}\right)=\frac{\sigma\tau P_p}{h\nu_p\pi w_p^2}\left(1-\exp\left(-\alpha_p l_c\right)\right)\left(1-\exp\left(\frac{-2w_p^2}{w_s^2}\right)\right) \tag{6-28}$$

Equation (6-28) can be obtained from equation (6-25) when $W\rightarrow 0$.

Figure (6-4) shows the effect of ETU on the small-signal gain as a function of the absorbed pump power. In figure (6-3), the solid line is calculated neglecting ETU and the dotted lines includes ETU and it has been assumed that the signal and pump beam radii are equal. The pump beam radius in the amplifier used to plot figure (6-4) was chosen to be

$$w_p^2 = \frac{P_{P,ETU}\alpha_P W\tau^2}{h\nu_P \pi} \tag{6-29}$$

As can be seen from figure (6-4), the gain increases as the pump power is increased. However, the effects of ETU reduce the small-signal gain. When $P_P=P_{P,ETU}$, the small-signal gain has already been reduced by 25%. The value of $P_{P,ETU}$ is inversely proportional to the product of the ETU parameter , the absorption coefficient and the square of the fluorescence lifetime. Therefore, those materials for which this product is large will suffer more strongly from the effects of ETU.

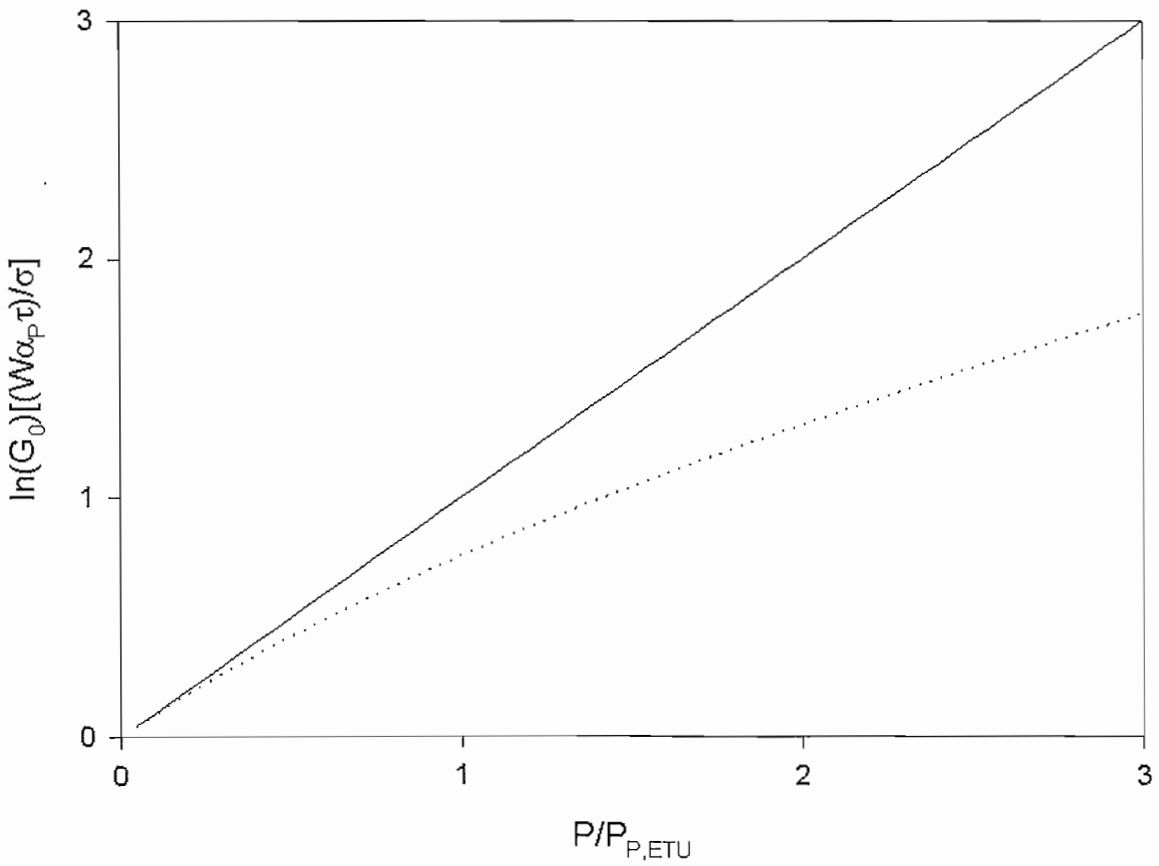

Figure (6-4). Effect of ETU on small signal gain with pump power. The solid line neglects pump power and the dotted line includes ETU.

Figure (6-5) shows the variation of the small signal gain with pump beam radius. In figure (6-5), the solid line is for the small-signal gain neglecting ETU and the dotted line is for the small-signal gain including ETU. The pump power used in figure (6-5) is given by

$$P_P = \frac{h\nu_p \pi w_{P,ETU}^2}{\alpha_p W \tau^2} \tag{6-30}$$

From figure (6-5), it can be seen that for pump beam radii above those given by equation (6-30) there is not much difference between the small-signal gains with and without ETU. However, as the pump radius is reduced below this the effect of ETU becomes rapidly pronounced. It can be seen from figure (6-3) that the increase in gain achieved by decreasing the pump beam radius is always greater than the increase in the losses caused by ETU.

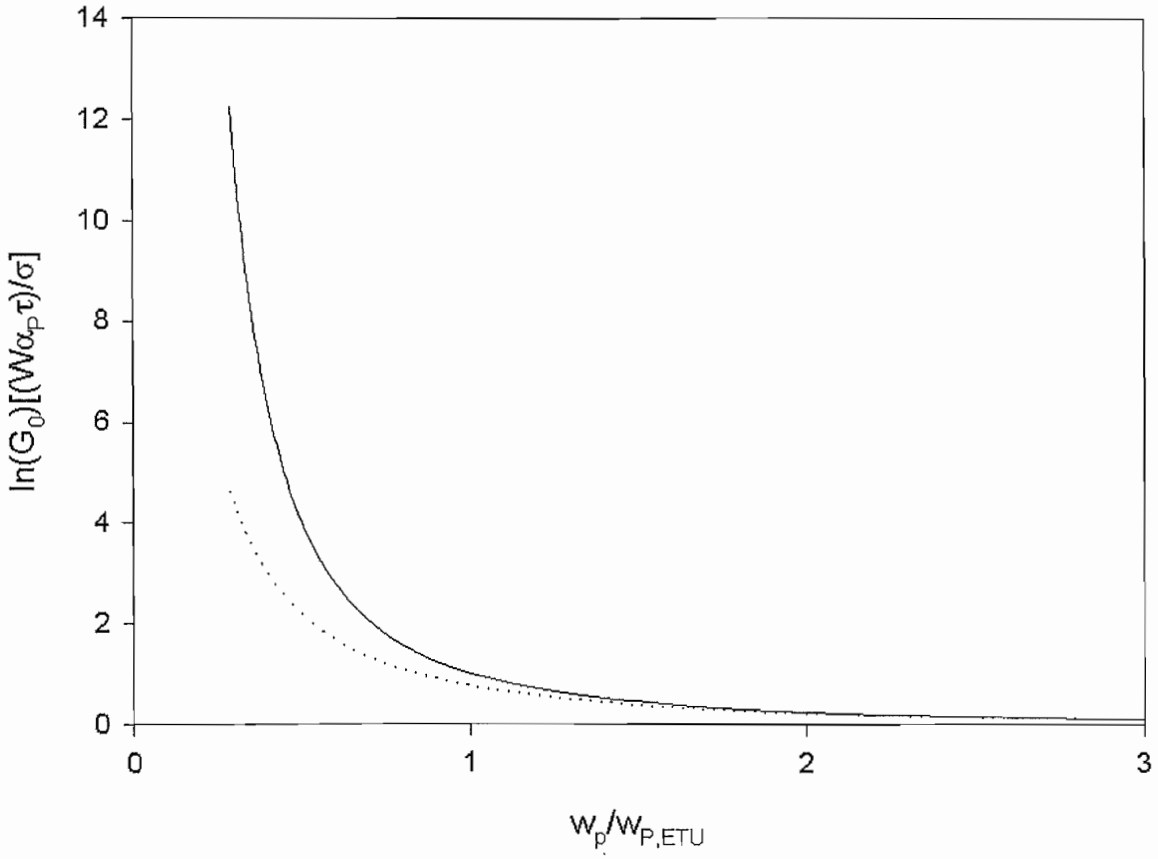

Figure (6-5). Effect of ETU on amplifier gain as the pump beam radius varies. The solid line is with ETU neglected and the dotted line includes ETU.

6.4 Effect of Pump Beam Quality on Gain

Figures (6-4) and (6-5) show that there is no limit placed on the power-scaling of amplifiers due to the impact of ETU on small-signal gain. The absorbed pump power can be increased or a smaller beam radius used and there will still be an improvement in the small-signal gain. However as discussed in the next section, the beam quality of the pump source, places a limit on the smallest average pump beam radius in the amplifier and therefore on small-signal gain.

By minimising the pump volume the gain of the amplifier will be maximised. When the beam waist of the pump beam occurs at the centre of the amplifier medium, the smallest beam waist in the laser crystal can be achieved. However, the pump beam quality will influence the size of this smallest pump volume because it limits the smallest beam radius achievable and increase the rate of the pump beam expansion in the crystal. The smallest beam size not necessarily giving the smallest pump volume. The propagation of the pump beam as it travels through the laser crystal is given by

$$w_P(z) = w_{P,0}\left[1+\left(\frac{(z-l_c/2)}{z_R}\right)^2\right]^{1/2} \tag{6-31}$$

where $w_{P,0}$ is the radius of the pump beam waist and is positioned at the centre of the amplifier crystal z_R is the Rayleigh range given by

$$z_R = \frac{w_{P,0}^2 \pi n}{M^2 \lambda_p} \tag{6-32}$$

where n is the refractive index of the amplifier crystal at the pump wavelength and M^2 is the beam quality factor of the pump. The pump volume is then given by

$$V_p = \int_0^{l_c} \pi w_P^2(z)dz \tag{6-33}$$

The average pump beam radius in the crystal can then be determined from

$$w_{p,av} = \sqrt{\frac{V_p}{\pi l_c}} = w_{P,0}\sqrt{1+\frac{1}{12}\left(\frac{l_c}{z_R}\right)^2} = w_{P,0}\sqrt{1+\frac{1}{12}\left(\frac{l_c M^2 \lambda_p}{\pi w_0^2 n}\right)^2} \tag{6-34}$$

Equation (6-34) shows that for long amplifier crystals or pump beams with poor beam quality factors, the average pump beam radius in the crystal rapidly increases, demonstrating that if the pump beam quality is poor then for efficient amplification the

amplifier crystal needs to be short. It can be shown from equation (6-34) that the minimum average beam radius is given by

$$w_{P,AVMIN} = \sqrt{\frac{1}{2\sqrt{3}}\left(\frac{l_c M^2 \lambda}{\pi n}\right)} \tag{6-35}$$

The effect of pump beam quality on small-signal gain is shown in figure (6-6). in figure (6-6) solid line is given by inserting a constant beam radius into equation (6-31) and assuming that the signal and pump beam radii are equal, the dotted line is calculated by putting the average value of the beam radius calculated from equation (6-34) into equation (6-31). The values used in figure (6-6) are P_P=5W, M^2=100, l_c=10mm, σ=15.6x$10^{-23}m^2$ and τ=100μs. These values are typical under end-pumping conditions. As can be seen with the effect of pump beam quality is considered, as the pump beam waist radius is initially reduced, the gain increases. However, as the pump beam waist is further reduced, the pump volume increases and the average spot-size in the laser crystal increases decreasing the gain, so that any further reduction in the pump beam waist will reduce the small-signal gain. The value of $w_{P,AVMIN}$ for this situation is ~200μm, and is the beam waist radius at which the small-signal gain is mximum. However, it was shown in chapter 4, that the thermal lensing under similar pumping conditions can be very strong and the effect of the thermal lens on the signal beam needs to be considered.

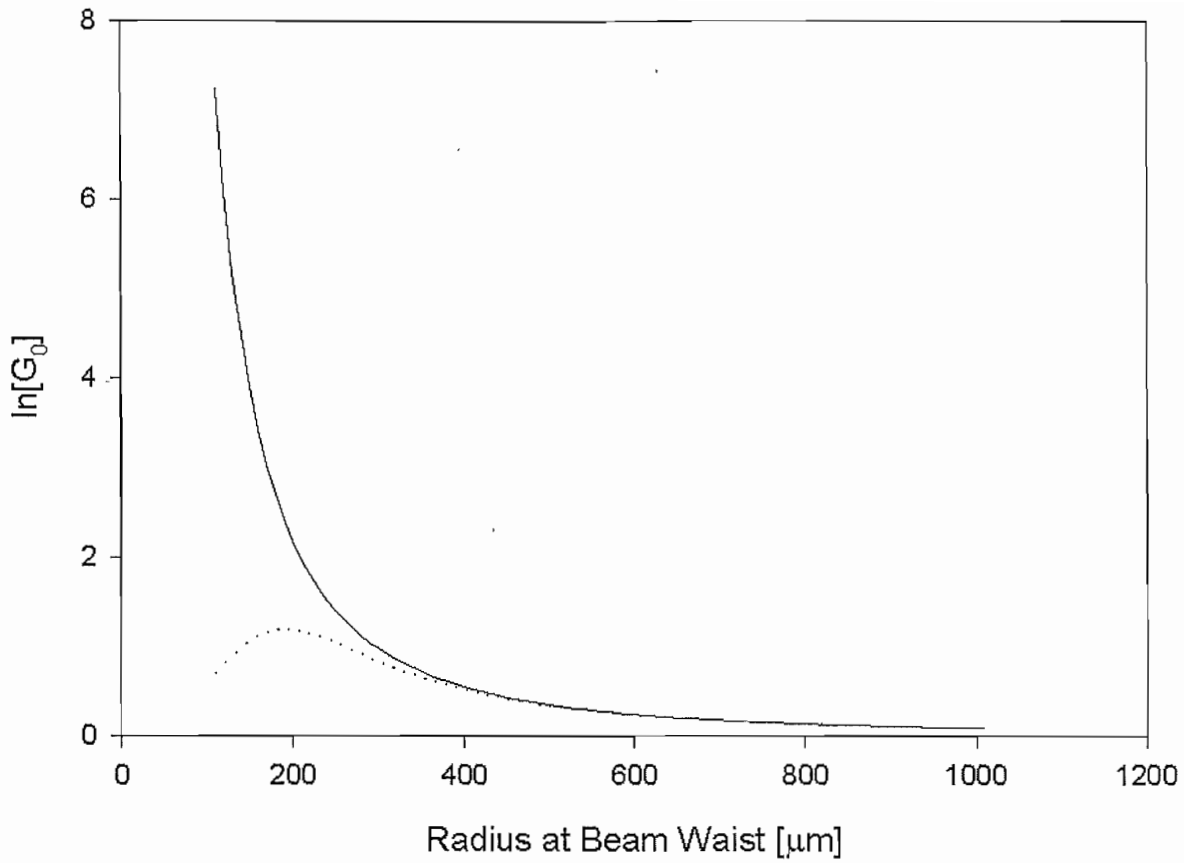

Figure (6-6). Combined effects of ETU and pump beam quality on the small-signal gain. The solid line is for a constant pump beam radius through the crystal and the dotted is for the average radius for a beam quality factor of M^2=100.

Inserting equation (6-35) into equation (6-26) leads to the maximum possible small-signal gain including ETU and pump beam quality of

$$\ln\left(G_{0,\max}\right) \approx 2\sigma\sqrt{\frac{Pn}{hcM^2W}} \tag{6-36}$$

where it has been assumed that $l_c=(2\sqrt{3})/\alpha_P$. As discussed in the previous chapters the ultimate limit that a material can be pumped to is the stress fracture limit. This limits the gain to

$$\ln\left(G_{0,STRESS}\right) \approx 32\sigma\sqrt{\frac{\pi Rn}{\alpha_P\delta_{nl}hcM^2W}} \tag{6-37}$$

where R is the thermal shock parameter defined in chapter 2, and $\delta_{q,nl}$ is the fraction of absorbed pump power that is converted to heat under non-lasing conditions. Table (6-1) shows the maximum small-signal gains achievable before stress fracture occurs and the values used to calculate them from Nd:YVO_4, Nd:YAG and Nd:YLF. It has been assumed

that the pump has a beam quality factor of 100, that 25% of the absorbed pump power is converted to heat and the refractive index of the material is 2. From table (6-1) that with its superior thermo-mechanical properties, the small-signal gains possible in Nd:YAG are much higher than those in Nd:YVO_4 and Nd:YLF. With the maximum predicted small-signal gain being greater in Nd:YVO_4 than in Nd:YLF. This suggests that Nd:YAG is more suitable for very high-power amplifier systems. If the effects of ETU are reduced by choosing a lower dopant concentration with a reduced absorption coefficient then it can be seen that significant improvement in the maximum possible small-signal gain before stress fracture occurs. As shown in table (6-1), where two dopant concentrations of Nd:YVO_4 are compared. By decreasing the dopant concetration by a factor of 10, the possible small-signal gain has tripled. It would be unlikely that these levels of small signal gain would be achieved in practice because it is likely that under non-lasing conditions the amount of pump power converted to heat is significantly more than 25%. Also mentioned above, under the pumping conditions required to reach these levels of small-signal gain, the crystal will have quite severe thermal lensing degrading the beam quality.

	Nd:YVO_4		Nd:YAG	Nd:YLF
Nd^{3+} [%]	1	0.1	1	1
α_P [cm^{-1}]	40	4	3	11
σ [x$10^{-19}cm^2$]	15.6		4.6	1.9
R [Wcm^{-1}]	4.8		11	2
W [x10^{-16} cm^3s^{-1}]	3.5		0.5	1.7
K_c [$Wcm^{-1}K^{-1}$]	0.052		0.13	0.063
dn/dT[x10^{-6} K^{-1}]	3.9		13	-2.00
$\ln(G_{0,S})$	1000	3300	4500	500
$\ln(G_{0,BQ})$	7.13		4.8	1.9

Table (6-1). Maximum small-signal gains possible before stress fracture occurs before the thermal lens in the amplifier degrades beam quality for crystals of Nd:YVO_4, Nd:YAG and Nd:YLF.

In reality the upper limit on the small-signal gain is going to be set by the necessity of obtaining diffraction limited output. For a top-hat beam it was discussed in chapter 2, that there should be no beam quality degradation for a beam passing through the thermal lens. As discussed in chapter 4, ETU increase the fraction of absorbed pump power converted to heat. The equation to calculate the maximum pump power before the quaritc phase aberrations degrade the signal beam quality is no longer diffraction limited is modified, by replacing the term for quantum defect heating for a the fraction of heat generated under non-lasing conditions with ETU present. This fraction is a function of the absorbed pump power, and so it is not a trivial matter to solve, however it can be assumed that when the amplifier is operating in a heavily saturated regime, there will be depletion of the upper laser level, and to give an order of magnitude estimate for the small-signal gain possible before beam quality degradation becomes a problem the value of quantum defect heating under lasing conditions will be used. Inserting the equation for the maximum absorbed pump power before thermal lensing causes beam quality degradation into equation (6-36) gives

$$\ln\left(G_{0,BQ}\right)=2\sigma\sqrt{\frac{0.32K_c\lambda n}{\delta_{q,nl}(dn/dT)M^2W}} \tag{6-37}$$

where K_c is the thermal conductivity of the material. The values for the maximum small-signal gain possible, before the thermal lens in the amplifier causes the beam quality of the signal to be degraded are shown in table (6-1) for Nd:YVO_4, Nd:YAG and Nd:YLF. As can be seen from table (6-1) that although Nd:YAG suffers from a lower rate of ETU and Nd:YLF has a smaller change in refractive index with temperature, the highest small-signal gains are possible in Nd:YVO_4 before the signal beam quality is degraded.

6.5 Multiple Rod Amplification

As can be seen from the above analysis, the beam quality degradation due to the thermal lens in a single crystal amplifier limits the small-signal gain achievable with this type of amplifier. The small-signal gain available can be increased by increasing the number of amplifier crystals, so that the amplified out from one amplifier crystal is imaged into a second amplifier crystal as shown in figure (6-7). In figure (6-7) the output from the first crystal, is imaged into the second crystal by two lenses. With the length of population inversion increased, the possible gains achievable should be as well. With the signal beam

power increased by the amplification of the first crystal, operation of the second amplifier crystal under saturated conditions should be easier. However, there will be a transmission loss in going from one amplifier crystal to the other caused by the lens system.

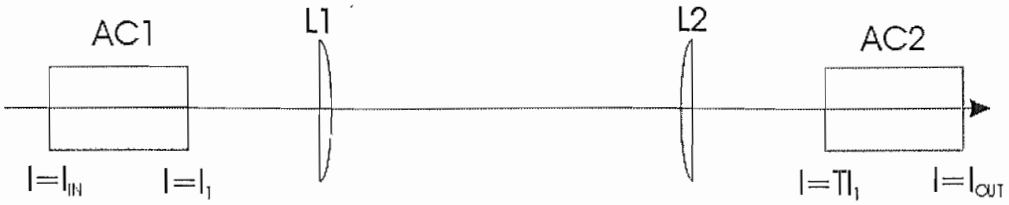

Figure (6-7) Multiple rod amplifier, with the amplified output from the first crystal imaged into the second crystal.

The methodology demonstrated previously to calculate the relationship between the input, and the output intensities and the gain in the crystal can be modified to include the transmission loss of the relay imaging optics. In the context of the amplifier system, the relay-imaging optics are very important, because they maintain the signal beam radius in the input and output image planes irrespective of thermal lensing in either amplifier crystal. This can be achieved by assuming the input intensity to the second crystal is TI_1 where I_1 is the output from the first crystal and T is the transmission of the lens system. Using the methodology demonstrated above to calculate the single pass gain of a crystal the single pass gain of the two crystals can be evaluated in a similar way. For the situation shown in figure (6-7), equation (6-14) can be re-written for the two crystals so that for the first crystal the output intensity I_1 is related to the incident intensity I_{IN} by

$$\ln\left[\frac{I_1}{I_{IN}}\right]+\frac{1}{I_{sat}}\left(I_1-I_{IN}\right)=\ln\left(G_{0,1}\right) \tag{6-38}$$

where $\ln(G_{0,1})$ is the small signal gain of the first crystal. The relation for the second crystal, the output intensity I_{OUT} is given by

$$\ln\left[\frac{I_{OUT}}{TI_1}\right]+\frac{1}{I_{sat}}\left(I_{OUT}-TI_1\right)=\ln(G_{0,2}) \tag{6-39}$$

where $\ln(G_{0,2})$ is the gain for the second crystal. Adding equations (6-38) and (6-39) together yields

$$\ln\left[\frac{I_{OUT}}{I_{IN}}\right]+\frac{1}{I_{sat}}\left(I_{OUT}-I_{IN}\right)=\ln\left[G_{0,1}G_{0,2}T\right]-\frac{I_1}{I_{sat}}\left(1-T\right) \tag{6-40}$$

For small signal gains the intensities are much smaller than the saturation intensity so equation (6-36) can be written as

$$\ln\left[\frac{I_{OUT}}{I_{IN}}\right]+\frac{1}{I_{sat}}\left(I_{OUT}-I_{IN}\right)\approx \ln\left[G_{0,1}G_{0,2}T\right]=\ln\left[G_{0,DC}\right] \tag{6-41}$$

where $\ln[G_{0,DC}]$ is the combined small signal gain for the two rods. However, the full figure for the small-signal gain may not be realised, if the overlap between the signal and pump beams is reduced, by for example, thermal lensing as discussed in the next section.

6.6 Effect of Thermal lens on Amplifier

As discussed in chapter 2, thermal lensing can lead to several deleterious effects such as degrading the beam quality and reducing the overlap of pump and laser beams inside laser crystals. The overlap of the pump and the signal beam being changes to the laser and pump beams that alter the value of the effective gain, this might be the signal beam changing in size as it passes through the laser crystal. The signal beam might change in radius due to diffraction or effects or if it is converging or diverging due to lenses, thermal or otherwise, in the laser crystal. In an amplifier system, the size of the signal beam in the amplifier crystal is defined by the input into the amplifier, whereas the laser mode in a resonator is governed by the interplay of the thermal lens and the cavity. In amplifiers the amount of absorbed pump power converted to heat is greater, because the population inversion is not pinned like it is at threshold pump power in lasers. This greater thermal loading leads to stronger thermal lensing in amplifiers than in resonators for similar absorbed pump power and beam radii. The relay imaging optics has unitary magnification generating an inverted image in the plane of the second crystal. The magnification is chosen to be unitary, so that the two crystals can be pumped with the same beam radius, and the signal beam waist in the first crystal is imaged into the second crystal. For simplicity, it is assumed that the thermal lenses occur at the mid-points of the amplifier crystals and the input plane of the amplifier is chosen to lie at the mid-point of the first crystal, so the signal and pump beam waists coincide at this plane. The effect of thermal lensing on the signal beam can be determined for an output plane at the mid-point of the second crystal using the ABCD ray-transfer matrix for the amplifier

$$M_{1pass}=\begin{pmatrix}1 & 0\\ \frac{-1}{f_t} & 1\end{pmatrix}\begin{pmatrix}-1 & 0\\ 0 & -1\end{pmatrix}\begin{pmatrix}1 & 0\\ \frac{-1}{f_t} & 1\end{pmatrix}=\begin{pmatrix}-1 & 0\\ \frac{2}{f_t} & -1\end{pmatrix} \tag{6-42}$$

where f_t is the thermal lens focal length of the amplifier crystal and it is assumed that the focal lengths of the two thermal lenses are the same. For an incident complex beam parameter of q_1 the complex beam parameter in the second crystal, q_2 is then given by

$$\frac{1}{q_2} = \frac{1}{q_1} - \frac{2}{f_t} \tag{6-43}$$

Equation (6-39) shows that the imaginary part of q_1, which specifies the local beam radius, remains unchanged but the thermal lens alters the real part of the beam parameter, representing the divergence. Figure (6-7) shows the effect of the thermal lenses in the amplifier on the signal beam. In figure (6-7) the dashed line shows that of the signal beam without thermal lensing, with the solid line being the signal beam with thermal lensing present. As can be seen the effect of the first thermal lens is to change the divergence of the signal beam. The relay imaging optics, then image the signal beam in the second crystal where the second thermal lens further modifies the beam divergence.

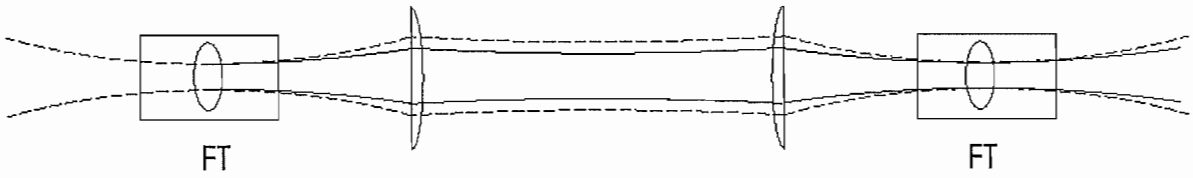

Figure (6-7). Effect of thermal lensing on the signal beam in the amplifier.

Examining the situation using the ABCD matrices, the beam leaving the amplifier after passing through the two thermal lenses, acts as if the beam waist has been displaced from the image plane. The distance between the image plane in the second crystal and the beam waist, z_o, can be determined from

$$z_o = \frac{R}{1+\left(\frac{\lambda R}{\pi w^2}\right)^2} = \frac{-f_t}{2\left(1+\left(\frac{-f_t}{2z_{Rs}}\right)^2\right)} \tag{6-44}$$

where R is the radius of curvature of the signal beam in the image plane and z_{Rs} is the Rayleigh range of the incident signal beam. The radius of the signal beam at the waist is given by

$$w_o^2 = \frac{w_i^2}{1+\left(\frac{\pi w_i^2}{\lambda R}\right)^2} = \frac{w_i^2}{1+\left(\frac{2z_{Rs}}{f_t}\right)^2} \tag{6-45}$$

Equation (6-44) shows that at large thermal lens focal lengths the position of the beam waist is coincident with the image plane, but as the focal length of the thermal lens decreases the beam waist moves away from this plane, before the thermal lens becomes so short that it approaches the image plane again. If it is assumed that the beam has effectively propagated from this beam waist position through the second crystal, this is of course not strictly true, but allows an estimate to be made of the decrease in the gain of the second amplifier crystal due to the change in signal beam radius as it passes through the crystal. The average beam radius in the crystal can be calculated by a similar method to that used previously i.e. by calculating the volume in the second amplifier crystal and then dividing by the crystal length. The signal beam volume is given by

$$V_s = \pi w_o^2 \int_{z_o-\frac{l_c}{2}}^{z_o+\frac{l_c}{2}} \left[1+\left(\frac{z-z_0}{z_{Ro}}\right)^2\right] dz \qquad (6\text{-}42)$$

where z_{Ro} is the Rayleigh range of the signal beam in the second amplifier crystal. It can be shown that the average beam radius is given by equation (6-34) with the pertinent parameters inserted. The change in the average spot size in the amplifier for the signal beam can then be inserted into equation (6-25) to calculate the small signal gain as the signal beam radius changes with absorbed pump power. Figure (6-9) shows the small-signal gain for the second crystal after propagating through the two thermal lenses. The solid line in figure (6-9) is the small-signal gain for the second crystal for a 1% doped Nd:YVO_4 crystal and the dashed line is that for a 0.1% crystal. For the 1% doped crystal the crystal was 3mm long and 10mm long for the 0.1% case. As can be seen from figure (6-9) the gain begins to increase linearly with absorbed pump power, before decreasing as the thermal lenses and the reduction in gain due to ETU in the second amplifier crystal affect the small-signal gain of the second crystal.

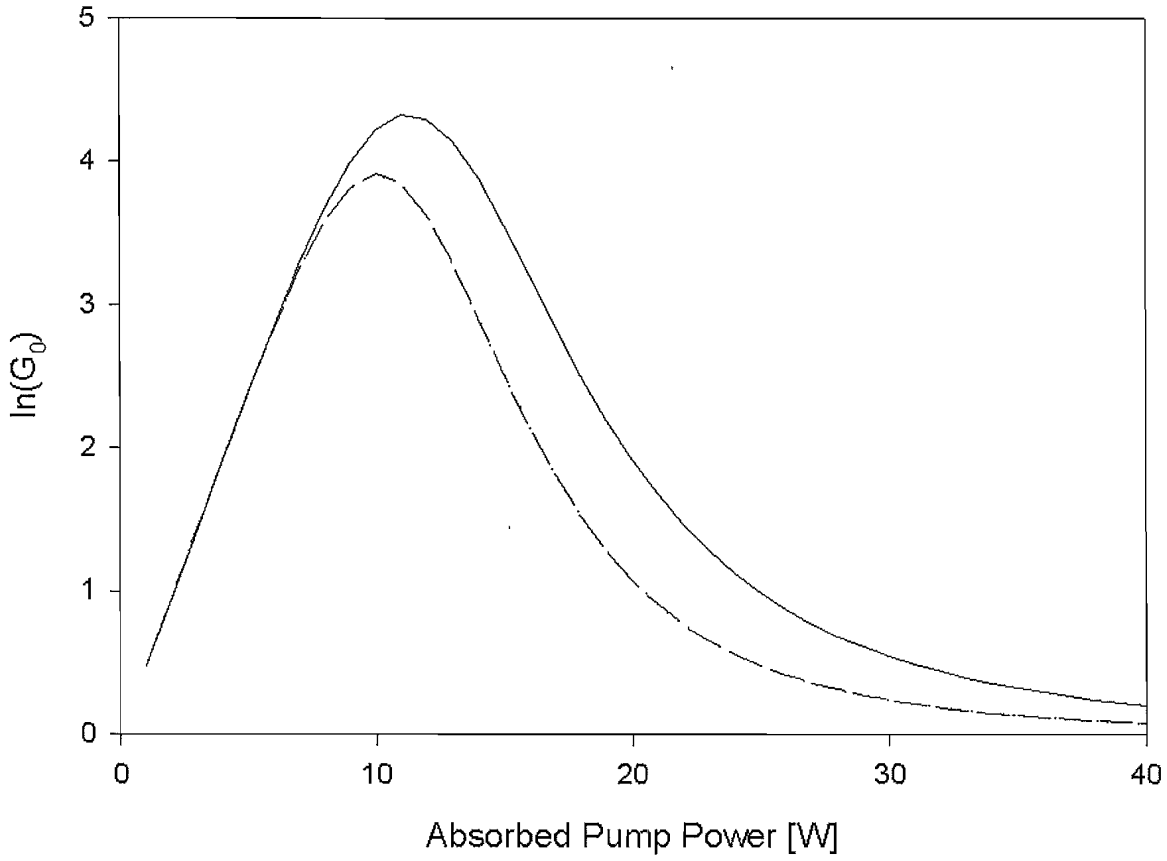

Figure (6-9). Variation of the small-signal gain with absorbed pump power for the second amplifier crystal under single pass amplification. The solid line is for a 1% doped Nd:YVO_4 crystal and the dashed line is for a 0.3% doped crystal.

6.7 Single Pass Amplifier Design

To verify the results of the theoretical approach so far undertaken, a two-crystal single-pass amplifier was constructed. Figure (6-10) shows the amplifier layout used to amplify the output from the master oscillator. The solid line shows the optical path of the signal beam and the dashed line shows the pump beam. The signal beam is chosen to have the same beam radius as that of the pump beam.

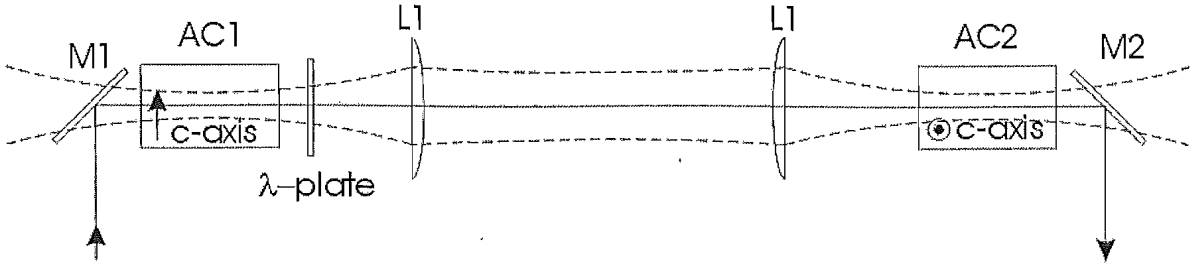

Figure (6-10). Simple single-pass amplifier with two amplifier crystals. The solid line is that of the signal beam and the dashed line that of the pump beam.

The signal beam is reflected of mirror M1, which is coated to be HR at 1.064μm at 45^0 and AR at 810nm at 45^0. This choice of coating enables amplifier crystal AC1 to be end-pumped through this mirror. The mirror is also chosen to be thin substrate so that the astigmatism for the pump beam on passing through this mirror is minimised. The signal beam is then amplified as it passes through AC1. Crystal AC1 is a 10mm long 0.1% doped Nd:YVO_4 crystal AR coated at 810nm and 1.064μm. The choice of 0.1% doped Nd:YVO_4 is explained in table (6-1) where it is shown that the reduced rates of ETU that occur with the lower dopant concentration lead to a factor of 3 increase in the potential small-signal beam. The small-signal gain possible before beam quality degradation of the signal beam occurs, is likely to increase as well because there will be less absorbed pump power converted to heat. The signal beam then passes through the wave-plate, λ-plate. This is a dual wavelength waveplate, being a half-waveplate at 1.064μm and a full wave-plate at 810nm. The consequence of this is that the polarisation of the signal beam is rotated by 90^0 whilst the polarisation of the pump beam is unaffected on passing through the waveplate. This is necessary because the two amplifier crystals are aligned with their c-axes perpendicular to reduce the effect of the asymmetric thermal lensing in the two planes. The signal beam therefore needs to be rotated, so that it is aligned with the high-gain axis of the second crystal. The polarisation of the pump is not rotated, because after passing through the first amplifier crystal the pump light polarised along the c-axis has been depleted more than the orthogonaly polarised pump light by the stronger absorption for this axis. So after passing through the waveplate the most of the pump light is polarised in the same direction as the signal beam, this direction of polarisation now corresponds to the strong emission and absorption axis. The signal beam and the unabsorbed pump light is then imaged into the second crystal. The imaging optics have a magnification of 1, so that the beam waist radii in the first amplifier crystal are the same as those in the second crystal. The signal beam experiences further amplification on

passing through AC2 before reflecting of mirror M2. Amplifier crystal AC2 is the same as AC1. Mirror M2 is HR coated at 1.064μm at 45^0 and AR coated at 810nm at 45^0. This enables the amplifier to be pumped through this mirror by a second pump beam. Mirror M2 is at 45^0 to the axis so that the signal beam leaves the amplifier.

The pump beams for the amplifier were provided by two fibre-coupled beam-shaped 20W diode bars. The diodes were coupled into fibres with a 365μm diameter core and an NA of 0.22. The beam emerging from the fibre had a beam quality of ~150 in orthogonal planes and was collimated using a 15mm spherical lens. The collimated beam was then focused into the amplifier crystal using a 50mm focal length spherical lens, producing a beam waist with a radius of ~300μm in the crystal. At maximum applied current, the pumps provided a combined pump power of 18W. It was found that only 80% of the incident pump power was absorbed in the amplifier, suggesting an effective absorption coefficient of $143m^{-1}$ for unpolarised light. It was shown in chapter 5 that the absorption coefficient of the c-axis is approximately twice that of the a-axis. This suggests that the absorption coefficient for punp light polarised along the c-axis is $200m^{-1}$ and $100m^{-1}$ for the a-axis. The signal beam had a radius of 240μm in the crystal, reduce beam quality degradation due to the thermal lensing. The measured small-signal gain as a function of the absorbed pump power is shown in figure (6-11). In figure (6-11) the dotted line is calculated from equation (6-24) where the effects of ETU and thermal lensing on the overlap in the second crystal have been included in the manner described previously, the solid line neglects these effects and the black circles are the measured small signal gains. As can be seen for small absorbed pump powers the two lines show good agreement with the experimental results, with reasonable agreement at maximum powers. From the small difference between the two lines it can be seen that the effect of ETU and thermal lensing for the single pass amplifier are relatively weak shown. The intercept with the y-axis is 10log(T), with T measured to be 93% in this case. The values used in the calculations other then mentioned in the text above are shown in table (6-2).

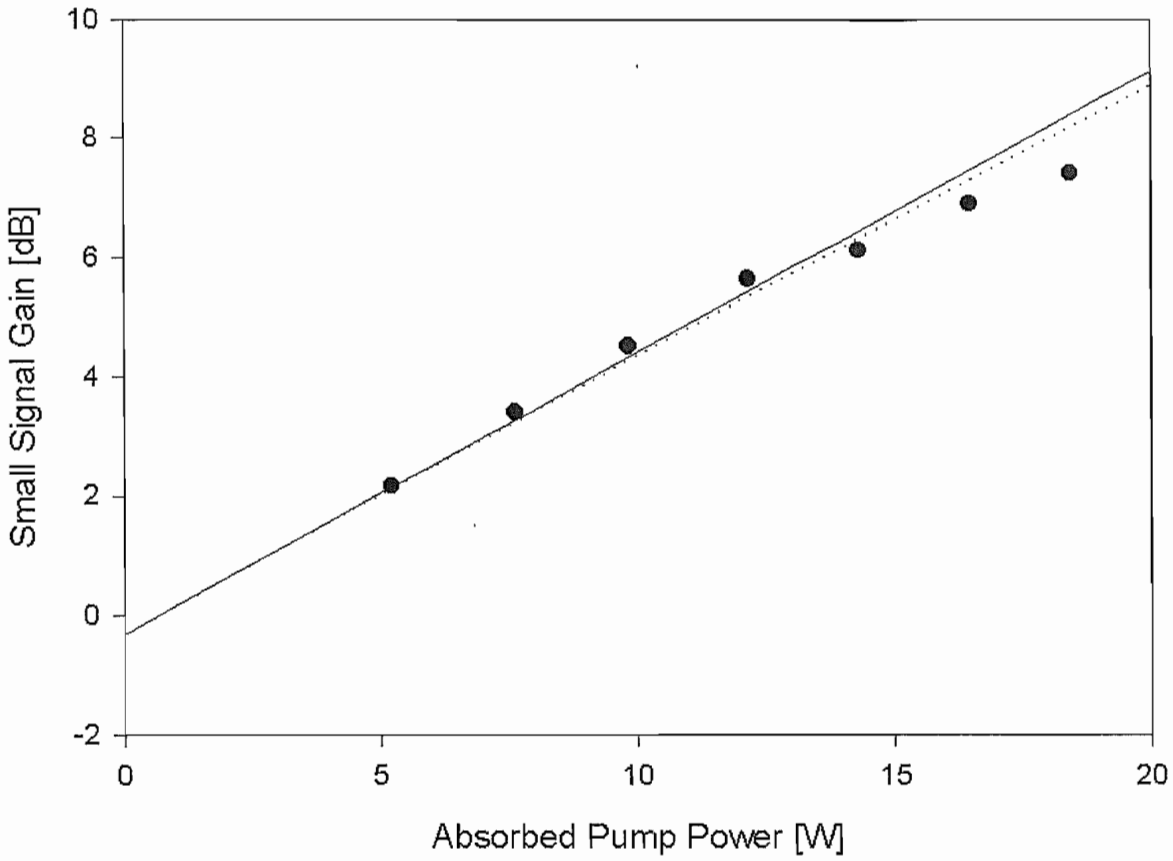

Figure (6-11) Small signal gain from a single pass amplifier with two crystals. The dotted line is calculated including thermal lensing effects and ETU, the solid line is calculated neglecting these effects.

σ	$15.6\times10^{-23}m^2$
τ	$100\mu s$
α_P	$143m^{-1}$
W	$3\times10^{-22}m^3s^{-1}$
K_c	$5.2Wm^{-1}K^{-1}$
dn/dT	$3.9\times10^{-6}K^{-1}$
δ	0.25

Table (6-2) Values used in the calculation of the small-signal gain shown in figure (6-10)

6.8 Amplifier Design Strategy

The discussion so far above has shown that it should be possible to achieve large small-signal gains using end-pumping, however, multi-pass amplifier schemes are required to extract this gain efficiently. It has also been shown that by imaging the signal beam within the crystal, the beam radii at the image plane can be maintained irrespective of the thermal lensing in the amplifier crystals. It has been found however, that the thermal lensing in the amplifier can have an impact on the small-signal gain of the amplifier by altering the overlap of the sign and pump beams in the laser crystals. This section looks at some amplifier configurations that have been under end-pumping geometries.

To generate multi-pass amplification, the polarisation of the incident laser beam can be used to select the number of passes of an amplifier [4] or mirrors [5, 6] amongst others. Figure (6-12) shows the application of polarisation to control the number of passes of an amplifier. The input beam passes through a Faraday isolator, preventing back reflections into the master oscillator. The beam then passes though a polarisor, which also acts to pick off the output on the beams second pass through it. The beam then passes through a Faraday rotator and a half-waveplate so that the p-polarisation is selected. The beam then makes a pass of the Nd:YAG amplifier crystal and is then rotated to the s-polarisation by a double pass of a Faraday rotator before passing through the amplifier crystal. The beam-splitter, then reflects the beam out where it is reflected of mirror M1 and then makes it's third pass of the amplifier. The next double pass of the amplifier, then rotates the polarisation of the beam back to the p-polarisation, the beam then makes its final pass of the amplifier crystal. The half-waveplate and Faraday rotator then rotate the polarisation once again, so that the beam is then reflected at the polarisor, forming the output beam. The set up as shown figure (6-12), cannot be used with Nd:YLF where the two orthogonal polarisations have different lasing wavelengths. For Nd:YVO_4 the two polarisations have different stimulated emission cross-sections so the gains on the alternate passes will not be equal. The thermal lensing for the orthogonal polarisations will be different for the two materials. Nd:YLF for example has a positive lens for the σ-polarisation and a negative lens for the π-polarisation, the strengths of the two lensing is not the same however, with the π-polarisation being the stronger, so there sill not be complete compensation between

the passes. For Nd:YVO_4 the thermal lensing is stronger for the σ-polarisation and is positive for both polarisations, so there is no compensations.

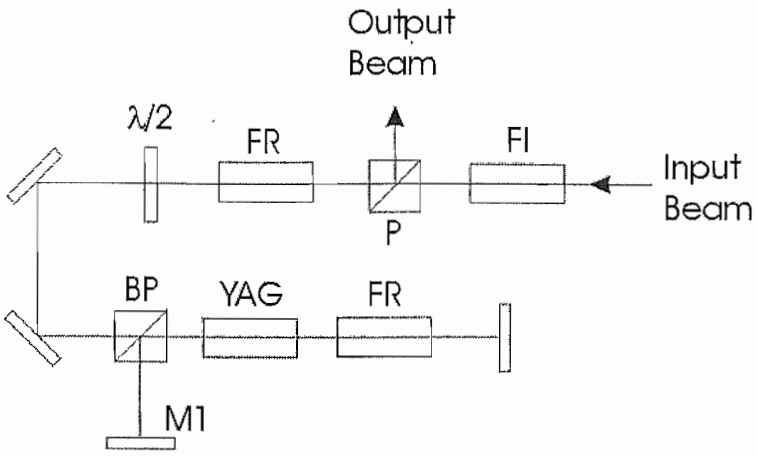

Figure (6-12). Laser beam polarisation used to determine the number of passes of an amplifier.

The use of mirrors to control the number of passes is shown in figure (6-13). Both the amplifiers shown in figure (6-13) are four pass amplifiers. In figure (6-13(A)) the input beam is brought to a focus in the gain medium, which has one face coated as a mirror at the signal wavelength. The beam passes through the lens off-axis, and is then collimated by the same lens after passing through the gain medium, which has one face coated as a mirror at the signal beam wavelength. The signal beam, then passes through a second lens where it is brought to a focus on a mirror and is reflected back through the second lens. This combination of mirror and lens displaces the beam horizontally, before passing through the first lens again. The separation of the two lenses is the sum of their focal lengths so that they form a relay-imaging system. The relay imaging of the beam waist in the crystal ensures that the beam in the crystal has the same radius at the focus of the first lens. The signal beam then makes a third and fourth pass of the gain medium. The first lens then collimates the signal beam again and it forms the output beam. In figure (6-13(B)) the gain medium again has a mirror coated on one face, and the signal beam is displaced, by the use of mirrors, although in this case there are no lenses, so the signal beam will not be the same for each pass of the amplifier crystal. Both amplifiers in figure (6-13) are end-pumped through the mirror face of the amplifier crystal. Since the polarisation of the signal beam is the same on each pass of the amplifier crystal, the signal beam experiences the same strength for the thermal lens on each pass. The strength of the lens depending on the polarisation of the signal beam for Nd:YLF and Nd:YVO_4. These two materials do not have equal thermo-mechanical properties in the orthogonal directions; the strength of the thermal lens will be asymmetric. If this astigmatism is not

compensated for, an originally circular beam will become progressively astigmatic as it passes through the amplifier.

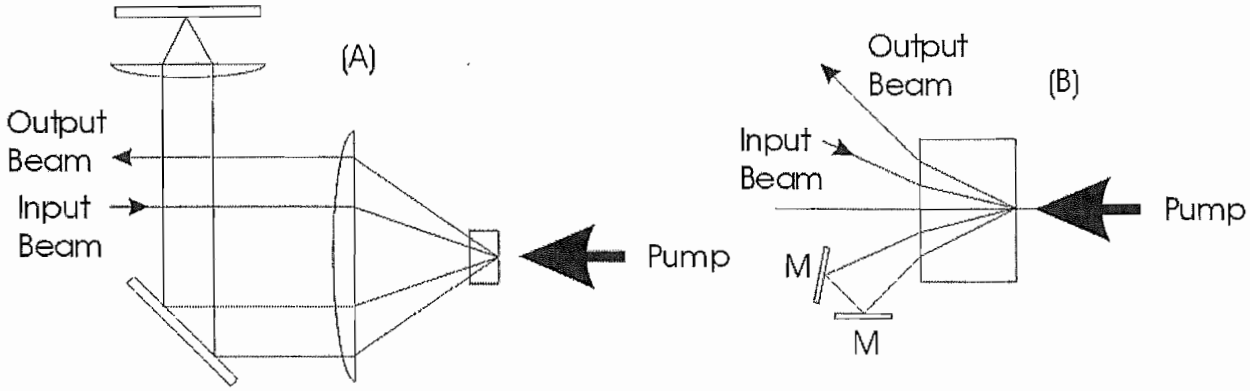

Figure (6-13). The use of mirrors to control the number of passes.

Rather then using lenses to relay-image the signal beam into a gain medium, mirrors can be used as an alternative as shown in figure (6-14). In figure (6-14) two mirrors are placed either side of the gain medium. The two mirrors are aligned confocally, with the gain medium located on-axis at the common focus. The signal beam is aligned parallel to the optical axis although slightly displaced from it and enters the amplifier through a hole in one of the mirrors. The signal beam reflects of the other mirror and is consequently brought to a focus in the gain medium. After passing through the gain medium the signal beam passes though a Brewster plate. The Brewster plate is flat and with parallel sides and is positioned adjacent to the gain medium. The purpose of the Brewster plate is to displace the signal beam further from the optical axis. Alternatively, the gain material iself could be Brewster cut, leading to a similar result, but the signal beam radii in the crystal will be unequal. The mirrors then focus the beam into the gain medium, re-imaging the original beam radius in the crystal. Mirror M1 is then used to select the beam from the amplifier. The number of passes that the signal beam makes of the amplifier is controlled by the distance between the optical axis and mirror M1. This amplifier design again suffers from the potential that the asymmetric, thermal lensing in the gain medium might produce astigmatism. The combination of the Brewster element and off-axis from the mirrors will also generate astigmatism, unless the correct combination of Brewster element thickness and angle of incidence are chosen. The proximity of the signal beams to the gain medium will also restrict the cooling of the crystal. End-pumping of this design through the curved mirrors can be achieved if the correct dichoric coatings are chosen.

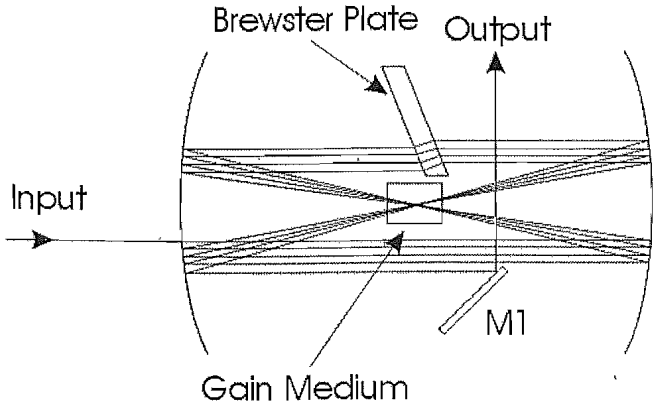

Figure (6-14). Multipass amplifier based on confocal imaging by two parabolic mirrors.

By imaging the signal beam into the amplifier crystal, the effect of the thermal lens on the signal beam size, can be negated in the image plane, ensuring in this plane that the beam radius remains constant. However, as discussed earlier the thermal lens, displaces the signal beam waist from this position, affecting the overlap between the signal and pump beams, decreasing the extraction efficiency and the potential gain. As has been shown in chapter 4, the thermal lensing in Nd:YVO_4 is asymmetric, this causes the signal beam to astigmatic unless there is some form of compensation. Therefore, whilst multi-pass amplifiers have the advantage that they enable the amplifier to become saturated and improve the extraction efficiency, the multiple passes of the amplifier crystal can lead to signal beams becoming astigmatic and their beam quality degraded.

6.9 Double Pass Amplification

As discussed in the introduction it is difficult to efficiently extract the stored energy in an amplifier. To extract the stored energy the amplifier must be operated in the saturated regime and can be achieved more easily with a multiple pass amplifier. Figure (6-15) shows the intensities and directions for a Rigrod analysis of a double pass amplifier. Using $I_+(z)$ and $I_-(z)$ to indicate the intensities travelling in the $+z$ and $-z$ directions. These intensities then grow in the following manner

$$\frac{dI_{\pm}(z)}{dz} = \mp g_0(z) I_{\pm}(z) \tag{6-43}$$

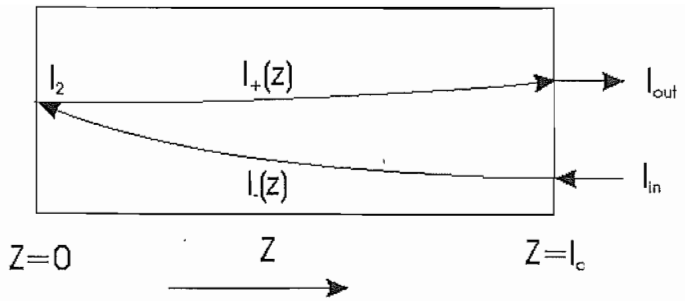

Figure (6-15). Intensities used in the Rigrod analysis of a double pass amplifier.

The gain coefficient at any plane z then saturates according to the total intensity at that plane in the following way

$$g_0(z) = \frac{g_0}{1 + \frac{I_+(z)}{I_{sat}} + \frac{I_-(z)}{I_{sat}}} \tag{6-44}$$

Combining the differential equations of (6-43), it can be seen that the product of the intensities in the two directions at any plane is constant

$$\frac{d}{dz}\left[I_+(z)I_-(z)\right] = -g_0 I_+ I_- + g_0 I_+ I_- = 0 \tag{6-45}$$

so that

$$I_+(z)I_-(z) = C \tag{6-46}$$

Using the result of equations (6-45) and (6-46) in equation (6-44) to rewrite equation (6-7)

$$\frac{dI_\pm(z)}{dz} = \frac{g_0 I_\pm(z)}{1 + \frac{I_\pm(z)}{I_{sat}} + \frac{C}{I_\pm(z) I_{sat}}} \tag{6-47}$$

Equation (6-47) can be integrated over the length of the amplifier in the form

$$\int_{I=I_2}^{I=I_{out}} \left(\frac{1}{I_{sat}} + \frac{1}{I_+} + \frac{C}{I_+^2 I_{sat}} \right) dI_+ = \int_{z=0}^{z=l_c} g_0 dz \tag{6-48}$$

where l_a is the length of the amplifier. Carrying out the integration for equation (6-48) and for the other direction leads to

$$g_0 L = \ln\left(\frac{I_{out}}{I_2}\right) + \frac{1}{I_{sat}}\left[I_{out} - I_2\right] - \frac{C}{I_{sat}}\left(\frac{1}{I_{out}} - \frac{1}{I_2}\right) \tag{6-49}$$

$$g_0 L = \ln\left(\frac{I_2}{I_{in}}\right) + \frac{1}{I_{sat}}\left[I_2 - I_{in}\right] - \frac{C}{I_{sat}}\left(\frac{1}{I_2} - \frac{1}{I_{in}}\right) \tag{6-50}$$

Using $C=I_{out}I_{in}$ and adding equations (6-49) and (6-50) yields

$$2g_0L = \ln\left(\frac{I_{ou}}{I_{in}}\right) + \frac{2}{I_{sat}}(I_{out} - I_{in}) \tag{6-51}$$

From equation (6-51) the extracted power is given by

$$I_{extr} = I_{out} - I_{in} = \ln(G_0) - \frac{\ln(G)}{2} \tag{6-52}$$

The available power remains the same, although the number of passes is increased there has been no increase in the pump power, so the extraction efficiency becomes

$$\eta_{extrd} = 1 - \frac{\ln(G)}{2\ln(G_0)} \tag{6-53}$$

A comparison of the extraction efficiencies achievable with a single and a double pass amplification are shows that the extraction efficiency is improved for a double-pass amplifier. At minimum extraction, i.e. small-signals, the maximum gain achievable for the single pass amplifier it the small-signal gain, however, for the double pass amplifier the maximum possible gain has increased to $2\ln(G_0)$. So by going to a double pass amplifier, not only is the extraction efficiency improved, but the possible small-signal gain is increased as well. Under small signal conditions, where there is minimal extraction of energy, it would be expected from a comparison of the small signal gain with a single pass and a double pass, that the small-signal gain would scale as $n\ln(G_0)$ where n is the number of passes and the effects of thermal lensing on the signal and pump beam have been neglected.

6.10 Multi-Pass Amplification

The number of passes of the amplifier described previously for single-pass amplification can be increased by the addition of mirrors. The arrangement for a 4-pass amplifier is shown in figure (6-16). In figure (6-16) only the signal beam has been shown, with the pump beam remaining as described earlier.

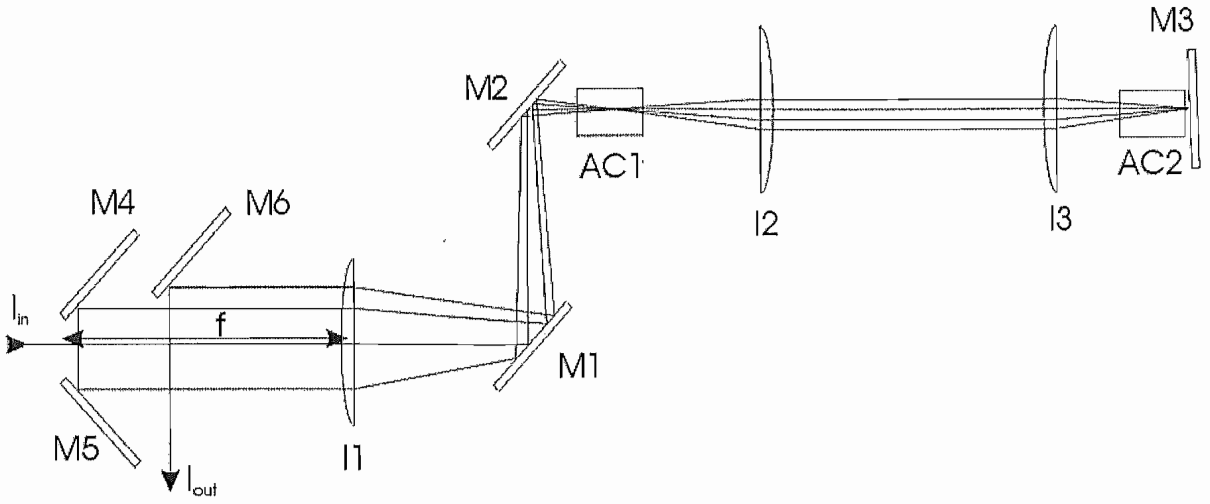

Figure (6-16) Four pass amplifier.

The signal to be amplified passes through lens L1, which is positioned a focal length away from amplifier crystal AC1. The signal then reflects off mirror M1 and M2 before entering amplifier crystal AC1, where it comes to a waist due to lens L1. The beam waist is then imaged into AC2 be the two lenses L2 and L3. The signal beam is then reflected off mirror M3 which is coated to be AR at 810nm and HR 1.064μm at normal incidence. Mirror M3 is tilted slightly off axis so that the signal beam takes a slightly different path back through the amplifier. On leaving the amplifier the signal beam is reflected off M1 where it passes through lens L1 again. Mirrors M4 and M5 then retroreflect the beam back into the amplifier having displaced the beam off-axis, the distance between mirrors M4 and M5 and lens L1 is the focal length of L1. This ensures that the signal beam is re-imaged back into the amplifier, maintaining the beam waist at the centre of the first crystal. The signal beam then makes another double pass of the amplifier. After reflecting off mirror M1 the signal beam then reflects of mirror M6 leaving the amplifier. Mirrors M4, M5, and M6 are all coated to be HR at 1.064μm at 45^0 The number of passes through the amplifier is controlled by the position of M6. If the mirror is placed closer to the axis of the lens then ony 2-passes are permitted, if the mirror is moved further away from the axis, then the number of passes allowed can be increased. By increasing the number of passes in this way, the beam doesn't become astigmatic due to reflections from off-axis curved mirrors, and the displacements of the signal beam means that the most is made of the available gain limiting the potential for spontaneous emission caused by undepleted gain in the wings of the pump beam.

The small-signal gain as a function of the absorbed pump power for the six-pass amplifier is shown in figure (6-17). In figure (6-17) the black circles are the measured small signal gains, the solid line is the calculated small-signal gain neglecting ETU and thermal lensing and the dotted line is the calculated small-signal gain including these effects. As can be seen the dotted line predicts small-signal gains greater that those measured. Indeed it could be argued that the measured small signal gain is almost linear with incident pump power. This might be due to the spatial overlap of the signal and pump beam, because the above described model neglects the angle of signal beam to the optical axis of the amplifier. This angle increases with the number of passes of the amplifier, consequently the signal beam experiences lower gain. However the significantly different values for the predicted small-signal gains for the model that includes ETU and thermal effects and the model that neglects them, provides an improved prediction of the measured small-signal gain.

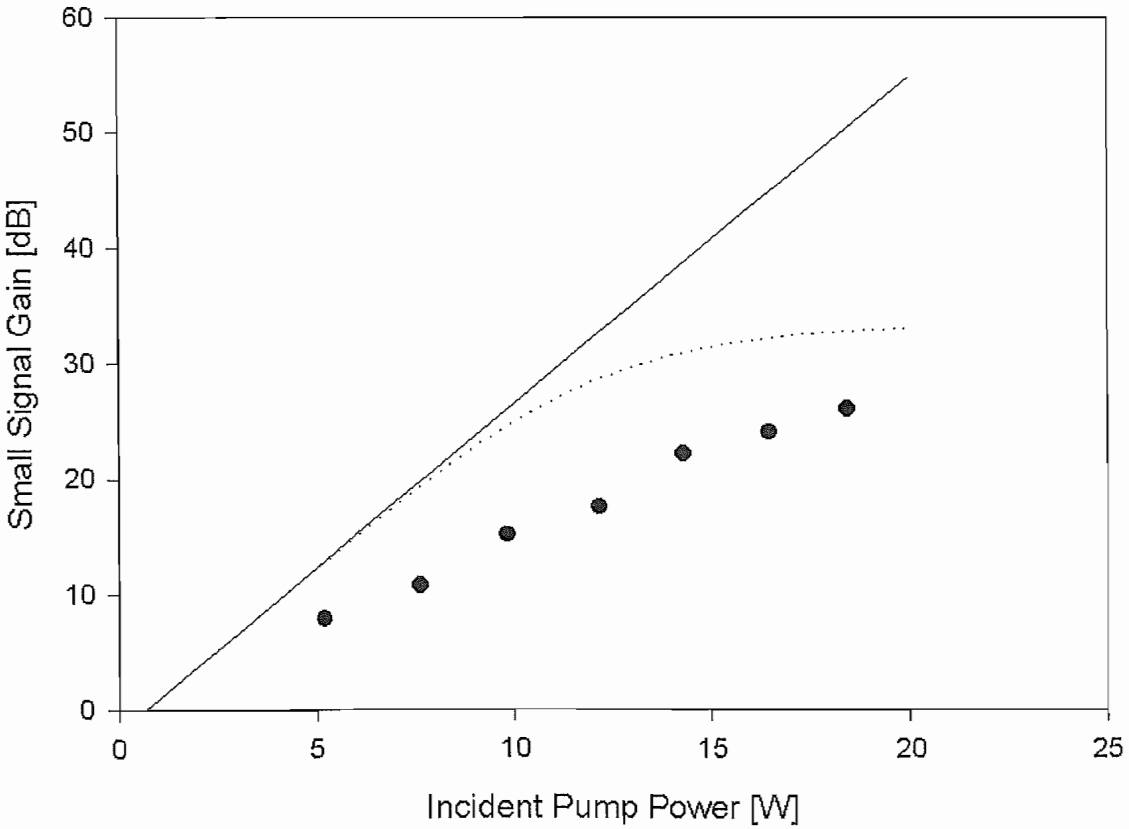

Figure (6-17). Small signal gain for the six-pass amplifier. The black circles are the measured values, the solid line is the predicted small-signal gain neglecting ETU and thermal lensing effects, whilst the dotted line includes these effects.

The extracted power for different number of passes of the amplifier as the gain of the amplifier varied is shown in figure (6-18). The gain of the amplifier was varied by changing the power of the incident signal beam power. This was achieved by controling the power of the input signal beam with a half-waveplate and a polarising beam splitter, the polarisations of the beam splitter and the first amplifier crystal being the same. As the half-waveplate is rotated the power of the signal beam can be adjusted. In figure (6-18) the black triangles are for single pass amplification, the white circles are for two-pass amplification, the black circles are for four pass amplification, the white triangles are for six-pass amplification and the sold lines are linear regressions fitted to the data. The intercept of the linear regression with the y-axis gives the available power for extraction from the amplifier. The small-signal gain of the amplifier is given by the intercept of the linear regression with the x-axis. For the six pass amplifier it was found that with no applied signal beam, but with the acousto-optic modulator on, several watts of output were detected from the amplifier. This is attributed to parasitic lasing caused by a cavity being formed between the output coupler of the master oscillator and a surface in the amplifie, because the output ceased when the path to the output coupler was blocked or the modulator switched off.

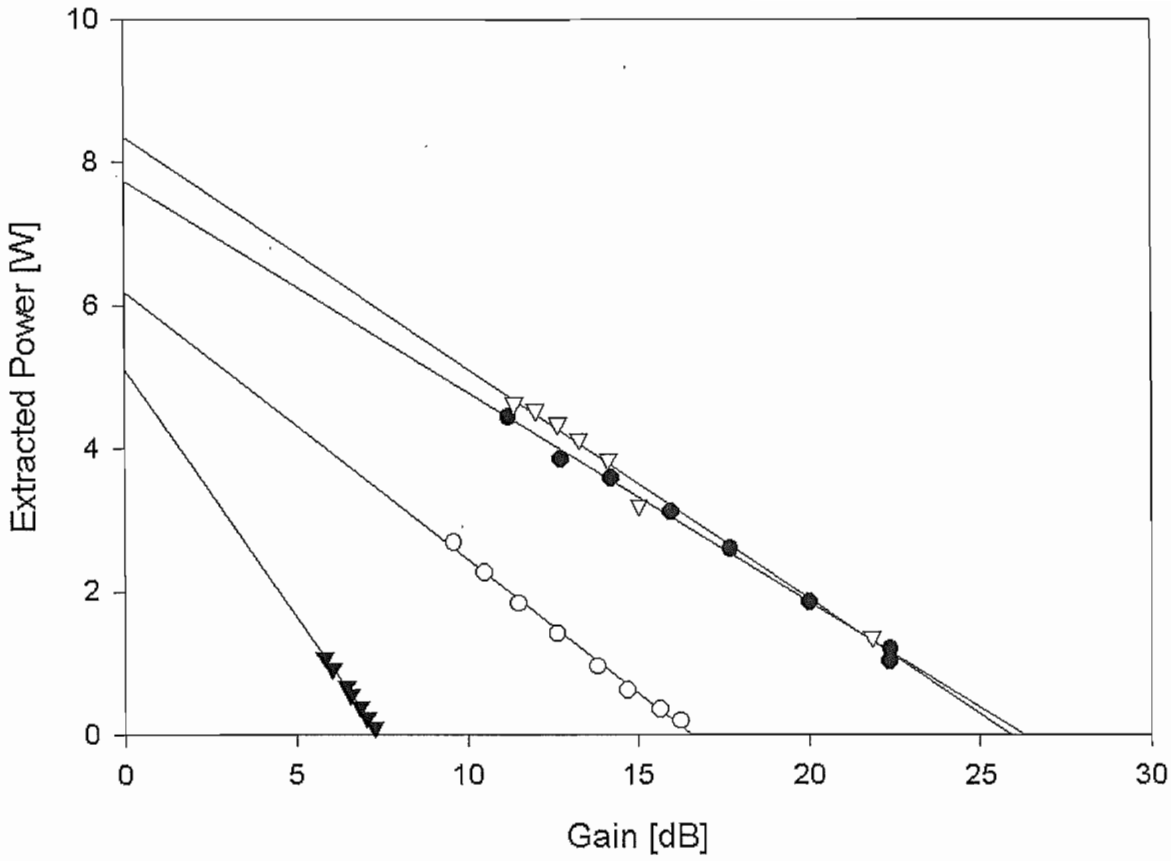

Figure (6-18) Extracted power from the amplifier as the power gain of the amplifier is varied. The black triangles are for single pass amplification, the white circles are for two-pass amplification, the black circles are for four pass amplifier, the white triangles are for six-pass amplifiers and the sold lines are linear regressions fitted to the data.

The available power for the different number of passes is plotted in figure (6-19). As can be seen the available power increases as the number of passes increases. However, as the number of passes increases the available power approaches the maximum possible with the available pump power. As noted in the Rigrod analysis section, the available power should not change because the pump power is not varied. The available power might be increasing because as the number of passes is increased the extraction efficiency is increasing so there is more extracted power circulating in the amplifier, this will reduce the amount of ETU occurring as the rate of stimulated emission is increased.

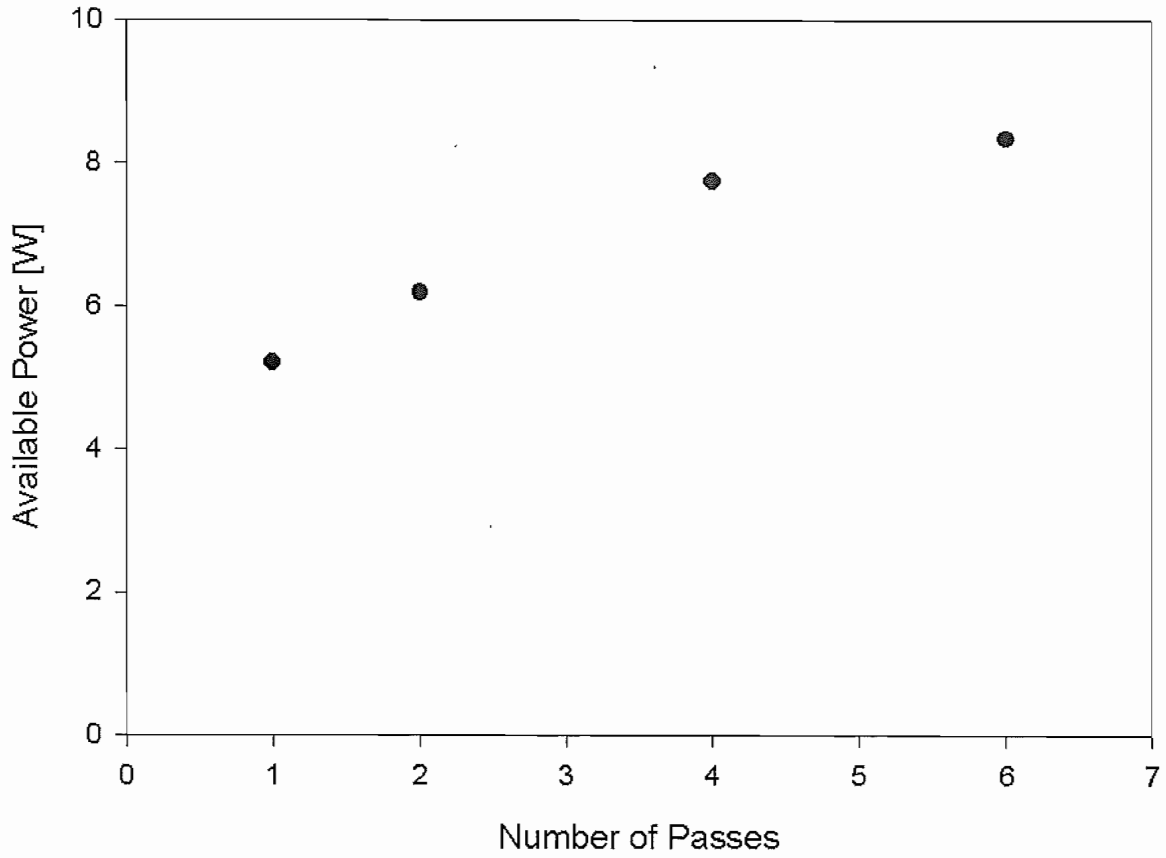

Figure (6-19). Available power for the different number of passes of the amplifier.

The small-signal gain as a function of the number of passes is shown in figure (6-20). In figure (6-20) the solid line is for the expected trend of the gain increasing as the number of passes is increased. The black circles are the measured small-signal gains and the white circles are the predicted small signal gains. According to the Rigrod analysis of the two pass amplifier, it can be seen that the small signal gain should double when going from single-pass to double-pass amplification and that for small-signal gain where there is minimal extraction of the available power that the small-signal gain would scale as $n\ln(G_0)$. As can be seen the small signal gain for the double pass amplifier is approximately twice that of the single pass amplifier. However, as the number of passes increases the small-signal gain deviates from this trend. This is due to the effects of thermal lensing and ETU and the model described throughout this chapter explains predicts the small-signal gain for the four pass amplifier well. However, the measured value for the small signal gain for the six-pass amplifier is not as great as that predicted, and has been discussed earlier

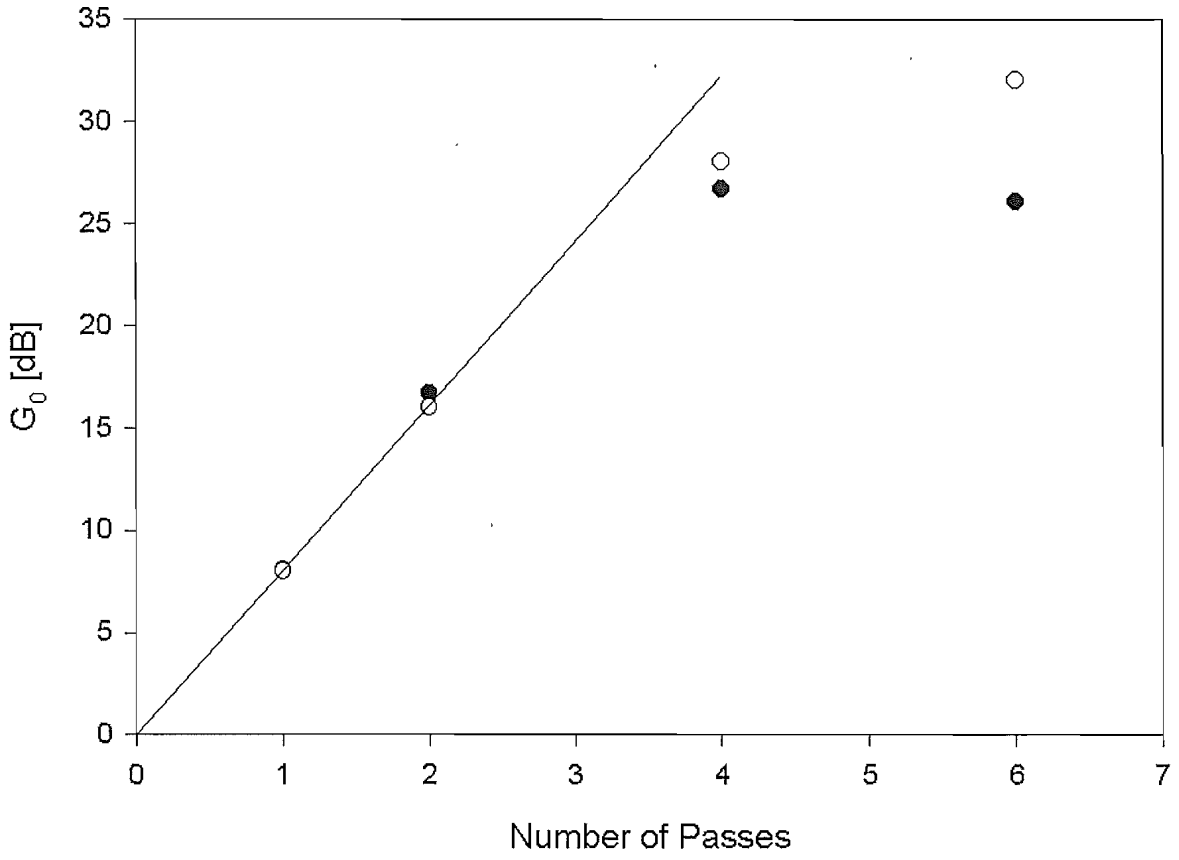

Figure (6-20) Small-signal gain with the number of passes. The solid line is calculated from $n\ln(G_o)$, the black circles are the measured small-signal gains and the white circles are the predicted small-signal gains.

6.11 Pulse Amplification

As discussed at the end of the previous chapter, an acousto-optic modulator was placed after the master-oscillator so that shorter trains of mode-locked pulses could be selected. This allows the gain to build up between trains of pulses. Examples of an amplified and un-amplified pulse generated by the modulator and the master oscillator operating in CW mode are shown in figure (6-21). The pulses were measured using a fast photo-diode. In figure (6-21) the solid line is the amplified signal and the dotted line is the un-amplified signal. As can be seen from figure (6-21), the initial part of the pulse, i.e. the leading edge if the switch on time of the modulator is short enough, experiences the unsaturated gain, with the rest of the pulse then experiencing the saturated gain.

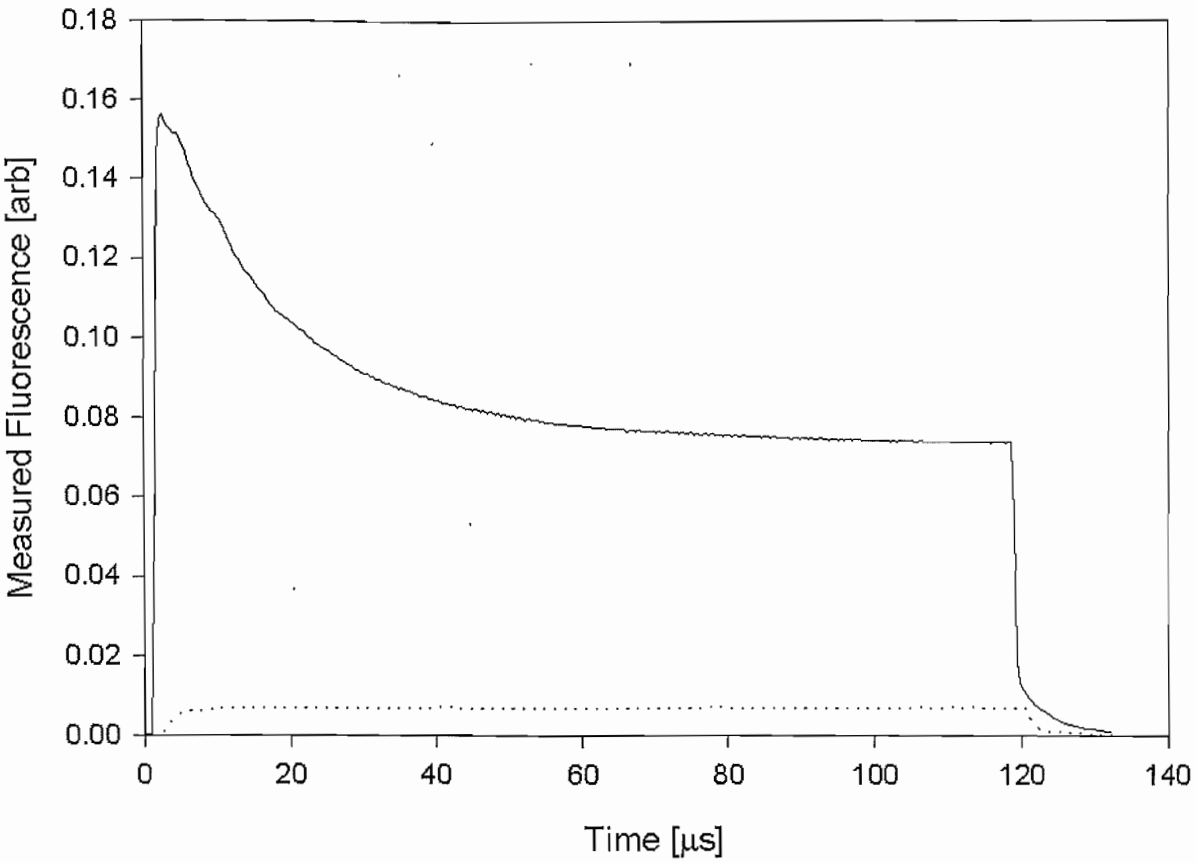

Figure (6-21). Intensity of an un-amplified pulse and an amplified pulse on the same scale. The solid line is the amplified pulse, and the dotted line is the un-amplified pulse.

For pulses where the pulse duration is shorter than the fluorescence lifetime the energy gain is given by [1]

$$G = \frac{E_S}{E_{IN}} \ln\left[1 + \left(\exp\left(\frac{E_{IN}}{E_S}\right) - 1\right)\ln(G_0)\right] \tag{6-54}$$

where E_S is the saturated fluence, E_{IN} is the input fluence and $\ln(G_0)$ is the small signal gain. The saturation fluence is given by

$$E_S = \frac{h\nu}{\sigma} \tag{6-55}$$

By measuring the average power of the beam, the repetition rate of the pulses, and integrating the intensity measured by the fast photo-diode the energy fluence can be calculated for the different pulse durations. The gain can then be determined for the pulses from a comparison of the amplified and un-amplified pulses. The gains calculated in this way are shown in figure (6-22). In figure (6-22) the black circles, are the measured gains for the different pulse durations, the solid line is calculated from equation (6-54) with the

measured value for the small-signal gain of the two pass amplifier being $\ln(G_0)=45$ and the dotted line is for a value of $\ln(G_0)=70$. As can be seen the theoretical lines do not match the gains for large pulse durations, when the pulse durations are greater than the fluorescence lifetime and equation (6-54) does not hold. The measured value for the small-signal gain gives good fit for the pulses in the 10-100μs region. With a better fit to the shorter pulse durations being achieved by the higher value for the small signal gain.

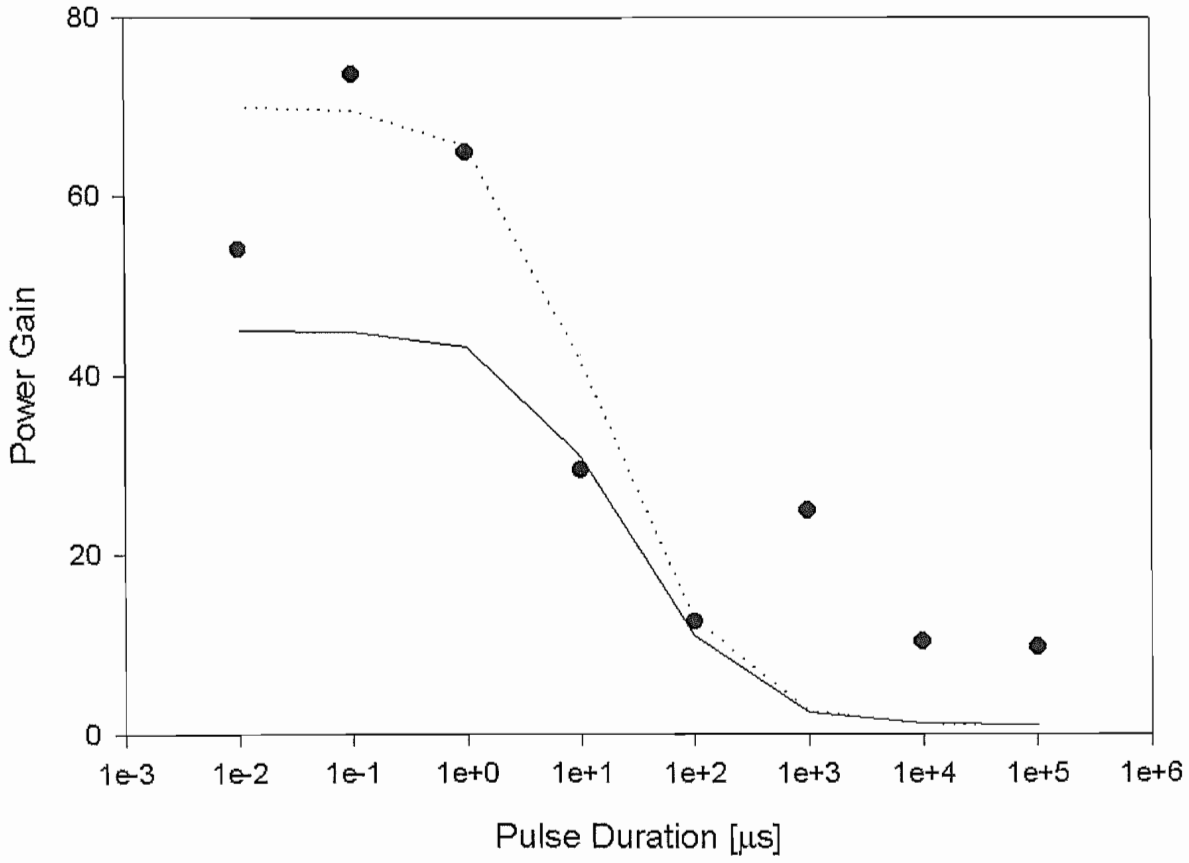

Figure (6-18). Measured values for the gain for different pulse durations. The solid line is obtained by using the measured value of the small signal gain (45), and the dotted line is for a value of 70 used in equation (6-54)

6.12 Discussion

This chapter has discussed the power scaling of solid-state lasers using amplifiers. It has been shown that both ETU and thermal lensing can decrease the potential gain of an amplifier, through a combination of a reduction in the population inversion density and a decrease in the overlap between the signal and pump beams in the amplifier crystals. However, there must come a point at which an amplifier not only increases the power of the signal beam but degrades its beam quality. At this point, the brightness of the laser source may no longer be increased by further amplification. The output beam brightness scales with the number of crystals and passes per amplifier and amplifier as

$$M_{OUT}^2 = \sqrt{\left(M_{IN}^2\right)^2 + n_c n_p n_a \left(M_Q^2\right)} \tag{6-56}$$

where $n_{c,p,a}$ are the number of crystals, passes and amplifiers respectively. The small-signal gain scales as

$$\ln\left(G_0\right) = n_c n_p n_a \ln\left(G_0\right) \tag{6-57}$$

For an incident beam of power P_{IN} and beam quality factor M_{IN}^2 in the two orthogonal planes, the initial brightness of the beam is given by

$$B_{IN} = \frac{P_{IN}}{\lambda\left(M_{IN}^2\right)^2} \tag{6-58}$$

The output beam will have a power of P_{OUT} and a beam quality factor M_{OUT}^2 in the two orthogonal planes, the output brightness of the beam will be

$$B_{OUT} = \frac{P_{OUT}}{\lambda\left(M_{OUT}^2\right)^2} \tag{6-59}$$

The brightness amplification or degradation is then given by the ratio of equations (6-58) and (6-59)

$$\frac{B_{OUT}}{B_{IN}} = \frac{n_c n_p n_a \ln\left(G_0\right)}{1 + n_c n_p n_a \left(M_Q^2\right)^2} \tag{6-60}$$

where it has been assumed that the incident beam is diffraction limited. For brightness amplification to occur equation (6-60) must be greater than one.

Inserting the maximum small-signal gain achievable before stress fracture occurs and the beam quality degradation at this absorbed pump power equation (6-60) becomes

$$\left[\frac{B_{OUT}}{B_{IN}}\right]=\frac{n_c n_p n_a 32\sigma\sqrt{\dfrac{\pi Rn}{\alpha_P \delta_{nl} hcM^2 W}}}{1+n_c n_p n_a\left(\dfrac{8\pi R(dn/dT)}{\alpha_P K_c \lambda\sqrt{2}}\right)^2} \tag{6-61}$$

If we have an indefinite number of gain media, passes an amplifiers equation (6-61) tends to a maximum value, and represents the highest small-signal gain that can be achieved without degrading the beam quality irrespective of the number of passes of different gain media and neglecting thermal lensing effects is given by

$$[MAX]=\left(\frac{\alpha_P}{R\pi}\right)^{1.5}\left(\frac{K_c\lambda}{(dn/dt)}\right)^2\sqrt{\frac{n}{\delta hcM^2 W}} \tag{6-62}$$

Table (6-3) shows the maximum small signal gain possible before stress fracture will occur, yet still increasing brightness. Due to its large thermal shock parameter, the pump power in Nd:YAG can be increased to such a level before stress-fracture occurs that serious beam quality degradation can be a problem. Nd:YLF, which is relatively susceptible to stress fracture, has the next highest possible gains. But Nd:YVO_4 with its large stimulated emission cross-section can generate the highest gains before beam quality degradation and stress fracture occur.

	Nd:YVO_4	Nd:YAG	Nd:YLF
K_c [$Wm^{-1}K^{-1}$]	5	13	6.3
R[Wm^{-1}]	480	480	200
α_P[m^{-1}]	4000	300	1100
W[$x10^{-22}$ m^3s^{-1}]	3.5	0.5	1.7
dn/dT [$x10^{-6}$]	3.9	7.3	4.3
σ [$x10^{-23}$ m^2]	15.6	4.6	1.9
MAX	28	0.4	5.5

Table (6-3). Maximum small–signal gain that can be achieved in a material before stress fracture will occur yet still increasing the brigthness

Reference:

1. Koechner, W., *Solid-State Laser Engineering*. 5 ed. Springer Series in Optical Sciences, ed. A.L. Schawlow, A.E. Siegman, and T. Tamir. Vol. 1. 1999, Berlin: Springer.
2. Siegman, A.E., *Lasers*. 1986, Sausalito, California: University Science Books.
3. Adams, R.A., *Calculus: A Complete Course*. 4 ed. 1999, Ontario: Addison-Wesley.
4. Nicolaescu, R., E.S. Fry, and T. Walther, *Generation of near-Fourier-transform-limited high-energy pulses in a chain of fiber-bulk amplifiers.* Optics Letters, 2001. **26**(1): p. 13-15.
5. Plaessmann, H., et al., *Multipass diode-pumped solid-state optical amplifier.* Optics Letters, 1993. **18**(17): p. 1420-1422.
6. Georges, P., et al., *High-efficiency multipass Ti:sapphire amplifiers for a continuous-wave single-mode laser.* Optics Letters, 1991. **16**(3): p. 144-146.

Chapter 7: Conclusions and Future Work

7.1 Conclusion

In conclusion, this thesis has shown that the power-scaling of diode-end-pumped solid state is an attractive means of efficiently generating laser emission and that Nd:YVO_4 represents a good choice for the gain medium. As was discussed, as the output power of these devices is increased the ensuing thermal effects hinder the maintenance of good beam quality. The strength of these thermal effects is further increased by unwanted spectroscopic processes. One such process is energy transfer upconversion, ETU. The amount of ETU that occurs in Nd:YVO_4 and the thermal effects as evidenced by thermal lensing were investigated in this thesis. Their impact was studied both theoretically and experimentally. Much of this work employed novel techniques and generated new results. As a consequence of these measurements a master oscillator power amplifier has been designed and constructed to power-scale these sources based on Nd:YVO_4. This MOPA generates high average output power in a diffraction limited beam for both CW and mode-locked operation.

The rate of ETU was measured by recording the fluorescence decay from the upper laser level. This measurement resulted in a value of $3.5 \times 10^{-22} m^3 s^{-1}$ for the 1% doped Nd:YVO_4 crystal and is lower than that measured elsewhere. This measurement also showed that the ETU process is migration assisted, which is something that until now has been assumed in the literature. A modified equation for the pump power required to reach threshold where the loss due to ETU has been included was derived for the first time. This was achieved by solving the rate equations for the upper laser level and the number of cavity photons. A cavity in which the cavity loss could be varied with a glass plate was used to verify the derived equation and provide further evidence for the measured value of the ETU parameter. It was found that the ETU parameter did not have a significant impact on the threshold pump power.

A modified Mach-Zehnder interferometer was used to make a detailed study of the thermal lensing in Nd:YVO_4 for the first time. The novel technique has several distinct advantages over other measurement techniques such as the ability to determine the thermal lensing in arbitrary directions and probe beam polarisations and

the lensing could be measured under lasing and non-lasing conditions. The thermal lens focal length can be determined by building up a phase profile of the optical path length difference caused by the thermal changes. The thermal lensing was determined for different cooling geometries, probe beam polarisations, lasing conditions and dopant concentrations. By analysing the thermal lensing with probe beam polarisation it was found that the π-polarisation that has the highest gain exhibits the weakest lensing. This analysis also showed that the bulk expansion significantly contributes to the strength of the thermal lensing. This was found because of the modification it makes to the expected ratio of the thermal lenses based on polarisation alone. By comparing the thermal lensing with cooling direction it was found that the weakest thermal lensing occurred when the cooling was provided along the a-axis. Cooling solely along this axis will however generate astigmatic thermal lenses that will require some form of compensation. The effect of ETU on thermal lensing was demonstrated by comparing the thermal lensing under lasing and non-lasing conditions and the different thermal lensing with dopant concentration. When the thermal lenses under lasing and non-lasing conditions are compared it demonstrates that the heating in the laser crystal under non-lasing conditions is significantly greater than under lasing conditions. This was shown by the thermal lenses being almost 5 times stronger under non-lasing conditions than under lasing condition for the 1% doped crystal. This would be expected because the larger population inversion densities that are achieved under these conditions increases the rate of ETU and consequently the generated heat. This ratio is greater than would be expected if all of the absorbed pump power is converted to heat. Therefore, it also shows that non-linear changes in the thermal conductivity and the thermo-optical coefficient could now be occurring with this configuration. By comparing the effect of dopant concentration on thermal lensing it could be seen, that under non-lasing conditions the thermal lensing for the 0.3% doped crystal was much lower than that of the 1% doped crystal. By comparing the variation of Γ, the ratio of thermal lenses with and without lasing, with absorbed pump power provided further evidence for the measured value of the ETU parameter.

Having investigated the thermal problems that hinder the efficient power-scaling of end-pumped solid-state lasers in Nd:YVO_4, the design concepts and the justification for using Nd:YVO_4 for this work was made. With its large $\sigma\tau$ product, naturally

polarised output, large absorption coefficient and broad absorption band at 800nm making Nd:YVO_4 a good choice for power-scaling solid-state lasers. An amplitude modulated mode-locked laser was built generating 600mW of diffraction limited output and 100ps pulses. This oscillator forms the master oscillator of a MOPA system.

Finally, an analysis of the effects of ETU and thermal lensing on amplification was made. A model was built up from existing gain equations to include the decrease in gain caused by ETU for the first time. The concept of an average spot size was used to highlight the effects of thermal lensing on amplifiers. Where it was found that the thermal lenses change the signal beam divergence this alters the overlap of the signal and pump beams in the amplifier and decreases the effective gain. This simple model was extended for multi-pass amplification with the effect of the thermal lenses becomes significantly stronger due to the increased number of passes. The predictions of this model were shown to give good predictions by constructing an amplifier containing 2 Nd:YVO_4 crystals. This amplifier could be made to be single or multi-pass by the addition of different mirrors. It was found that there was good agreement between the model and the experimental results for the small-signal gain up to a six pass configuration. There was not as good agreement for this configuration as compared to the others and this is attributed the signal beams being at an angle to the optical axis. This final effect is not included in the model and is expected to decrease the gain because the effective gain path is decreased. Using the output from the mode-locked laser built earlier and using a 4 pass amplifier configuration 5W of output was achieved, with the beam remaining diffraction limited. The prospects for further power scaling were investigated and it was shown that the limit to power scaling via amplifiers is the eventual beam quality degradation that will be suffered as the signal beam passes through the thermal lenses in the laser crystal. An equation was presented that analysed the limitations of scaling via amplifiers, finding that when stress-fracture and beam quality degradation are considered, Nd:YVO_4 represents an excellent choice for further power scaling.

7.2 Future Work

A stated motivation for this work was to build a source suitable for pumping synchronous optical parametric oscillators with the intention of generating tuneable light in the blue/UV region of the spectrum. For this to be achieved efficiently by nonlinear frequency conversion, high intensities are required. There are two ways that could be pursued to achieve higher intensities from the source. Increase the power of the beam or try to shorten the pulse duration of the pulses.

With the AM mode-locker being tuned to 100MHz, there is little prospect of pushing this device further to generate shorter pulses. However, the master oscillator could be developed into a hybrid system with perhaps a Kerr lens media in the cavity. The AM modulator could be used to initiate mode-locking and the Kerr-media with a suitable aperture, hard or soft, could then provide the intensity dependent loss that would encourage the evolution of shorter pulses. This system would retain the robustness of the active mode-locking system with the shorter pulses of the passive system.

The power of the master oscillator could be scaled by the use of more powerful pumps for the master oscillator itself. This would saturate the gain in the first amplifier and increasing the extraction efficiency. The pump sources for the amplifier could be increased so that higher gains would be possible in the amplifier, and extra amplifiers could be added in a chain. This has the advantage that the output from each successive amplifier is used to saturate the gain in the next one increasing the extraction efficiency of the overall system.

Appendix A: ETU Threshold Calculation

The rate equation analysis for the threshold pump power of Kubodera and Otsuka [1] is extended to include the losses due to ETU. This produces an expression for the pump power that includes ETU in terms of the threshold pump power without ETU.

The rate equation of the excited population given by

$$\frac{dn(r,z,t)}{dt} = r_p(r,z,t) - c_n \sigma s(r,z,t) n(r,z,t) - \frac{n(r,z,t)}{\tau} - \alpha n(r,z,t)^2 . \qquad \text{(A-1)}$$

Where $r_p(r,z,t)$ is the pumping rate, c_n is the speed of light in the gain medium, σ is the stimulated emission cross-section, $s(r,z,t)$ is the number of photons in the laser mode, τ is the fluorescence lifetime and α the upconversion parameter. The first term on the right hand side is the increase in population inversion density due to pumping, the second is the depopulation due to stimulated emission, the third is the depopulation due to spontaneous emission and the final that depopulation caused by upconversion. Upconversion only reduces the population inversion density by one because the rate of multiphonon is assumed to be fast enough for there to be a negligible population in the excited levels.

The rate equation of the number of photons in the laser mode is given by

$$\frac{ds(r,z,t)}{dt} = \int_{cav} c_n \sigma s(r,z,t) n(r,z,t) dV - \int_{cav} \gamma s(r,z,t) dV . \qquad \text{(A-2)}$$

Where $\gamma = 1/\tau_c$, with τ_c being the cavity lifetime. The first term on the right hand side is the increase in the number of photons in the cavity by stimulated emission and the second term is the decrease in the number of photons caused by cavity losses.

Under steady state conditions, the populations are invariant in time so

$$\frac{dn}{dt} = \frac{ds}{dt} = 0 . \qquad \text{(A-3)}$$

Using equations (A-1) and (A-3) to determine the steady state population inversion density $n_E(r,z)$ in terms of the steady state photon density, $s_E(r,z)$, and using a saturation intensity defined as $I_0 = 1/(c_n \sigma \tau)$ gives

$$\alpha\tau n_E(r,z)^2 + \left(1+\frac{s_E(r,z)}{I_0}\right)n_E(r,z) - \tau r_p(r,z) = 0 \qquad \text{(A-4)}$$

Equation (A-4) can be solved to give $n_E(r,z)$

$$n_E(r,z) = \frac{-\left(1+\frac{s_E(r,z)}{I_0}\right) + \sqrt{\left(1+\frac{s_E(r,z)}{I_0}\right)^2 + 4\alpha\tau^2 r_p(r,z)}}{2\alpha\tau} \qquad \text{(A-5)}$$

Substitution of (A-5) into (A-2) yields

$$2\alpha\tau^2\gamma I_0 = \int_{cav}\left[-\left(1+\frac{S_E s_0(r,z)}{I_0}\right) + \sqrt{\left(1+\frac{S_E s_0(r,z)}{I_0}\right)^2 + 4\alpha\tau^2 R r_0(r,z)}\right] s_0(r,z)dV \,. \qquad \text{(A-6)}$$

Where $r_0(r,z)$ and $s_o(r,z)$ are normalized distributions given by

$$\begin{aligned} s_E(r,z) &= S_E s_0(r,z) \\ r(r,z) &= R r_0(r,z) \end{aligned} \qquad \text{(A-7)}$$

and

$$\int_{cav} r_0(r,z)dV = \int_{cav} s_0(r,z)dV = 1 \,. \qquad \text{(A-8)}$$

Where S_E is the cavity photon number and R is the pump rate. The cavity photon number may be expressed in terms of the output power, P_{LO}.

$$S_E = \frac{2l_c P_{LO}}{ch\upsilon_L T} \,. \qquad \text{(A-9)}$$

Where l_c is the cavity length, υ_L is the laser frequency and T is the transmission of the output coupler.

If it is assumed that the pump causes negligible depletion of the ground state, the total pump rate is given by the incident pump power P_p

$$R = \frac{P_p\eta_q\left[1-\exp(-\alpha_p l)\right]}{h\upsilon_P} \,. \qquad \text{(A-10)}$$

Where η_q is the pumping quantum efficiency, α_p is the absorption coefficient, l is the length of the gain medium and υ_p is the pump frequency. The pumping quantum

efficiency is the number of atoms excited to the upper laser level for each absorbed pump photon.

At threshold, there is no stimulated emission with no laser output, P_{LO}=0, and inserting equation (A-8) into equation (A-6) leads to

$$2\tau^2\alpha\gamma I_0 = \int_{cav}\left[-1+\sqrt{1+\frac{4\alpha\tau^2 P_{th}\eta_q\left[1-\exp(-\alpha_P l)\right]}{h\upsilon_P}r_0(r,z)}\right]s_0(r,z)dV \qquad \text{(A-11)}$$

Assuming a top-hat profile for the pump distribution and a Gaussian distribution for the laser mode such that the normalized distributions become

$$r_0(r,z)=\frac{\alpha_P\exp(-\alpha_P z)}{\pi W_P^2\left[1-\exp(-\alpha_p l)\right]} \text{ for } r<W_p \text{ and } r_0(r,z)=0 \text{ for } r>W_p \qquad \text{(A-12)}$$

and

$$s_0(r,z)=\frac{2cf(z)}{c_n\pi W_L^2 l_c}\exp\left(\frac{-2r^2}{W_L^2}\right). \qquad \text{(A-13)}$$

Where $W_{p,L}$ are the pump and laser beam waists in the gain medium and $f(z)$ is the axial dependence of $s_0(r,z)$. The pump and laser spot sizes are assumed to be constant over the length of the gain medium. For single longitudinal-mode operation $f(z)=2\sin^2 kz$, since $f(z)$ varies more rapidly then the variation of the pump rate with distance and $l>\lambda$ then it can be assumed that $f(z)\approx 1$.

Substituting equations (A-12) and (A-13) into equation (A-11) and performing the integration over θ gives

$$\begin{aligned}2\tau^2\alpha\gamma I_0 = &\int_0^l\left(-1+\sqrt{1+\frac{4\alpha\tau^2 P_{th}\eta_q\alpha_p\exp(-\alpha_P z)}{\pi h\upsilon_P W_P^2}}\right)\int_0^{W_P}\frac{4c}{c_n W_L^2 l_c}\exp\left(\frac{-2r^2}{W_L^2}\right)rdrdz \\ &+\int_0^l\left(-1+\sqrt{1}\right)\int_{W_P}^{\infty}\frac{4c}{c_n W_L^2 l_c}\exp\left(\frac{-2r^2}{W_L^2}\right)rdrdz\end{aligned} \qquad \text{(A-14)}$$

Performing the integration of (A-12) over r gives

$$2\tau^2\alpha\gamma I_0 = \int_0^l\left(-1+\sqrt{1+\frac{4\alpha\tau^2 P_{th}\eta_q\alpha_p\exp(-\alpha_P z)}{\pi h\upsilon_P W_P^2}}\right)\frac{c}{c_n l_c}\left[1-\exp\left(\frac{-2W_P^2}{W_L^2}\right)\right]dz \qquad \text{(A-15)}$$

Equation (A-13) can be reduced in the following way

$$\frac{2\tau^2\alpha\gamma I_0 c_n l_c}{c}\left[1-\exp\left(\frac{-2W_P^2}{W_L^2}\right)\right]^{-1} = \int_0^l\left(-1+\sqrt{1+b\exp(-\alpha_P z)}\right)dz \tag{A-16}$$

where

$$b=\frac{4\alpha\tau^2 P_{th}\eta_q\alpha_p}{\pi h\upsilon_P W_P^2}. \tag{A-17}$$

Making the substitution U=exp(-$\alpha_p z$) equation (A-14) becomes

$$\frac{2\tau^2\alpha\gamma I_0 c_n l_c}{c}\left[1-\exp\left(\frac{-2W_P^2}{W_L^2}\right)\right]^{-1} = -l+\int_{\exp(-\alpha_p l)}^{1}\frac{\sqrt{1+bU}}{\alpha_p U}dU \tag{A-18}$$

With the following substitution V^2=bU equation (A-15) becomes

$$\frac{2\tau^2\alpha\gamma I_0 c_n l_c}{c}\left[1-\exp\left(\frac{-2W_P^2}{W_L^2}\right)\right]^{-1} = -l+\int_{\sqrt{b\exp(-\alpha_p l)}}^{\sqrt{b}}\frac{2\sqrt{1+V^2}}{\alpha_p V}dV = I \tag{A-19}$$

The integral of equation (A-16) can be determined by using the following identity [2]

$$\int\frac{\sqrt{x^2+a^2}}{x}dx=\sqrt{x^2+a^2}-a\ln\left(\frac{a+\sqrt{x^2+a^2}}{x}\right)+C. \tag{A-20}$$

Using equation (A-17) to solve (A-16) yields

$$I=-l+\frac{2}{\alpha_p}\left[\begin{array}{l}\sqrt{b+1}-\sqrt{b\exp(-\alpha_p l)+1}\\+\ln\left(\dfrac{1+\sqrt{b\exp(-\alpha_p l)+1}}{\sqrt{b\exp(-\alpha_p l)}}\right)-\ln\left(\dfrac{1+\sqrt{b+1}}{\sqrt{b}}\right)\end{array}\right] \tag{A-21}$$

$$I=-l+\frac{2}{\alpha_p}\left[\begin{array}{l}\sqrt{b+1}-\sqrt{b\exp(-\alpha_p l)+1}+\ln\left(1+\sqrt{b\exp(-\alpha_p l)+1}\right)\\-\ln\left(\sqrt{b\exp(-\alpha_p l)}\right)-\ln\left(1+\sqrt{b+1}\right)+\dfrac{1}{2}\ln(b)\end{array}\right] \tag{A-22}$$

$$I=-l+\frac{2}{\alpha_p}\left[\begin{array}{l}\sqrt{b+1}-\sqrt{b\exp(-\alpha_p l)+1}+\ln\left(1+\sqrt{b\exp(-\alpha_p l)+1}\right)\\-\dfrac{1}{2}\ln(b)-\dfrac{1}{2}\ln\left(\exp(-\alpha_p l)\right)-\ln\left(1+\sqrt{b+1}\right)+\dfrac{1}{2}\ln(b)\end{array}\right] \tag{A-23}$$

$$I=-l+\frac{2}{\alpha_p}\left[\begin{array}{l}\sqrt{b+1}-\sqrt{b\exp(-\alpha_p l)+1}+\ln\left(1+\sqrt{b\exp(-\alpha_p l)+1}\right)\\+\dfrac{\alpha l}{2}-\ln\left(1+\sqrt{b+1}\right)\end{array}\right] \tag{A-24}$$

$$I=\frac{2}{\alpha_p}\left[\sqrt{b+1}-\sqrt{b\exp(-\alpha_p l)+1}+\ln\left(\frac{1+\sqrt{b\exp(-\alpha_p l)+1}}{1+\sqrt{b+1}}\right)\right] \tag{A-25}$$

Inserting equation (A-22) into equation (A-16) gives

$$\frac{\tau^2\alpha\alpha_p\gamma I_0 c_n l_c}{c}\left[1-\exp\left(\frac{-2W_P^2}{W_L^2}\right)\right]^{-1}=\sqrt{b+1}-\sqrt{b\exp(-\alpha_p l)+1}+\ln\left(\frac{1+\sqrt{b\exp(-\alpha_p l)+1}}{1+\sqrt{b+1}}\right)$$

(A-26)

Assuming that all of the pump power is absorbed in the gain medium, so that exp(-$\alpha_p l$)~0, equation (A-23) becomes

$$\frac{\tau^2\alpha\alpha_p\gamma I_0 c_n l_c}{c}\left[1-\exp\left(\frac{-2W_P^2}{W_L^2}\right)\right]^{-1}=\sqrt{b+1}-1+\ln\left(\frac{2}{1+\sqrt{b+1}}\right) \qquad \text{(A-27)}$$

At low powers, the first term of the right hand side is greater then the term in the logarithm and is close to 0 at low powers so equation (A-27) approximates to

$$\frac{\tau^2\alpha\alpha_p\gamma I_0 c_n l_c}{c}\left[1-\exp\left(\frac{-2W_P^2}{W_L^2}\right)\right]^{-1}\approx\sqrt{b+1}-1 \qquad \text{(A-28)}$$

Solving equation (A-25) for the threshold pump power gives

$$P_{th}=\frac{\gamma I_0 c_n l_c \pi h\upsilon_P W_P^2}{4c\eta_q}\left[1-\exp\left(\frac{-2W_P^2}{W_L^2}\right)\right]^{-1}\left(2+\frac{\tau^2\alpha\alpha_p\gamma I_0 c_n l_c}{c}\left[1-\exp\left(\frac{-2W_P^2}{W_L^2}\right)\right]^{-1}\right)$$

(A-29)

When α=0 equation (A-26) becomes

$$P_{th}=\frac{\gamma I_0 c_n l_c \pi h\upsilon_P W_P^2}{2c\eta_q}\left[1-\exp\left(\frac{-2W_P^2}{W_L^2}\right)\right]^{-1} \qquad \text{(A-30)}$$

Inserting $\gamma=c(L+T)/2l_c$ and substituting for I_0 yields

$$P_{th\alpha 0}=\frac{\pi h\upsilon_P (L+T)W_P^2}{4\sigma\tau\eta_q}\left[1-\exp\left(\frac{-2W_P^2}{W_L^2}\right)\right]^{-1} \qquad \text{(A-31)}$$

This is obtained by inserting (A-12) and (A-13) in the equation for the threshold power without ETU [3]

$$P_{pth}=\frac{h\upsilon_P\gamma I_0}{\eta_q\left[1-\exp(-\alpha_p l)\right]}\left[\int_{cav} r_0(x,y,z)s_0(x,y,z)dV\right]^{-1} \qquad \text{(A-32)}$$

The threshold pump power with ETU can be expressed in terms of the threshold pump power without ETU by

$$P_{th} = P_{th\alpha 0}\left(1+\frac{(L+T)\alpha\tau\alpha_P}{4\sigma}\left[1-\exp\left(\frac{-2W_P^2}{W_L^2}\right)\right]^{-1}\right) \qquad \text{(A-33)}$$

References

1. Kubodera, K. and K. Otsuka, Journal of Applied Physics, 1979. **50**: p. 653.
2. Adams, R.A., *Calculus: A Complete Course*. 4 ed. 1999, Ontario: Addison-Wesley.
3. Clarkson, W.A. and D.C. Hanna, *Effects of transverse-mode profile on slope efficiency and relaxation oscillations in a longitudinally-pumped laser*. Journal of Modern Optics, 1989. **36**(4): p. 483-498.

Appendix B: Fraction of absorbed pump converted to heat.

In this appendix the fraction of absorbed pump power that is converted to heat in a four-level laser system is derived. It is assumed that there is negligible ground state bleaching and that there is an insignificant population in the higher excited levels. The number of ions that decay via fluorescence, $\gamma(r,z)$, is given by

$$\gamma(r,z)=\frac{-1+\sqrt{1+4W\tau^2 r_p(r,z)}}{2W\tau^2 r_p(r,z)} \tag{B-1}$$

where W is the upconversion parameter, $r_p(r,z)$ is the pump rate into the upper laser level and τ is the fluorescence lifetime of the upper laser level.

The amount of absorbed pump power converted to heat per unit volume is given by

$$Q(r,z)=\alpha_p I_p(r,z)\left[1-(1-\rho)\gamma(r,z)\right] \tag{B-2}$$

Inserting (B-1) into (B-2) gives

$$Q(r,z)=\alpha_p I_p(r,z)-(1-\rho)\frac{\alpha_p I_{ETU}}{2}\left[-1+\sqrt{1+\frac{4}{I_{ETU}}I_p(r,z)}\right] \tag{B-3}$$

where α_p is the absorption coefficient, $I_p(r,z)$ is the pump intensity, I_{ETU} is the upconversion saturation intensity defined as

$$I_{ETU}=\frac{h\nu_P}{\alpha_P W\tau^2} \tag{B-4}$$

The amount of heat generated in the crystal can then be determined by integrating over the pumped volume.

$$P_{heat}=\int_0^l\left\{\begin{array}{l}\displaystyle\int_0^{3w_p}\alpha_p I_p(r,z)2\pi r dr+\int_0^{3w_p}(1-\rho)\frac{\alpha_p I_{ETU}}{2}2\pi r dr\\ \displaystyle-\int_0^{3w_p}(1-\rho)\frac{\alpha_p I_{ETU}}{2}\sqrt{1+\frac{4}{I_{ETU}}I_p(r,z)}2\pi r dr\end{array}\right\}dz \tag{B-5}$$

Using the methodology and substitutions employed in appendices A and B the third integration of (B-5) can be performed over r to give

$$P_{heat} = \int_0^l \left\{ \begin{array}{l} \alpha_p P \exp(-\alpha_p z) + \\ (1-\rho)\frac{\alpha_p P_{ETU}}{2}\left[\begin{array}{l} 1 - \sqrt{\frac{8P}{P_{ETU}}\exp(-\alpha_p z)+1} \\ + \ln\left(\frac{1+\sqrt{\frac{8P}{P_{ETU}}\exp(-\alpha_p z)+1}}{2} \right) \end{array} \right] \end{array} \right\} dz \qquad \text{(B-6)}$$

Where P_{ETU} is defined as

$$P_{ETU} = \frac{h\nu_p \pi w_p^2}{\alpha_p W \tau^2} \qquad \text{(B-7)}$$

Splitting equation (B-6) into five smaller integrals

$$I_1 = \int_0^l \alpha_p P \exp(-\alpha_p z) dz = P(1 - \exp(-\alpha_p l)) \qquad \text{(B-8)}$$

$$I_2 = \int_0^l (1-\rho)\frac{\alpha_p P_{ETU}}{2} dz = (1-\rho)\frac{\alpha_p P_{ETU}}{2} l \qquad \text{(B-9)}$$

$$I_3 = \int_l^0 (1-\rho)\frac{\alpha_p P_{ETU}}{2}\sqrt{\frac{8P}{P_{ETU}}\exp(-\alpha_p z)+1} dz$$

$$= (1-\rho)P_{ETU}\left\{ \begin{array}{l} \sqrt{\frac{8P}{P_{ETU}}\exp(-\alpha_p l)+1} - \sqrt{\frac{8P}{P_{ETU}}+1} \\ + \ln\left(\frac{1+\sqrt{\frac{8P}{P_{ETU}}+1}}{1+\sqrt{\frac{8P}{P_{ETU}}\exp(-\alpha_p l)+1}} \right) - \frac{\alpha_p l}{2} \end{array} \right\} \qquad \text{(B-10)}$$

Splitting the final term into two so that there are two integrals, the fourth integration becomes

$$I_4 = \int_0^l (1-\rho)\frac{\alpha_p P_{ETU}}{2} \ln\left(1 + \sqrt{\frac{8P}{P_{ETU}}\exp(-\alpha_p z)+1}\right) dz \qquad \text{(B-11)}$$

Equation (B-11) can be evaluated by making the following substitution

$$W = \sqrt{\frac{8P}{P_{ETU}}}\exp\left(-\frac{\alpha_p z}{2}\right) \qquad \text{(B-12)}$$

So that equation (B-11) becomes

$$I_4 = -(1-\rho)P_{ETU}\int_{\sqrt{\frac{8P}{P_{ETU}}}}^{\sqrt{\frac{8P}{P_{ETU}}\exp(-\alpha_p l)}} \ln\left(1+\sqrt{W^2+1}\right)\frac{1}{W}dW \qquad \text{(B-13)}$$

This can be further simplified by using the substitution

$$U = \sqrt{W^2+1} \qquad \text{(B-14)}$$

Leading to a final integral of

$$I_4 = -(1-\rho)P_{ETU}\int_{\sqrt{\frac{8P}{P_{ETU}}+1}}^{\sqrt{\frac{8P}{P_{ETU}}\exp(-\alpha_p l)+1}} \ln(1+U)\frac{U}{U^2-1}dU \qquad \text{(B-15)}$$

This has the solution

$$I_4 = \frac{(1-\rho)P_{ETU}}{2}\left\{\begin{array}{l}\frac{1}{2}\left(\ln\left(1+\sqrt{\frac{8P}{P_{ETU}}+1}\right)^2 - \ln\left(1+\sqrt{\frac{8P}{P_{ETU}}\exp(-\alpha_p l)+1}\right)^2\right) \\ +\ln(2)\ln\left(\frac{\sqrt{\frac{8P}{P_{ETU}}+1}-1}{\sqrt{\frac{8P}{P_{ETU}}\exp(-\alpha_p l)+1}-1}\right) + \int_{\frac{1}{2}+\frac{1}{2}\sqrt{\frac{8P}{P_{ETU}}+1}}^{\frac{1}{2}+\frac{1}{2}\sqrt{\frac{8P}{P_{ETU}}\exp(-\alpha_p l)+1}} \frac{\ln(t)}{1-t}dt\end{array}\right\} \qquad \text{(B-16)}$$

The fifth integral is the following

$$I_5 = \int_l^0 (1-\rho)\frac{\alpha_p P_{ETU}}{2}\ln(2)dz = (1-\rho)\frac{\alpha_p P_{ETU}}{2}\ln(2)l \qquad \text{(B-17)}$$

Assuming that all of the pump power is absorbed then the addition of equations of (B-8) and (B-9) gives

$$I_2 + I_3 = (1-\rho)P_{ETU}\left\{1-\sqrt{\frac{8P}{P_{ETU}}+1}+\ln\left(\frac{1+\sqrt{\frac{8P}{P_{ETU}}+1}}{2}\right)\right\} \qquad \text{(B-18)}$$

Combining equations (B-16) and (B-17) gives

$$I_4 + I_5 = \frac{(1-\rho)P_{ETU}}{2}\left\{\begin{array}{l}\frac{1}{2}\left(\ln\left(1+\sqrt{\frac{8P}{P_{ETU}}+1}\right)^2 - \ln(2)^2\right) \\ +\ln(2)\left(\ln\left(\sqrt{\frac{8P}{P_{ETU}}+1}-1\right)-\ln\left(\frac{4P}{P_{ETU}}\right)\right)+\int_{\frac{1}{2}+\frac{1}{2}\sqrt{\frac{8P}{P_{ETU}}+1}}^{1}\frac{\ln(t)}{1-t}dt\end{array}\right\} \quad \text{(B-19)}$$

Finally combining equations (B-18) and (B-19) gives

$$P_{heat} = P + (1-\rho)P_{ETU}\left\{\begin{array}{l}1-\sqrt{\frac{8P}{P_{ETU}}+1}+\ln\left(\frac{1+\sqrt{\frac{8P}{P_{ETU}}+1}}{2}\right)\left(1+\frac{1}{4}\ln\left(2+2\sqrt{\frac{8P}{P_{ETU}}+1}\right)\right) \\ +\frac{\ln(2)}{2}\left(\ln\left(\sqrt{\frac{8P}{P_{ETU}}+1}-1\right)-\ln\left(\frac{4P}{P_{ETU}}\right)\right)+\frac{1}{2}\int_{\frac{1}{2}+\frac{1}{2}\sqrt{\frac{8P}{P_{ETU}}+1}}^{1}\frac{\ln(t)}{1-t}dt\end{array}\right\} \quad \text{(B-20)}$$

Appendix C: List of Publications

Published

I.O.Musgrave, W.A.Clarkson, D.C.Hanna 'Detailed study of thermal lensing in Nd:YVO_4 under intense diode end-pumping',*CLEO 2001* Baltimore 6-11 May 2001 CTuM26

I.O.Musgrave, W.A.Clarkson, D.C.Hanna 'Thermal lensing in Nd:YVO_4 under intense diode-end-pumping',*QEP-15* Glasgow 3-6 Sep 2001 pp.107

In Preperation

I.O. Musgrave, M.J. Yarrow, W.A. Clarkson 'ETU and its impact on CW laser operation in Nd:YVO_4'

I.O. Musgrave and W.A.Clarkson 'Influence of ETU on thermal lensing in Nd:YVO_4'

I.O. Musgrave and W.A.Clarckson 'Measurement of thermally induced aberrations in end-pumped solid-state lasers'

I.O. Musgrave, M.J. Yarrow and W.A. Clarkson 'Effect of ETU on the performance of diode-end pumped Nd:YVO_4 amplifiers'